Scanning Tunneling Microscopy Visualisation of Emergent Grain Boundaries on Cu (111) Surfaces

A thesis presented to the University of Dublin, Trinity College

for the degree of

Doctor of Philosophy in Chemistry

İpen Demirel

Under the supervision of Prof. John J. Boland

School of Chemistry & CRANN

Trinity College Dublin

2023

Declaration

I declare that this thesis has not been submitted as an exercise for a degree at this or any other university and it is entirely my own work.

I agree to deposit this thesis in the University's open access institutional repository or allow the library to do so on my behalf, subject to Irish Copyright Legislation and Trinity College Library conditions of use and acknowledgement.

_____ _____

İpen Demirel Date

Summary

While nanocrystalline materials offer numerous advantages in various applications due to their superior properties, the presence of grain boundaries inherent to these materials can have a detrimental impact on their efficiency in certain applications. Nonetheless, grain boundaries also provide an opportunity to manipulate the microstructure of nanomaterials for the benefit of developing and designing high-performance materials. In the past few decades, improved high resolution microscopy techniques and computational atomistic simulations have enabled the identification and quantitative characterization of grain boundaries in various materials at atomic scale, leading to the discovery of the desirable unique properties of each grain boundary. However, there are still areas of uncertainty and knowledge gaps regarding the structural transformation of grain boundaries and the impact related to their interaction with the free surfaces, which this thesis aims to address.

This thesis aims to provide new insight in the study of emergent grain boundaries on Cu (111), grain boundaries that emerge at the free surfaces of copper, using Scanning Tunneling Microscopy (STM). The STM, a pioneering probe microscopy technique in surface science, is a powerful tool to visualize and analyse the structural characteristics of grain boundaries that appear at the surface in atomic-scale detail, providing a novel perspective for the exploration of grain boundaries.

Emergent [111] tilt grain boundaries have been investigated on the surface of a 50 *nm* thick nanocrystalline (NC) Cu (111) thin film and on the surface of an engineered Cu (111) bicrystal (BC). The microstructural evolution of the NC Cu thin film through thermal annealing and the effect of the annealing temperature were demonstrated, along with the initial stages of dewetting. Following the optimization of the annealing temperature range for the improvement of the surface

morphology, the grain boundary rich texture of the Cu (111) surface was uncovered and the grain boundaries, built of arrays of edge dislocations were investigated.

The out-of-plane grain rotation, within the framework of grain boundary restructuring phenomenon, has been shown to manifest as valleys and ridges at the triple junctions, for various grain boundaries on the surface of NC Cu thin films. Driven by energy minimization, the grain boundary restructuring mechanism occurs as the dislocation cores shift towards [112], to a lower energy configuration, resulting in so-called core-shifted grain boundaries. Through comparative STM analysis of various valley type grain boundaries, a general trend in the out-of-plane grain rotation angle and behaviour was demonstrated, as a function of the misorientation angle. While in general the out-of-plane rotation scales with the misorientation angle, the manifestation of its extent is more localised for high-angle grain boundaries.

The STM analysis of the engineered grain boundary on the Cu BC revealed frequent step dynamics at room temperature, due to reconfiguration of highly unstable sites. The transmission of a screw dislocation across the grain boundary was captured dynamically in real-time. At metastable sites, a polytype phase with a 9R-like periodicity was found. Although the extrinsic (shear stress, temperature) or intrinsic (density of defects) conditions and the dislocation emission mechanism leading to this observation are not quantified in this work, it was attributed to the facilitated emission of Shockley partial dislocation loops as part of the relaxation near the surface at the triple junction, at room temperature.

At low temperature, vertical dislocation jumps and vertical faceting were demonstrated along the grain boundary, attributed to the relaxation of elastic strain introduced by the low twist component. The out-of-plane grain rotation seen on the NC Cu thin films was also observed on the surface of fully-relaxed well-

annealed Cu (111) BC, demonstrating it is the free surface that facilitates the restructuring in emergent grain boundaries in copper.

Through high resolution STM measurements, the periodicity and misorientation angle have been confirmed in atomic detail. Finally, these experimental observations were compared and supported by the molecular statics simulations of [111], $\theta = 13.17°$ core-shifted emergent tilt boundary, described as a wedge disclination at the free surface. The subsurface restructuring, *i.e.*, core-shift, was illustrated and the optimized depth of rotation, *i.e.*, extent of restructuring, corresponding to the energy minimum, was found to be determined by the interplay between the interfacial energy and the elastic stress.

Acknowledgements

First of all, I would like to thank Prof. John J. Boland, my PhD supervisor, for giving me the opportunity to pursue this research in his group, and for his support, guidance and encouragement throughout the years. John's enthusiasm and dedication towards science have been a great source of inspiration and have helped making this experience truly invaluable.

I would like to thank Dr. Borislav Naydenov, for sharing his extensive knowledge with me, not only on STM and UHV, but also on interpreting and representing data. His endless support has made the times spent in the basement worthwhile.

I'd like to thank Dr. Xiaopu Zhang for all the support and insight he provided on material science and simulations. I'd like to thank the rest of the Boland group members, Shannan, Joshua and Peter for all their help and support. I'd like to thank the former members of the Boland group, Prabhava, Sam, Emmet, Felim and Sahar, who helped me through the first few months of my time in the group. I'd like to Mary McCarthy for all her support.

I would like to use this opportunity to express my appreciation to Prof. H. Özgür Özer for introducing me to the fascinating field of surface science and for providing me with his invaluable guidance and support during my time in his research group. I'd also like to extend my gratitude to Prof. Graham Cross for numerous insightful discussions throughout the years.

I'm grateful to my special friends, Majid, Dicle, and Ahmed, who have been there at all times to back me up and make me smile. I'd like to thank Cathal, for always believing in me and my work, and always being there to uplift me. Go raibh maith agat, for helping us get through a global pandemic COVID-19 and bearing with me through my PhD.

I'd like to thank my little brother Demir, for all the joy he brings into my life and making me feel lucky. Finally, I'd like to express my deepest gratitude to my dear parents Hülya and Mehmet, to whom I dedicate this thesis. I owe my heartfelt thanks to you for your endless support and belief in me at every stage of my life. It's because of your unconditional and irreplaceable love, that I have been able to achieve my aspirations.

Contents

Summary i
Acknowledgements iv
Contents vi
List of Figures viii
List of Abbreviations xi
Publications & Presentations xii
1. Nanocrystalline Thin Films 1
1.1. Grain boundaries in metal thin films 3
1.1.1. Thin film interconnects 3
1.1.2. Cu interconnects and size effect 7
1.1.3. Grain boundary engineering in nanomaterials 11
1.2. Processing of Cu films 13
1.2.1. Oxidation and removal of oxide 13
1.2.2. Thermal processing of Cu thin films: grain growth & Mullins grooving 16
1.2.3. Dewetting 19
1.3. Observation of dislocations and grain boundaries 21
2. Experimental Techniques and Methods 28
2.1. Scanning tunneling microscopy 28
2.1.1. Elastic tunneling through a one-dimensional rectangular potential barrier 29
2.1.2. The WKB approximation – potential barrier of arbitrary shape 32
2.1.3. The Bardeen theory of tunneling current 33
2.1.4. Tersoff-Hamann model and Chen's expansion 37
2.1.5. Instrumentation 40
2.1.6. Imaging modes 43
2.1.7. Scanning tunneling spectroscopy 43
2.1.8. UHV system 47
2.1.9. Tip preparation 49
2.2. Atomic force microscopy 51
2.3. Molecular dynamics simulations 54
2.4. Scanning electron microscopy 56
2.5. Electron backscatter diffraction 58
3. Dislocations and Grain Boundaries 61
3.1. Defects in crystals 61
3.1.1. Point defects 63

3.2. Dislocations 65
3.2.1. Edge dislocation and Burgers vector 67
3.2.2. Screw dislocation 69
3.2.3. Stress field and strain energy of a single, straight dislocation 71
3.2.4. Stacking fault 73
3.2.5. Partial dislocations in fcc metals 75
3.3. Grain Boundaries 80
3.3.1. Grain boundary geometry 80
3.3.2. Symmetric tilt grain boundary 82
3.3.3. Elastic stress field and energy 86
3.3.4. Microscopic degrees of freedom and grain boundary relaxation 89
3.3.5. Coincidence site lattice 90
4. Emergent Grain Boundaries on the Surface of Cu Nanocrystalline Films 92
4.1. Introduction: the STM perspective of emergent grain boundaries 93
4.2. Preparation of NC Cu (111) surface 94
4.2.1. Chemical etching of the copper oxide 94
4.2.2. Thermal processing of NC Cu thin films 97
4.3. STM results on NC Cu film 105
4.3.1. Emergent grain boundaries and dislocations at the surface 107
4.3.2. Out-of-plane rotation 109
4.3.3. Low-angle/high-angle grain boundaries 111
4.4. Conclusion 116
5. Emergent Grain Boundary on Cu (111) Bicrystal 120
5.1. Bicrystal geometry 122
5.2. STM results on Cu bicrystal emergent grain boundary 124
5.2.1. Clean Cu (111) bicrystal surface 129
5.2.2. STM measurement on emergent grain boundary in nanoscale 131
5.2.3. STM measurement on emergent grain boundary in atomic scale 147
5.3. Conclusion 153
6. Conclusion & Future Work 158
Bibliography 164
Appendix 181

List of Figures

Figure 1.1: Schematic of a typical integrated circuit in a microprocessor unit 4
Figure 1.2: Resistivity scaling with linewidth of Cu interconnect wires 8
Figure 1.3: Hardness – grain size relationship 12
Figure 1.4: Mullins grooving in polycrystalline thin films 17
Figure 1.5: Stages of dewetting in thin films 19
Figure 1.6: STEM images of grain boundary complexions in copper 22
Figure 1.7: Valleys and ridges at grain boundaries on NC Cu (111) 24
Figure 1.8: MD simulations of restructured eGB $\theta = 3.89°$ 25
Figure 2.1: Electron tunneling in a one-dimensional potential barrier 30
Figure 2.2: Illustration of the Bardeen approach. 35
Figure 2.3: Energy level diagram for sample and the tip bias voltage in STM.....36
Figure 2.4: Chen's approach and reciprocity principle in STM.....39
Figure 2.5: Schematic of the operating principle of STM.....41
Figure 2.6: Schematic of the Omicron VT-STM. 45
Figure 2.7: Schematic of the CreaTec LT-STM 46
Figure 2.8: Close-up view of the Omicron VT-STM STM stage 48
Figure 2.9: Schematic of the tip etching set-up.....50
Figure 2.10: Force-distance curve derived from Lennard-Jones potential 51
Figure 2.11: Illustration of operating principle of AFM 52
Figure 2.12: Schematic of the electron beam in SEM and signals.....57
Figure 3.1: Face-centred cubic unit cell and close-packed plane stacking.....62
Figure 3.2: Schematic of fundamental point defects in crystals 64
Figure 3.3: Illustration of plastic deformation mechanism by slip 65
Figure 3.4: Edge and screw dislocation formation in an ideal crystal 67
Figure 3.5: Positive ($\perp$) and ($\top$) negative edge dislocation 68
Figure 3.6: Construction of a Burgers circuit for an edge dislocation 69
Figure 3.7: Construction of a Burgers circuit for a screw dislocation 70
Figure 3.8: Intrinsic and extrinsic stacking faults in cpp stacking 73
Figure 3.9: Stacking fault formation by slip of partial dislocations 75
Figure 3.10: Illustration of Thompson tetrahedron 78
Figure 3.11: Recovery and polygonization by dislocation climb and annihilation 79
Figure 3.12: Grain boundary construction from median lattice 81
Figure 3.13: Symmetric tilt grain boundary as an array of edge dislocations 83
Figure 3.14: Grain boundary energy vs. misorientation angle (Read-Shockley) ...87
Figure 4.1: STEM image showing columnar grains in 50 nm NC Cu film 95
Figure 4.2: TM-AFM topography of 50 nm NC Cu film after acetic acid etch and thermal processing in UHV 98

Figure 4.3: SEM images of NC Cu film annealed at 400℃ in UHV 99
Figure 4.4: TM-AFM topography images of dewetted NC Cu films after thermal processing at 450℃ in UHV 100
Figure 4.5: TM-AFM topography image and line profile analysis of the features in dewetted region.....102
Figure 4.6: STM topography and line profile analysis of the NC Cu film surface after acetic acid etch, before and after annealing at 300℃ and 380℃ in UHV, at room temperature 103
Figure 4.7: STM topography of NC Cu film surface after annealing at 380℃ in UHV, at room-temperature 105
Figure 4.8: STM and STS analysis of well-prepared clean NC Cu film surface, at room-temperature 106
Figure 4.9: STM topography image of grain boundary junctions of arrays of edge dislocation on well-prepared NC Cu film surface, at room-temperature 107
Figure 4.10: Examples of typical emergent grain boundaries on the well-prepared NC Cu film surface, at room-temperature.....108
Figure 4.11: STM topography image of valleys and ridges at grain boundary triple junctions on NC Cu film surface, at room-temperature 109
Figure 4.12: Schematics of emergent grain boundary geometry relating in-plane angle θ, out-of-plane angle φ and inclination angle ψ 110
Figure 4.13: STM topography and groove profile analysis of an emergent low-angle grain boundary on the NC Cu film surface, at room-temperature 112
Figure 4.14: STM analysis of a low-angle emergent grain boundary on the NC Cu film surface, at room-temperature 113
Figure 4.15: STM topography and groove profile analysis of an emergent high-angle grain boundary on the NC Cu film surface 114
Figure 5.1: Schematic of Cu BC geometry and construction of a symmetric [111] (θ=13.17°) tilt grain boundary from median lattice.....123
Figure 5.2: SEM and EBSD analysis of the Cu BC with single eGB.....124
Figure 5.3: STM topography images of step morphology evolution 125
Figure 5.4: Localized contamination of the grain boundary on Cu BC surface and analysis of 2D OHC pattern, at room-temperature.....126
Figure 5.5: LEED pattern, LT-STM and STS on the clean Cu BC surface.....129
Figure 5.6: LT-STM visualisation of standing waves near grain boundary on the clean Cu (111) BC surface. 130
Figure 5.7: STM images of screw dislocation transition dynamics across the grain boundary, at room-temperature.....132
Figure 5.8: STM image of the dislocation pattern phase along the grain boundary on Cu BC, at room-temperature.....135
Figure 5.9: STM and line profile analysis of the dislocation stripes emanating from

the grain boundary on Cu BC, at room-temperature.....136
Figure 5.10: STM topography of the metastable 9R-like phase formation near the grain boundary on Cu BC, at room-temperature.....137
Figure 5.11: LT-STM images of pinned screw dislocations across the eGB on Cu BC 140
Figure 5.12: LT-STM topography and cross section analysis of the edge dislocation array along the grain boundary on Cu BC.....141
Figure 5.13: LT-STM topography and line profile analysis of the vertical faceting of dislocation array along the grain boundary on Cu BC 144
Figure 5.14: STM topography of disconnections along the Cu BC [111] grain boundary.....146
Figure 5.15: LT-STM measurement of the groove profile and out-of-plane rotation analysis of the Cu BC [111] (θ =13.17°) tilt boundary. 147
Figure 5.16: Atomic-resolution LT-STM topography and periodicity analysis of the Cu BC [111] (θ=13.17°) tilt boundary 149
Figure 5.17: Molecular statics simulations of Cu BC [111] (θ =13.17°) simulation cell and perspective view of the core-shifted grain boundary.....150
Figure 5.18: Molecular statics simulations of Cu BC [111] (θ =13.17°).....151
Figure 5.19: Molecular statics simulation rotation depth optimisation.....153

A. 1: STM topography images of screw dislocation dynamics across the grain boundary, at room-temperature.....181
A. 2: STM topography images of step dynamics along the grain boundary, at room-temperature.....182
A. 3: STM topography images of step dynamics along the grain boundary, at room-temperature.....183
A. 4: STM topography images of step dynamics along the grain boundary, at room-temperature 184
A. 5: LT-STM topography corresponding to Fig. 5.6, with line profile analysis along the grain boundary 184
A. 6: STM analysis of dislocation pattern emanating from Cu BC (θ=26.01°), at room-temperature 185
A. 7: LT-STM topography image shown in Fig. 5.12 (a), without line profiles..185
A. 8: LT-STM topography images corresponding to Fig. 5.13, without line correction.....186
A. 9: LT-STM topography image corresponding to Fig. 5.13, high-contrast 186
A. 10: Multiple-bias LT-STM topography images and groove profile.....187
A. 11: LT-STM atomic-resolution images corresponding to Fig. 5.13, with high-contrast.....187

List of Abbreviations

AFM – Atomic Force Microscopy

BC – bicrystal

CSB – core-shifted boundary

CSL – Coincidence Site Lattice

DOS – density of states

EBSD – Electron Backscatter Diffraction

fcc – face-centred cubic

GB – grain boundary

eGB – emergent grain boundary

HAGB – high-angle grain boundary

IC – integrated circuit

LAGB – low-angle grain boundary

LDOS – local density of states

LEED – Low Energy Electron Diffraction

LT – low temperature (77 K)

MD – molecular dynamics

MS – molecular statics

NC - nanocrystalline

OHC – open honeycomb

RC – resistive-capacitive

RMS – root-mean-square (Rq)

RT – room-temperature (298 K)

SEM – Scanning Electron Microscopy

STGB – symmetric tilt grain boundary

STM – Scanning Tunneling Microscopy

STS – Scanning Tunneling Spectroscopy

TEM – Transmission Electron Microscopy

UHV – ultra-high vacuum

Publications & Presentations

Publications

X. Zhang, I. Demirel, and J.J.Boland, "*Wedge disclination description of emergent core-shifted grain boundaries at free surfaces*", Scripta Materialia, 234, 115562, (2023).

Oral Presentations

"Engineering Grain Boundaries at Surfaces of Metals – Why it's important"

EngSurf-Twin Course I: Recent Developments in Surface Engineering and Films (Konya, Turkey, November 2022)

"Scanning Tunneling Microscopy Visualisation of Grain Boundary Dynamics on Nanocrystalline Copper (111) Films"

Trinity College, University College Dublin DubChem 3rd Year Postgraduate Talk (Dublin, Ireland, September 2021)

Poster Presentations

"STM Visualisation of Grain Boundaries on the Surface of Nanocrystalline Copper (111) Films"

DCMS Summer School Materials 4.0 Deep Mechanics, TU Dresden

(Dresden, Germany, August 2019)

1. Nanocrystalline Thin Films

In his first report introducing the field of nanocrystalline (NC) materials in the late 1980s, Gleiter referred to these structures as the future of material science and solid state physics[1]. The unique properties of this new class of solids with a high volume fraction of defects - nanocrystalline materials have driven the nanotechnology revolution. In fact, the global market size of nanomaterials is forecast to reach over USD 40 billion by 2030, at a growth rate of 14.9% per year[2]. Although the global industry market share of nanomaterials is projected to grow exponentially, the ongoing demand for downsizing raises concerns for the production and development of novel nanomaterials.

The continued demand for down-scaling has not only revealed how characteristic material properties change with size, it has also sparked an interest in the investigation of trends in transformation of bulk material properties to help design novel nanomaterials and well-engineered devices. Extensive research in the hopes of exploiting how material properties deviate from bulk properties at the nanoscale has generated an understanding of the importance of the microstructure within these nanomaterials[3], since a significant fraction of the atoms within a nanomaterial are located in the defect cores, including grain boundaries and dislocations.

A particularly interesting class of nanomaterials is nanocrystalline thin films. Today, nanocrystalline metal thin films are used in a wide range of applications including microelectronics and optoelectronics[4–7], biomedicine[8–11], solar cells[12,13], and catalysis[14–18], due to their significantly advantageous properties over their bulk counterpart. Nanocrystalline Cu films, in particular, are the backbone of the device technology and microelectronics industry, where they are used as interconnects in large-scale integrated circuits (ICs) due to their high conductivity. These

applications require production of ultra-smooth and highly-stable nanocrystalline Cu wires, with high-durability to survive the processing involved in device fabrication[19]. In addition, nanocrystalline Cu films and nanoparticles are of significant benefit in the electrochemical catalysis reactions utilized in the production and optimization of renewable fuels due to their enhanced kinetics, stability and versatility[16,18]. The high surface area to volume ratio of nanocrystalline Cu films and nanoparticles enables increased performance in catalysis which relies on the efficiency and tunability of surface morphology, and the density of active sites.

The ongoing demand for device miniaturization has revealed the detrimental role grain boundaries have in the resistivity of metal interconnects, resistance and capacitance (RC) delay, and the speed and overall performance of IC devices[6]. On the other hand, the natural presence of grain boundaries creates the potential to modulate the microstructure of polycrystalline materials to transform the bulk properties for the benefit of designing high performance and functionalized materials, via grain boundary engineering[20]. Grain boundary engineering exploits the tunability of the microstructure, both the character and the distribution of grain boundaries in nanomaterials, in order to optimize the mechanical, electrical, or electrochemical material properties[21–27]. This is most commonly achieved by employing specific processing methods including thermal/thermo-mechanical treatment, alloying or impurity addition[21,28–30]. Today, enhanced performance of nanocrystalline metal catalysts can be achieved by the fine-tuning of catalytic activity via tailoring the grain boundary density and distribution, to increase the density of catalytically active sites[18,31–34]. However, the processing and engineering of nanomaterials, and in particular, understanding and controlling the nature of the grain boundaries that emerge therein, remain common challenges in their

application.

The aim of this PhD thesis is to develop an understanding of the structure and behaviour of grain boundaries emerging on the surface of Cu (111), using scanning tunneling microscopy (STM). The accommodation and restructuring of the naturally occurring bulk grain boundaries as they emerge on the free surface at the triple junctions (Fig. 1.6 (c)) is expected to show nanoscale variations both on the surface and the grain boundary structure, depending on the boundary characteristics. The STM is a powerful candidate to discover the interaction of grain boundaries with the free surface in atomic scale, bringing a novel perspective to the visualisation and analysis of grain boundaries.

This chapter provides an introduction to uncover why surface-grain boundary interactions matter in thin films and their applications in nanomaterials, and how emergent grain boundaries represent a novel route to the grain boundary engineering of materials. The chapter starts by introducing the concept of grain boundaries and the effect of their presence in copper thin films. The relevant background information on the processing, grain growth, surface preparation and related phenomena in nanocrystalline Cu thin films is provided. Finally, the most common techniques in the investigation and observation of grain boundaries are presented along with a brief overview of the relevant literature, that underpins the motivation behind this thesis.

1.1. Grain boundaries in metal thin films

1.1.1. Thin film interconnects

The Nobel-prize winning discovery of the transistor effect by Bardeen, Brattain and Shockley in 1947 is regarded as a technological revolution, initiating the field of

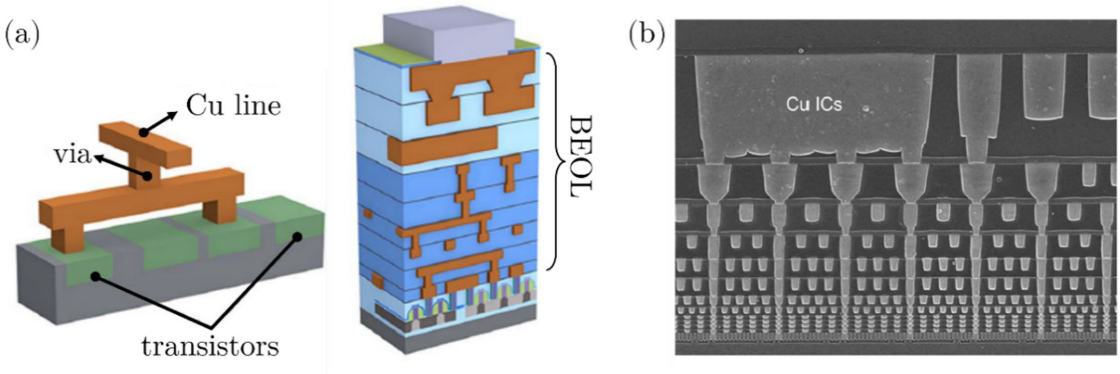

Figure 1.1: Schematic of a typical integrated circuit in a microprocessor unit device. Displaying (a) back-end-of-the line hierarchical scaling consisting of base transistors and connecting Cu lines and vertical vias (b) SEM image of cross-sectional Cu interconnect layers (Intel Broadway microprocessor unit device)[35].

microelectronics with the implementation of semiconductors[36,37]. In 1958, Jack Kilby designed a "solid-circuit" composed of the circuit elements including transistors, resistors, and capacitors connected via gold "flying wires" on a piece of germanium, made entirely from the same piece of semiconductor crystal[38,39]. In 1959, Robert Noyce developed a more practical silicon-based design that incorporated aluminum metal lines on top of the oxide SiO_2 layer, to interconnect the circuit elements, instead of detached wiring[40]. This design was patented as the first monolithic integrated circuit (IC) and is regarded as a milestone in the development of microelectronics implementing large-scale ICs.

Less than a decade later, these preliminary designs were further developed into the batch fabrication of low-cost large-scale ICs with higher complexity and transistor density. In 1965, Moore predicted that the number of components in a dense integrated circuit device will double in every two years[41]. Since then, Moore's law sheds light on the future of how the transistor count will scale with further miniaturisation of microelectronics composed of high-density ICs with enhanced efficiency and reliability[42].

In a large-scale IC, the metal interconnects in the metal-oxide-semiconductor assembly are the polycrystalline metal film lines that connect multiple components

of the circuits. A typical assembly of an IC is shown in Fig. 1.1. In the 30 years following the development of the first IC, metal interconnect design was dominated by aluminium, mainly due to its high conductivity ($3.1\ \mu\Omega - \mathrm{cm}$), as well as its good adhesion to the insulating oxide layer. By the early 1990s, it was well established that the quality and reliability of the interconnects have a fundamental role in determining the overall IC device efficiency and performance as the device size shrinks below 1 μm. Electromigration – a mechanism which occurs via diffusion of atoms due to momentum transfer from conducting electrons, in Al films became unavoidable at increasing current densities, leading to breakages of the film and open circuit in the device. Below 0.75 μm technology device performance was predominantly dependent on the interconnect RC delay[43,44].

The extensive research on electromigration in Al pointed out a challenge that naturally comes with all polycrystalline thin films: the presence of defects and grain boundaries. Remarkably, electromigration in Al was shown to be dominated by diffusion at the grain boundaries[45–47], due to the low activation energy of ions relative to those in bulk and surfaces.

The majority of initial research on the effect of density and microstructure of grain boundaries in thin films of Al and its alloys was limited in delivering a quantitative explanation on the contribution of grain boundary diffusion at atomic level. The migrating atomic flux associated with the grain boundary (a function of grain size, density of ions in the boundary and boundary width) had to be approximated in case of any irregularity in the grain size or grain boundary microstructure[47–51]. Later, experimental studies on the relationship between the failure due to electromigration and grain size for a distribution of tilt grain boundaries in Al (111) films found that the median time to failure is proportional to average grain size, in the case of a homogeneous size distribution[52–54]. These studies were mainly concerned with

columnar grains (normal to the film length), with much larger average grain sizes (2-8 μm) compared to that of the thin films that are employed in the current technology (≤50 nm). However, their conclusions highlighted the necessity of deeper consideration of grain size and distribution characteristics of thin films and atomic structure of the grain boundaries, which was soon found to be more crucial in the new material that replaced Al interconnects.

In the mid-1990s, copper was proposed as an alternative to Al, considering its advantages over Al and Al-based interconnects[43,55]. Copper has 40% higher electrical conductivity, ($1.7\ \mu\Omega - \mathrm{cm}$), higher resistance to electromigration[56] (higher activation energy) and much better thermo-mechanical properties compared to Al. Therefore, its application as an interconnect was expected to bring higher scalability while allowing higher current densities. In 1997, IBM Corp. and Motorola, Inc. developed the first device technology with Cu interconnects, around the timeframe of 0.25 μm node[55,57]. This replacement also necessitated the development of a relatively complicated fabrication process for Cu, due to its poor adhesion to oxides, with added risk of contamination of silicon device via interfacial diffusion of Cu[58]. Furthermore, unlike Al, Cu itself does not form a passivating layer of oxide, but rather oxidizes in air and easily corrodes.

The search for a stable diffusion barrier layer was mainly focused on two requirements. Firstly, the need to maintain good conductivity of the contact interface and, secondly, to obtain a uniform material with low defect and grain boundary density, thus preventing the leakage paths for Cu diffusion through the barrier. Durable metals such as titanium, tantalum and tungsten, amorphous alloys of these and metal nitrides were reported to have outstanding performance as barrier layers, hampering the diffusion of Cu into silicon. This was mainly put down to the high durability, thermal stability and chemical inertness of these materials

with Cu. The improvements on the diffusion barrier structure have shown that Ta/TaN has better barrier performance, due to its lower electrical resistivity, higher thermal stability, and higher activation energy for diffusion of Cu (lower diffusion constant), even at small thicknesses.

The interconnect was thus fabricated by a dual-damascene process; electroplating of Cu on top of a Ta/TaN diffusion barrier layer, followed by planarization by chemical mechanical polishing. Although the Ta has a significant performance as diffusion barrier, the diffusion of Ta into Cu itself and a consequent risk of intermixing is reported to occur at high temperatures[59], as will be discussed in section 4.2.1.

1.1.2. Cu interconnects and size effect

Initially, the employment of Cu interconnects showed a remarkable increase in the performance and efficiency of IC devices, with significantly reduced RC delay and power consumption, and faster operating devices. As the device size continued to shrink, even though the devices were thermo-mechanically stable, overall performance was challenged due to the increase in RC delay and power degradation[60–62]. By the 2000s, when the technology node was down to 100 nm, the increase in resistivity was attributed to down-scaling interconnects. Cu interconnects, now at nanoscale, were observed to bring an increase in resistivity as their dimensions approached the electron mean free path ($\lambda_{MFP} \sim 39\ nm\ in\ Cu$), as shown in the Fig. 1.2. (a) [63]. The drastic increase in resistivity was shown to be a result of additional electron scattering mechanisms introduced in the nanoscale thin films. As the film thickness decreases below 100 nm, increased surface and grain boundary scattering mechanisms, illustrated in Fig.

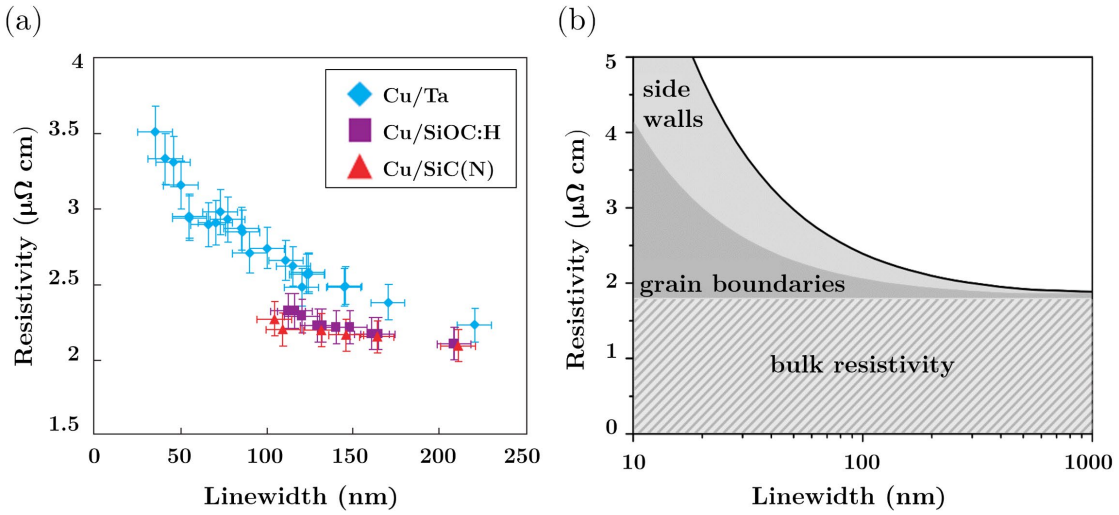

Figure 1.2: Resistivity scaling with linewidth of Cu interconnect wires (a) resistivity – linewidth plot of Cu lines deposited on SiC(N), SiOC:H, TaN/Ta barriers show increasing resistivity as Cu line width becomes smaller.[63] (b) resistivity – linewidth plot for Cu interconnect as linewidth scales down to 10 nm. Side-wall/surface scattering and grain boundary scattering contributions to resistivity is shown. Reproduced from [64].

1.2. (b), dominate the increase in resistivity[65]. This size-dependent increase in resistivity, called "size effect", is recognized as a major limitation in the efficiency of Ics[66].

A brief insight to the physical origins of the additional scattering mechanisms can be provided by the fundamental models of resistivity in thin films. In free-electron gas-like thin metal films, like Cu interconnects, electrons are scattered by phonons (lattice thermal vibrations) and impurities, as well as by surfaces and grain boundaries[67,68]. Upon scattering, conduction electrons lose momentum which consequently results in an increase in resistivity. The most common model that provides a quantitative explanation for the contribution of electron-surface scattering to resistivity in thin films is provided by the Fuchs-Sonderheimer (FS) theory[69,70]. For a monocrystalline thin film of thickness d, resistivity associated with the surface scattering is given as

$$\rho_{FS} = \rho_0 + \frac{3}{8}\frac{\rho_0 \lambda_0 (1-p)}{d} \tag{1.1}$$

where ρ_0 is the bulk resistivity (due to phonons) and λ_0 is the electron mean free path in bulk. The FS model handles the electron-surface scattering via a constant specularity parameter p, that defines the probability of a scattering being "specular" (p) or "diffuse" ($1-p$ or $p=0$), based on the assumption of a relatively flat surface. However, when different interfaces are considered (substrate-metal or metal-vacuum), (RMS) deviation of the surface from the mean level of d is irregular and non-negligible[67]. Soffer provided another model of electron-surface scattering in thin films that takes into account the surface roughness (angle-dependent specular reflection)[71].

The other major scattering mechanism that contributes to the size effect is grain boundary scattering. Mayadas and Shatzkes's work provided the first quantitative model on the electron-grain boundary scattering mechanism in polycrystalline thin films composed of columnar (perpendicular to current flow) grains of mean width g as[72],

$$\rho_{MS} = \rho_0 + \frac{3}{2}\frac{\rho_0\lambda_0}{g}\left(\frac{R}{1-R}\right) \tag{1.2}$$

where, the contribution of an electron to the resistivity is determined by a reflection coefficient R, which represents the probability of transmission or reflection of the electron by the grain boundary upon collision. In polycrystalline thin films, as the grain size typically scales with the film thickness, Eq. (1.2) demonstrates the inverse relationship between resistivity and the film thickness.

Due to the anisotropy arising from the angular dependence of scattering from planar defects such as surfaces and grain boundaries, it is argued that these two mechanisms cannot be handled independently. Furthermore, the surface scattering models provided so far show a substantial increase with temperature, indicating a strong temperature (phonon) dependence, whereas the grain boundary scattering

model given by Eq. (1.2) shows only a modest increase[67,73].

The separation of each of these contributions to the size effect was investigated with various temperature-dependent experiments[67,74–76]. In the work of Wu et al. on 130 nm-thick polycrystalline copper thin films deposited on Ta/TaN, the comparison of the experimental resistivity values with the theoretical values calculated using FS model for a temperature range from 4.2 K to 293 K indicated that the dominant contributing factor to resistivity is grain boundary scattering[65]. They also showed that room temperature resistivity increases with reducing film width (95-240 nm).

Kitaoka et al. also observed this inverse relationship between the resistivity of 240 nm thick damascene Cu films and line width (70-500 nm), using a four-tip scanning tunneling microscopy method which enabled a minimum probe spacing on the scale of mean grain size[77]. Increasing the probe spacing, the measured resistance revealed jumps of 1.0-1.4 $\mu\Omega - \mathrm{cm}$ every ~200 nm suggesting the increase is due to individual grain boundaries without further structural characterization.

A similar attempt by Kim et al. using four-probe STM method combined with scanning electron microscopy (SEM) and electron backscatter diffraction (EBSD) identified a correlation between grain boundary structure and its contribution to resistivity[78]. High angle grain boundaries with low level of symmetry showed much higher resistivity jumps relative to coincidence site lattice (CSL)-type boundaries, a description of which is provided in chapter 3, with high level of structural symmetry. They postulated that this effect was due to an intrinsic characteristic associated with the lattice relaxation region.

A recent study by Bishara et al., employing a SEM-based four-probe method combined with EBSD characterization and molecular dynamics (MD) simulations, investigated the relationship between the tilt grain boundaries of different structure

and the resistivity on segments of polycrystalline Cu (111) thin films[79]. They showed that the contribution of the higher range of LAGBs (14°-18°) to resistivity was twice that of high angle tilt grain boundaries. While a correlation between CSL-type grain boundaries and resistivity was observed, it was not found to be affected significantly by any imperfections/phase variations within the same CSL-type.

Currently on the verge of 2 nm technology node, the continued interest in the size effect has focused on the atomic structure of grain boundaries and its effect on electron transport mechanisms (resistivity). In fact, in their original model, Mayadas and Shatzkes noted that grain boundary scattering mechanism is a combined function of the angle between incident and scattered electron wave and the orientation of the boundary. Recently, with use of high-resolution microscopy techniques, the information on the orientation and atomic arrangement at the grain boundaries is more accessible. In situ experiments combined with MD simulations allow comparative experiments on the relationship between the grain boundary character (orientation, inclination, defect concentration, energy, excess volume) and the nanocrystalline thin film resistivity.

1.1.3. Grain boundary engineering in nanomaterials

The fundamental mechanical, physical, and thermal properties of polycrystalline thin films as applied in nanotechnology are governed by the presence of grain boundaries and their microstructure. Notwithstanding the aforementioned drawbacks associated with the presence of grain boundaries in Cu interconnects, ongoing research has also revealed the potential advantages of grain boundaries to

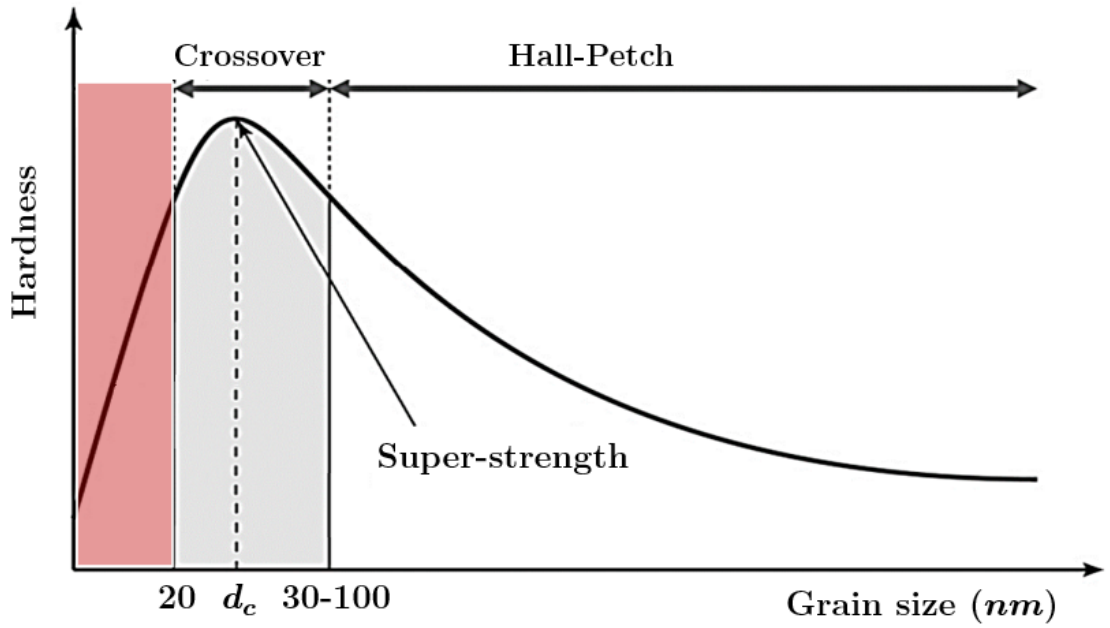

Figure 1.3: Hardness – grain size plot illustrating the Hall-Petch and inverse Hall-Petch (shaded red) behaviour as grain size in nanomaterials becomes smaller. A transition in hardness behaviour is observed for the region $\sim 20 - 100$ nm, at a critical grain size d_c.[80]

'functionalize' polycrystalline materials and their properties. This has given rise to the field of study known as grain boundary engineering[21].

In the past few decades, extensive research and development aiming to produce high performance materials has led to the discovery of novel processing techniques that allow control of grain growth and microstructure. Of particular interest in the development of high-end materials to achieve high-strength and durable nanomaterials, relying on the typically increasing behaviour of hardness with the reducing grain boundary size due to Hall-Petch effect. Below a critical mean grain size d_c, however, hardness starts to decrease due to a phenomenon known as inverse Hall-Petch effect, limiting the development of robust nanomaterials[81,82], as shown in Fig. 1.3. As the grain size becomes smaller, the dislocation-mediated classical deformation mechanism transitions into a grain boundary-mediated deformation, due to increased grain boundary dynamics, including grain rotation, grain boundary migration and sliding[80,83]. These mechanisms are strongly correlated with the atomic

arrangement of individual grain boundaries and demands further atomic scale characterization for the production of robust nanomaterials.

As part of the search for high-efficiency electrochemical energy conversion reactions using renewable energy, another novelty in the field of grain boundary engineering application of nanomaterials has emerged. Grain boundary-rich nanocrystalline thin films are frequently used as electrocatalysts in such reactions due to their large surface area and high selectivity. In fact, Cu-based nanoparticles are shown to be the most efficient catalysts for CO_2 reduction reaction (CO_2RR)[84,85]. The efficiency of such electrochemical reactions significantly relies on the surface morphology and microstructural features emerging at the surfaces, *i.e.*, grain boundaries and dislocations. The unique energetic characteristics of individual grain boundaries allow selective enhancement of catalytic activity on the surfaces of metallic thin films, on a length scale associated with the grain boundary strain field, scaling with the dislocation content in each grain boundary geometry[15]. The selectivity of electrochemical activity on the surface is substantially improved not only by increasing the grain boundary density, but also careful tuning of grain boundary character distribution[14,16,18,23,32,86].

1.2. Processing of Cu films

1.2.1. Oxidation and removal of oxide

Copper readily oxidizes in ambient conditions, even at low temperatures, due its high reactivity. When exposed to air, the copper surface is activated by the dissolved oxygen in water as follows

$$\begin{aligned} Cu + H_2O &\rightarrow CuO + H_2 \\ 2Cu + H_2O &\rightarrow Cu_2O + H_2 \end{aligned} \tag{1.3}$$

$$Cu + 2H_2O \rightarrow Cu(OH)_2 + H_2$$

The two main types of oxides formed on copper are Cu_2O (cuprous oxide, Cu^I) and CuO (cupric oxide, Cu^{II}). Extensive experimental and theoretical research on the oxidation mechanisms of copper indicates that the chemical composition and structure of copper oxide play an important role in the electrical, optical and mechanical properties of copper[87–91]. Various applications of Cu in electrochemistry, sensors, optoelectronics and solar cell technologies exploit the altered properties due to the naturally emerging band gap of 1.5 eV-2.1 eV (for CuO and Cu_2O, respectively)[92–95] in its oxides. For most applications of Cu in the microelectronics device industry, the oxide layer is seen as a considerable challenge in the direct implementation of copper films as interconnects, hindering the adhesive properties of the surface and causing an increase in contact resistance[96]. High-resolution surface analysis of emergent grain boundaries at the surfaces of Cu thin films using STM, as in this thesis, demands the removal of the thin layer of insulating surface oxide formed due to exposure to ambient air prior to transfer into UHV.

In addition to chemical mechanical polishing; chemical dry etching, reactive ion etching, and O_2 plasma etching are the most commonly employed dry-etch methods to remove or eliminate the surface oxide as part of the dual-damascene process of copper interconnects. Etch rate and etch selectivity can be optimized by the addition of H_2 and/or other gases[97–100]. Despite the inefficiency in etching sub-nanometre features due to the isotropic behaviour[100], liquid-phase etching was shown to offer an overall more advantageous etch process for copper oxides of Cu thin film electrodes with fewer stages[101]. Among the commonly used non-oxidizing acids including formic, citric, acetic, and sulfuric acid, acetic acid etch was shown to result in a relatively more efficient and controlled etch rate at room temperature, while providing an excellent environment for copper to resist corrosion[102–105]. Acetic

acid does not attack the copper while selectively reacting with copper oxide as

$$\begin{aligned} \mathrm{CuO} + 2\mathrm{CH_3COOH} &\rightarrow \mathrm{Cu(CH_3COO)_2} + \mathrm{H_2}O \\ \mathrm{Cu_2O} + 4\mathrm{CH_3COOH} &\rightarrow 2\mathrm{Cu(CH_3COO)_2} + \mathrm{H_2}O + \mathrm{H_2} \end{aligned} \tag{1.4}$$

Studies of O_2 adsorption and desorption on different facets of Cu have yielded important information on the microstructural properties associated with thin layers of surface oxides[87,106–111]. STM studies on oxidation stages of Cu(111) revealed distinct phases of long-range ordered '29' and '44' reconstructions, transitions between well-ordered and disordered structures and chemical transition between Cu_2O and CuO, obtained at different conditions of O_2 concentration and temperature[108,109,112,113]. On polycrystalline Cu surfaces, the O_2 adsorption occurs by nucleation at active sites, namely step edges and vacancy islands, and proceeds along close-packed directions to terraces and on-grains. Among the defects emerging at the surface, grain boundaries play a significant role in providing preferential sites for the oxide nucleation[107,114].

Correlation between the surface morphology and oxidation kinetics was found, whereby oxidation proceeds faster in films with finer-grained microstructure. The greatest difference in reaction rates in nanocrystalline and coarse-grained films was observed between 300°-700°C[115,116]. Oxidation rate is roughly approximated by the square root of the grain density for nanocrystalline films as $\sqrt{\rho_{grain}} \approx k$, under the assumption that oxidation proceeding by the mass transport of Cu is enhanced along the grain boundaries, as indicated by the relatively low activation energy for diffusion along Cu_2O grain boundaries (40 kJ mol^{-1})[116].

1.2.2. Thermal processing of Cu thin films: grain growth & Mullins grooving

Implementation of Cu thin films in industrial devices and nanotechnology typically employs cycles of thermal annealing as part of the fabrication process, in order to optimize the microstructure of thin films and to remove structural defects for enhanced device/material properties. This challenges the overall macroscopic stability and continuity of films due to dewetting, and also by introducing a risk of diffusion at the film-substrate interface and at grain boundaries[100]. Upon annealing, surface morphology, granularity and stress state of thin films change due to the relaxation of defects and rearrangement of dislocations into lower energy configurations. At sufficiently high temperatures, recrystallization occurs by nucleation and growth of new grains with reduced defects. This is followed by grain growth via grain boundary migration, caused by coarsening of the recrystallized grains, forming larger grains[117,118]. Post-recrystallization, material properties of the thin film – including electrical and thermal conductivity, hardness, and strength – change drastically. The impact of thermal annealing and annealing parameters *i.e.*, temperature, duration and annealing atmosphere on the grain growth and surface evolution has been widely studied to correlate grain structure and relaxation surface morphology and roughness, diffusion rate, and film stability.

The interplay between the driving forces arising from surface, elastic stress, and chemical energy released during film growth and post-growth annealing determines the microstructural evolution[119]. As part of this, disruptions in the film morphology occur due to nucleation and growth of voids, which eventually lead to breakages in the film by dewetting (discussed in section 1.2.3.). This hinders the film stability and limits the grain growth. Apart from the film-substrate interface; defects, especially grain boundaries at triple junctions, play a pivotal role in the formation

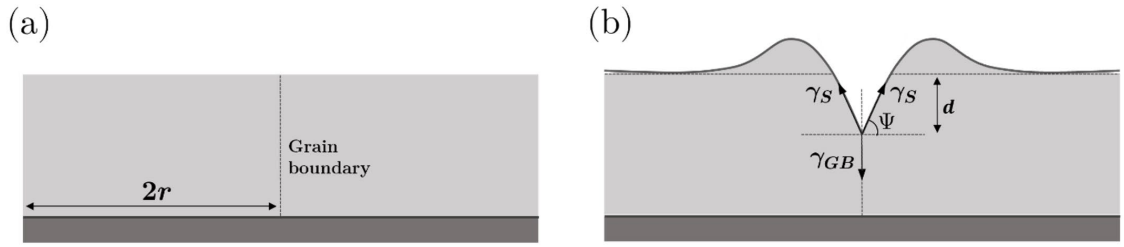

Figure 1.4: Mullins grooving in polycrystalline thin films (a) film comprising of grains of width $2r$, is flat before grooving (b) grain boundary grooving at the triple junction where the grain boundary meets the surface plane. The equilibrium angle Ψ resulting a groove depth d is established by balancing of the interfacial tension of boundary and surface tension of adjoining grains at the triple junction.

of such voids, through a mechanism known as grain boundary grooving[120–124]. Also known as Mullins grooving, a general framework for the grain boundary grooving model was provided by Mullins in 1957[125]. This model considered the triple junction where the grain boundary meets the surface plane, as sketched in Fig. 1.4., assuming isotropic surface free energy. Here, the interplay between the surface tension associated with the free surfaces on either side of the grain boundary and the grain boundary plane itself, determines the shape of the groove geometry.

The equilibrium angle at which the net interfacial tension is balanced is the dihedral angle Ψ, determined by the condition,

$$\frac{\gamma_{\mathrm{GB}}}{\gamma_{\mathrm{S}}} = 2\sin\Psi \tag{1.5}$$

where γ_{S} and γ_{GB} are the surface and the boundary free energies per unit area. The groove profile determined by the dihedral angle Ψ is accommodated by the migration of atoms dominated by capillary driven surface diffusion[126–131]. Consequently, moving away from the triple junction, the surface slopes sharply into a local maximum and flattens further from the grain boundary. The chemical potential difference between the valley and the relatively flat regions further away results in a free-energy gradient driving the surface diffusion uphill. Thus, to

maintain the equilibrium angle Ψ at the triple junction, the groove grows deeper scaling with time as $t^{1/4}$.[125] As the groove deepens, the local film thickness and the grain boundary area decreases, whereas the surface area increases to minimise the surface/interface energy. The change in the net free energy of the triple junction system by the establishment of equilibrium angle Ψ as local film thickness reduces by Δd, is given by

$$\Delta G = \gamma_{\mathrm{GB}}\, \Delta d - 2\gamma_{\mathrm{S}} \sin\left(\frac{\Psi}{2}\right) \Delta d \tag{1.6}$$

For a nanocrystalline film with uniform thickness and dominant surface orientation of (111), the net free energy, therefore the kinetics and the shape of the groove at the triple junction are predominantly determined by the characteristic free energy of individual grain boundaries. In general, grain boundaries with higher energies, *i.e.*, high-angle grain boundaries, which will be introduced in chapter 3, groove faster relative to low-energy ones[132,133]. Surface diffusion is dependent on the surface energy anisotropy and crystallographic orientation, and it occurs fastest on (111) plane in copper, at a rate 1.5-3 times faster relative to the other low-index planes, depending on the temperature[131,134,135].

Typically, since the mean grain size scales with the film thickness, the largest grain size can go up to ≈10 times that of the film thickness[136–138]. For a 50 nm thick film with initial mean grain size of 50 nm, the groove will have an approximate depth of 13 nm for grains of maximum size[121]. For a thin film with columnar grains of radius r, the equilibrium groove depth established by equilibrium angle Ψ is given by[120]

$$d = r\frac{2 - 3\cos\Psi - \cos^3\Psi}{3\sin^3\Psi} \tag{1.7}$$

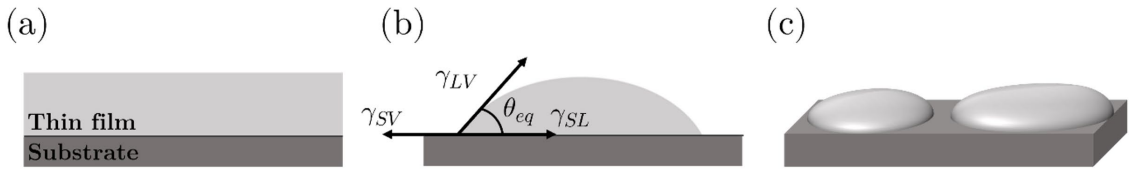

Figure 1.5: Dewetting (a) thin film on substrate is flat and continuous before dewetting (b) equilibrium shape of thin film established by the balance of surface tension at the film-substrate interface (c) agglomerated film formed 3D islands as a result of dewetting.

Mullins grooving mechanism suppresses the growth of larger grains by introducing deeper grains and increased surface roughness. This will be explored in further detail during the discussion of the microstructural evolution of nanocrystalline Cu thin films in chapter 4.

1.2.3. Dewetting

Dewetting is the agglomeration of an initially continuous thin film to form isolated islands upon thermal annealing[132]. The driving force for dewetting is minimization of the surface free energy by decreasing the surface to volume ratio of thin films on a substrate. This is known to occur by means of mass transport, predominantly via surface diffusion, at temperatures well below melting temperature. Factors that affect dewetting are film thickness[139]; surface and interface microstructure; morphology and relative energies; surface energy anisotropy; residual stress[140]; diffusivity; and temperature.

Dewetting occurs upon introduction of an external perturbation large enough to destabilize the initially continuous as-deposited thin film. The thin film over the substrate becomes thermodynamically unstable at elevated temperatures and establishes an equilibrium morphology determined by the interplay between the surface energies of the three interfaces: surface energy per unit area of the film (γ_{LV}), surface energy per unit area of the substrate (γ_{SV}) and the interfacial energy per area (γ_{SL}) of the film-substrate interface, following the relation given by

Young's equation[141]

$$\gamma_{SV} = \gamma_{SL} + \gamma_{LV} \cos\theta_{eq} \tag{1.8}$$

where θ_{eq} is the equilibrium contact angle which determines the tendency of the thin film to dewet over the substrate. If $\gamma_{SV} > \gamma_{SL} + \gamma_{LV}$ $(\theta_{eq} = 0)$, the film is stable and will not dewet. Otherwise, the film is thermodynamically unstable and will transition from its continuous flat state into isolated islands.

Dewetting occurs through void nucleation and growth, which eventually leads to breakage of the thin film. The tendency to dewet and the dewetting rate increase with decreasing film thickness. In metal thin films, void nucleation is a mechanism predominantly driven by grain boundary grooving, as mentioned earlier. Consequently, grain size, grain boundary energy and character distribution have a significant impact on the dewetting behaviour of nanocrystalline thin films.

Dewetting behaviour in copper thin films has been of great interest due to reliability concerns in microelectronics and other industrial applications. Various Cu thin film-substrate interfaces have been studied to understand the effects of deposition; processing conditions and annealing temperature; Cu film thickness; substrate; and encapsulation layer on dewetting kinetics and morphology[122,123,142–145]. While thicker Cu thin film deposited on Si and SiO_2 show a capillary driven nonfractal void growth assisted by hillocks; in very thin films ($t < 40$ nm), void growth is of fractal type and proceeds mainly through grain boundary grooving[145]. Any anisotropy in the local and macroscopic compressive stress state that may arise from the difference in thermal expansion coefficients, anisotropy in elastic constants and/or plasticity (by Schmid factor), or increase in film thickness will induce the formation of hillocks via diffusion[145,146]. For instance, a locally low compressive stress in a grain (relative to its surroundings) will induce a diffusion gradient towards it, leading to

the formation of hillocks. Inversely, if the stress is tensile, e.g., locally low tensile stress in a grain, the diffusion gradient will be in opposite direction, forming a void in the film.

The dewetting behaviour of Cu thin films on Ta substrate is analysed in chapter 4. The design and development of UHV thermal processing conditions for optimized surface morphology in 50 nm nanocrystalline Cu thin films is presented.

1.3. Observation of dislocations and grain boundaries

The first observation of the granular microstructure of iron-steel using optical microscopy by Sorby[147] in the 1880s demonstrated the effects of processing and chemical composition on the macroscopic evolution and distribution of grains. The first experimental work that verified the presence of dislocations was a bubble raft demonstration, published by Bragg in 1947[148]. This was followed by the experimental observation of dislocation traces on the surfaces as etch pits in optically transparent crystals of AgBr, by Hedges and Mitchell in 1953[149] and of NaCl by Amelinckx in 1956[150].

Eventually, the first direct observation of the arrangement and motion of individual dislocations in the interior of the Al foils by transmission electron microscopy (TEM) was achieved in 1956 by Hirsh and Horne[151–153].

Today, experimental observation of surface microstructure, grain boundaries and dislocations is achieved with extreme resolution. Grains of diameter less than 10 nm are resolved using high-resolution TEM (HRTEM) and SEM-based EBSD[154], the latter providing an orientation map of the surface and quantitative analysis of the microstructure. In fact, grain boundary complexions, defined as thermodynamically stable, chemically and physically distinct interfacial states that are in equilibrium with the abutting bulk phases, and the transitions between

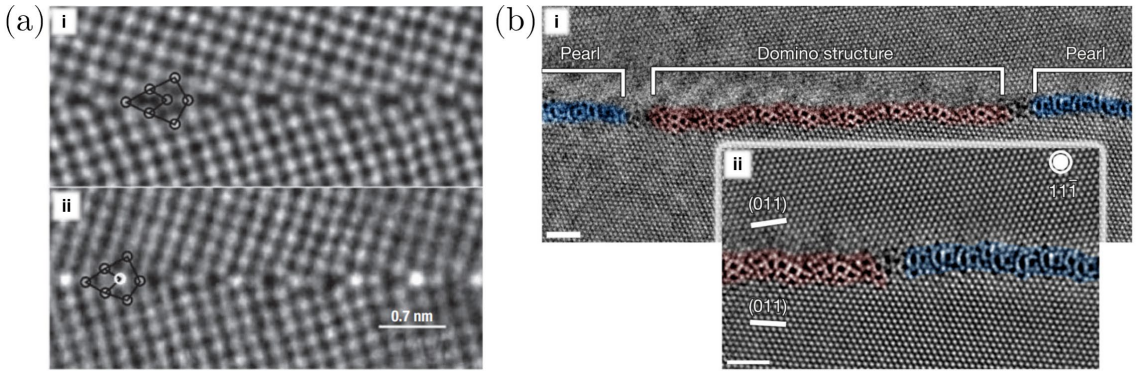

Figure 1.6: (a) Atomic resolution STEM images of the symmetric <001> tilt grain boundary with 36.8° misorientation angle in (i) pure copper and in (ii) bismuth-doped copper segregated post-annealing, with bright sites indicating the bismuth segregation. Adapted from [155] (b) Atomic resolution STEM images of GB phase transition at a near-symmetric $\Sigma 19b\ [11\bar{1}]$ tilt grain boundary in pure Cu showing two distinct structure of pearl and domino phases with (ii) magnified view of the different structural units. Scale bar is 1 nm. Adapted from [156].

complexions have been extensively studied and classified in both non-pure complex systems and in pure metals, as presented in Fig. 1.6 (a)[155,157–160]. The atomic structure and composition at the interfacial phases, referred to as grain boundary complexions, have been characterized with high resolution. This has led to significant progress in constructing a comprehensive framework to understand the role of grain boundary complexions in material science.

More recently, the study by Meiners et al. demonstrated the complexion transitions in $\Sigma 19b\ [11\bar{1}]$ tilt grain boundaries in elemental copper, using scanning transmission electron microscopy (STEM) at room temperature[156]. Their atomic-scale resolution experimental observation revealed for the first time the structure of the two grain boundary phases, *i.e.*, domino and pearl, that exist together at room temperature in pure copper as shown in Fig. 1.6 (b), confirmed with their MD simulation calculations.

On the other hand, TEM allows design of in situ experiments to investigate the microstructural dynamics of nanocrystalline materials or their properties, with controlled annealing of the samples, or application of stress. However, despite its

high-resolution imaging capabilities, TEM comes with several disadvantages when it comes to imaging grain boundaries and dislocations in thin films. The major drawback is due to the geometrical constraints of the thin film samples, introduced to optimize contrast and resolution. Prior to TEM measurement, samples need to be thinned down to enhance the electron transparency, which involves a complex sample preparation and thinning process that introduces plastic deformation and associated strain fields into the film. Consequently, this results in changes in the dislocation concentration and activity by dislocation emission in the film surface, as well as triggering grain boundary dynamics such as sliding and migration[161,162]. The presence of TEM-induced plastic deformation effects in the very thin film geometry have been demonstrated by TEM experiments and computational simulations. These MD simulations of 12-nm-thick parallel surfaces representing a Ni TEM lamella revealed that the surface relaxation effects are felt also in the bulk by emission of dislocations in sub-surface grains[162]. It was suggested that for very thin films with thickness in the order of two grains – the typical maximum thickness in TEM experiments – one must be careful when interpreting TEM images as thin film geometry can produce artefacts. For atomic-resolution investigation of dislocations and grain boundaries emerging at the surfaces of thin films of columnar grains, TEM is considered to be limited in terms of its sensitivity to any misalignments of tilt axis from well-defined crystallographic orientations and due to the requirement to use a capping layer[163–166]. This effect significantly restricts TEM studies of emergent grain boundaries and the manifestation of the relaxation on the surface.

For the study of dislocation and grain boundaries at the surfaces, scanning tunneling microscopy (STM), one of the most central tools in surface science, has proven to be an ideal technique[164,165]. STM provides atomic-resolution 3-dimensional

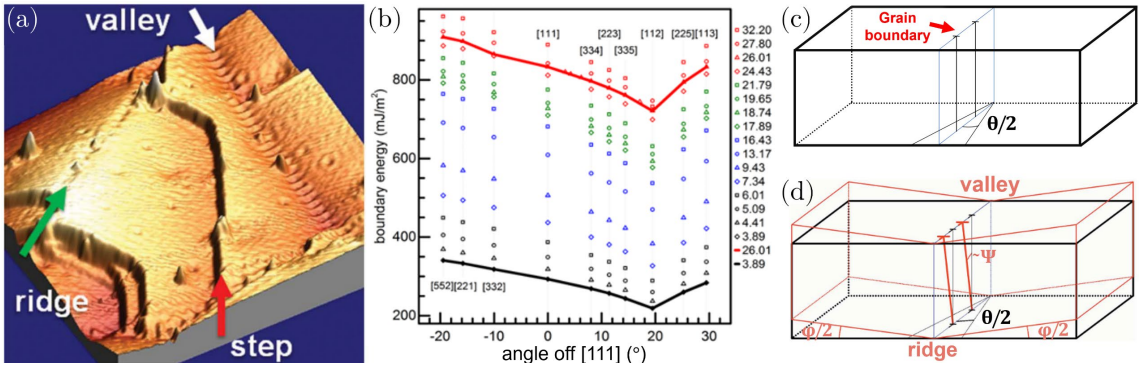

Figure 1.7: (a) Perspective view of the STM topography image of nanocrystalline Cu (111) surface illustrating ridges and valleys at the grain boundaries as indicated by the green and white arrows, respectively (b) Relationship between grain boundary energy and inclination angle ψ, calculated for different values of θ. Grain boundary energy shows minimum at ψ=19.47°.[163,167] (c) schematic of the emergent grain boundary-free surface triple junction (d) schematic of the relation between out-of-plane rotation φ, dislocation line inclination angle ψ and misorientation angle θ after grain rotation.

topography map of the surfaces. Unlike TEM, STM's excellent vertical resolution makes it sensitive to even the smallest level of grain rotation while its atomic resolution allows a detailed analysis of GB structure. Early STM studies focusing on the surface defects revealed atomic scale details of individual edge and screw dislocations on surfaces of metal thin films[164,165].

Zhang et al., in their recent LT-STM study of grain boundaries on the surfaces of 50-nm-thick nanocrystalline Cu (111) films revealed for the first time the introduction of valleys and ridges on the surface, where the grain boundaries meet the surface, due to the out-of-plane rotation of the adjoining grains, as illustrated in Fig. 1.7 (a)[163]. As evidenced by the MD simulations as part of the study, this "restructuring" is established through the inclination of the dislocation core (line) by ψ, along the boundary, driven by the energetic preference of the dislocation cores to lie along close-packed planes – due to the anisotropy of the dislocation core energy. The geometrical relationship between in-plane (misorientation) angle θ, inclination angle ψ and the out-of-plane rotation φ as shown in Fig. 1.7 (d), is given by $\tan\psi = \tan(\varphi/2) \,/\, \sin(\theta/2)$. By establishing a geometry given by this relation,

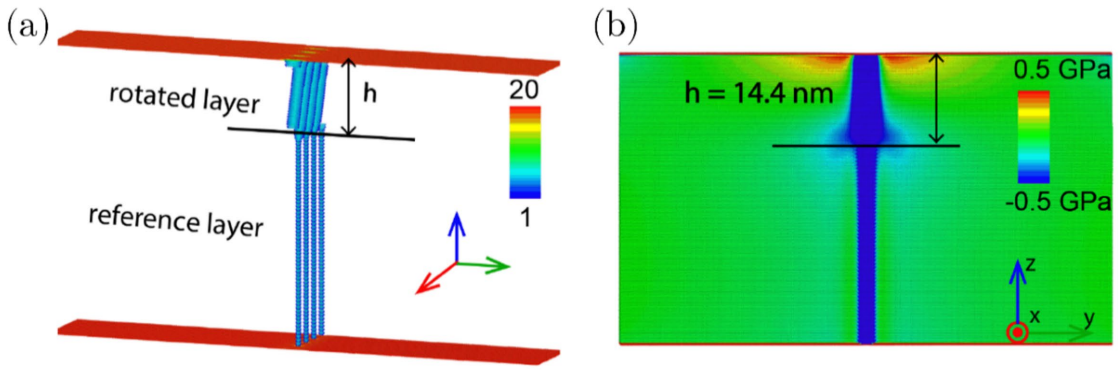

Figure 1.8: MD simulations of emergent grain boundary with $\theta = 3.89°$ misorientation. (a) rotated layer of depth **h**=14.4 nm, due to restructuring, as coloured by central symmetry parameter (b) Stress distribution along through the thickness of the simulation cell.[167]

grain boundary energy is minimized, as shown by Fig. 1.7 (b). Here, the grain boundary energy shows a minimum at inclination angle ψ =19.47°, calculated for a wide range of misorientation angle θ.

The length scale of the rotated layer, hence the structure of the strain field around the triple junction, is determined by the interplay between the elastic stress field introduced by the restructuring and core stabilization, as illustrated for a low-angle grain boundary($\theta = 3.89°$) in Fig. 1.8 (a)[167]. The depth of restructured dislocation core layer may extend from a few nanometres to 15 nm, depending on the misorientation angle θ. This is a result of the fact that the level of atomic rearrangement at the boundary and both the distribution (shape) and magnitude of the elastic stress field associated with it is determined by the degree of misorientation.

Remarkably, these results revealed that producing perfectly smooth two-dimensional nanocrystalline surfaces is challenged by the presence of grain boundaries, for face-centred cubic metals with high elastic anisotropy. The out-of-plane tilt of φ, induced by grain boundary energy minimization, leads to the unavoidable roughening of the film surface due to presence of grain boundaries. The discovery of naturally emerging core-shifted (restructured) grain boundaries,

meanwhile, reveals a potential to reduce electron-interface scattering in applications of [112] tilt boundaries, since the inclination allows the dislocation cores to lie in the close-packed plane, where the electron transport predominantly occurs. Additionally, the impacts and manifestation of the elastic stress field on the surface remain an intriguing aspect in the context of the catalysis applications of metal films, which rely on the grain boundary character, surface morphology and energy to fine-tune and control the electrocatalytic activity[168].

The restructuring is believed to be an unavoidable phenomenon at triple junctions whenever a bulk boundary meets the surface. To understand, exploit and suggest ways to engineer this naturally driven mechanism, an extensive surface study of emergent grain boundaries using STM is necessary.

The goal of this thesis is to discover and visualise the grain boundary restructuring phenomenon in various grain boundaries as manifested on the surface of Cu (111), and to investigate its dependence on the grain boundary characteristics. To achieve this goal, two systems of samples are chosen. Firstly, presented in chapter 4, the emergent grain boundaries on the surface of microstructurally optimized nanocrystalline Cu (111) thin films are studied using STM. Secondly, for a comparative study and generalization of the restructuring observed at the triple junctions on the surface of nanocrystalline Cu (111) thin films, and to better understand the natural driving force behind this phenomenon, an engineered emergent grain boundary on the surface of Cu (111) bicrystal is studied using STM and the results are detailed in chapter 5. Finally, computer simulations are employed to support the experimental observations of grain boundary structure with atomic resolution, as well as to investigate the subsurface restructuring mechanism of the so-called core-shifted emergent grain boundaries and understand the interplay that determines the extent of this surface effect.

2. Experimental Techniques and Methods

In this chapter, the equipment used throughout this thesis, including scanning tunneling microscopy (STM) and atomic force microscopy (AFM) is introduced. The theoretical basis behind the operation of the equipment and the methods are provided in detail and the instrumentation is explained.

2.1. Scanning tunneling microscopy

Scanning probe microscopy techniques enable nanoscale investigations of the properties of surfaces. STM, the very first of the surface probe microscopy techniques, was invented in 1982 by Binnig and Rohrer[169,170], bringing them the Nobel Prize in physics, in 1986. From its early days, STM was a milestone in the field of surface science since it provided atomic-resolution topographic information of the surfaces of conductive materials, in real space. This was achieved by an operating principle based on quantum mechanical tunneling. Using a very sharp metallic tip brought within a few Ångströms of a conductive surface, the electron flow between the tip and the sample across a very small vacuum gap is enabled when a potential difference is applied. The tunneling current as a result of this electron flow is then fed into a feedback loop. Keeping the tunneling current constant, the tip-surface distance is controlled, and the surface is raster scanned. The movement in z direction to maintain the set-point current maps the surface topography.

Over the years, STM has evolved into a tool that provides much more than atomic scale surface topography image. It has paved the way for the investigation of a wide range of systems, including insulators, using a spin-off of STM - atomic force microscopy (AFM).

2.1.1. Elastic tunneling through a one-dimensional rectangular potential barrier

In STM, the tunnel current is obtained as the electrons can tunnel through the vacuum gap between the surface and the tip, a classically forbidden region. The operating principle of STM is based on quantum mechanical tunneling phenomenon, where an electron has non-zero probability of tunneling through a potential barrier. Here, the case of elastic tunneling through a one-dimensional rectangular potential barrier[171] is considered in order to demonstrate this mechanism and establish an analogy in its application to STM.

In classical mechanics, momentum of an electron with mass m and energy E in a potential $V(z)$ is described as

$$p = \sqrt{[2m(E - V(z))]} \tag{2.1}$$

The electron can only exist in classically allowed regions $E > V(z)$ where momentum is non-zero and cannot pass through a region where $E < V(z)$, of a potential barrier of V_0 (see for example region II in Fig 2.1).

In quantum mechanics, however, a wavefunction $\psi(z)$ which satisfies the time-independent Schrödinger equation describes the electron in potential $V(z)$ by the expression

$$-\frac{\hbar^2}{2m}\frac{d^2}{dz^2}\psi(z) + [V(z) - E]\psi(z) = 0 \tag{2.2}$$

where $\hbar$ is the reduced Planck constant. Fig. 2.1 shows the wavefunction $\psi(z)$ of an electron in the potential $V(z)$. In the regions I and III, the potential is defined as $V = 0$ whereas in region II, the potential barrier is of height V_0 and width d.

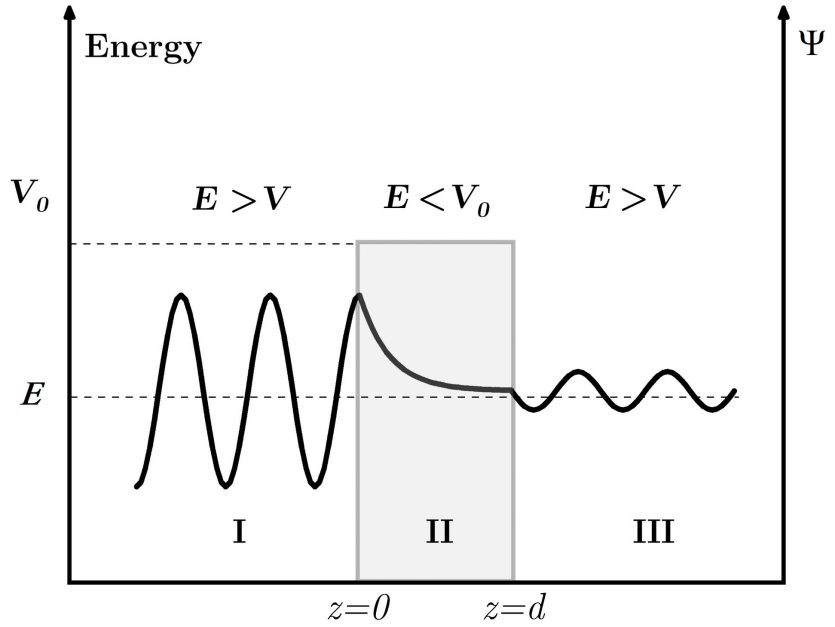

Figure 2.1: Interaction of an electron with wavefunction $\psi(z)$, with a one-dimensional potential barrier of height V_0.

The solution to Eq. (2.2) in region I and region III where $E > V(z)$ is of the form,

$$\psi_{\mathrm{I,III}}(z) = \psi(0)e^{\pm ikz} \tag{2.3}$$

a travelling wave with velocity $v = \hbar k/m$ where the wave vector is $k = \sqrt{2mE}/\hbar$. In region II, where $E < V_0$, Eq. (2.2) has real solutions and the wavefunction is in the form of an exponentially decaying wave,

$$\psi_{\mathrm{II}}(z) = \psi(0)e^{\pm \kappa z} \tag{2.4}$$

where $\kappa = \sqrt{2m(V_0 - E)}/\hbar$ is the decay constant.

The general solution for an electron approaching the potential barrier V_0 from the left (negative z) is given by the linear combination of the solutions for each region:

$$\psi(z) = \begin{cases} Ae^{ikz} + Be^{-ikz}, & \text{for } z < 0 \\ Ce^{-\kappa z} + De^{\kappa z}, & \text{for } 0 \leq z \leq d \\ Fe^{ikz}, & \text{for } z > d \end{cases} \tag{2.5}$$

where A, B, and F are the amplitudes of the incident, reflected and transmitted wavefunctions outside the potential barrier, respectively, and C and D are the amplitudes of the transmitted and reflected wavefunctions inside the potential barrier. The relationship between these amplitudes can be obtained by solving the system of equations for continuity conditions of $\psi(z)$ and $d\psi(z)/dz$ at the boundaries $z = 0$ and $z = d$.

The *transmission coefficient*, describing the absolute squares of the ratio between the transmitted wave amplitude F and incident wave amplitude A, can then be obtained

$$T = \left|\frac{F}{A}\right|^2 = \frac{4k^2\kappa^2}{(k^2+\kappa^2)^2\sinh^2(\kappa d) + 4k^2\kappa^2} \tag{2.6}$$

In case of a wide, high barrier, where $\kappa d \gg 1$ (wider barrier width than decay length), the tunneling probability is lower and the expression for the transmission coefficient simplifies to

$$T = \left(\frac{4k\kappa}{\kappa^2+k^2}\right)^2 e^{-2\kappa d} = \frac{16E(V_0-E)}{V_0^2}e^{-2\kappa d} \tag{2.7}$$

This result shows that there is non-zero probability of an electron tunneling through the potential barrier, even when the electron energy is lower than the potential barrier. Most significantly, the transmission probability (tunneling current as applied to STM) is exponentially dependent on the barrier width, d. This high sensitivity of tunneling transmission to the barrier width is what lies behind STM's capabilities in extreme spatial resolution in surface topography and the detection of surface electronic states[169].

2.1.2. The WKB approximation – potential barrier of arbitrary shape

The Wentzel-Kramers-Brillouin (WKB) approximation is a semi-classical method to obtain solutions to the time-independent Schrödinger equation, mostly in one-dimensional cases[172]. It expands on the solutions for one-dimensional rectangular potential barrier for potential barriers of arbitrary shape, more accurately reflecting reality.

The WKB approximation handles the case of non-constant $V(z)$, based on the presumption of an exponential wavefunction with amplitude and phase, slowly varying with z. The initial mathematical approach provided by the WKB approximation is through slicing the arbitrary-shaped barrier into infinitesimal rectangular barriers in the region between the classical turning points z_1 and z_2, where $E \approx V(z)$. The overall probability of an electron tunnel through the barrier is then obtained by integrating the transmission coefficient given by Eq. (2.7) for individual infinitesimal rectangular barriers as

$$T = \left|\frac{\psi(z_2)}{\psi(z_1)}\right|^2 = exp\left\{-2\int_{z_1}^{z_2} dz\sqrt{2m(V(z)-E)}/\hbar\right\} \tag{2.8}$$

This expression is valid for conditions where the electron energy E is not close to $V(z)$ and requires more careful handling at the turning points z_1 and z_2.

The approach for the transmission coefficient obtained in Eq. (2.8) can be applied to metal-insulator-metal (MIM) junctions, under the assumption that the electrodes with free electron behaviour are at thermal equilibrium. In terms of the analogy with STM, the vacuum is the insulator, and the tip and the sample are separated metal electrodes. In order to define the tunneling barrier height in STM, consideration of the metal work functions is required. Work function, Φ, is the minimum energy required to detach an electron from the metal electrode to the

vacuum level. It's specific to the material, and it is also dependent on the crystallographic orientation of the material. In the case of different electrodes, an average work function, $\overline{\Phi}$ is considered to define an average tunneling barrier. The tunneling barrier height is defined as the energy difference between the Fermi level E_{F} of the corresponding electrode and the vacuum level. Here for simplicity, similar metal electrodes are considered, *i.e.*, sample and tip work functions are assumed to have the same Φ. For states with energy level E relative to E_{F}, the average tunneling barrier height is $\Phi + \frac{eV}{2} - E$. Assuming the work functions of the similar electrodes are equal, upon application of a bias voltage, the probability of an electron tunneling from one electrode to the other can be expressed by rearranging Eq. (2.8) as,

$$T \propto exp\left\{-\alpha z\sqrt{\Phi + \frac{eV}{2} - E}\right\} \tag{2.9}$$

where $\alpha = 2\sqrt{2m}/\hbar$ and z is the barrier width. Eq. (2.9) demonstrates, for states with lower E, the exponential decay of the transmission factor is stronger, hence the contribution of these electrons to the tunneling current is weaker.

2.1.3. The Bardeen theory of tunneling current

In STM, the most commonly applied quantitative theory of the tunneling current was developed by Bardeen in 1961[173]. His model first considers the MIM junction as two independent regions, rather than a combined system. Time-independent Schrödinger equation is solved for each electrode individually, to find their electronic states. These unperturbed wavefunctions of each electrode are then used to calculate the *tunneling matrix element* M, which defines the amplitude of total tunneling transmission.

As Bardeen's method is applied to STM, one starts by considering the two

electrodes A and B, for tip and sample, respectively. Using time-dependent perturbation theory, probability of the initial μth state of tip (electrode A) with wavefunction $\psi_{T,\mu}$, having νth state of sample (electrode B) with wavefunction $\psi_{S,\nu}$ in time t is obtained[174]:

$$p_{\mu\nu}(t) = \left|M_{\mu\nu}\right|^2 \frac{4\sin^2[(E_\mu^T - E_\nu^S)t/2\hbar]}{(E_\mu^T - E_\nu^S)^2} \tag{2.10}$$

where the tunneling matrix element is given by this surface integral at separation surface, z_0

$$M_{\mu\nu} = \frac{\hbar^2}{2m}\int_{z=z_0}\left[\psi_{S,\nu}\,\frac{\partial\psi_{T,\mu}^*}{\partial z} - \psi_{T,\mu}^*\,\frac{\partial\psi_{S,\nu}}{\partial z}\right]dxdy \tag{2.11}$$

When the large time scale of tunneling t compared to the energy resolution ΔE is considered, for large $t/\hbar$, the tunneling probability per unit time, Eq. (2.10) becomes

$$p_{\mu\nu}(t) = \frac{2\pi}{\hbar}\left|M_{\mu\nu}\right|^2\delta(E_\mu^T - E_\nu^S) \tag{2.12}$$

The representation of Eq. (2.10) as Eq. (2.12) with Dirac delta function $\delta(E_\mu^T - E_\nu^S)$ shows that $(E_\mu^T - E_\nu^S)$ is a function decaying away from the peak centred at $E_\mu^T = E_\nu^S$. This is not solely due to a mathematical identity, but more importantly, it is an implication of the characteristics of *elastic tunneling*, allowing the electrons to tunnel only between the states with equal energy, ensuring the conservation of energy.

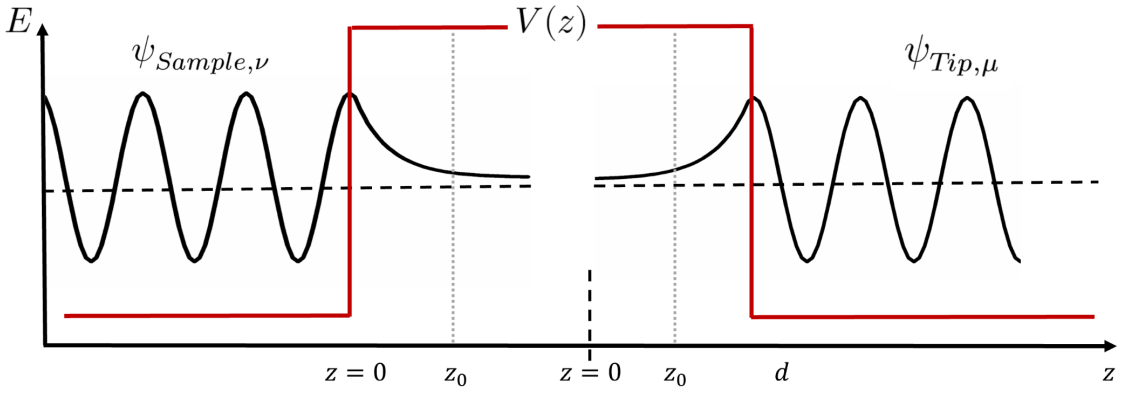

Figure 2.2: Illustration of the Bardeen approach. Wavefunctions of the sample and the tip decay exponentially in the barrier.

At the low temperature limit ($T \approx 0$ K), the available states both in the sample and the tip are defined by their Fermi level, E_{F}. The allowed energy window for tunneling is defined by the potential difference between the tip and the sample, which results in a shift in the occupancies of the tip and sample states. When a bias voltage is applied, a net tunneling current occurs between the tip and the sample. The direction of the current depends on the polarity of the applied bias voltage. If a positive bias voltage is applied to the sample, the sample $E_{\mathrm{F,S}}$ is shifted by eV_{bias} below the tip $E_{\mathrm{F,T}}$ level. The net tunneling current between the tip and the sample with a potential difference V_{bias} can be expressed as $2ep_{\mu\nu}(t)$, where Eq. (2.12) is multiplied by 2 × elementary charge of electron e, taking into account the two possible spin states (spin degeneracy),

$$I = \frac{4\pi e}{\hbar}\sum_{\mu\nu}[f(E_{\mu}^{T} - E_{\mathrm{F}}) - f(E_{\nu}^{S} - E_{\mathrm{F}})]\left|M_{\mu\nu}\right|^{2}\delta(E_{\nu}^{S} - E_{\mu}^{T} - eV_{\mathrm{bias}}) \qquad (2.13)$$

where $f(E) = (1 + \exp\left[(E - E_{\mathrm{F}})/k_{\mathrm{B}}T\right])^{-1}$ is the Fermi-Dirac distribution function that describes the electrons available for tunneling.

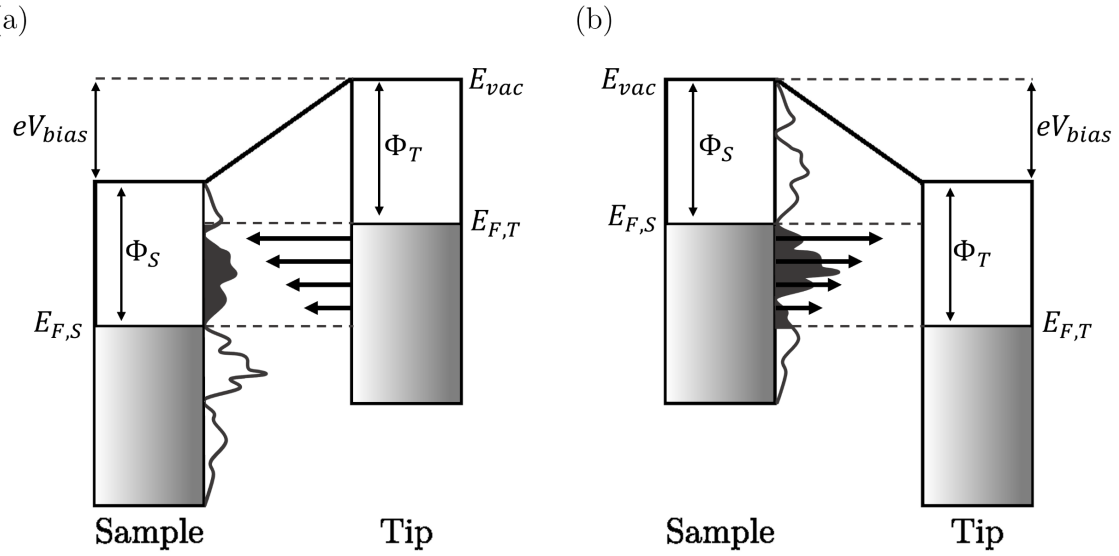

Figure 2.3: Energy level diagram for sample and the tip in STM. Illustration of tunneling direction dependence on the polarity of the bias. In case of (a) positive bias V_{bias} applied to the sample, electrons tunnel from the tip to the sample. (b) negative bias V_{bias} applied to the sample, electrons tunnel from the sample to the tip. The contribution of electrons to the tunneling is illustrated with the black arrows. The sample LDOS is shown, while the tip LDOS is not and is ideally flat to enhance the contribution of the sample to the recorded STM data.

Introducing the term density of states (DOS), the number of electrons per unit volume per unit energy, $\rho(E) = \sum_n \delta(E - E_n) \rightarrow \int \rho(E)\, dE$, the expression for the net tunneling current in terms of DOS of the tip and the sample becomes

$$I = \frac{4\pi e}{\hbar} \int_0^{eV_{bias}} \rho_S\left(E_{\text{F}} + \epsilon\right) \rho_T(E_{\text{F}} + \epsilon - eV_{\text{bias}})\ |M(\epsilon)|^2 d\epsilon \tag{2.14}$$

where $M(\epsilon)$ is the energy dependent tunneling matrix element, for which the energy dependence comes from the energy dependence of wavefunctions through their decay constants. Bardeen assumed that for small energy windows or small applied biases, the variations in the amplitude of the tunneling current, $M(\epsilon)$ is negligible. In the case of one-dimensional potential barrier, the tunneling matrix element Eq. (2.11) is approximated by the transmission factor T (Eq. (2.9)), as a result of Bardeen model estimation of the energy dependence of transmission factor[175]. Therefore, the tunneling current derived with Bardeen's approach, as provided by

Eq. (2.14), is the convolution of both the tip and the sample DOS and the transmission factor, T. The tip and the sample electronic structures take part in the tunneling current symmetrically, which makes them interchangeable. This provides the basis of the reciprocity principle in STM[176].

Fig. 2.3 shows the energy level diagrams for the sample and the tip in case of Fig. 2.3 (a) positive and Fig. 2.3 (b) negative sample bias voltage. The higher contribution to the transmission probability and the tunneling current comes from the topmost states of the energy interval. In the case of a positive V_{bias} applied to the sample, the sample E_{F} is lowered by eV_{bias} with respect to the tip E_{F}. Tunneling is allowed in this energy window, from the filled states of the tip E_{F}, to the empty states of the sample at $E_{\mathrm{F}} + eV_{\mathrm{bias}}$, while the tip states are populated near E_{F}. Likewise, when the sample is negatively biased, the electrons tunnel from the filled states of the sample near E_{F}, to the empty states of the tip. Since it is the empty states of the tip that contribute to the tunneling current in determining the sample DOS, one must make certain that the tip DOS is flat.

2.1.4. Tersoff-Hamann model and Chen's expansion

An extension of the Bardeen model was delivered by Tersoff and Hamann in 1983, to help tackle the complexity arising from the ambiguity of the tip states in solutions to tunneling matrix element[177]. Their assumption is valid for low tunneling voltage (V_{bias}), in order to eliminate the energy dependence of the tunneling matrix element, as well as the DOS. To further simplify the relation of tunneling to sample DOS, Tersoff-Hamann proposed a model for the tip as a spherically symmetric potential with localized wavefunction.

They imagined the tip as a geometrical point with radius R, about a point r_0 – in essence, a single atom with wavefunction in the form of an s-wave. Solving the tunneling matrix element in Eq. (2.11) for the wavefunctions of the tip and the sample derived by this assumption, using Eq. (2.14)[178]:

$$I(r_0, V) \propto \rho_T |\psi(r_0)|^2 \int_0^{eV_{\text{bias}}} \rho_S \left(E_{\text{F}} + \epsilon\right) \equiv \int_0^{eV_{\text{bias}}} \rho_S \left(E_{\text{F}} + \epsilon, r_0\right) d\epsilon \qquad (2.15)$$

where the tunneling matrix element is approximated to $M \propto \psi(r_0)$ by the Tersoff-Hamann approximation, $\rho_S(V, r_0) \equiv |\psi(r_0)|^2 \rho_S(V)$ and ρ_T is simply constant. This result shows that the tip follows the contour of the local density of states (LDOS) of the sample surface E_F and the STM image is simply the map of LDOS of the sample.

Despite being the most straightforward expression for interpretation of STM images, this approach was shown to be limited in its applicability to a wide V_{bias} range but also in its ability to describe the electronic states associated with real STM tips. The basis of Tersoff-Hamann assumption considers the tip wavefunctions as s-waves, ignoring all the other wavefunctions. In 1989, soon after the atomic resolution STM topography was achieved on the low Miller index metal surfaces, Chen pointed out that the Tersoff-Hamann approximation could not explain these results. The atomic distances achieved on the close-packed surfaces of metals including Au[179,180], Al[181], and Cu[182] were in the order of 2.5-3 Å, well-below the resolution limits that were predicted by Eq. (2.15). In addition, the corrugation amplitude of the atomically resolved STM images on these surfaces were too large, compared to what was predicted by Eq. (2.15). This suggests that in STM images of structures smaller than ~3 Å, DOS corrugation height will most prominently involve the effects from non-spherical (other than s-wave) tips. As a result, Chen extended this approximation for other tips beyond s-wave wavefunctions[183].

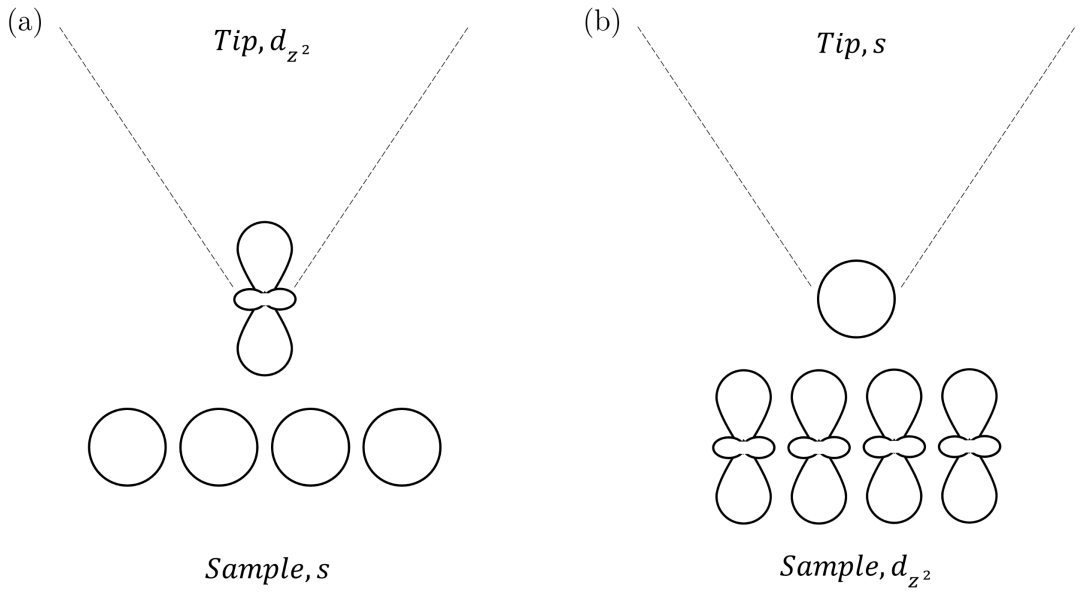

Figure 2.4: Illustration of the reciprocity principle in STM. The contribution of the tip states and the sample states are interchangeable. (a) schematic model of an STM tip with a d_{z^2} state tip apex, on a metal surface with free electron behaviour (b) schematic model of a tip with *s*-type wavefunction on a surface with d_{z^2} state top-layer atoms will have stronger corrugation.

A helpful illustration of the effect of tip states on the DOS corrugation in the STM image is shown in Fig. 2.4, which depicts a tip with s-wave and a tip with d_{z^2} state, imaging in STM. Exploiting the reciprocity principle, the tip with d_{z^2} state follows the charge-density contour of a 'fictitious surface' with d_{z^2} state on each atom rather than the surface LDOS contour at E_{F}, which results in a stronger corrugation.

Chen's quantitative treatment considers the solutions that satisfy the Schrödinger equation in the vacuum gap, with the implementation of leading Bloch wave approximation for close-packed surface metals with hexagonal symmetry. For an approximation of the tip wavefunction, the sample wavefunction is expanded near the centre of the apex atom as,

$$\psi_S(|R-r_0|) = \sum_{l,m} C_{lm} i_l(\kappa|R-r_0|) Y_{lm}(|\widehat{R-r_0}|) \tag{2.16}$$

where $\kappa = \sqrt{2m\Phi}/\hbar$, C_{lm} are renormalization constants, Y_{lm} are the spherical harmonics[184], $i_l(\xi)$ are the spherical modified Bessel function such that[176]:

$$i_l(\xi) = (-1)^l \xi^l \left(\frac{1}{\xi}\frac{d}{d\xi}\right)^l i_0(\xi) \tag{2.17}$$

which is the origin of Chen's derivative rule in evaluating the contribution of tip-orbital. Considering the predominantly used STM tip – tungsten, which tends to form d_{z^2} dangling bonds, inserting Eq. (2.16) into Bardeen's tunneling matrix element Eq. (2.11)[185],

$$M \propto \frac{2\pi C_{20}\hbar^2}{\kappa m}\left[\frac{\partial^2}{\partial z^2}\psi_S(R) - \frac{1}{3}\kappa^2\psi_S(R)\right] \tag{2.18}$$

the tunneling matrix element that corresponds to a tip wavefunction with d_{z^2} state is obtained. It is possible to evaluate the tunneling matrix element, hence the tunneling current, for different orbitals. Since tunneling current is proportional to tunneling matrix element, Chen was able to demonstrate with Eq. (2.18) that the contribution of tip state angular dependence cannot be negligible, when such small atomic distances are considered. This result highlights the limitation of the Tersoff-Hamann approximation.

2.1.5. Instrumentation

STM (Fig. 2.5) consists of a very sharp metallic tip that is mounted on a piezoelectric actuator. Piezoelectric materials expand or contract when voltage is applied due to the generation of a shear strain in the corresponding direction of the electric field, with a precision that is determined by the piezo constant as distance per unit voltage. In STM, the piezoelectric actuator is most commonly implemented in the form of a piezotube, due to its high piezo constant and high resonance frequency[186]. The piezotube allows high precision positioning of the tip over the

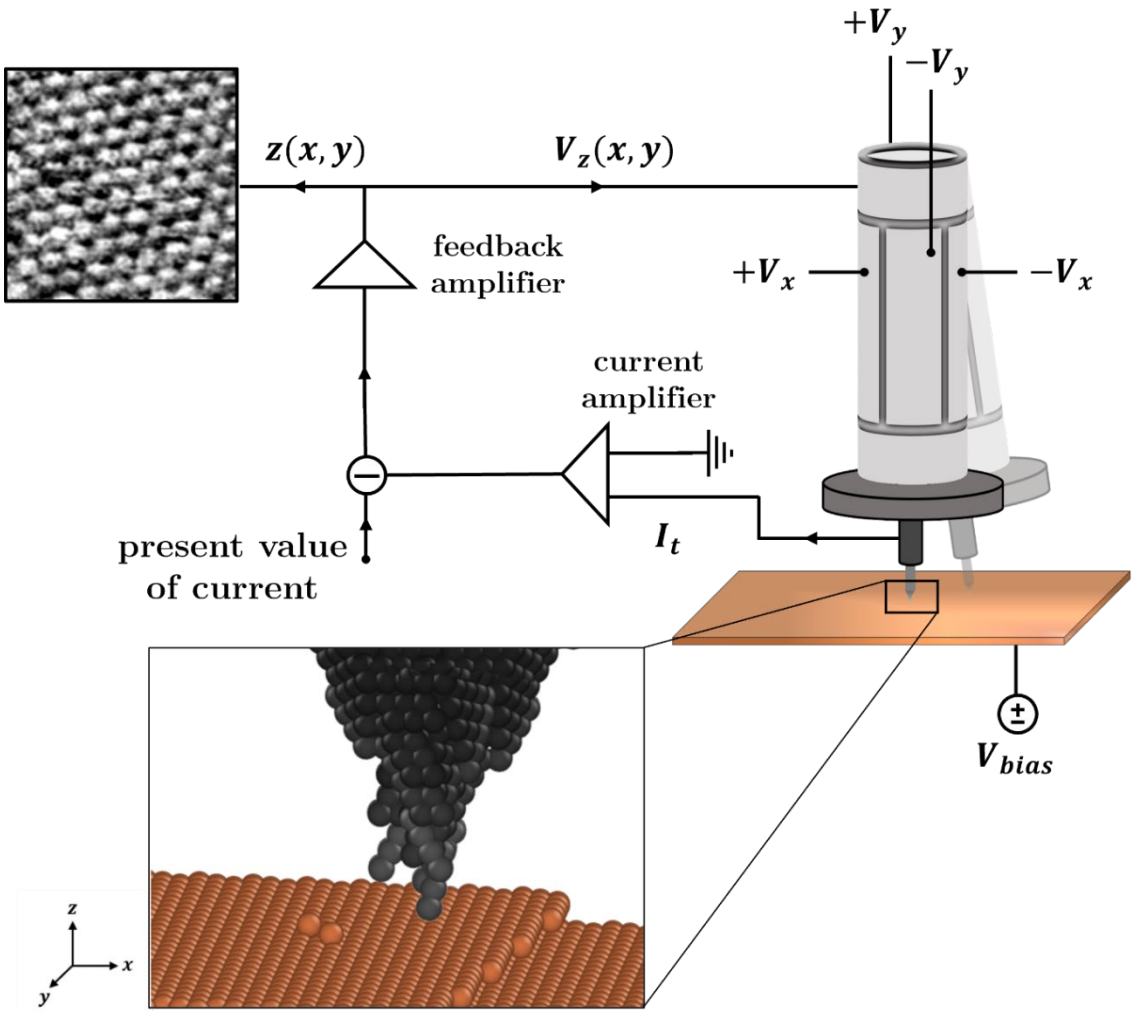

Figure 2.5: Schematic of STM. A sharp metallic tip mounted on a piezotube is raster scanned on the sample surface, on xy plane. A bias voltage is applied to the sample and tunneling current is measured. The feedback circuit adjusts the voltage of the z-piezo to keep the tunneling current at the set-point value. The z-piezo voltage is plotted, and surface topography map is obtained.

sample surface, with an accuracy of 10 pm in x and y, and 1 pm in z, typically[187]. The four-quadrant design of the piezotube scanner allows the application of potential to quadrants in pairs of x and y, and separately to z. This way the sample is scanned in xy plane, of an area specified by the applied voltage.

Initially, the tip is brought close to the sample using a coarse approach mechanism, involving slip-stick motion of the piezotube. At a safe but short distance from the sample, the set-point for the tunneling current is set, and the feedback loop is activated. The tip is then let to approach the sample automatically with a

controlled one-coarse-step at a time mechanism, allowing the search for the set-point to be established at each step, in the range of the piezotube. After the tip is brought to a distance where the set-point is reached, usually less than a nanometer from the sample surface, it is scanned over the surface, while a potential difference is applied between the two.

The tunneling current is acquired using an I-V converter, which both amplifies and converts the current into a voltage, with a gain determined by the required sensitivity. The I-V converter is attached to the tip and to a feedback control mechanism to adjust the tip-surface distance, maintaining the feedback current. The feedback circuit consists of a logarithmic amplifier. This linearizes the response to the exponential dependence of tunneling current on the tip-surface distance. The amplified signal is compared with the reference voltage and the resulting error signal is then sent to the feedback circuit to regulate the z piezo voltage for the tip to follow the set-point current contour.

The acquisition of tunneling current is a highly sensitive process, that requires a sufficiently stable environment for atomic resolution. This is achieved by the implementation of a vibration isolation mechanism, one of the essential components in STM, in order to reduce mechanical noise. The vibration isolation systems typically include eddy-current damping, compressed air suspension legs, mechanical springs, and a floating stage. Once a stable environment is achieved, the STM is set up for imaging.

There are two main modes of imaging in STM. These are determined by the parameter that is held constant and to be controlled by the feedback mechanism during imaging. These modes are constant-current mode and constant-height mode.

2.1.6. Imaging modes

In the constant-current mode, the tunneling current is kept constant, while the distance between the tip and the sample is regulated by the feedback loop, which minimizes the deviation of the actual current from the current set-point. Using this feedback signal, the tip moves in z direction in response to fluctuations in the tunneling current to maintain the pre-set current value. This movement in z is mapped, and it reflects the surface topography, when the surface is assumed to have constant LDOS at applied bias[176]. The feedback error signal, *i.e.*, the instantaneous difference between the measured tunnel current and pre-set current value is also recorded as the current error channel.

The other imaging mode is the constant-height mode. In this case, the tip position in z is kept constant and the feedback loop is deactivated. The tip is raster scanned in xy sample plane while the z piezo is stable, and the current is recorded. Changes in the measured current then reflect the surface topography. Since the feedback circuit is not active, the delay as a result of tip-surface gap adjustment does not exist, constant-height mode allows for much faster scanning as a result. The lack of feedback circuit however might result in the tip crashing into the surface unless the surface is atomically flat.

2.1.7. Scanning tunneling spectroscopy

In addition to providing surface topography information by measuring the current and controlling the distance between the surface and the tip gap, STM is also capable of providing spectroscopic information locally. As discussed in previous sections, the tunneling current I is a function of the V_{bias} and the tip-sample distance: $I(V_{\text{bias}}, z)$. By controlling one these parameters, it is possible to obtain spectroscopy information regarding the relation between the other two, revealing

further information on the DOS characteristics of the sample. The most common spectroscopy techniques are $I(V_{\text{bias}})$ spectroscopy, $Z(V_{\text{bias}})$ spectroscopy and $I(z)$ spectroscopy.

In $I(V_{\text{bias}})$ spectroscopy, the tunneling current is measured as a function of bias voltage, while the tip-sample distance z is kept constant at a value that corresponds to I_{set}. In order to measure the variation in the current, the feedback circuit is interrupted. In the regions where $I - V_{\text{bias}}$ is linear, $I(V_{\text{bias}})$ spectroscopy provides the basis for differential conductance measurement $\mathrm{d}I/\mathrm{d}V$, which reveals information including the sample DOS at the energy eV_{bias} relative to Fermi level[188]. This is achieved either by the post-processing of the spectroscopy data, by differentiating the tunneling current I with respect to the bias voltage V_{bias}, or by an additional experimental set-up, which provides a measurement with higher resolution. By applying a relatively small amplitude AC signal on the bias voltage at a particular frequency using a lock-in amplifier, the bias signal is modulated. The bias modulation frequency must be above the cut-off frequency of the feedback loop, so the feedback cannot follow the modulation to keep the current constant. Scanning the bias voltage, $\mathrm{d}I/\mathrm{d}V$ is measured directly at each bias, as a convolution of sample and tip DOS. As noted in the previous section, knowing the tip DOS is crucial for the determination of the sample DOS. In the assumption of a flat DOS tip (with negligible variation in DOS in the energy interval of interest), using Eq. (2.15), the differential conductance is approximated to the sample states as

$$\frac{\mathrm{d}I}{\mathrm{d}V} = \rho_S(E_{\mathrm{F}} + eV_{\text{bias}}) \tag{2.19}$$

In $Z(V_{\text{bias}})$ spectroscopy, while the feedback is active to maintain the tunneling current at a set-point value I_{set}, the movement of z piezo is monitored as a function of bias voltage. Also known as constant current spectroscopy, this method allows

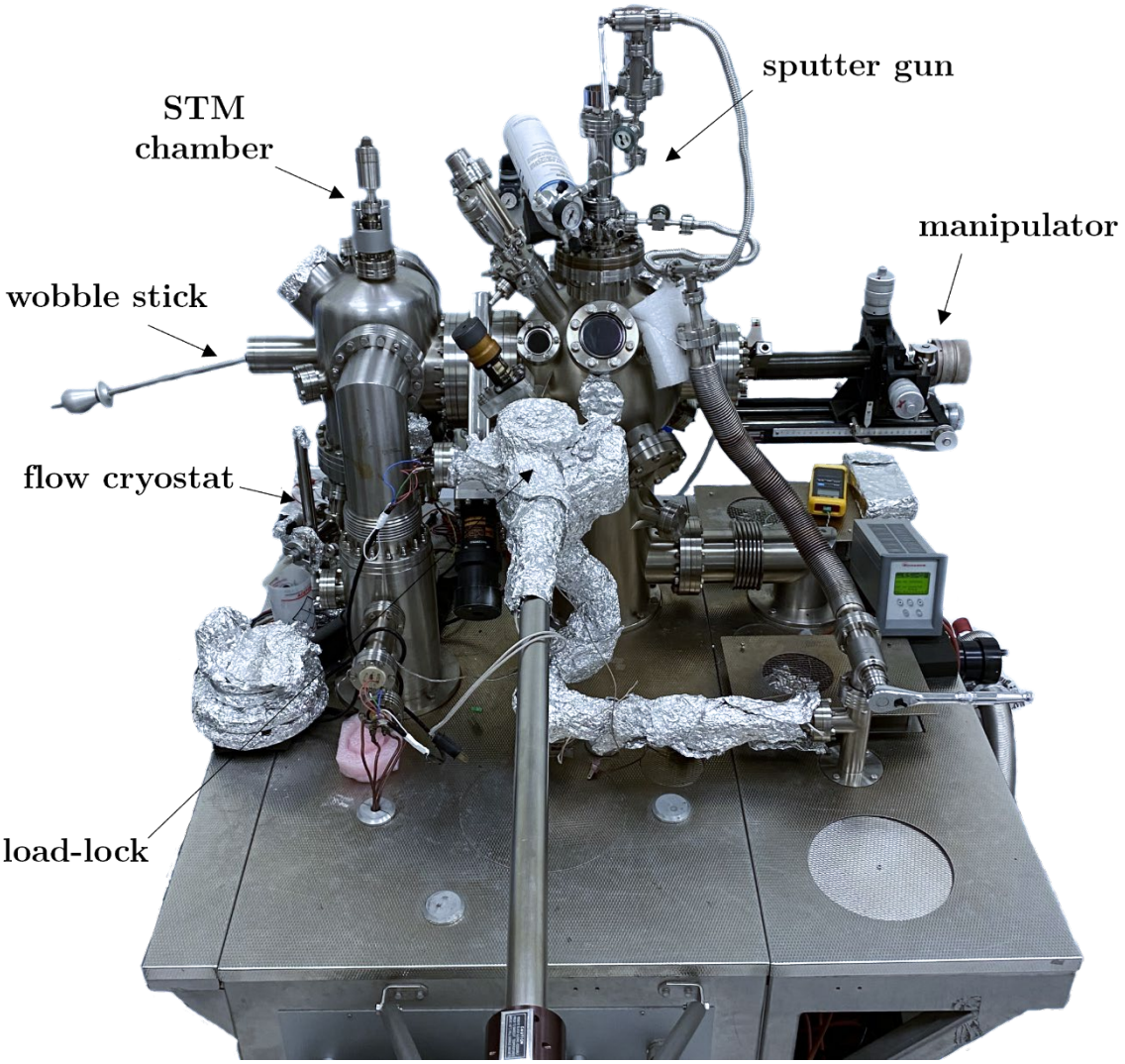

Figure 2.6: Schematic of the Omicron VT-STM showing the load-lock, preparation and STM chambers. The load-lock is attached to the preparation chamber. The preparation chamber is equipped with a manipulator and a sputter gun. The STM chamber has a flow-type cryostat for cooling the sample stage.

for the detection of the standing waves, when the bias range is above the average work function. Due to the reflection of electrons in the region between the sample surface and the barrier, electron standing waves show up as oscillations in the tunneling current[189], hence the z piezo movement. $Z(V_{\text{bias}})$ spectroscopy data reveals information regarding the surface-specific reflectance characteristics, and therefore characterization of different surfaces and tunneling barriers is made possible. Standing waves are also observed in STM images of 2D surface states[190],

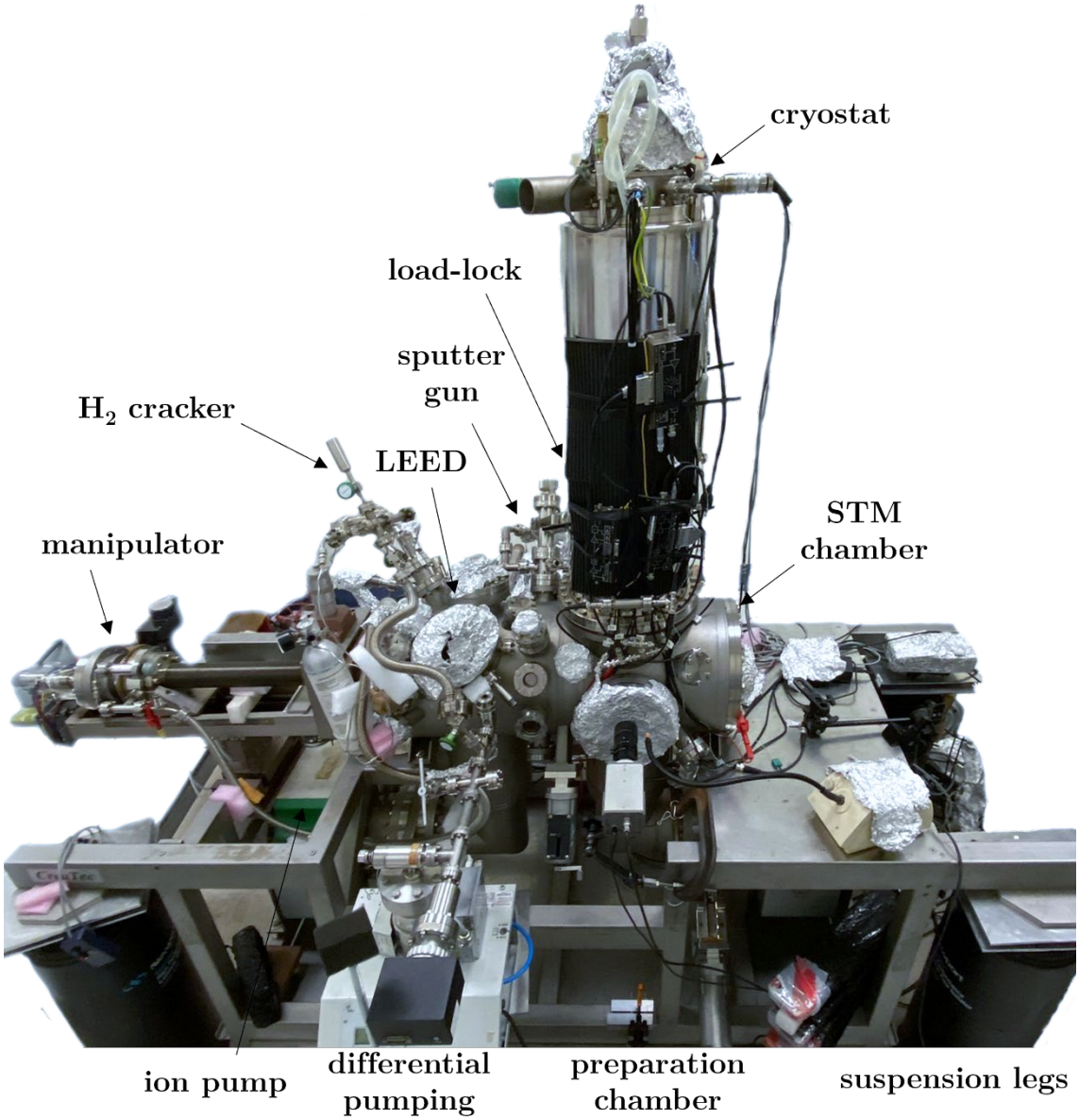

Figure 2.7: Front view of the CreaTec LT-STM UHV system, used for the low-temperature measurements in this work. The UHV system consists of three chambers: The load-lock for sample/tip transfer into/from the UHV, without breaking the vacuum. Preparation chamber equipped with preparation components. The STM chamber placed in a bath-type cryostat. The system is lifted on the suspension legs for vibration isolation.

due to scattering near local features such as step edges; adsorbate atoms; dislocations; and other defects including grain boundaries, which will be discussed later.

In $I(z)$ spectroscopy, the tunneling current is measured as a function of tip-sample distance, while the bias voltage is kept constant. This is achieved by interrupting

the feedback circuit while approaching or retracting the tip in tunneling regime, with the controlled change of z piezo voltage. The tunneling current changes exponentially as given in Eq. (2.8). From the same equation, the average tunneling barrier height is extracted from an exponential fit to the spectroscopy data.

2.1.8. UHV system

Fig. 2.6 and 2.7 show schematics of the UHV systems used for the measurements of the results presented in this thesis. The UHV system consist of three chambers: load-lock, preparation and STM chambers. The load-lock is the transfer into the ultra-high vacuum (UHV), without breaking the vacuum. The load-lock is vented, and samples and tips are put in the load-lock, where it is pumped down with the turbo-molecular pump, backed by a rotary pump and baked for at least 24 hours following a sample/tip load, prior to transfer into the preparation chamber. Once the load-lock pressure is sufficiently low ($<1 \times 10^{-8}$ mbar), the gate valve that separates the two chambers is opened and samples/tips are transferred into the

preparation chamber. The preparation chamber has a base pressure of 1×10^{-10} mbar. This level of low pressure is maintained by an ion getter pump (IP) and a titanium sublimation pump (TSP), and monitored with a hot-filament ion gauge. The chamber is also isolated from both the STM analysis chamber and load-lock by gate valves. It is equipped with multiple components that enable essential *in situ* sample preparation prior to the STM analysis. A quadrupole mass spectrometer is attached to the chamber for residual gas analysis during sample preparation, which is also essential especially for leak detection following a bake. For sample preparation, an ion sputter gun, and a low-energy electron diffraction (LEED), a manipulator unit for sample/tip positioning with direct and resistive heating capability are available in the chamber.

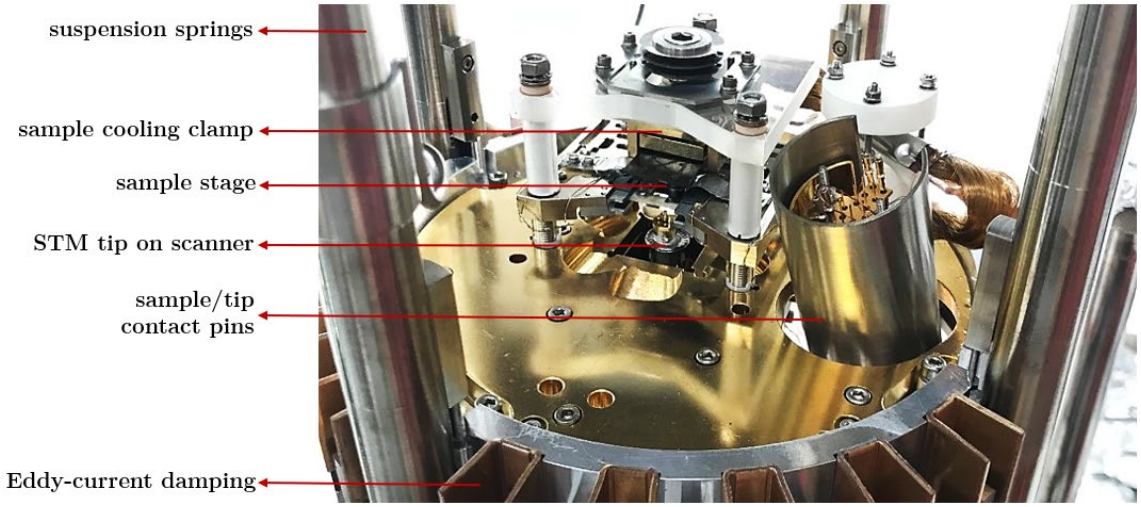

Figure 2.8: Close-up view of the Omicron VT-STM STM stage. STM stage is placed in the STM chamber, on a two-stage plate. Stage is suspended with springs isolated from the base plate, in addition to the eddy-current damping system. Cooling/heating elements: Cooling clamp connected to the copper braid for cooling and contacts on the sample stage for heating.

The STM analysis chamber is where the STM stage (scanner unit) is located. The chamber is attached to the preparation chamber and separated by a gate valve. It has a base pressure lower than 5×10^{-11} mbar. Similarly, its vacuum level is maintained by the use of an IP and TSP. There is a wobble-stick in the STM analysis chamber to transfer the samples/tips to the STM stage.

The STM measurements presented in this thesis includes measurements obtained both at room-temperature (RT: 298 K) and low-temperature (LT: 77 K), as will be specified in the following chapters. To reduce the thermal drift and noise, as well as diffusion, LT-STM measurements are preferred. This is enabled by a two-staged bath-type cryostat. Both the inner and outer cryostats are filled with liquid nitrogen (LN_2) and the STM stage, which includes the tip and the sample, is cooled down to 77 K. The STM stage itself is suspended with springs and equipped with eddy-current dampers. The whole system rests on a heavy stage isolated from the ground. Fig. 2.8 shows a close-up view of the STM stage of Omicron Variable-Temperature (VT) STM.

VT-STM is amongst the first of its kind, developed just a couple of years after the invention of the STM. It was specially designed to allow STM operation at a variable temperature range, for investigation of thermally activated fast processes and reactions on the surfaces dynamically, in real-space. This is facilitated by a flow-type cryostat (for LN_2 and LHe) attached to a cooling clamp block on the sample, and a sample stage with direct and resistive annealing capabilities, equipped with a radiation shield. The room-temperature experiment results presented in this thesis are obtained in Omicron VT-STM.

Low-temperature experiments are essential for freezing the diffusion and motion on surfaces. For the low-temperature investigation of the surfaces presented in this thesis, CreaTec LT-STM is used with LN_2. CreaTec LT-STM allows STM operation at LN_2 (77 K) and LHe (4.7 K) temperatures, in addition to RT experiments. The STM stage is thermally isolated with a radiation shield, which allows STM to be kept at low-temperature for a longer time.

2.1.9. Tip preparation

The tip is the key element for determining the quality of STM data. A sharp tip, ideally with a single atom in the end of the apex, is essential not only for achieving good atomic resolution but also for accurate spectroscopy measurements. The tip and the sample contribute to the tunneling current symmetrically as per the reciprocity principle. This means that the state and stability of the tip play a significant role in determining and extracting the real contribution of the sample DOS. Therefore, the process of forming a good STM tip is the first important step in the STM experiment. STM tips are formed by electrochemical etching of tungsten wire[191], using the Omicron Tip Etching Unit placed on a vibration isolation stage. A 10 mm piece cut from high purity tungsten wire (t=250 μm), which acts as the anode, is mounted on a vertical micro-positioner above the beaker with 5M

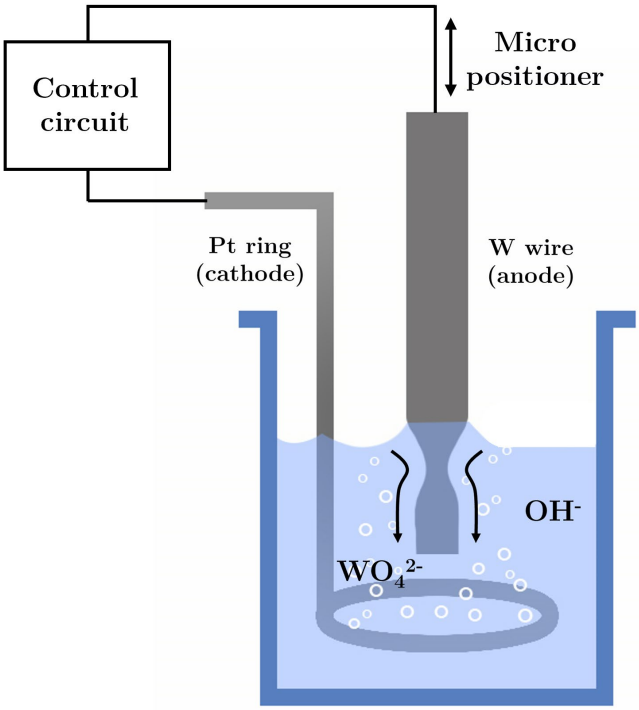

Figure 2.9: Schematic of the tip etching set-up. The tungsten wire attached to a micro-positioner is immersed in the NaOH solution. The circuit attached to the Pt ring and W wire controls the differential current upon application of a potential difference.

NaOH solution, as shown in Fig. 2.9. A Pt wire ring, which acts as the cathode, is then placed in the centre of the beaker. The micro-positioner is aligned in the centre of the xy plane above the NaOH beaker and the Pt ring, so that a centrosymmetric tip apex is formed. The tungsten wire is lowered into the solution while an initial potential difference of ~10 V is applied between the anode and the cathode, for the removal of the oxide. The tip position is then adjusted to ~3 mm below the solution and the tip is etched with a potential difference of ~5 V. The etching occurs at the air-solution interface, forming a neck at the meniscus:

$$\text{Cathode: } 6\ H_2O + 6\ e^- \rightarrow 3\ H_2 + 6\ OH^-$$

$$\text{Anode: } W + 8\ OH^- \rightarrow WO_4^{2-} + 4\ H_2O + 6\ e^-$$

$$W + 2\ OH^- + 2\ H_2O \rightarrow WO_4^{2-} + 3\ H_2$$

After a few minutes, when the neck is etched to a point where the weight below

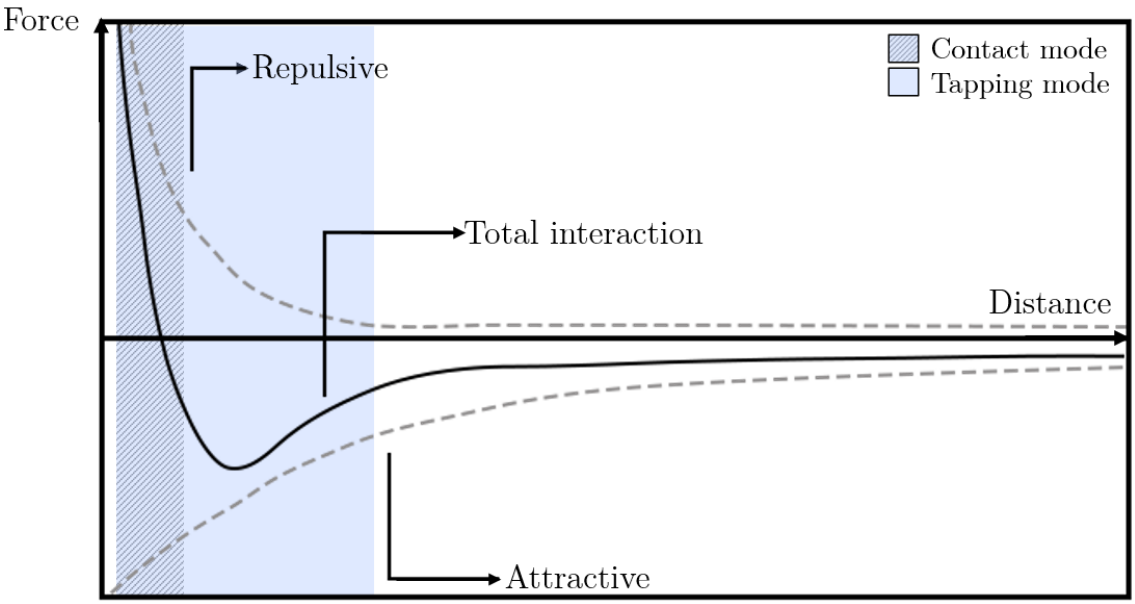

Figure 2.10: Force-distance curve derived from Lennard-Jones potential. The total interaction force (black, solid) between the cantilever and the surface, as a result of repulsive and attractive forces (dashed, grey), as a function of tip-surface distance.

the meniscus overcomes the tensile strength of the neck, the wire breaks from the neck leaving a sharp tip. This breakage is detected by the control circuit as a sharp drop in the differential current and the power is turned off immediately. The precision of the process is maintained by the fast response of the control circuit and further etching is avoided, which would result in a round and blunt tip. The etched tungsten wire is then dipped in deionised water in order to remove the residual salt. After a general inspection under the optical microscope, the tip is loaded into the UHV chamber.

2.2. Atomic force microscopy

Invented three years after STM, AFM[192] is a scanning probe microscopy tool that is used for high resolution topographical mapping[193] and characterisation of surfaces. One significant advantage AFM offers over STM is its ability to visualize and investigate surfaces and surface properties of any material, including insulators. Over recent decades, it has become an impactful tool, capable of providing a wide

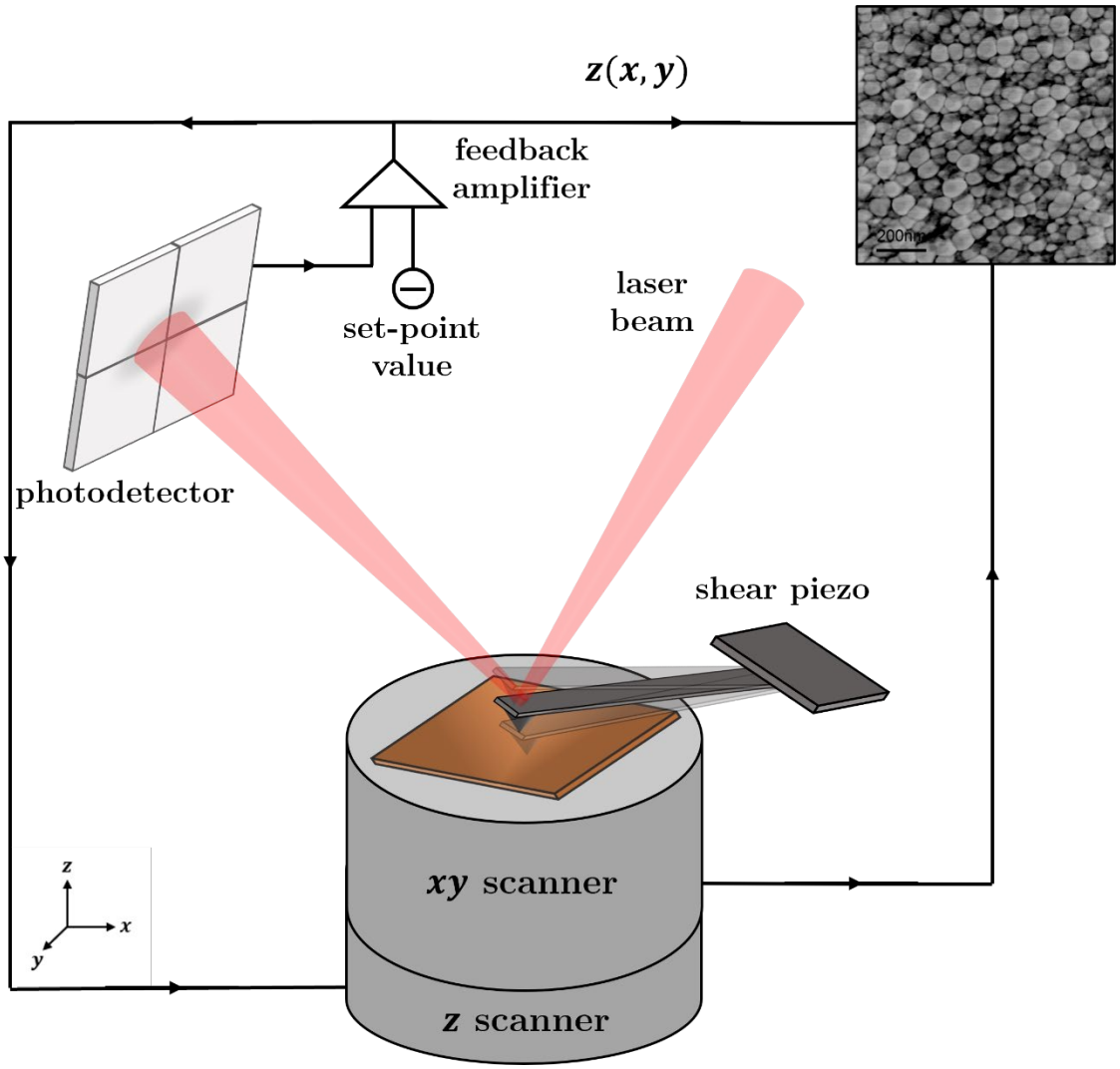

Figure 2.11: Illustration of operation principle of an AFM. The cantilever is excited to oscillate with the use of a shear piezo. Laser beam is reflected from the back of the cantilever onto the photodetector, fed to the feedback circuit. The surface is raster scanned with the xy scanner, as the z scanner adjusts the cantilever-surface distance as a response to the feedback circuit, to maintain the set-point oscillation amplitude.

range of information on mechanical[194], electrical[195,196], and magnetic[197] properties of surfaces in ambient, vacuum[198], or liquid[199–201] conditions.

The AFM also differs from STM in terms of *what* it measures – force interaction between a cantilever and the surface. These interaction forces include electrostatic forces, van der Waals forces, magnetic forces, adhesion, and capillary forces[202]. The total interaction force changes for different operation modes of AFM, as shown in Fig. 2.10. At close enough separations, the overlap energy is repulsive due to Pauli

exclusion principle. When the distance between the cantilever and the surface is increased, the overall force interaction is dominated by attractive, primarily van der Waals forces.

There are two main modes of operation in AFM: dynamic mode and contact mode. Tapping mode (amplitude modulation) and non-contact mode (frequency modulation[203]) are classified as dynamic modes[204]. The typical operation mechanism is illustrated in Fig. 2.11. In tapping mode, the cantilever is excited to oscillate at or near its resonance frequency. The cantilever snaps the surface as it oscillates in repulsive and attractive force regime, as shown in Fig. 2.10. The oscillation causes deflection of the flexible cantilever. The deflections are quantified with the use of a four-quadrant photodiode, by the reflection of a laser beam focused on the highly-reflective back of the cantilever. This reduced oscillation amplitude is used as the set-point for the feedback circuit. As the sample surface is raster scanned in xy plane, due to the changes in the tip-surface interaction and the surface topography, the position of the reflected beam on the photodiode changes. This is fed into the feedback circuit along with the set-point amplitude, and the vertical position of the cantilever is adjusted by a z piezo. The movement of the z piezo is used to obtain 3D mapping of the surface topography. The resolution of the topography data is directly reliant upon the condition of the tip and its sharpness.

The tapping mode also provides information on the phase variations of the oscillation, on every pixel. In contact mode, the cantilever is scanned over the surface whilst in constant physical contact with the surface, in the repulsive regime of the force-distance curve as shown in Fig. 2.10. The cantilever is set to keep a constant deflection value and the changes in the deflection due to the surface topography are controlled by the feedback circuit. Since contact mode relies on the direct physical contact between the cantilever and the surface, it is possible to

extract quantitative data of both normal and lateral forces upon calibration of the cantilever[205]. Mechanical properties of the surface, including stiffness, friction and adhesion can also be obtained[206]. Contact-mode is also implemented as a controlled method for nanoscale surface machining[207–209] and milling with the use of extremely stiff cantilevers.

Due to its extensive capabilities in obtaining a wide range of information on surfaces as well as high resolution topography maps without operating condition, environment and sample limitations, AFM is recognized as a powerful tool for scanning probe microscopy applications. In this thesis, tapping mode AFM has been used for macroscopic characterisation of surface topography in ambient conditions.

2.3. Molecular dynamics simulations

Computer simulations are frequently used to test, compare and confirm experimental observations of systems involving dislocations, interfaces and grain boundaries. In this work, molecular statics simulations have been employed to compare and support the experimental results obtained using STM in atomic detail, as well as to investigate the subsurface restructuring that occurs at emergent grain boundaries in fcc metals[163,167].

Molecular dynamics simulations evaluate the total potential energy of the system by numerically computing the Newtonian forces (and derivatives) acting on individual atoms. The specification of the suitable energy function that defines the potential energy in terms of the configurational space of materials, as a function of the positions of individual atoms, is provided by interatomic potential functions[210,211]. Molecular statics also employ an interatomic potential input, to determine the optimized (minimum energy) configuration system by minimization of its total potential energy and iterative displacement relaxation, with respect to

the atomic equilibrium positions within specific boundary conditions, at 0 K. These computational methods allowing calculation of large-scale cells with an extensive number of atoms in microscale, typically 0.1-10 nm and 1-10 ps, are ideal for simulation of low-energy configurations of grain boundaries in atomistic detail, as well as their interaction with other defects and free surfaces[212].

The simulation cell is constructed by defining the geometry of the reference crystal, that will be used to generate the grain boundary. The grain boundary with misorientation angle θ is built by merging the two crystals obtained after equal and opposite rotations ($\pm\theta/2$), about the given rotation axis. The symmetric tilt grain boundary is built by this method. Once the simulation cell is defined and lattice constant, interatomic potential, and periodic boundary conditions are provided, the minimum energy configurations are searched by energy minimization. A detailed description of boundary geometry is provided in Section 3.2.1.

The MS simulations presented in chapter 5 were performed by Dr. Xiaopu Zhang using the LAMMPS code[167,213,214]. The Cu bicrystal $\theta = 13.17°$ grain boundary with tilt axis [111], mean boundary plane normal $[1\bar{1}0]$ (x) and mean period vector $[\bar{1}\bar{1}2]$ (y) was built as described above, in Cartesian coordinate system. The simulations cell comprised two parallel grain boundaries with equal and opposite misorientation ($\theta = \pm 13.17°$) and periodic boundary conditions were applied in x, y and z. Grain boundary energy was calculated by pairwise interactions using embedded-atom method (EAM) interatomic potential for Cu[48].

The structure is then relaxed to achieve the lowest-energy configurations. A two-stage minimization of conjugate gradient algorithm is used for iteratively adjusting the atomic coordinates, in each defined timestep. This proceeds as in each step, the new search direction is determined based on the information of direction from previous iteration step, and continues until the critical predetermined value of

energy is reached. In the second minimization, the simulation cell is allowed to relax, so that it can expand/contract to adjust into lowest energy configuration. The simulations of emergent grain boundaries (eGBs) were carried out in suspended films comprising stacks of relaxed boundaries along [111] direction, creating two parallel grain boundaries with top and bottom surfaces and an additional vacuum layer. The emergent core-shifted grain boundaries were then obtained by systematically shifting the dislocation core line, by deleting or inserting core atoms and these are added back to or taken from the Cu bulk, respectively. In correlation with the energy balance described by straight wedge disclination geometry[216], discrete defect (eGB) energies were computed at each stage, as described in chapter 5. The optimized core-shifted emergent grain boundary configurations corresponding to the minimum energy structure are visualized in OVITO[217].

2.4. Scanning electron microscopy

Since its development, scanning electron microscopy (SEM) stands as a powerful tool for the nanoscale characterization and visualisation of materials[218,219]. In contrast to conventional optical microscopy that employs visible light, SEM operates by the utilization of a focused electron beam to produce high-resolution images of the samples. The high resolving power of SEM relies on the remarkably small (de Broglie) wavelengths of electrons compared to those of visible light, given by de Broglie relationship as $\lambda = h/mv$, where h is Planck's constant, m is mass of the electron and v is velocity of the electron.In a modern SEM, the electrons that are typically accelerated to an energy of 0.5-30 keV are collected to form a beam and focused onto the sample with the use of a system that employs condenser and electromagnetic lenses and adjustable apertures. The focused electron beam is then raster scanned over the sample surface using the scan coils and the interaction of

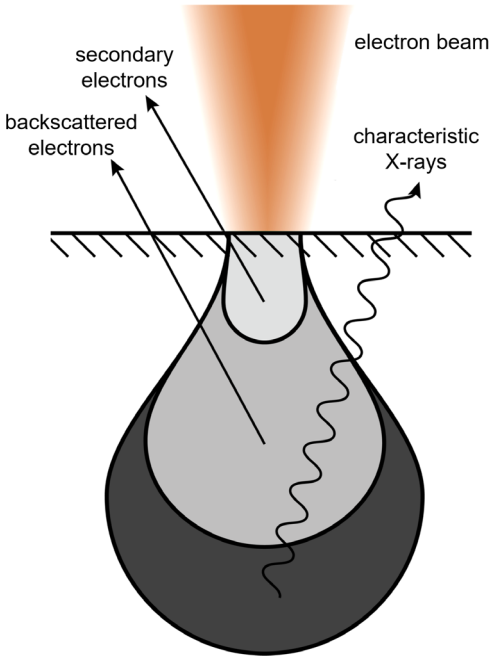

Figure 2.12: Schematic of the electron beam in SEM and signals resulting from the electron beam-surface interaction, including secondary electrons, backscattered electrons and characteristic X-rays.

the incident electrons with the sample results in the emission of various signals upon elastic and inelastic scattering. These signals consist of secondary electrons (SE), backscattered electrons (BSE) and characteristic x-rays as shown in Fig. 2.12,which are collected using a set of specific detectors to generate an image of the sample[220]. Due to the difference in surface sensitivity of each of these signals, interpretation of each signal leads to distinct information regarding the sample. Secondary electrons of relatively low energy (< 50 eV) are emitted from a shallow depth, close to the surface and therefore possess information about the topography and morphology of the sample surface[221]. Backscattered electrons (with higher energy) are generated by the emergence of the scattered electrons from the surface as a result of several elastic collisions of the incident electrons with the sample atoms, which make them highly sensitive to the atomic number of the scattering atoms. Therefore, the BSE image contrast is informative on the elemental composition of the sample. The characteristic x-rays, specific to each element, are

emitted when a higher energy electron fills the hole created by the inelastic collision of the incident electrons with the core electrons in the sample atoms and energy is released. The analysis of the signal collected from characteristic x-ray emissions allows quantitative detection and mapping of the elemental composition of the sample, a technique known as energy dispersive x-ray spectroscopy (EDX).

SEM has been occasionally used in this work to visualize the surface morphology of NC Cu film after thermal treatment and of Cu (111) bicrystal to investigate the grain boundary structure macroscopically. The SEM images presented in chapter 4 and chapter 5 were acquired using a Zeiss SUPRA FE-SEM.

2.5. Electron backscatter diffraction

Electron backscatter diffraction (EBSD) is a commonly used technique for quantitative microstructural characterization of materials. EBSD is capable of providing crystallographic orientation maps, grain size/distribution and grain boundary analysis and texture characterization, with a resolution similar to that of SEM, with which it is used jointly[222,223]. As explained in the previous section, following the elastic scattering of the high energy incident electrons by the atoms in the sample in various directions dictated by the atomic planes, the electrons are backscattered from the sample. If Bragg condition ($n\lambda = 2d \sin\theta$) is satisfied, the backscattered electrons form a diffraction pattern, also known as Kikuchi pattern, which is detected at each pixel with the use of a specific detector with an embedded phosphor screen[224]. The sample is tilted by 70° towards the detector in order to improve the intensity (signal to noise ratio, *i.e.,* the ratio of diffracted electrons to background yield) of the pattern by increasing the total interaction volume within the sample and proper aligning of the backscattered electron signal relative to the detector. The position and angle of the Kikuchi lines are analysed, and

crystallographic lattice planes are quantitatively identified using Hough transform. Through comparison of the resulting pattern with a reference pattern, orientations and phases can be determined and thus, a range of maps is acquired. Among these, one of the most common ways to represent the grain orientation is the inverse pole figure (IPF) map. IPF maps, where the two-dimensional projection of the *poles* corresponding to normals to chosen sample directions are plotted with respect to a specific crystal axis (normal, longitudinal or transverse direction) display the microstructure texture with the help of an assigned colour coding key[225].

For this work, a Bruker QUANTAX EBSD was used to confirm the pattern quality and the misorientation angle of the two grains within the studied Cu (111) bicrystal. The EBSD analysis and IPF maps are presented in chapter 5.

3. Dislocations and Grain Boundaries

In this chapter, the background information on the concept of defects and dislocations, as well as their role in the formation of grain boundaries is provided. The relevant theory and terminology around grain boundaries are presented.

3.1. Defects in crystals

In 1912, Max Von Laue's discovery of x-ray diffraction by crystals was first published along with the work of his colleagues Walther Friedrich and Paul Knipping's on a copper sulfate single crystal[226,227]. Their work showed that the diffraction of x-rays by these crystals forms specific interference patterns. This proved the idea that crystalline materials are formed by a three-dimensional periodic arrangement of their constituent atoms/group of atoms in space. However, the periodic arrangement of atoms is not always perfect and might occasionally be disturbed by the presence of defects. These defects are generalized according to their dimensions so they may occur as point, line, or planar defects. In the context of the results presented in this thesis, the structural properties of defects and dislocations will be described as they form in copper, in a generalized approach that is relevant to all fcc metals.

The face-centred cubic (fcc) lattice, shown in Fig. 3.1 (a), is exhibited by most metals, such as noble metals, including Cu, Au and Ag; and some significant transition (Ni, Pd, Pt) and higher valence metals (Al, Pb). The structure of the conventional cell shows the atoms located at the centre of each face, in addition to the atoms located at each corner. The conventional unit cell of volume a^3, where a is the lattice parameter, consists of four lattice points that correspond to four atoms

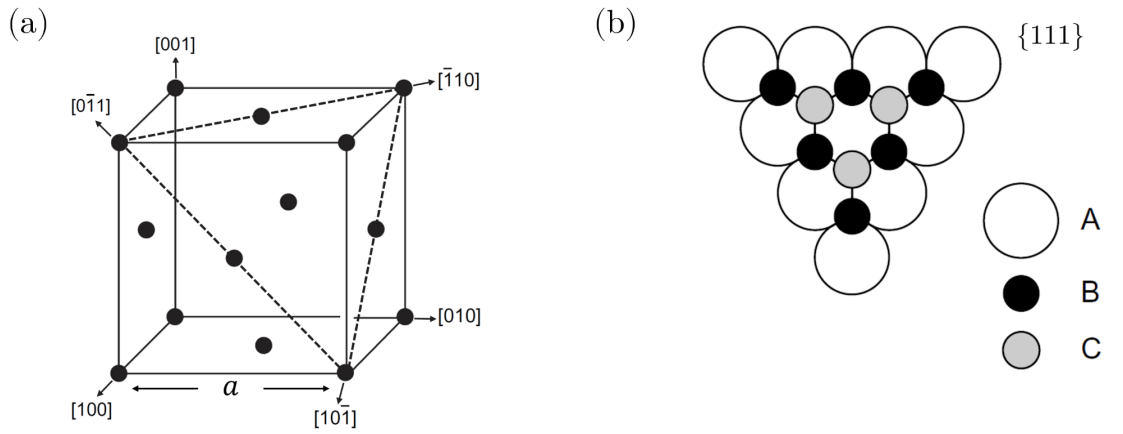

Figure 3.1: (a) face-centred cubic structure conventional unit cell with lattice parameter a (b) close-packed plane stacking viewed along $\langle 111 \rangle$ direction[228].

per unit cell. There are a total of 8 atoms located at the corners. There are a total of 6 atoms at the centre of each face, at coordinates of type $(0, \frac{1}{2}, \frac{1}{2})$. Each of these atoms has 12 nearest neighbours, at a distance of $a/\sqrt{2}$ and 6 next-nearest neighbours at a distance of a.

In the fcc lattice, the closest-packed arrangement of atoms is on the set of $\{111\}$ planes, along the $\langle 110 \rangle$ directions which are referred to as close-packed planes and close-packed directions, respectively. There are four of these close-packed planes, and each of these possess three close-packed directions altered by 60° rotation, shown as dashed lines in Fig. 3.1 (a). The shortest lattice vectors connecting the nearest neighbours are of the form $a/2\langle 110 \rangle$, in the close-packed direction.

The top-view schematic of close-packed plane (111) is shown in Fig. 3.1 (b). The crystal is built by successive stacking of (111) planes on top of each other, with a distance of $a/\sqrt{3}$ – referred to as interplanar distance. The position of the centre of an atom A, is shifted by $a/6$ $[11\bar{2}]$ to position B in the adjacent layer and then by $a/6$ $[\bar{2}11]$ to position C, in the next adjacent layer, when viewed along [111]. In every third (111) plane, successive shifting results in a position equivalent to

position A. The planar stacking sequence along the [111] direction can then be referred to as $ABCABCABC$ stacking, with a period of three (111) planes.

3.1.1. Point defects

Point defects are the most common type of defects occurring in almost all crystalline materials as disturbances in the ideal crystal extending to a few interatomic distances. There are two types of intrinsic point defects, as shown in Fig. 3.2. First is the case of a missing atom from an atomic site that should be occupied in the ideal crystal, referred to as vacancy defect. Secondly, interstitial defect is the presence of an additional atom on a site that is normally unoccupied. The character of the interstitial defect is determined by the type of added atom. Where the additional atom is identical to that of the host crystal, this is known as an *intrinsic* interstitial defect, whereas an *extrinsic* interstitial defect is characterised by the addition of a non-identical atom. These are mostly due to chemical defects, known as impurities.

As shown in Fig. 3.2, during vacancy formation, removal of an atom from the crystal results in an extra volume, whereas during interstitial formation an additional atom has to be fitted in the same volume of an ideal crystal. In both cases, the neighbouring sites move in a particular direction, with a particular magnitude depending on the degree of local distortion caused by the defect type. To relax the disturbance in the crystal back to the equilibrium spacing of the ideal crystal structure, neighbouring atoms move towards the centre of vacancy defects and outwards from the centre of the interstitial defects. The calculation of equilibrium defect concentration requires the estimation of the defect formation energy, which is the energy required to break/make the bonds between the removed atom and its neighbours.

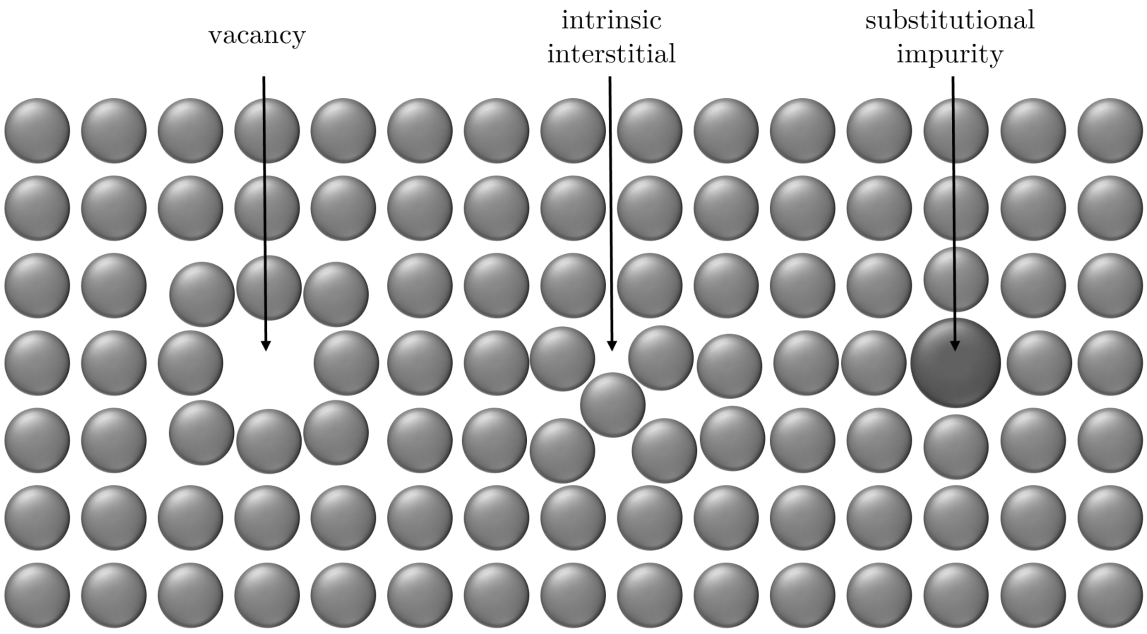

Figure 3.2: Schematic of fundamental point defects in crystals. A vacancy is created by removal of an atom from its ideal site. An intrinsic interstitial is formed due to the addition of an atom identical to the host crystal. An extrinsic interstitial is created due to an impurity.

There is a number of point defects present in a real crystal at finite temperatures, in thermodynamic equilibrium with the lattice. For close-packed metals, Johnson[229] demonstrated a correlation between the experimental values of vacancy formation energy E_f^v and melting temperature T_m of the material, such that $8.5\,kT_\mathrm{m} < E_f^v < 10\,kT_\mathrm{m}$. Detailed calculations by Huntington-Seitz[230,231] and Lomer[232] found that the vacancy formation energy in copper is approximately ~1.5±0.5 eV. Based on similar calculations, the formation energy of an interstitial E_f^i, was however shown to be about 3 to 4 times higher in general, leading to ~4±0.5 eV in copper[233]. This result explains the low concentration of interstitial defects in close-packed metals at equilibrium, compared to that of vacancies.

Imperfections in crystals are not only limited to vacancies or interstitial defects. These intrinsic point defects introduced by plastic deformation either externally by high-energy particle irradiation or by quenching, or naturally during crystal growth may play an important role in noble metal crystals, as they assist self-diffusion.

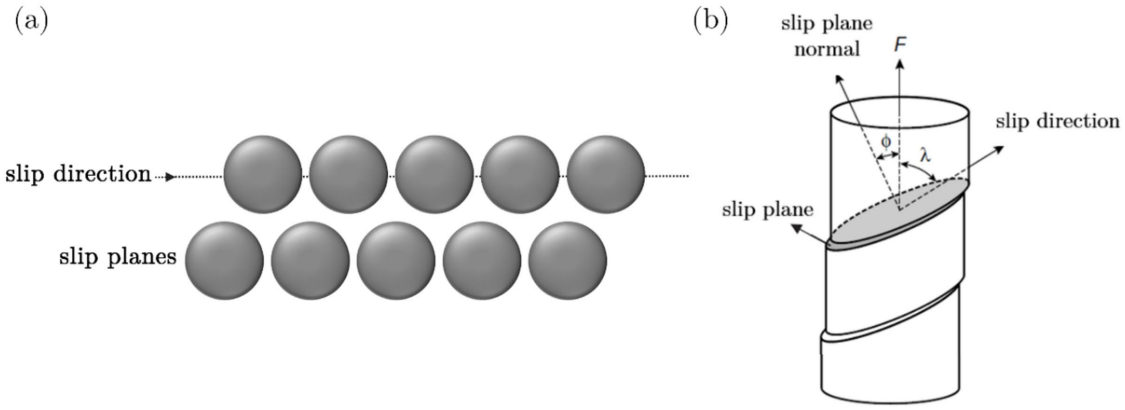

Figure 3.3: Illustration of plastic deformation mechanism by slip. (a) Close-packed planes slip along slip directions once the yield shear stress is exceeded. (b) Schematic of effective component of applied stress. Critical resolved shear stress is evaluated as the yield stress component that applies on the slip planes.

This movement may allow the organization of vacancies or interstitials to take part in formation or accommodation of line defects such as edge dislocations, which will be discussed in the next section. By a similar mechanism, these line defects, as well as planar defects (grain boundaries and surfaces), may act as sources or sinks, and result in nucleation or disappearance of intrinsic point defects to lower the local elastic strain.

3.2. Dislocations

Dislocations are defined as linear discontinuities of the atoms in the crystal, separating two regions of the crystal. In 1907, Vita Volterra provided the initial theoretical framework which would lead to the development of the theory of dislocations and elasticity[234]. Although the term dislocation was not explicitly used, the new idea of discontinuity of displacement in an elastic body was introduced[235]. They were only theoretically predicted to exist in an attempt to explain plastic deformation in crystals, a process which occurs via slip of particular parallel planes on top of each other as a result of the applied force, as shown in Fig. 3.3 (a).

In the early experiments on plastic deformation, the deformation traces on the surfaces of deformed crystals were observed to lie along the close-packed directions, indicating the slip of close-packed planes[236,237]. The yield shear stress, which is the shear stress required to initiate the slip motion was theoretically determined by the force component acting on these slip planes, in the close-packed direction. This force component, called *critical resolved shear stress*[238],

$$\tau_{\mathrm{CRSS}} = \frac{F}{A}\cos\phi\cos\lambda \tag{3.1}$$

where F is the applied force, A is the cross-sectional area, ϕ is the angle between the F and slip plane normal, and λ is the angle between F and the slip direction, as demonstrated in Fig. 3.3 (b). τ_{CRSS} is a characteristic property of a material and it sets the critical value for initiation of slip in plastic deformation. Experiments revealed that the applied force to initiate the plastic deformation was much lower than the theoretically calculated values for various single crystals. This necessitated the consideration of an additional mechanism contributing to the slip motion: the presence of line defects. This was recognized in three separate papers by Orowan[239], Polanyi[240] and Taylor[241], which led to the proposal of the existence of (edge) dislocations. In the work of G. I. Taylor, the inability of a real crystal to resist theoretically predicted large values of shear stress was attributed to the presence of local concentrations of stresses due to internal surfaces of misfit (arrays of edge dislocations) or cracks in the material. The distribution of stress near a unit dislocation was calculated via the theory of elasticity. This prompted further development of the theory of dislocations, and was followed by Burgers' generalization of Taylor's work in completing the geometrical definition of dislocations[242]. These works brought new terminology to the field of dislocation theory with the definition of the dislocation line and provided a geometrical

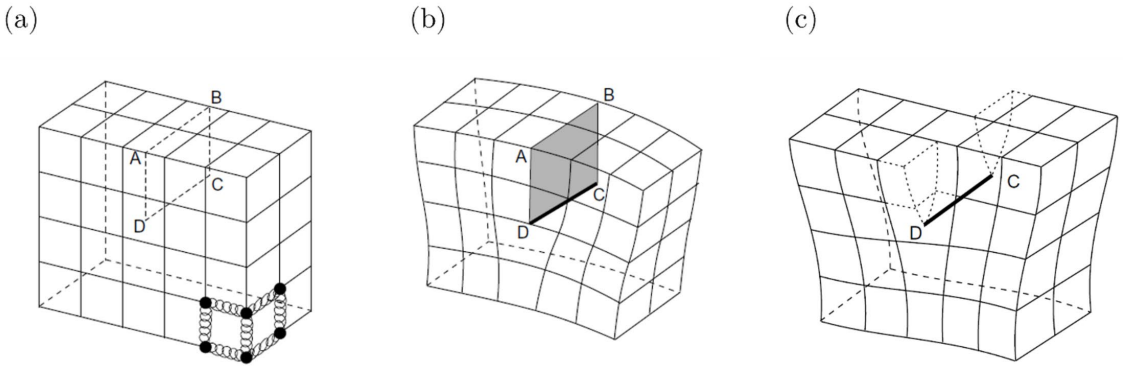

Figure 3.4: Edge and screw dislocation formation in an ideal crystal. (a) ideal crystal before deformation (b) An edge dislocation is created by addition of a half-plane in the cross-section of $ABCD$. (c) A screw dislocation is created by shifting the ideal crystal along AC. Dislocation line is along DC.[228]

classification of edge (Fig. 3.4 (b)) and screw (Fig. 3.4 (c)) type of dislocations, with the introduction of a cyclic constant which was later eponymously named the *Burgers vector*[243]. The two main types of dislocations, edge and screw dislocations are discussed next.

3.2.1. Edge dislocation and Burgers vector

Burgers vector is a practical method to characterize the geometry of any type of dislocation by describing the direction and extent of the distortion in the ideal crystal. Here the Burgers vector will be defined as it applies to an edge dislocation.

The structure of simple cubic lattice is illustrated in Fig. 3.4. In the case of cutting this perfect crystal along the $ABCD$ plane and inserting (or removing) an extra layer of atoms, a distortion is formed (Fig. 3.4 (b)). This distortion is returned back to the ideal perfect simple cubic structure by inserting the atoms on the $ABCD$ plane, hence there is no discontinuity in the area above the cut. The largest deviation of the atoms is centred around a line along DC, where the atoms in each side of this line are displaced from their original sites by half interatomic spacing. This line along DC is the dislocation line. The position of the extra half-plane $ABCD$ with respect to the dislocation line determines the "sense" of a dislocation.

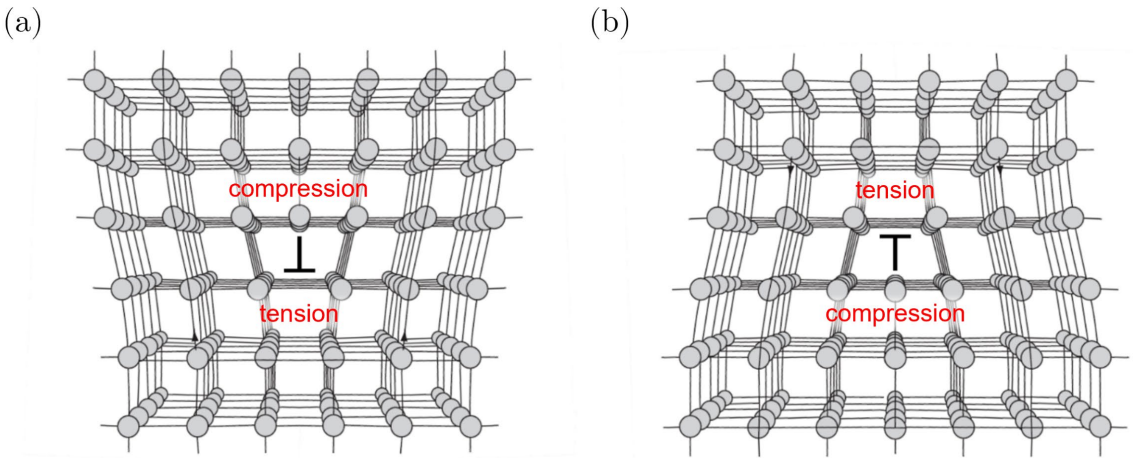

Figure 3.5: Close-up view of a (a) positive edge dislocation, extra half-plane inserted above the dislocation line, denoted by ⊥. The atoms just above the dislocation line are compressed and the atoms just below are extended due to the extra half-plane. (b) negative edge dislocation, extra half-plane is below the dislocation line, denoted by ⊤. The atoms just above the dislocation line are extended and the atoms just below are compressed due to the extra half-plane.

When the extra half-plane of atoms is inserted above (below) the slip plane on which the dislocation line lies, this edge dislocation is represented by the symbol ⊥ (⊤) and denoted as positive (negative) edge dislocation. The spacing of atoms immediately above the dislocation line is compressed whereas immediately below it's extended, as illustrated in the close-up view of an edge dislocation in Fig 3.5 (a). What completes the geometrical definition of a dislocation is the strength and direction of the discontinuity it creates in the perfect crystal. In the case of the edge dislocation described above, this is quantified by drawing a circuit around the edge of the inserted half-plane, as shown in Fig. 3.6. The difference between this circuit in Fig. 3.6 (a) and the one drawn on the perfect crystal Fig. 3.6 (b), gives the displacement component introduced by the dislocation. This displacement component along QM is a cyclic constant, known as Burgers vector $\boldsymbol{b}$, as illustrated in Fig. 3.6. (b). The Burgers vector describes the magnitude and direction of the distortion introduced in the perfect crystal by the dislocation. Evidently, the edge

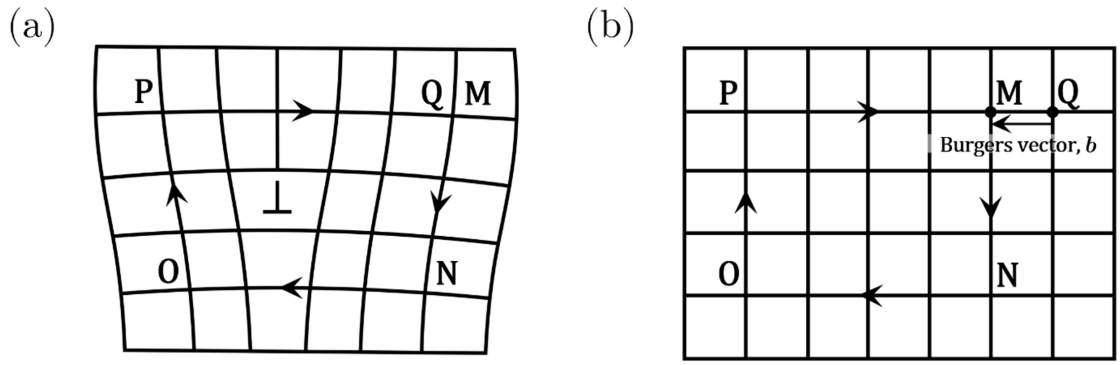

Figure 3.6: Construction of a Burgers circuit for an edge dislocation. (a) A circuit enclosing the edge dislocation is constructed on the distorted crystal and (b) on the ideal crystal. The additional segment QM is the Burgers vector. For an edge dislocation, Burgers vector is perpendicular to the dislocation line.[228]

dislocation is a type of dislocation with the Burgers vector perpendicular to the line of dislocation.

3.2.2. Screw dislocation

The other fundamental type of dislocation is screw dislocation, which was first described by J. M. Burgers in 1939[242]. Following the introduction of the Burgers vector, he considered a dislocation with the displacement component along the dislocation line. To illustrate this, the same simple cubic crystal in Fig. 3.4 (a) is considered. In this case, the perfect crystal is cut on the plane $ABCD$ and the sides divided by this plane are shifted relative to each other along the direction AB, as shown in Fig. 3.4 (c). It is clear that the resulting distortion is corrected almost back to the ideal configuration, in the region of the $ABCD$ plane along the planes perpendicular to it, further from DC. In fact, the displacement component is largest at DC, which is the dislocation line. Similarly, the magnitude and direction of the displacement component is obtained by drawing a circuit surrounding the dislocation line on the ideal crystal, as shown in Fig. 3.7 (a). The additional segment required to close this circuit when drawn on the distorted crystal gives the Burgers vector $\boldsymbol{b}$, parallel to QM (Fig. 3.7 (b)). Here, Burgers vector is along the dislocation

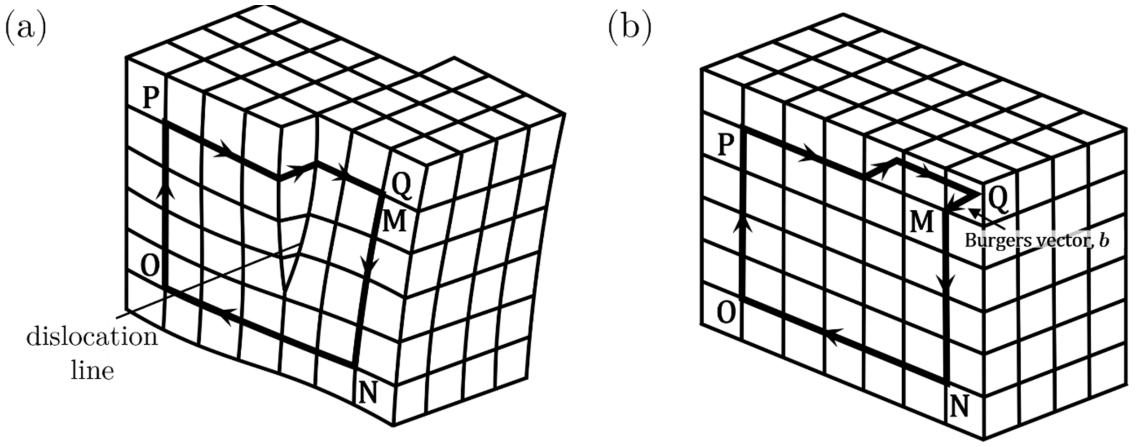

Figure 3.7: Construction of a Burgers circuit for a screw dislocation. (a) A circuit enclosing the screw dislocation is constructed on the distorted crystal and (b) on the ideal crystal. The additional segment along QM is the Burgers vector. For screw dislocation, Burgers vector is parallel to the dislocation line.[228]

line. Screw dislocation is a type of dislocation whose Burgers vector is parallel to the line of dislocation. The inspiration behind the term "screw dislocation" may be better understood by visualising the assembly of the nearest neighbour atoms surrounding the dislocation line as a helical path (Fig. 3.7(a)), similar to threads of a screw. Plastic deformation occurs by the gradual slip of planes over one another with the assistance of dislocations.

The slip of dislocations may be summarised in the context of the relationship between its direction and Burgers vector. Essentially, it is the Burgers vector that translates the atoms from one position to another, while preserving the lattice. In the case of a perfect dislocation, the Burgers vector is the shortest lattice translation vector parallel to a close-packing (slip) direction.

When the critical resolved shear stress is exceeded, dislocations glide in the slip direction, on the slip plane. For edge dislocations, slip plane is the one that contains both its Burgers vector and the dislocation line. Therefore, the movement is in the slip direction, which is parallel to the Burgers vector. Since the Burgers vector of a screw dislocation is parallel to its dislocation line, any plane containing the screw

dislocation is a possible slip plane. The dislocation line moves perpendicular to Burgers vector, hence the slip direction.

3.2.3. Stress field and strain energy of a single, straight dislocation

In addition to offering a fundamental understanding of how to build a geometrical frame for dislocations, the Burgers vector is also of great use in calculating and characterizing many other properties of dislocations, including the stress field and the strain energy associated with it. The elastic strain that is introduced by the deformation due to a dislocation and the associated elastic stress are quantified as a function of the Burgers vector and material elastic constants by the application of elasticity theory on a single, straight dislocation, *i.e.*, Volterra dislocation[244].

The distortion introduced by the dislocations imparts an energy in the crystal associated with the strain. The total strain energy is expressed as

$$E_{\text{total}} = E_{\text{elastic}} + E_{\text{core}} \tag{3.2}$$

where E_{core} corresponds to the energy due to dislocation core ($\leq r_0$) and E_{elastic}, the elastic component of the total strain energy corresponds to the region outside the dislocation core, r_0, extending to a cut-off radius, R where the strain due to dislocation is negligible. E_{elastic} is the elastic stress field per unit length and using the corresponding stress components for a screw dislocation it can be expressed as[245],

$$E_{\text{elastic}} = \frac{G\boldsymbol{b^2}}{4\pi} \ln\left(\frac{R}{r_0}\right) \tag{3.3}$$

and similarly for an edge dislocation,

$$E_{\text{elastic}} = \frac{G\boldsymbol{b^2}}{4\pi(1-\nu)} \ln\left(\frac{R}{r_0}\right) \tag{3.4}$$

where G is the shear modulus and ν is Poisson's ratio. Eq. (3.3) and Eq. (3.4) demonstrate the logarithmic dependence of elastic strain energy on R and core radius r_0. In a real crystal with a high dislocation density, the effective radius of elastic stress field for an individual dislocation is restricted by the other dislocations. The elastic stress field will vanish far from the dislocation due to the superimposition of long-range elastic fields in presence of multiple dislocations. The interaction of dislocations will determine the arrangement of multiple dislocations, so that the effective radius of each individual stress field will be the mean distance between dislocations.

To calculate total strain energy, the energy that corresponds to the dislocation core must be considered. E_{core} is estimated by the atomic level computational methods taking the high-level lattice distortion in the immediate vicinity of the dislocation core into account via the implementation of pair potentials, as mentioned in section 2.3. These pair potentials allow precise determination of E_{core} provided the detailed atomic structure is known. The above expressions for screw Eq. (3.3) and edge dislocations Eq. (3.4) demonstrate the internal energy of a dislocation. However, the calculation of free energy requires consideration of thermal and configurational entropy terms, which were shown to be negligible in comparison to the strain energy. Cottrell showed that the strain energy of a dislocation can be approximated to its free energy[246]. Thus Eq. (3.3) and Eq. (3.4) demonstrate the relationship of the dislocation free energy to its Burgers vector in a simple form

$$E_{\text{elastic}} = \alpha G\boldsymbol{b^2} \tag{3.5}$$

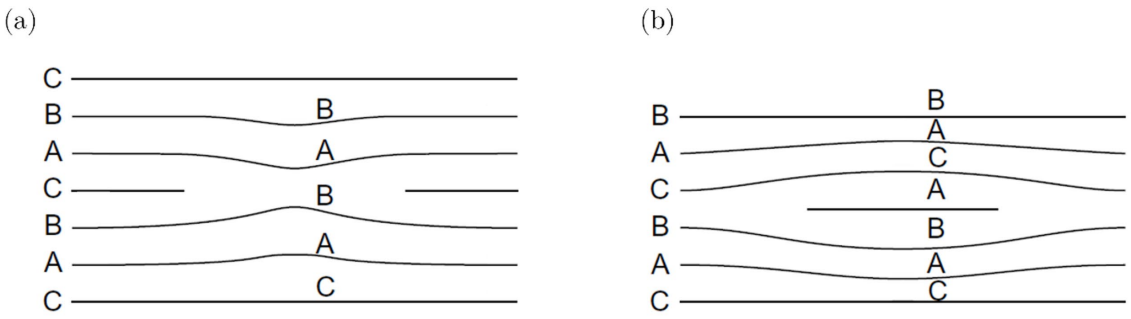

Figure 3.8: Illustration of interruption of the ideal $ABCABCABC$ stacking sequence in an fcc metal. (a) an intrinsic fault due to partial removal of C layer (b) an extrinsic fault due to introduction of a new A layer.

where α is a function of R, dislocation core radius and elastic coefficients, and the dependence of the shear modulus G in the crystal anisotropy is neglected. This relationship is crucial in demonstrating that the thermodynamic stability of a dislocation is dictated by its Burgers vector, as well as the likelihood of dislocation reactions to form a new dislocation or dissociation, as in the case of partial dislocations discussed in the next section.

Finally, it is noted that Eq. (3.5) is derived for an isotropic crystal within the linear elasticity assumption. In an anisotropic medium, the elastic components and dislocation core structure have some degree of orientation dependence, yet the relation in Eq. (3.5) is preserved. Burgers vector is also crucial in determining parameters of an array of edge dislocations, *i.e.*, grain boundaries. These include the energy, the stress field, and the degree of misorientation, as will be discussed in the following sections.

3.2.4. Stacking fault

The crystal is built by the subsequent stacking of atomic planes on top of each other. For a face-centred cubic crystal, the crystal is built by successive stacking of close-packed (111) planes on top of each other, resulting in an $ABCABCABC$ stacking, as discussed earlier.

The assumption of atoms as hard spherical balls allows that geometrically there are two possible ways to place a new close-packed layer of atoms on top of the layer A. The new layer could either be at position B or at position C. Thus, any planar fault that results in an irregularity in the stacking period of the close-packed planes is known as stacking fault. As shown in Fig. 3.8, in fcc metals the stacking fault may be due to the removal or addition of a layer, defined as intrinsic and extrinsic stacking fault, respectively[247]. It is understood that stacking faults may occur during the crystal growth. They also occur due to the presence or interaction of other defects. They separate two regions of crystal which belong to a single reference crystal, by a rigid translation whose vector is shorter than a lattice vector. Inside the fault region, the close-packed arrangement of atoms is still continued; hence the nearest-neighbour bonds are not disrupted. This suggests that compared to other types of defects where the nearest-neighbour bonds are disturbed (such as free surface), a lower interfacial energy is associated with stacking faults of both types, when it's limited with a single plane.

At the edges of the faulted region, the transition from the stacking fault to the ideal stacking is organized (bounded) by dislocations of an imperfect type, known as partial dislocations. Yet still the plane of stacking fault introduces a deviation in the energy state of the ideal crystal. The disruption caused by the introduction of a stacking fault comes at the cost of energy. This energy per unit area of the fault is referred to as stacking fault energy, γ_{SFE}, which will be derived with the introduction of partial dislocations. Stacking fault energy plays an important role in the plasticity and yield strength of the materials that rely on mechanisms such as glide and cross-slip due to dislocation motion. It is the stacking fault energy γ_{SFE} that determines the energetic feasibility and characteristics of dislocation reactions, including dislocation splitting (dissociation), specific to each material.

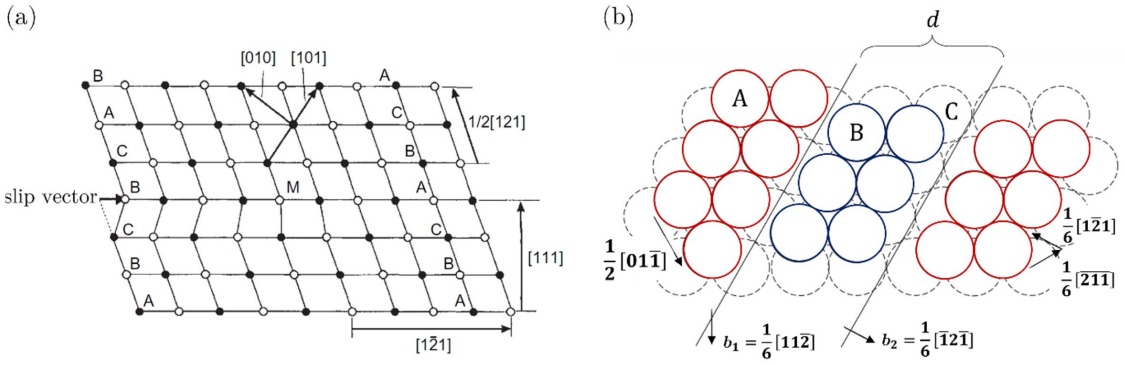

Figure 3.9: Stacking fault due to partial slip of close-packed planes above C layer. (a) Interruption of the ideal stacking above C layer, as viewed along $[10\bar{1}]$ direction. The slip vector is along slip direction, of type $[1\bar{2}1]$. (b) Stacking fault ribbon of width d, due to partial dislocations.

3.2.5. Partial dislocations in fcc metals

First described by Heidenreich and Shockley, the relationship between dislocation structure and crystal structure are highly correlated[248]. A perfect dislocation as defined above is a dislocation whose Burgers vector is equal to the shortest possible lattice translation vector. However, the structure of dislocations in fcc metals was shown to be different than that of a perfect dislocation, as the Burgers vector is no longer the shortest lattice vector. Originally called imperfect dislocations or half dislocations, the fcc lattice accommodates dislocations as partials with dissociated Burgers vectors whose vector sum is equal to that of a perfect dislocation. This is due to the crystal having more than one mechanically stable configuration to accommodate a disruption associated with slip, in addition to the energetic feasibility of a dissociation of the dislocation. Thus, the perfect dislocation dissociates into two partial dislocations, which are separated by a stacking fault, a misfit with a low interfacial or stacking fault energy, whose width is determined by the magnitude of this stacking fault energy (Fig. 3.9).

Eq. (3.5) shows the relationship of the dislocation energy to its Burgers vector. According to Frank's rule[247], the energy criterion for a dislocation reaction $\boldsymbol{b}_3 = \boldsymbol{b}_1 + \boldsymbol{b}_2$, is determined by the following conditions

$$\begin{aligned} \boldsymbol{b}_3^2 &< \boldsymbol{b}_1^2 + \boldsymbol{b}_2^2 \qquad \text{(stable)} \\ \boldsymbol{b}_3^2 &> \boldsymbol{b}_1^2 + \boldsymbol{b}_2^2 \qquad \text{(unstable)} \end{aligned} \tag{3.6}$$

According to the set of Eq. (3.6), a dislocation is energetically stable when $\boldsymbol{b}_3^2 < \boldsymbol{b}_1^2 + \boldsymbol{b}_2^2$ whereas a dissociation reaction is more favourable when $\boldsymbol{b}_3^2 > \boldsymbol{b}_1^2 + \boldsymbol{b}_2^2$, where dislocation $\boldsymbol{b}_3$ is dissociated into two partial dislocations, $\boldsymbol{b}_1$ and $\boldsymbol{b}_2$.

An important type of partial dislocations is *Shockley partials*, which form due to the slip of one close-packed plane $\{111\}$ over another, creating a stacking fault as illustrated in Fig 3.9 (b). First, it is assumed that during the ideal $ABCABC\,...$ stacking of the $\{111\}$ planes, slip is initiated in the next layer. This layer would ideally slip into a position equivalent to position A, to maintain the ideal $ABCABC\,...$ stacking. Here, the Burgers vector lies on the stacking fault plane, parallel to slip direction. However, following Frank's energy criterion in Eq. (3.6), it is energetically more favourable that this slip should follow a two-step path, from position A to position B and then from B to A. This two-step transition creates a stacking fault, and two partial dislocations with dissociated Burgers vectors. Instead of following a two-step path, if the transition occurred at once in a single path ($A \rightarrow A$), *i.e.*, producing a perfect dislocation, this would correspond to the shortest lattice vector of type $\boldsymbol{b}_{\text{perfect}} = a/2\langle 110 \rangle$. However, each of the two steps in favoured transition ($A \rightarrow B \rightarrow A$) correspond to a Shockley partial with Burgers vector of type $\boldsymbol{b}_{\text{partial}} = a/6\langle 112 \rangle$, confirming the Frank's energy criterion since[249]

$$\boldsymbol{b}_{\text{perfect}}^2 \rightarrow \boldsymbol{b}_{\text{partial}}^2 + \boldsymbol{b}_{\text{partial}}^2 \tag{3.7}$$

$$\frac{a^2}{2} > \frac{a^2}{3}$$

To describe the geometry of partial dislocation in the context of an fcc lattice crystallography, Thompson's tetrahedron must be introduced[250]. This is a helpful illustration which provides a notation to visualise and identify the perfect dislocations and partial dislocations in an fcc lattice, as shown in Fig. 3.10. It is a regular tetrahedron constructed by joining the four different {111} slip planes in the fcc lattice: each face of the tetrahedron represents one of the four {111} planes and each edge of each face represents a ⟨110⟩ slip direction. These edges join at the corners of the tetrahedron, which are denoted as A, B, C and D. Conveniently, the midpoints of each face opposing each corner are named as α, β, γ and δ. The Burgers vectors of both perfect and partial dislocations in an fcc lattice are easily defined on the tetrahedron, by its initial and final point. For instance, one possible perfect dislocation and its Shockley partials on the $ABC = \delta$ face that corresponds to (111) surface are denoted as,

$$AB = \frac{a}{2}[\bar{1}10], \quad A\delta = \frac{a}{6}[\bar{1}2\bar{1}], \quad \delta B = \frac{a}{6}[\bar{2}11] \tag{3.8}$$

The region that separates the partial dislocations is called a *stacking fault ribbon*. In a stacking fault ribbon bounded by partial dislocations of same sense (like-signed) on either side, the dislocations are repelled by each other to minimize the dislocation energy (Eq. (3.3) and Eq. (3.4)) and the stacking fault ribbon becomes wider. The balance of elastic repulsive forces between partials and the attractive surface tension of the stacking fault, which is determined by γ_{SFE}, gives an equilibrium width of separation, where the free energy is minimized. Evidently, in an fcc metal with low γ_{SFE}, the elastic repulsive forces will dominate and result in

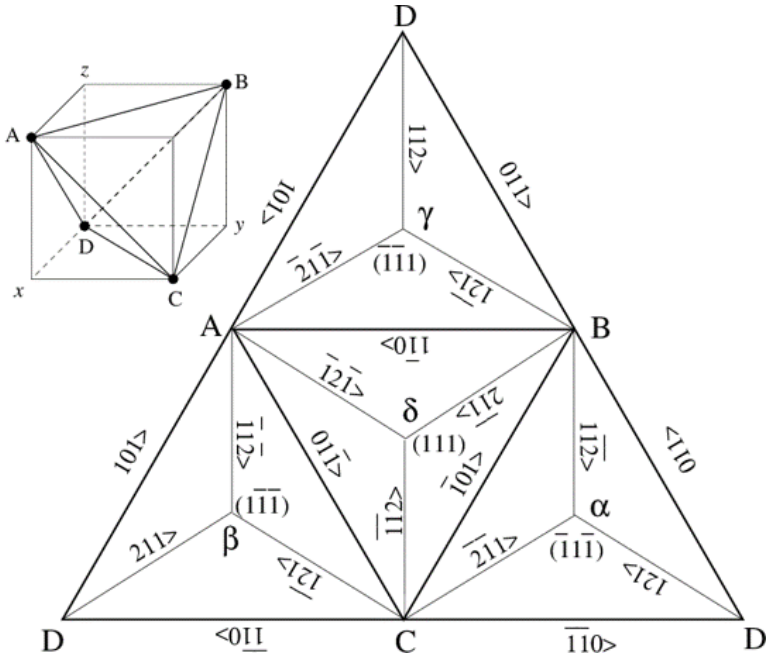

Figure 3.10: Thompson tetrahedron composed of four close-packed {111} planes of fcc lattice structure, denoted as α, β, γ and δ. The possible directions and magnitudes for perfect and partial dislocations on each plane are provided.

a wider stacking fault ribbon. The stacking fault ribbon equilibrium width d is approximated by the expression[248,251,252]

$$d = \frac{G\boldsymbol{b}^2}{4\pi\gamma_{\mathrm{SFE}}} \tag{3.9}$$

where the magnitude of γ_{SFE} is equated to the force per unit length derived by the Eq. (3.3) or Eq. (3.4), and the small coefficient capturing the Poisson's ratio is left out.

The theory of dislocations is an extensive field of research, covering dislocation types, their energy and elastic stress fields, as well as other phenomena involving dislocation nucleation and mobility. These mechanisms are mainly governed by plastic deformation, which may lead to changes in the distribution density and arrangement of dislocations.

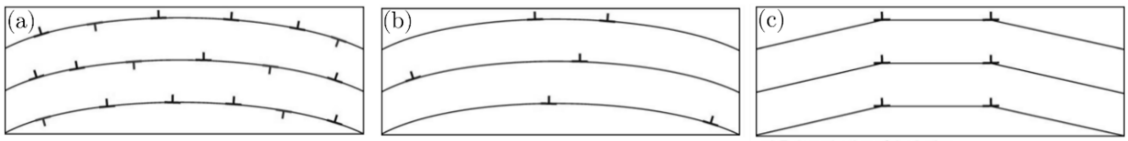

Figure 3.11: Dislocation dynamics (a) after the plastic deformation. The crystal is bent and randomly distributed opposite-signed dislocations glide on slip planes (b) recovery via relaxation of excess energy by annihilation of stress generator dislocations upon thermal activation (c) dislocations forms arrays of low-energy configurations, known as polygonization[253].

For low temperature plastic deformation of crystals, a portion of the transferred energy is stored within the crystal in terms of elastic strain energy due to an increase in dislocation density. This mechanism results in strain hardening of crystals, caused by restricted mobility due to high dislocation and defect densities. The release of this excess energy may be activated by thermal annealing, encouraging dislocation movement. Upon annealing, the physical and mechanical crystal state is recovered by reduction of defects, accompanied by the softening of the crystal. Fig. 3.11 (b) shows a later stage of the cancellation (annihilation) of dislocations, a mechanism that will be introduced shortly in terms of the two opposite-signed dislocation model. The dislocations then align themselves into arrays, to lower the elastic energy through polygonization[253], forming grain boundaries (Fig. 3.11 (c)). At higher temperatures, nucleation and growth of the grains result in recrystallization, which minimizes the strain energy further due to the reduced density of grain boundaries comprising arrays of dislocations.

The rearrangement of dislocations into 3D arrays to form grain boundaries plays a crucial role in the microstructural evolution of polycrystalline materials, and allows for the application of well-established dislocation theory in description of grain boundaries. As shown in detail in the next section, modelling of interfaces as arrays of dislocations is of significant use in providing a quantitative description of the geometrical and energetic properties of grain boundaries.

3.3. Grain Boundaries

So far, the discussion has covered the presence, geometrical and elastic properties of point defects, and dislocations in a crystal. Macroscopically, these single crystals are observed as individual *grains* that merge to form polycrystalline materials. Polycrystalline materials form by the aggregation of multiple randomly oriented identical single crystals. The macroscopic continuity throughout the polycrystalline material is maintained by the grains that are bonded together. The interfaces where two grains join are called *grain boundaries*. Grain boundaries are planar defects that maintain the continuity of the two misoriented but adjoining single crystals.

3.3.1. Grain boundary geometry

A grain boundary is constructed by bringing two identical single crystals with a different orientation together. The characterization of this grain boundary is defined by specific parameters. These parameters, outlined by Sutton and Baluffi[161], once determined, can be modified and applied to a wide-range of grain boundaries.

There are a total of five macroscopic degrees of freedom that characterize a grain boundary. Three of the five macroscopic degrees of freedom are necessary to define the rotation associated with the misorientation of the two grains. There are two more degrees of freedom required to characterize the boundary plane (unit normal, $\hat{\boldsymbol{n}}$), relative to one of the two grains. The grain boundary is created by defining the coordinate systems of the two crystals using the coordinate system of the median lattice, as illustrated in Fig 3.12. The five degrees of freedom are expressed in the coordinate system of this common median lattice. The five degrees of freedom are derived by considering a proper rotation. In the median lattice, two planes with the surface normal unit vectors $\hat{\boldsymbol{n}}$ and $\hat{\boldsymbol{n}}'$ are assumed. The rotation axis is designated as $\hat{\boldsymbol{\rho}}$**.** The two surface normals $\hat{\boldsymbol{n}}$ and $\hat{\boldsymbol{n}}'$ are then rotated about the rotation axis

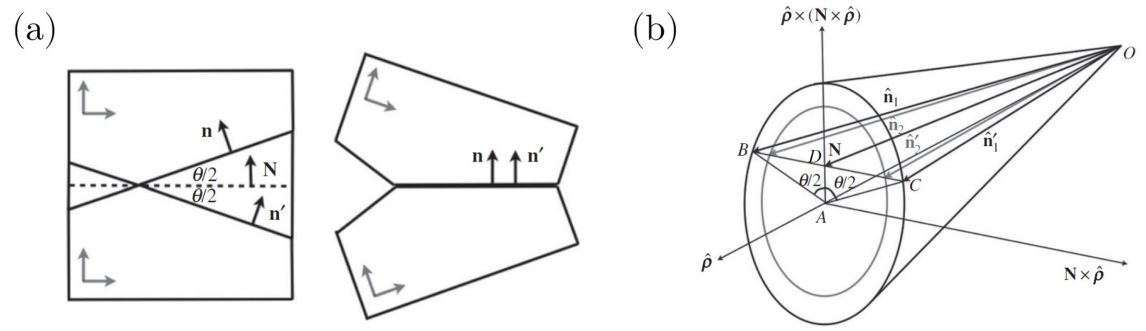

Figure 3.12: Schematic of grain boundary construction using the median lattice method. (a) three-step representation of the construction process. (a) Left: a single crystal with the desired boundary plane (dashed line) and boundary normal $\boldsymbol{N}$. Right: Crystals with plane normals $\boldsymbol{n}$ and $\boldsymbol{n}'$, on either side of the dashed line are rotated by $\pm\theta/2$. (b) Geometrical representation of the derivation of Eq. (3.10)[254].

$\hat{\boldsymbol{\rho}}$, by $+\theta/2$ and $-\theta/2$ respectively, as shown in Fig. 3.12 (a). This creates a grain boundary with a misorientation angle θ, on the median lattice. This means that as $\theta \to 0$, the $\boldsymbol{n}$ and $\boldsymbol{n}'$ vectors which are no longer unit vectors, can be used to define $\boldsymbol{N} = (\boldsymbol{n} + \boldsymbol{n}')/\boldsymbol{2}$, as the mean boundary plane normal. Following the rotation, $\boldsymbol{n}$ and $\boldsymbol{n}'$ are now parallel to the grain boundary normal on the median lattice. The illustration of this process is given in Fig 3.12 (a). The vectors are then expressed as[161]

$$\begin{aligned} \boldsymbol{n} &= \boldsymbol{N} - m(\boldsymbol{N} \times \hat{\boldsymbol{\rho}})/|\boldsymbol{N} \times \hat{\boldsymbol{\rho}}| \\ \boldsymbol{n}' &= \boldsymbol{N} + m(\boldsymbol{N} \times \hat{\boldsymbol{\rho}})/|\boldsymbol{N} \times \hat{\boldsymbol{\rho}}| \end{aligned} \tag{3.10}$$

where $m = |BD| = |DC| = |\boldsymbol{N} \times \hat{\boldsymbol{\rho}}| \tan\theta/2$, which is shown graphically in Fig 3.12 (b). Eq. (3.10) can then be rearranged as

$$\begin{aligned} \boldsymbol{n} &= \boldsymbol{N} - \boldsymbol{N} \times \boldsymbol{\rho}^R \\ \boldsymbol{n}' &= \boldsymbol{N} + \boldsymbol{N} \times \boldsymbol{\rho}^R \end{aligned} \tag{3.11}$$

following the definition of the Rodrigues vector as

$$\boldsymbol{\rho}^R = \hat{\boldsymbol{\rho}} \tan\theta/2 \tag{3.12}$$

Rodrigues vector $\boldsymbol{\rho}^R$ is a rational vector that generates any grain boundary with a given rotation axis $\boldsymbol{\rho}$, using any rational mean boundary plane allowed in the crystal lattice system, by Eq. (3.12). The Rodrigues vector has the information regarding the rotation of the two crystals relative to each other: two for the unit vectors for rotation axis $\hat{\boldsymbol{\rho}}$, and rotation angle θ. The remaining two degrees of freedom are associated with the mean boundary plane normal, relative to the two crystals.

The misorientation of two crystals can be expressed in terms of its degree of tilt and twist. In the case of tilt rotation, the Rodrigues vector is given as

$$\boldsymbol{\rho}^R_{\text{tilt}} = \left|\widehat{\boldsymbol{N}} \times \boldsymbol{\rho}^R\right|(\hat{\boldsymbol{n}} \times \hat{\boldsymbol{n}}')/|\hat{\boldsymbol{n}} \times \hat{\boldsymbol{n}}'| \tag{3.13}$$

where $\tan^2(\theta_{\text{tilt}}/2) = (\widehat{\boldsymbol{N}} \times \boldsymbol{\rho}^R)^2$ is used, from the Fig 3.12 (b). Further simplifications are provided to the above expressions, with the implementation of trigonometric properties and the geometrical conditions, in "Interfaces in Crystalline Materials"[161].

3.3.2. Symmetric tilt grain boundary

A rotation that only involves a tilt component is provided by the condition that $\hat{\boldsymbol{\rho}}$ lies in the boundary plane, $\theta = \theta_{\text{tilt}}$, as $\theta_{\text{twist}} = 0$ and $\boldsymbol{\rho} = \boldsymbol{n} \times \boldsymbol{n}'$. This type of boundary is called pure tilt grain boundary. In symmetric pure tilt grain boundaries, the boundary plane normals in either crystal are defined symmetrically, of the form $[hkl]$, *i.e.*, $1/2[7\bar{8}1]$ for one crystal and $1/2[\bar{8}7\bar{1}]$ for the other. Then, the mean boundary plane normal is given by the vector sum of the boundary plane normals of the two crystals. In asymmetric tilt grain boundaries, boundary plane normals are no longer symmetrical. The construction of symmetric tilt grain boundary using median lattice method is demonstrated in chapter 5, for $[111]$ tilt boundary with $[1\bar{1}0]$ mean boundary plane and $\theta_{\text{tilt}} = 13.17°$.

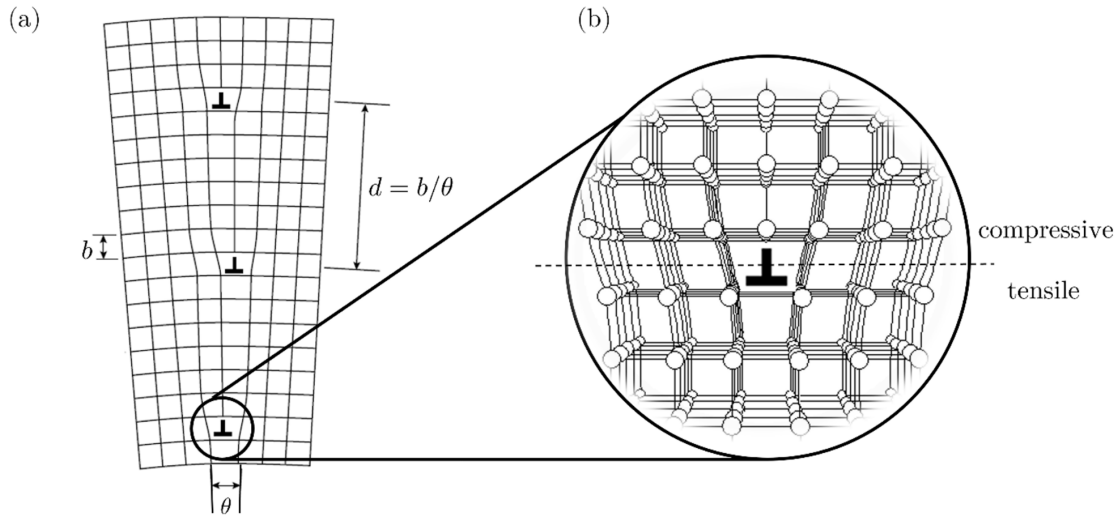

Figure 3.13: (a) Dislocation array model as applied to symmetric tilt grain boundary with misorientation angle θ. (b) The close-up schematic of a single edge dislocation in the interfacial array of dislocations. Compressive and tensile stress fields localized at the dislocation line are denoted.

As mentioned earlier, a mechanism to build these interfaces in an otherwise continuous crystal is explained by the dislocation model. First introduced by G. I. Taylor, the concept of edge dislocation array which accommodates an interface of misfits between two crystals is driven by the tendency of the system to maintain a low energy configuration, by minimising the elastic energy cost. This interface describes a symmetrical tilt grain boundary, formed of a locally arranged wall of edge dislocations. These dislocation arrays are considered to be free of a long-range stress field at a distance far from the dislocations. As per the geometrical definition of a single edge dislocation, just above the slip plane, the effective elastic stress is compressive whereas just below the slip plane it is tensile, as shown in Fig. 3.13 (b).

One proposed model of formation and arrangement of dislocation arrays can be summarized as part of the plastic deformation of crystals. Upon elastically bending a stress-free crystal symmetrically on both sides, like the one shown in Fig. 3.11, the resulting long-range distortion is equivalently described by that of a continuous

dislocation density, referred to as stress-generators. The long-range elastic stress field is balanced out by the introduction of randomly-distributed opposite-signed dislocations, referred to as stress annihilators. The dislocations then arrange into an array lying on the same plane, namely the grain boundary plane, to reduce the excess elastic energy. The resulting short-range stress field is determined by the Burgers vector density of the stress annihilators.

Alternatively, as proposed by Read and Shockley[255], the bicrystal comprising a symmetric tilt grain boundary, formed by merging two already misoriented and rotated crystals with a small misorientation of θ about the rotation axis $\hat{\boldsymbol{\rho}}$, is energetically equivalent to that described by two opposite-signed dislocation arrays, as long as the short-range stress field is ensured. This low-angle symmetric tilt grain boundary is shown in Fig. 3.13.

For this particular type of interface, it is possible to characterize the boundary by its dislocation content using the geometrical definition of the dislocations, employing the Frank-Bilby equation[256]. These geometrically necessary dislocations make up for the incompatibilities that arise from the rotational transformation, ensuring there is no long-range stress fields[257].

The Frank-Bilby equation provides a net Burgers vector $\boldsymbol{b}$, for a period vector $\boldsymbol{p}$ along the dislocation array on the interface. The two crystals are derived from a reference lattice so that they have a misorientation of θ about the rotation axis $\hat{\boldsymbol{\rho}}$. First, the individual deformations in each lattice are expressed with respect to the reference lattice. Then, a common Burgers circuit is constructed across the interface. By inverse transformation on this circuit, the net distortion is expressed in terms of the distortions of each crystal, with respect to the reference lattice. This results in a net Burgers vector that defines the dislocation content of the grain boundary, in terms of the boundary geometry, given $\boldsymbol{p}$. When the reference lattice

is replaced by the median lattice introduced in the previous section, Frank's formula is obtained as

$$\boldsymbol{b} = 2\,\sin(\theta/2)(\boldsymbol{p} \times \hat{\boldsymbol{\rho}}) \tag{3.14}$$

Frank's equation, Eq. (3.14) highlights a significant rule in the theory of interfaces. In addition to providing a complete picture of grain boundary geometry in terms of an array of dislocations, it also relates the degree of misorientation to the dislocation content. For a given $\boldsymbol{p}$ perpendicular to the rotation axis $\hat{\boldsymbol{\rho}}$, Eq. (3.14) demonstrates that the Burgers vector has to be perpendicular to both $\boldsymbol{p}$ and $\hat{\boldsymbol{\rho}}$. Since $\boldsymbol{p}$ is along the boundary plane, the Burgers vector is normal to the boundary plane and therefore $\hat{\boldsymbol{\rho}}$ lies in the boundary plane. In this case, the boundary is of symmetric tilt type, with dislocation lines positioned parallel to $\hat{\boldsymbol{\rho}}$ along the boundary plane, hence perpendicular to the Burgers vector and $\boldsymbol{p}$. Therefore, the distance between dislocations can be expressed using Eq. (3.14) as

$$d = |\boldsymbol{b}|/2\,\sin(\theta/2) \tag{3.15}$$

where $\boldsymbol{p} \times \hat{\boldsymbol{\rho}} = |\boldsymbol{p}| \approx d$. Remarkably, Eq. (3.15) shows that as the degree of misorientation increases, the dislocation spacing d decreases. Using the Frank's formula in Eq. (3.14), for a symmetric pure tilt grain boundary, it is possible to estimate the misorientation angle θ, from the dislocation spacing in a dislocation array. This method is implemented in characterizing the grain boundaries that are presented in the results obtained in this thesis, as will be demonstrated in the next chapters.

It is also important to note that the character of these dislocations is highly dependent on the lattice structure, as mentioned in the theory of dislocations. In symmetric tilt grain boundaries in fcc metals, the interfacial dislocations arranged

along the grain boundary are in the form of previously described partial dislocations. The resulting stacking fault introduces a width across the boundary, associated with the stacking fault ribbon. The stacking fault ribbon width is determined by the stacking fault energy γ_{SFE} and the Burgers vector $\boldsymbol{b}$, as described in Eq. (3.9). In the case of interfacial partial dislocations, since the Burgers vector is related to θ by Eq. (3.15), the stacking fault width is determined by the degree of misorientation and the stacking fault energy γ_{SFE}. Notably, for particularly small dislocation spacings in the range of a few atomic distances, the dislocation interactions become non-negligible. The application of Eq. (3.15) is regarded to be less straightforward for grain boundaries with higher degrees of misorientation, known as high-angle grain boundaries. The distinction concerning the degree of misorientation is introduced in the next section, in the context of elastic energy.

3.3.3. Elastic stress field and energy

The modelling of grain boundaries as arrays of dislocations enables the quantification of the elastic strain and stress fields and their associated elastic energy. This is achieved through the application of isotropic linear elasticity approximation within the dislocation theory, which already covers the calculation of elastic stress fields and strain energies for a single screw (Eq. (3.3)) or edge dislocation (Eq. (3.4)).

For a symmetric tilt grain boundary composed of an array of edge dislocations of spacing d, the elastic energy stored in the elastic stress field per unit length of a single edge dislocation on the array is given by rearranging Eq. (3.4) as

$$E_{\mathrm{elastic}} = \frac{G\boldsymbol{b}^2}{4\pi(1-\nu)} \ln\left(\frac{d}{r_0}\right) \tag{3.16}$$

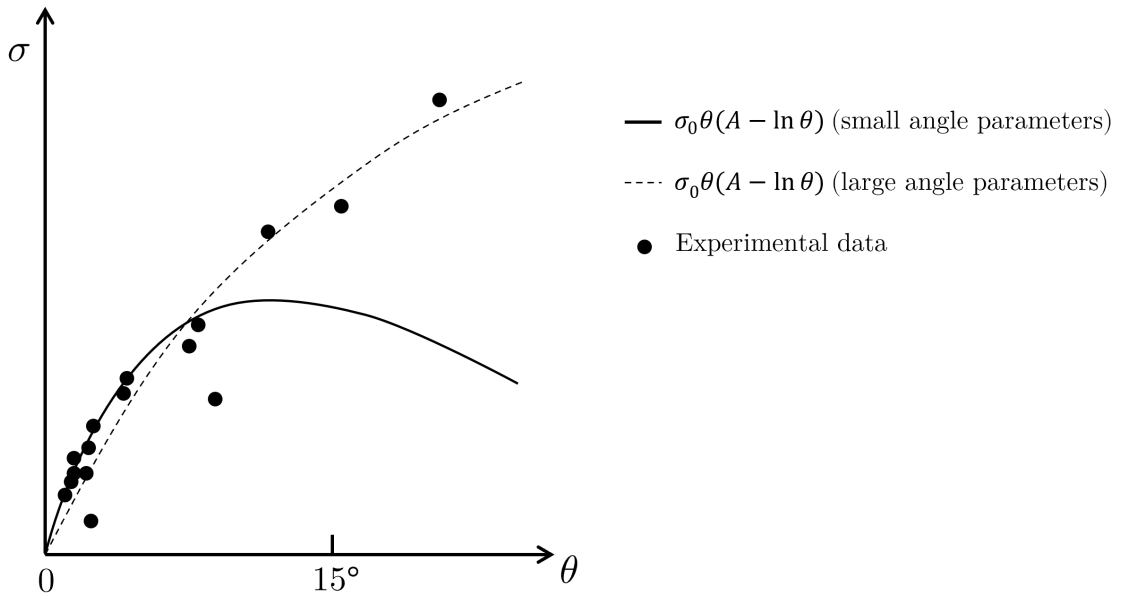

Figure 3.14: Read-Shockley formulation of grain boundary energy[255]. The solid curve: grain boundary energy as a function of misorientation angle, using the parameters for low-angle ($\leq 15°$) grain boundaries (as assumed by Read-Shockley). The dashed curve: Read-Shockley formula, plotted with modified parameters for high-angle grain boundaries ($> 15°$). Experimental data obtained for Cu [001] tilt boundaries[258].

Eq. (3.16) is the elastic component of the total strain energy associated with a single dislocation, whereas the total energy expressed by Eq. (3.2) also accounts for the dislocation core energy. Using Frank's formula in Eq. (3.15), for a low angle grain boundary $\theta \cong b/d$. Rearranging Eq. (3.16) using small angle approximation and inserting in Eq. (3.2), the total strain energy per unit length is then expressed as

$$E_{\mathrm{d}} = \frac{G\boldsymbol{b}^2}{4\pi(1-\nu)} \ln(1/\theta\alpha) + E_{\mathrm{core}} \tag{3.17}$$

where the dislocation core radius is expressed in terms of the Burgers vector and constant α, such that $r_0 = \alpha\boldsymbol{b}$. The elastic constants G and ν, the Burgers vector $\boldsymbol{b}$, and the dislocation core energy E_{core} can be assigned to be constants independent of θ, to rearrange Eq. (3.17) for a boundary with $1/d$ dislocation lines per unit length as [251]

$$\sigma(\theta) = \sigma_0 \theta(A - \ln(\theta)) \tag{3.18}$$

where $A = [4\pi(1-\nu)E_{\text{core}}/Gb^2] - \ln\alpha$ and $\sigma_0 = Gb^2/4\pi(1-\nu)$, Eq. (3.18) gives the energy per unit area of a low-angle grain boundary. This formula, which was originally derived by Read and Shockley[255], demonstrates a significant relation between the misorientation angle and the grain boundary energy, mainly valid for the grain boundaries with $\theta \leq 15°$ (small angle approximation). The sketch of the energy as a function of the misorientation angle is given in Fig. 3.14. The energy $\sigma(\theta)$ increases as the misorientation angle θ increases, with a sharp decrease near $\theta = 0$. Indeed, the energy is drastically minimized in the absence of any misorientation. The behaviour of the energy per dislocation, however, is actually hidden in the term $\ln(\theta)$. As the misorientation angle θ increases, the dislocation spacing d decreases. With reduced spacing, the stress fields of dislocations start overlapping, hence the elastic energy per dislocation decreases as θ increases. Similarly, as $\theta \to 0$, the energy per dislocation is infinite. The breakdown of the validity of Eq. (3.18) is mainly attributed to this overlap, for $\theta > 15°$. The revision of Eq. (3.18) for high-angle grain boundaries showed that, upon modification of σ_0 and A, the Read-Shockley formula is applicable to the boundaries with $\theta > 15°$ as confirmed both by computer simulations and experiments.

Another fundamental result of the Read-Shockley formulation is the presence of sharp decreases in the energy at some specific angles, as it scales with θ. This is observed on the energy-misorientation angle curve as cusps, at certain specific angles. The reason behind the slight decrease, *i.e.*, cusps in energy, at these specific angles is attributed to the uniformity of dislocation spacing, which was the assumption behind the derivation of Eq. (3.18). This condition introduces a restriction on θ, determined by the geometry of the crystal. In between these specific angles, the irregularities in the dislocation spacing cause an increase in the energy.

At low-angle grain boundaries, this is responsible for the energy variation with orientation. As per the Read-Shockley formula, a distinction of low-angle and high-angle grain boundaries has also been formally made, about a misorientation angle θ~15°. The grain boundaries with $\theta \leq 15°$ are referred to as low-angle grain boundaries, whereas the boundaries with higher degree of misorientation are considered high-angle grain boundaries.

3.3.4. Microscopic degrees of freedom and grain boundary relaxation

As the degree of misorientation increases, the dislocation spacing decreases and the effect of overlapping dislocation cores becomes non-negligible. For low-angle grain boundaries with arrays of partial dislocations, the interface becomes more complex than predicted by the linear elasticity formulation.

The calculation of dislocation core energy and atomic-level interaction effects mainly rely on computational methods such as molecular statistics, molecular dynamics, or Monte Carlo simulations, that use various models of realistic pseudo-potentials, *i.e.*, embedded-atom, or Finnis-Sinclair potentials with proper rigid/periodic boundary conditions, to evaluate the structural models of grain boundaries. The microscopic degrees of freedom are defined by the relaxation at the boundary, which account for the atomic-level dislocation core effects to achieve a low-energy configuration structure of the boundary[161]. These are mainly concerned with rigid body translations parallel to the boundary plane ($\perp \widehat{\boldsymbol{N}}$), expansion normal to the boundary plane ($\| \widehat{\boldsymbol{N}}$), or atom by atom optimization of the local structure.

3.3.5. Coincidence site lattice

The most widely used notation of grain boundaries is the coincidence site lattice (CSL) model developed from bicrystallography. When two misoriented crystal lattices are allowed to overlap, at certain degrees of misorientation (*special* angles), some sites of the two lattices coincide[259]. The resulting overlap forms a superlattice, known as coincidence site lattice. The reciprocal density of coincident sites, that is the ratio of the number of coincidence sites to the number of lattice sites in the elementary cell, is denoted by Σ. For example, Σ=1 boundary would correspond to an ideal tilt boundary, *i.e.*, $\theta = 0°$, whereas in reality the lowest-Σ boundary corresponds to Σ=3 boundary, namely the $\theta = 60°$ twin boundary[260].

The common preference for using the CSL notation throughout grain boundary-related literature was motivated by the realization of significant correlations between grain boundary properties and CSL boundaries. For instance, although exceptional cases arise in the trend to the relative orientation of the boundary plane, some special low-Σ grain boundaries would tend to correspond to local energy minima. Naturally, a simple classification was made as CSL and non-CSL (random) boundaries[261]. Even though there is a good amount of research to the contrary that shows variations of properties within the same CSL type, it is still the most commonly used notation to categorise the structure and periodicity of grain boundaries. In this thesis, the grain boundaries are described by the specification of rotation axis $[hkl]$, boundary plane (hkl) and misorientation angle θ, e.g., in chapter 5, the Σ=57 grain boundary is described as [111] symmetrical tilt boundary with mean boundary plane $(1\bar{1}0)$ and $\theta = 13.17°$.

4. Emergent Grain Boundaries on the Surface of Cu Nanocrystalline Films

Nanocrystalline thin films comprise a rich microstructure consisting of small, single-crystalline grains and boundaries between them[1]. As mentioned in chapter 1, the surface morphology and microstructure of nanocrystalline copper thin films are of great interest. Their performance in a wide range of applications in the microelectronics industry[6,55,66,100], or as catalysts[16,18,84,262], however, is fundamentally determined by their microstructure, and the density and characteristics of the grain boundaries within them[3,263–265].

Refinement of the microstructure and surface texture of thin films to explore and understand the grain boundaries may be achieved by the careful design of post-deposition thermal processing. As explained in section 1.2.2, upon thermal annealing, recrystallization and grain growth lead to the evolution of surface microstructure, as well as changes in stress state[119,140,266] of the thin film, and in other grain boundary phenomena-related material properties such as electrical conductivity or hardness[82,83,267,268].

For many applications that rely on the high surface-to-volume ratio of NC materials and thin films, the post-deposition quality of the surface, often measured by the surface roughness, is of significant importance[269]. This necessitates the consideration of the proven impact grain boundaries have on the surface morphology and roughness, *i.e.*, the surface quality of thin films, as they emerge on the surface from within the bulk[76,137,270–272].

This chapter will explore the emergent grain boundaries on the surface of NC Cu (111) films, to understand their structuring and impact on the surface using STM.

A reproducible post-deposition thermal processing method in UHV is developed to optimize the film microstructure and grain growth in 50 *nm* thick NC Cu films. Then, a selection of emergent grain boundaries, which represent what's typically observed on the surface of well-prepared films, are structurally analysed using STM topography information and the grain boundaries are successfully characterized in terms of their distinguishable structural features.

4.1. Introduction: the STM perspective of emergent grain boundaries

Grain boundaries in thin films have been the focus of much computational and experimental research concerned with the nanocrystalline material and their electrical[6,66,75–77,79,263,273], thermal[274], and mechanical[81,82,268] properties, along with their performance as catalysts[14,15,17,18,32]. As mentioned in section 1.3, of all microscopy-based techniques, TEM has been the most commonly used method for high-resolution structural characterization of grain boundaries and dislocations in the bulk material[275,276]. Even though there is an extensive amount of research focused on the surface-related phenomena of various NC noble metals, only a few of them were concerned with the structural characterization and detailed analysis of grain boundaries[163,167] and dislocations[164,165,277,278] emerging at the surface, and their impacts on the surface quality. For the investigation of grain boundaries at the surfaces of well-prepared NC Cu films which still reveal to have an atomic level roughness as shown in Fig. 4.7, we suggest that STM may be of use in tackling the aforementioned challenges that reportedly limit the TEM experiments[162,163,165,166], by providing a high-resolution 3D topography map of the emergent grain boundaries in real-space, from a novel perspective[164,170].

This chapter begins by providing an introduction on the *ex situ* chemical etching method for the removal of the copper-oxide on Cu surface, before transferring into

the UHV. This is followed by a discussion of the thermal processing of 50-nm-thick Cu nanocrystalline thin films and determination of the optimized annealing temperature, in section 4.2.2. The challenges in maintaining the overall stability and continuity of the thin films susceptible to interlayer diffusion through the barrier layer, as well as dewetting, are addressed. AFM and STM characterization of the surface at different stages/temperatures of annealing is presented, and the evolution of surface roughness is explained. In section 4.3, STM results on the clean and well-annealed (111) surface of the nanocrystalline Cu thin films are presented. Naturally occurring surface features such as dislocations and grain boundaries are introduced in section 4.3.1. In section 4.3.2, variations in the surface morphology of the clean (111) surface of nanocrystalline Cu film induced by emergent grain boundaries are discussed, and the concept of out-of-plane grain tilt on NC Cu surface is introduced, as part of the grain boundary restructuring phenomenon. Finally in section 4.3.3, an angular characterization of emergent grain boundaries is accomplished based on the variations in the structure; dislocation content and curvature (global/local angle) associated with the grain boundaries, as observed by STM.

4.2. Preparation of NC Cu (111) surface

4.2.1. Chemical etching of the copper oxide

Nanocrystalline Cu thin films studied in this thesis were provided by Intel. While the precise procedures involved in the preparation are considered confidential and cannot be explicitly outlined, a brief description of the process is provided as follows. NC Cu thin films of thickness 50 nm were prepared at the Intel fabrication facility, by sputter physical vapour deposition in Ar^+ plasma. Copper was deposited on top of a Ta diffusion barrier layer of 7 nm thickness, coated on a silicon wafer.

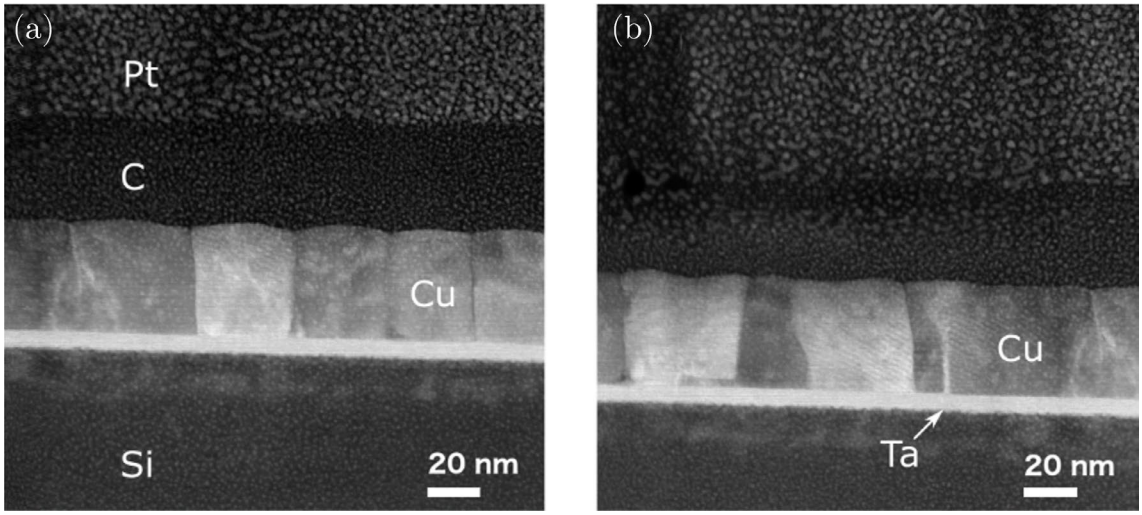

Figure 4.1: STEM image of 50 nm thick NC Cu thin film showing (a) uniform columnar grain boundaries with widths scaling with the film thickness and (b) columnar grains with non-uniform structure in thicker areas of the lamella. Adapted from [279].

The layer of Ta, as explained in section 1.1.1, is employed as a diffusion barrier to prevent leakage paths for Cu diffusion into silicon, as well as providing a good adhesion layer while maintaining the conductivity. All depositions were carried out with the substrate at room temperature. In a previous TEM study by Dr. Megan Canavan on these samples, it was shown that these NC Cu films consist of columnar grains with widths scaling with the ~50 nm film thickness, as illustrated in Fig. 4.1[279].

The post-deposition preparation of the surface and microstructure of NC copper thin films for the purposes of STM study of clean Cu (111) surface and eGBs, is accomplished mainly in two-stages: the *ex situ* removal of the copper-oxide layer that forms in ambient conditions prior to transfer to UHV, followed by the *in situ* preparation by thermal processing of the nanocrystalline thin films in UHV.

As explained in section 1.2.1, copper surface readily oxidizes in ambient conditions when exposed to air, mainly in the form of Cu_2O and CuO, by the following reactions

$$\begin{aligned} Cu + H_2O &\rightarrow CuO + H_2 \\ 2Cu + H_2O &\rightarrow Cu_2O + H_2 \end{aligned} \tag{4.1}$$

To date, various experimental techniques were used by different groups to study the formation and structure of Cu_2O, CuO, and a few other metastable copper oxide phases, as well as their effect on material properties[87–92,106,108]. The effect of oxidation environment, pressure and temperature, and the surface texture on the reaction rate of the spontaneous oxidation of copper have been the focus of many studies[107,114–116,280–284]. These works revealed that on polycrystalline copper, Cu_2O forms considerably faster compared to the other oxide phases, while a significant portion of the oxidation, corresponding almost to half of the total thickness of the oxide layer in long term, occurs in the first few hours after exposure to ambient air at room temperature[285–288]. The investigation of clean surfaces of nanocrystalline copper thin films using STM requires the removal of the oxide layer prior to the transfer of the samples into the UHV, as it hinders the direct investigation of the copper surface and surface defects including dislocations and grain boundaries.

Acetic acid, among the commonly used non-oxidizing acids, was shown to provide a controllable chemical etch of the copper oxide, without attacking copper[102–105]. It selectively reacts with copper oxide to form cupric acetate, which is readily removed from the surface through N_2 flow[102], providing a rapid, effective and reproducible method for the removal of copper oxide immediately prior to the transfer to UHV for the purposes of this work. NC thin films of size 0.3×0.7 mm^2 immersed in 99.9% high purity grade glacial acetic acid (GAA) for 3-5 min were then rapidly loaded into the N_2 flowing load-lock chamber which was pumped down for *in situ* processing.

4.2.2. Thermal processing of NC Cu thin films

The main goal in determining the optimized annealing temperature for the purposes of our work was to reach sufficiently high temperatures to enable recovery and grain growth while maintaining the overall film continuity across the Ta substrate. For NC Cu films, like all thin films on a substrate, this is challenged by a phenomenon known as dewetting, which occurs due to the agglomeration of the film into isolated 3D islands at temperatures well below the melting point[123,132,146].

As explained in section 1.2.2, in NC thin films with a high density of grain boundaries, dewetting is mainly initiated at the voids of triple junctions that are formed due to Mullins grooving by surface diffusion[125,128,145,289–291]. The voids at the grain boundaries and triple junctions, as well as other defect sites, also give rise to a potential pathway for Ta outdiffusion into copper which triggers the intermixing and further diffusion of copper into silicon[59,292–296]. Consequently, the upper limit to the annealing temperature of the NC Cu thin films is roughly set by the formation of voids.

Thermal processing of NC thin films is determined by factors such as annealing temperature, duration, pressure and atmosphere. In this work, the *in situ* preparation of 50-nm-thick NC copper films is carried out in the UHV preparation chamber with a base pressure of 1×10^{-10} mbar, following the chemical etching using acetic acid. The NC Cu films transferred into UHV were prepared by several cycles of high energy Ar^+ sputtering followed by thermal annealing. The annealing temperature is optimized in UHV using an indirect heating technique. The sample is placed onto a high-purity pyrolytic boron nitride (PBN) type heater (Tectra GmbH), which provides rapid temperature ramp with a uniform thermal gradient. While temperature on both the PBN heater and the sample surface is measured

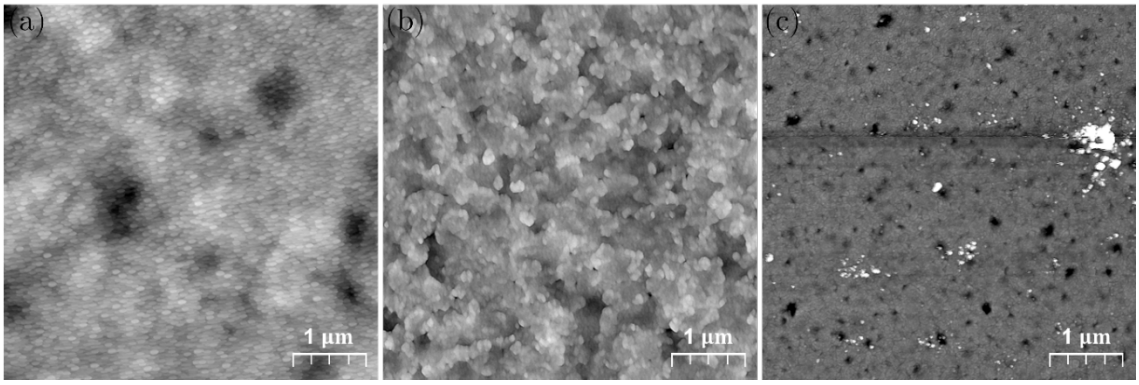

Figure 4.2: TM-AFM topography images of 5×5 µm^2 areas on surfaces of NC Cu films after acetic acid etch and thermal processing in UHV at different temperatures. (a) pre-anneal, Rq = 2.94 nm. (b) annealed at 350℃ for 10 min, Rq=1.80 nm. (c) annealed at 400℃ for 10 min, Rq=2.51 nm.

with a thermocouple and a pyrometer, the applied power and temperature was calibrated, enabling controlled and reproducible thermal processing of samples. Following the *in situ* preparation cycles of Cu film, the microstructural and granular evolution of the copper surface annealed at different temperatures was characterized using AFM, STM and SEM. Temperature was varied up to 450℃ while the number of cycles; annealing duration of 10 min; and sputtering energy of 1 keV, and sputtering duration of 10 min were fixed. The correlation between annealing temperature and the level of grain boundary grooving, void formation and consequent kinetics through dewetting was examined. The effect of temperature on the surface texture was analysed by root-mean-square (RMS) roughness, extracted using the SPM analysis softwares *Gwyddion*[297] and *WSxM*[298]. The grain size evolution was investigated by the inspection of AFM and STM topography.

Prior to any thermal treatment, the surface of chemically-etched NC Cu film was inspected using ambient tapping mode (TM)-AFM. The AFM topography image of size 5×5 µm^2 revealed the NC nature of the surface comprising small grains with RMS roughness Rq=2.94 nm, as shown in Fig. 4.2 (a). Despite the general uniformity of small grains, local deviations in the surface level were observed as macroscopic depressions and protrusions, which explains the high RMS roughness.

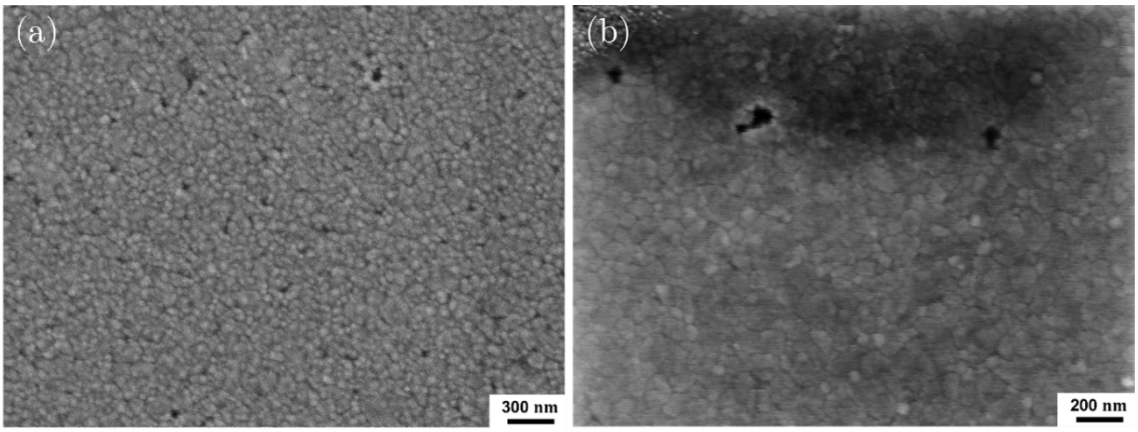

Figure 4.3: SEM images of NC Cu film annealed at 400℃ for 10 min in UHV (a) the initial stages of void formation at the grain boundaries and triple junctions (b) the initial stages of the void growth observed detected on another area of the surface.

Fig. 4.2 (b) shows the same size AFM image of the Cu film surface annealed at 350℃. The surface texture reveals a slightly flatter texture, which results in the relatively reduced roughness value of Rq=1.80 nm. Although the macroscopic AFM topography image does not resolve the grain boundaries and triple junctions clearly at this scale, the larger features indicate grain growth by coarsening of grains due to higher annealing temperature.

Increasing the annealing temperature further up to 400℃, as shown in Fig. 4.2 (c) caused an increase in the surface roughness to 2.51 nm, excluding the protrusions due to contamination. This is attributed to the formation of voids (holes), which are assumed to have nucleated mainly at the grain boundaries and triple junctions, upon further development from Mullins grooving via surface diffusion[120–124].

In Cu thin films, depending on the factors such as substrate, film thickness and annealing environment, dewetting has been reported to occur both by the capillary driven nonfractal and fractal growth of voids[267,291,299,300]. For instance, in polycrystalline Cu films of thickness <40 nm on silicon substrate annealed in vacuum, dewetting is initiated at the voids which typically grow as fractals whereas thicker films showed formation of hillocks[145].

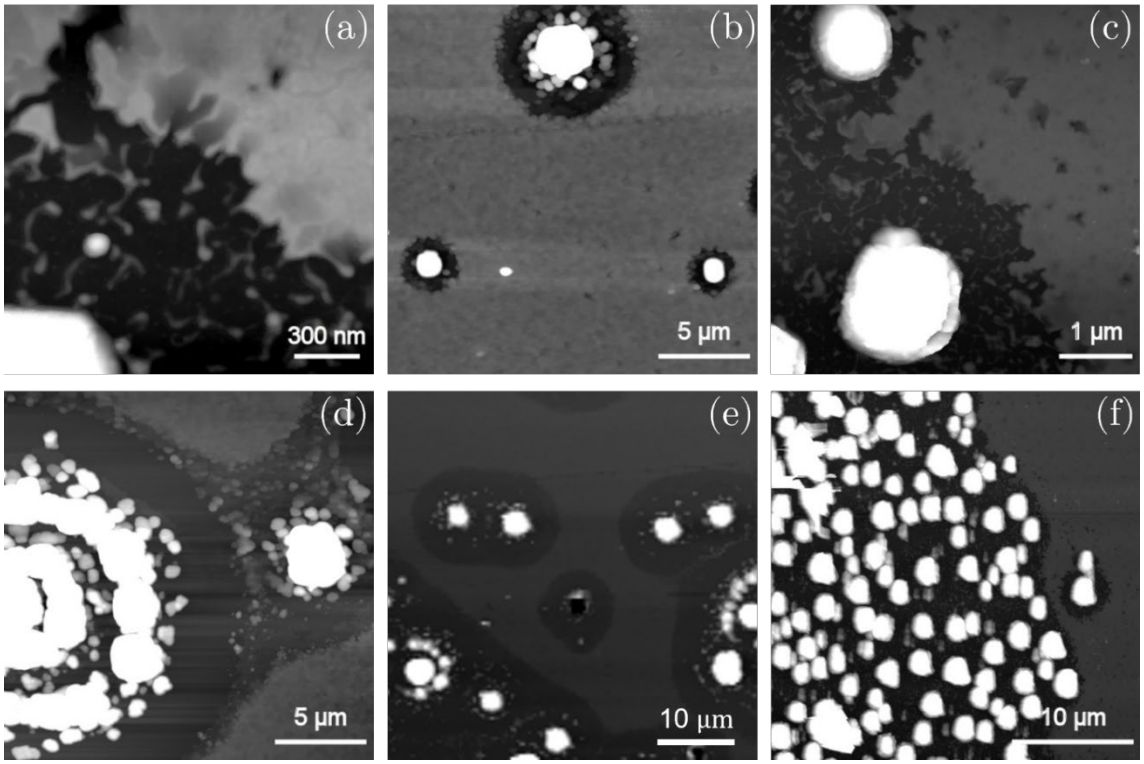

Figure 4.4: TM-AFM topography images on surfaces of NC Cu films after thermal processing with annealing temperature at 450℃ in UHV (a) detailed close-up view of the border of Cu film resolving grain boundaries and dewetted region of substrate (b) zoomed-out image showing three of the circular dewetted features with different sizes (c)-(d) growing circles coalesce and merge to form larger breakages (e) merged groups of dewetted circles grow (f) and form colonies of dewetted regions centred with protrusions.

Explained earlier in section 1.2.2, further grain growth is mainly suppressed by Mullins grooving, which results in disruptions on the surface, *i.e.,* voids, where dewetting or inlayer diffusion nucleates in NC thin films. In Fig 4.3 (a)-(b), this process is better visualized in the SEM image of the NC Cu film surface, annealed at 400℃. The formation of voids is observed at the grain boundaries and triple junction points, while the SEM image on another area of NC Cu film surface shown in Fig 4.3 (b) illustrates the initial stages of growth of some voids.

Upon further annealing at 450℃ in UHV, the surface shows significant morphological changes of circular dewetted areas over the substrate, observed by TM-AFM topography (Fig. 4.4 (a)). Here, a protrusion (bright) on the bottom left is surrounded by a darker area, while the rest of the film surface texture reveals

grains. The visible difference in the contrast suggests that the protrusions are an accumulation of material with a height much greater than the film level, whereas the darker regions below the film level are dewetted areas exposing the substrate. These dewetted circles of varying diameter distributed over the surface (Fig. 4.4 (b)), are observed to grow and coalesce (Fig. 4.4 (c)-(d)) to form colonies (Fig. 4.4.(e)), resulting in larger dewetted areas, as visualized in Fig. 4.4 (f). Notably, the growth in the height of the protrusion at the zone correlated with denuded areas as Cu is removed from the substrate, suggesting an increase in the copper content of these protrusions.

Holloway et al. attributed these protrusions at the circular zones to the formation of Cu_3Si precipitates due to initial penetration of Cu through Ta upon annealing at 630℃ at the Ta/Si interface, preceded by Ta outdiffusion into Cu, in Cu (50 nm)/Ta (50 nm)/Si stack[59].

As mentioned earlier, the columnar boundary structure of copper and the formation of voids enhance the diffusion pathways for Ta into Cu, which is followed by copper diffusion through Ta. At the Ta-Si interface, Cu_3Si is reported to form locally at the preferential sites for the initial nucleation of Cu diffusion to Ta. In our Cu (50 nm)/Ta (7 nm)/Si configuration, this reaction is likely to occur at relatively low annealing temperatures due to the reduced thickness of the Ta layer. The precipitates observed in Fig 4.4 are too large to indicate any crystallographic orientation with respect to the silicon layer.

The detailed AFM topography image of a single circular zone is shown in Fig. 4.5 (a). In the dark region surrounding the central protrusion the copper film has been stripped away. Two line profiles obtained across the dark layer outside the protrusion and at the centre of the protrusion on the height data in Fig. 4.5 (a) are shown in Fig. 4.5 (b), indicated by the black and red lines, respectively. The

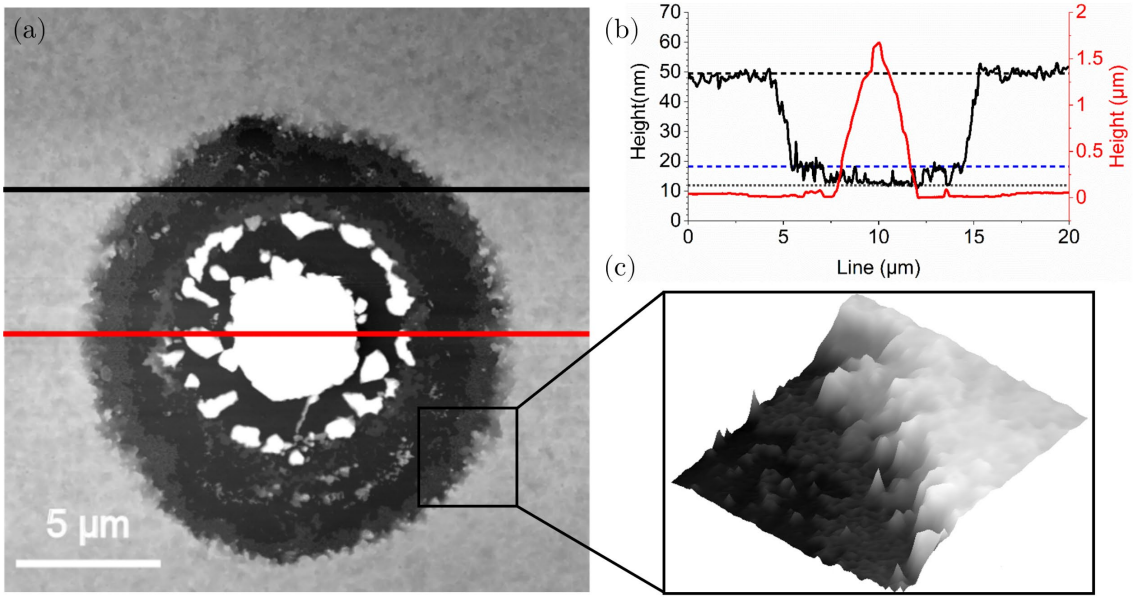

Figure 4.5: TM-AFM topography image of a 20×20 µm^2 area depicting (a) the circular dewetted feature (b) line profiles obtained across the protrusion at the centre, indicated by red line and across the denuded (dark) region exposing the substrate, indicated by the black line. The corresponding y-axes are colour-matched. Cu film level, interlayer level, and substrate level are marked by the horizontal black dashed, blue dashed and black dotted lines, respectively. (c) 3D perspective view of the zoomed-in area marked by the square on (a). From left (dark) to right (bright) the substrate and Cu film layers are distinguished as Si/Ta/Cu.

difference in the height of the Cu film level (black dashed line) and the lowest point of the film level (black dotted line) is ~38.4 nm. This is slightly thinner than the initial Cu thickness (50 nm), partly due to sputtering and the removal of the oxidized copper layer. There is a ~6.5 nm corrugation from the lowest point of the substrate level to an intermediate layer marked by the blue dashed line, which is close to the deposition thickness of Ta (7 nm). The details of this border is better visualized by a 3×3 µm^2 3D perspective view shown in Fig. 4.5 (c), where the exposed substrate is observed as a depression (dark).

The protrusion itself is measured to be ~1.67 µm high, of diameter ~4.44 µm indicating a larger volume than that of the pre-annealed Cu and Ta configuration. Exposure to the air during ambient TM-AFM measurement necessitates the consideration of the formation of a fresh copper oxide phase, as well as the

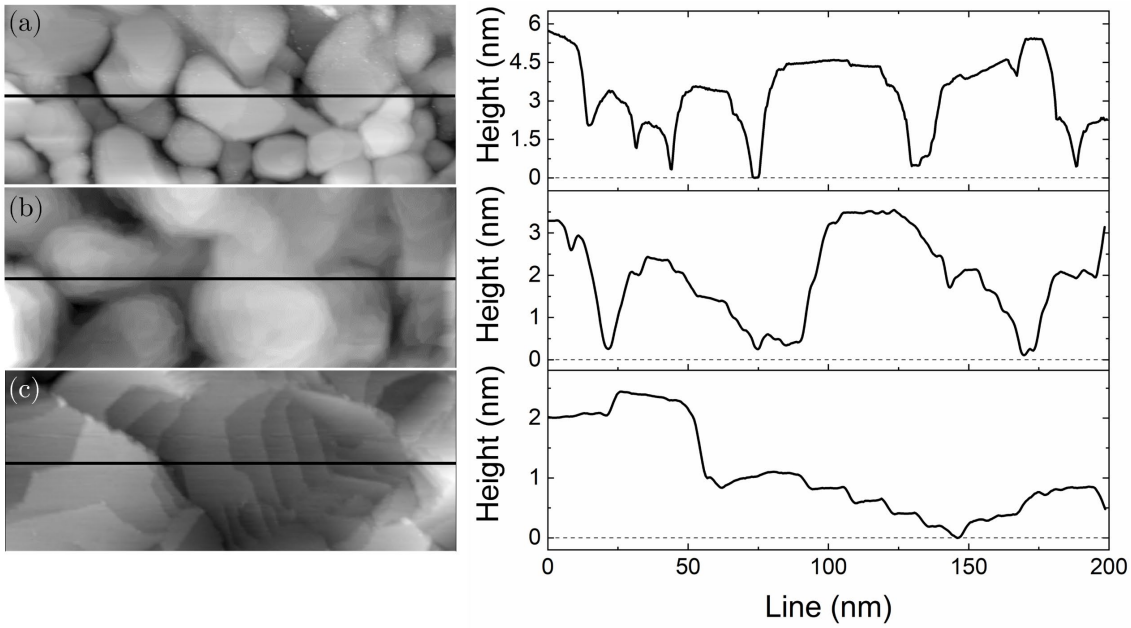

Figure 4.6: STM topography images on the surface of NC Cu films after thermal processing in UHV following the acetic acid etch (on the left panel) and corresponding line profiles obtained across the line marked on the topography images (on the right panel) (a) pre-anneal, Rq=1.36 nm, imaging conditions: 0.2 nA, 0.3 V (b) annealed at 300℃, Rq=1.41 nm, imaging conditions: 30 pA, 1 V (c) annealed at 380℃, Rq=0.42 nm, imaging conditions: 50 pA, 0.3 V.

formation of SiO_2 between the Cu_3Si and silicon layer, as previously reported in the literature. Although the sample surface still contained areas of continuous NC Cu film in between the dewetted areas as shown in Fig. 4.4, the obvious presence of contamination due to diffusion and intermixing is not ideal for the observation of clean emergent grain boundaries. Therefore, the thermal annealing temperature is optimized in the range 300-400℃ with an upper limit set at slightly below the temperature that leads to the formation of voids and the dewetted circles.

The optimization in this range is achieved by confirming the evolution of surface morphology by STM measurements, following the *in situ* preparation (by cycles of thermal annealing and sputtering) of the GAA etched NC Cu film surfaces, as shown in Fig. 4.6. Prior to *in situ* preparation, the surface reveals grains as tall stacks of layers with deep equilibrium grooves in between, as shown in Fig. 4.6 (a), with a surface roughness of 1.36 nm. This is thought to be due to the fact that in

as-deposited nanocrystalline thin films, the relative orientations of grains are not optimised, and there is a consequent high mismatch between grains.

The evolution of the surface texture after processing at an annealing temperature of 300℃ is shown in the left panel of Fig 4.6 (b). The corresponding line profile in the right panel of Fig. 4.6 (b) shows that the average groove depth is relatively reduced, indicating the initiation of diffusion to enable the grains to relax and recover by annihilation of defects and the arrangement of dislocations into arrays. Conversely, the roughness analysis shows a slight increase in roughness to ~1.41 nm, attributed to the uneven surface level due to insufficient annealing temperature following the Ar^+ sputtering.

Fig. 4.6 (c) shows the STM topography of the NC Cu film annealed at ~380℃, and the corresponding line profile obtained across the line marked on the image. Increasing the annealing temperature up to 380℃, the surface morphology completely changes, providing the sufficient activation energy for recovery and growth of grains. The STM topography image shows grains with wide facets and a significantly reduced corrugation difference over the film, as confirmed by the line profile in the right panel of Fig. 4.6 (c). The arrangement of the film into a uniform low energy configuration is observed through the formation of large low energy facets and atomic steps, as well as the significant reduction in the grain boundary groove depth across the line profile, consistent with the radically reduced surface roughness of ~ 0.42 nm at this scale. The step edge directions change by about 120°, in good agreement with the preferential growth direction on close-packed (111) plane. As will be shown in the next section, the atomic step height also confirms the (111) orientation of the surface. The optimal annealing temperature range to form the ideal surface texture decorated with relaxed emergent grain boundaries for further structural characterization was determined to be 350−380℃.

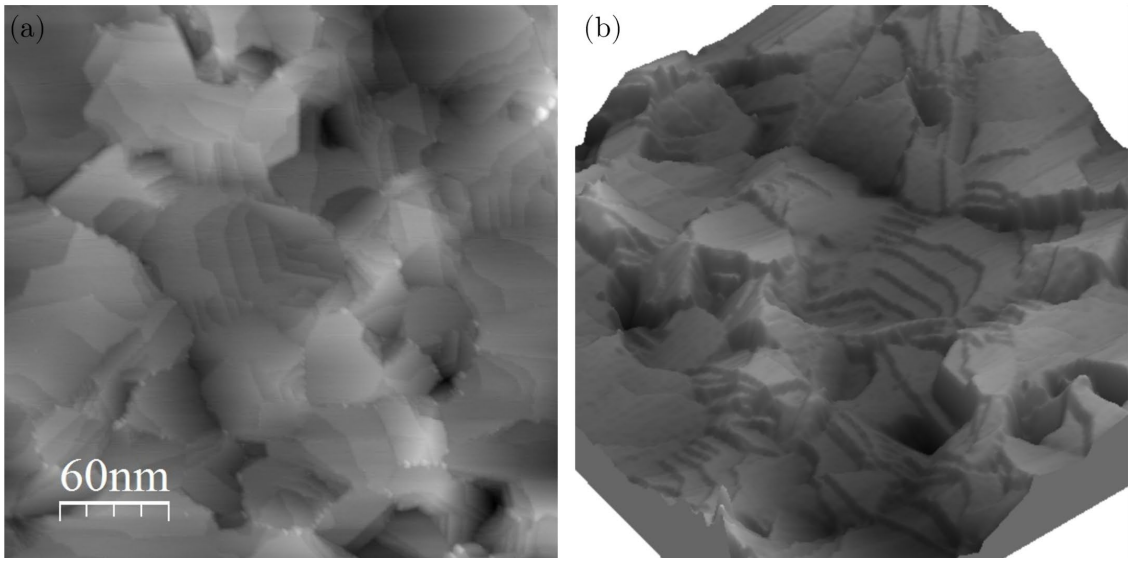

Figure 4.7: STM topography images of a 200×200 nm^2 region on the surface of NC Cu films after thermal processing in UHV following the acetic acid etch (a) showing the clean Cu surface steps and terraces (b) 3D perspective view of the same area reveals out-of-plane tilted grains (parallel to the surface normal), resulting into the roughening of the surface. Imaging conditions: 50 pA, 0.3 V.

A large-scale STM topography image of the clean Cu (111) surface is shown in Fig. 4.7 (a). The surface consists of steps of atomic layers after refinement of the surface texture, annealed at 380℃. The 3D perspective view of this STM topography image is illustrated in Fig. 4.7 (b), which highlights the corrugation throughout the film surface in better detail. Interestingly, the flat atomic terraces are observed to be tilted in a direction normal to the surface plane, which introduces a new kind of atomic scale roughness to the film.

4.3. STM results on NC Cu film

Here, the clean Cu (111) surface is characterized before the emergent grain boundaries, dislocations and other features are discussed. As mentioned in section 3.1, copper is a noble metal with fcc lattice structure. The crystal is built by the close-packed arrangement of atoms along ⟨110⟩ in close-packed {111} planes, which are stacked in *ABCABCABC* sequence along ⟨111⟩ direction. Cu has a lattice constant of 3.61 Å. In Cu (111), the interplanar spacing (step height) is 2.08 Å,

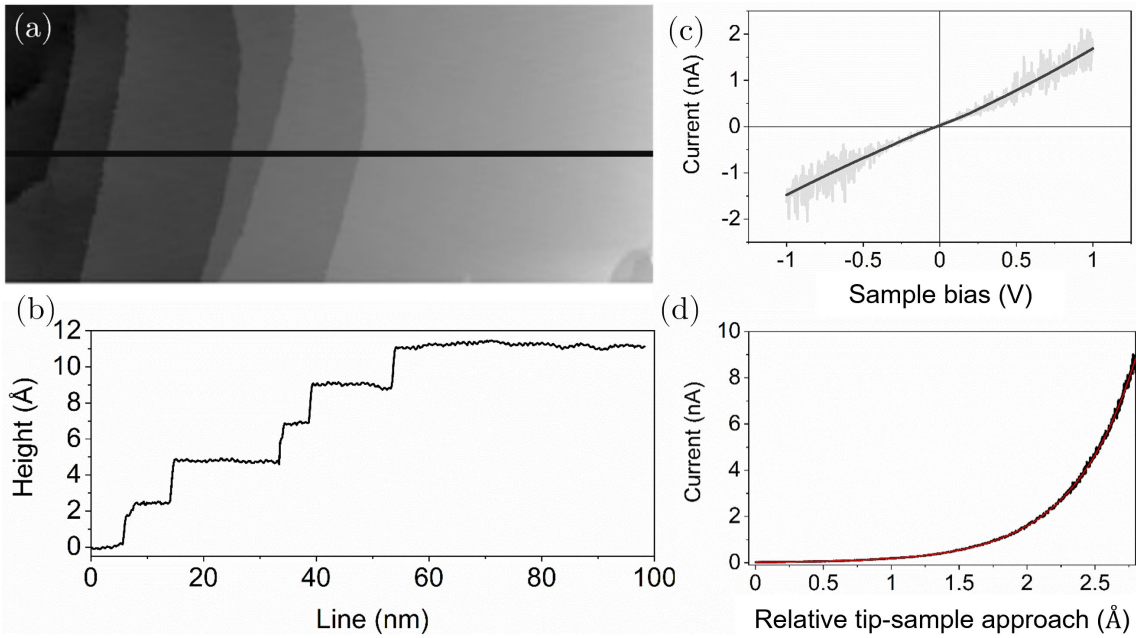

Figure 4.8: STM analysis of well-prepared NC Cu film surface (a) STM topography images of atomic steps on the Cu (111) surface, imaging conditions: 50 pA, 0.5 V. (b) line profile obtained across the line marked in topography image in (a). (c) $I(V_{\text{bias}})$ spectroscopy and (d) $I(z)$ on clean Cu (111) measured at room temperature. The apparent barrier height Φ from the fit in (d) is approximately ~4.86 eV, extracted from $I \propto e^{-\alpha z\sqrt{\Phi}}$ using the relationship given by Eq. (2.9) (4.94 eV for Cu (111)[301,302]).

and the nearest-neighbour distance is 2.55 Å[303]. The (111) plane, which has 3-fold symmetry, has the lowest surface energy in fcc metals and was initially studied a few years after the invention of STM[182]. These studies which showed the atomic resolution surface topography of Cu (111) also revealed the presence of standing waves as 2D surface states due to electron scattering near local features such as defects like step edges, dislocations, grain boundaries or point defects such as impurities *i.e.*, adsorbate atoms[190,304]. The electronic characterization by STS studies measured surface state at 450 mV below Fermi level and a work function of 4.94 eV[302,305,306].

Fig. 4.8 (a) shows the STM image of clean steps on the nanocrystalline Cu (111) film surface, measured at room temperature. In Fig. 4.8 (b), the line profile measured across the steps shows a step height of ~2.1 Å corresponding to the interplanar spacing of the close-packed (111) planes in Cu, confirming the z-

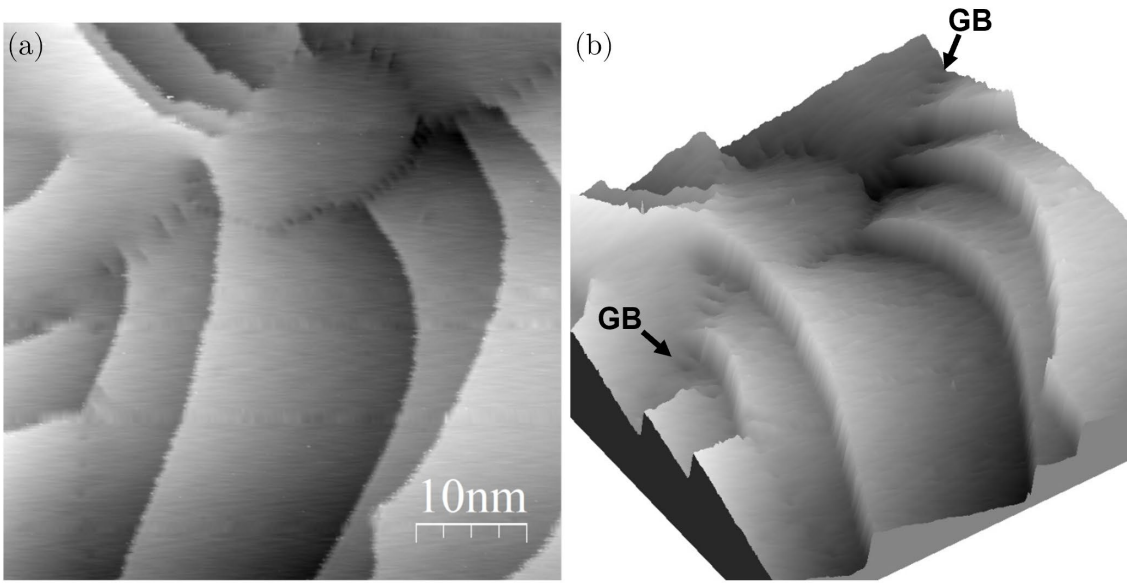

Figure 4.9: STM topography images of a 40×40 nm^2 area on well-prepared NC Cu film surface decorated with grain boundaries comprised of arrays of edge dislocations (a) showing the typical microstructure of grain boundaries and their junctions on Cu surface with atomic steps (b) 3D perspective view of the same area reveals out-of-plane tilted grains (parallel to the surface normal). Grain boundaries are marked by the black arrows, denoted as GB. Imaging conditions: 50 pA, 0.5 V.

distance calibration for the STM study of NC films. The quality of the metallic tip is confirmed by the linear $I(V_{\text{bias}})$ spectroscopy, and the exponential dependence of tunneling current as presented in $I(z)$ spectroscopy acquired on clean Cu (111) surface, as shown in Fig 4.8 (c) and Fig. 4.8 (d), respectively.

4.3.1. Emergent grain boundaries and dislocations at the surface

Fig. 4.9 shows a close-up STM image at the surface of NC Cu film, which reveals the topography of a region of atomic steps and terraces interrupted by grain boundaries comprised of zipper-like arrays. As mentioned earlier in section 3.2.1, tilt (twist) grain boundaries are formed by arrays of edge (screw) dislocations, to accommodate the misfit where the two grains meet, illustrated in Fig. 4.12 (a). For general grain boundaries, the dislocation content defined by the net Burgers vector $\boldsymbol{b}$, is related to the misorientation angle by Frank's equation (Eq. 3.14) through the period vector $\boldsymbol{p}$. As explained in section 3.3.2., in symmetric tilt grain boundaries

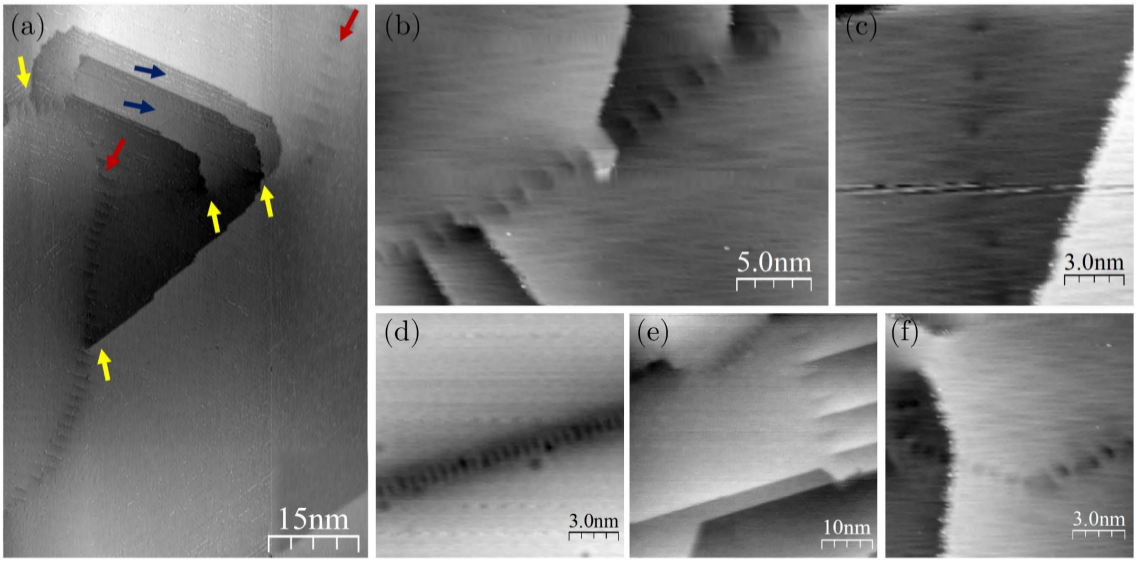

Figure 4.10: STM topography images of examples of typical emergent grain boundaries on the well-prepared NC Cu film surface (a) A junction of grain boundaries and screw dislocations. Grain boundaries, screw dislocations and steps are indicated by red, yellow and blue arrows respectively. (b)-(c)-(d)-(e)-(f) Close-up views of various grain boundaries comprised of arrays of edge dislocations surrounded by screw dislocations and steps. In (f) the grain boundary rotates by 120°. Imaging conditions: (a) 50 pA, 0.2 V (b)-(c)-(f) 50 pA, 0.5 V (d)-(e) 50 pA, 0.3 V.

comprised of an array of edge dislocations with a spacing d (Fig. 4.12 (a)), Frank's formula is simplified to $d = |\boldsymbol{b}|/2\sin(\theta/2)$ (Eq. 3.15), since the grain boundary tilt axis is perpendicular both to the Burgers vector and the period vector, hence $\boldsymbol{p} \times \hat{\boldsymbol{\rho}} = |\boldsymbol{p}| \approx d$.

As expected, the configuration of edge dislocations varies among grain boundaries. This is visualized in Fig. 4.9 (a), both by the changing spacing of stacking faults (observed as depressions), and the width of the stacking fault ribbon, indicating difference in grain boundary characteristics. Similarly, Fig. 4.10 (a) reveals a junction of three grain boundaries (red), in an area decorated with screw dislocations (yellow) and steps (blue), features that are frequently observed in the well-prepared NC Cu film. As expected with the grain boundary-rich nature of NC films, different boundary configurations are observed, as illustrated in Fig. 4.10 (b)-(f). Similar to that shown in Fig. 4.9, the structural differences in the arrays of edge

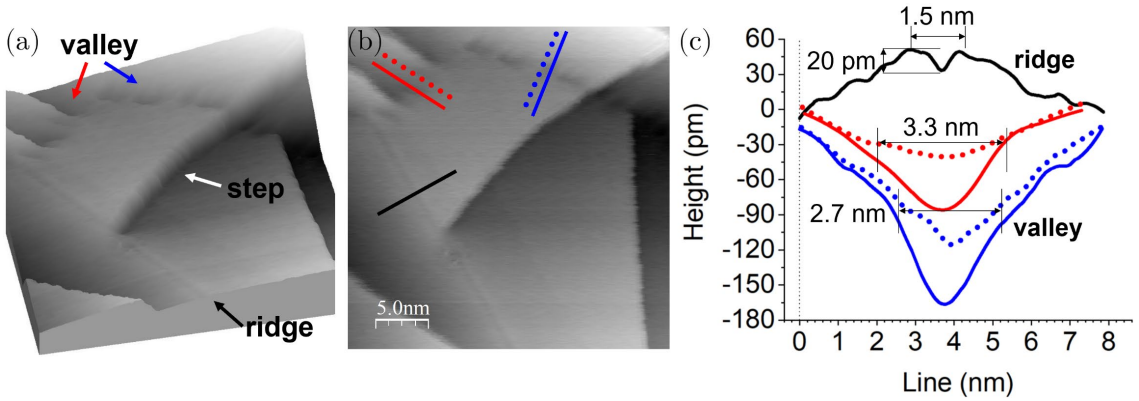

Figure 4.11: STM measurement on well-prepared NC Cu film surface (a) 3D perspective view of an area showing three grain boundaries. The symmetric out-of-plane rotation of grains about the grain boundary introduces valleys and ridges on the surface, indicated by blue/red and black arrows, respectively. (b) 2D STM topography of the same area. (c) line profiles obtained across the grain boundaries indicated in (b). Imaging conditions: 50 pA, 0.3 mV.

dislocations (stacking faults) in Fig. 4.10 (b)-(f) are indications of a variation in the grain boundary character, which is mainly defined by the misorientation degree, and the excess energy associated with the disordered atomic configuration.

The 3D perspective view of the area in Fig. 4.9 (a), presented in Fig. 4.9 (b), shows the behaviour of the surface plane in the vicinity of grain boundaries, two of which are indicated by the arrows. The surfaces of the grains on either side of the boundaries are observed to be tilted along the direction of surface normal, almost symmetrical about the grain boundary plane. Referred to as out-of-plane tilt, this rotation is clearly induced by and localized around the grain boundaries. Both the degree and direction of out-of-plane rotation is observed to be varied for different grain boundaries, as can be seen by a visual inspection of Fig. 4.9 (b).

4.3.2. Out-of-plane rotation

Fig. 4.11 shows the STM topography image on a different area on the surface, where two types of out-of-plane rotation is observed. The distinction between the two is best visualised in the 3D perspective view in Fig. 4.11 (a), where the surface

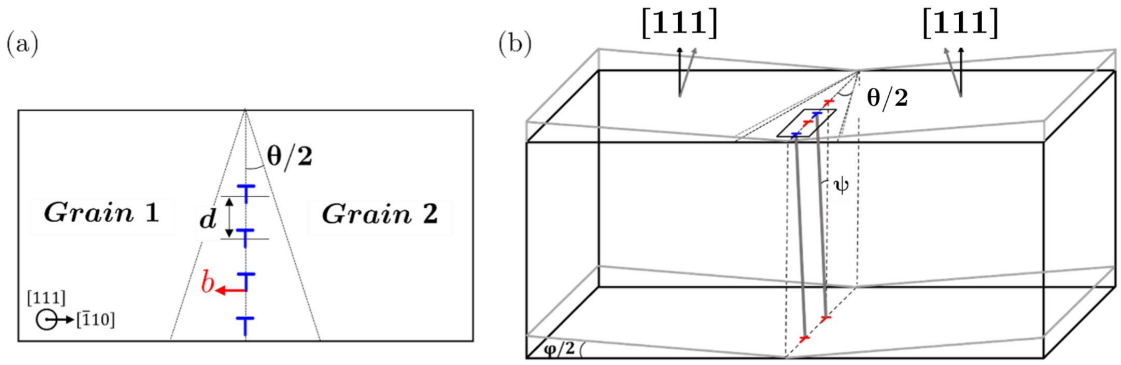

Figure 4.12: Schematics of grain boundary geometry emerging at the surface (a) the degree of misorientation, θ is accommodated by the array of edge dislocations of a spacing $\boldsymbol{d}$, and Burgers vector $\boldsymbol{b}$ (b) schematics of the geometry, showing the out-of-plane φ, in-plane θ rotations and inclination angle ψ.

normal of the film is symmetrically tilted, forming valleys and ridges[163], by an out-of-plane rotation in opposite directions with respect to each other. In grain boundaries of misorientation angle θ, Zhang et al. explained this out-of-plane rotation from surface normal [111] towards [112] through an angle φ as part of the restructuring of the grain boundary, introducing elastic stresses[167]. This was attributed to the anisotropic dislocation core energy which is minimized through the inclination of the dislocation cores (within the film) initially lying parallel to [111], towards [112], so that they lie along the energetically favoured close-packed {111} planes. The minimum grain boundary energy configuration was shown to be achieved when the boundary cores are inclined at angle $\psi = 19.47°$, for grain boundaries of all fcc metals, regardless of the value of the in-plane angle[167,213,214]. The geometry of this configuration is shown in Fig. 4.12 (b).

To further understand the out-of-plane rotation characteristics of different grain boundaries, line profiles performed across each grain boundary were analysed. The line profiles for the boundaries presented in Fig. 4.11 (c) show the opposite slopes in the valley (blue and red) and ridge (black) type boundaries, clearly. For this particular RT-STM image of the ridge type grain boundary, only the boundary groove is resolved which shows a corrugation amplitude about ~20 pm. In Fig. 4.11

(c), the line profiles represented by the solid lines correspond to the depressions along the boundaries, whereas the dashed lines correspond to the areas between these depressions, comprising the stacking faults of Shockley partials.

The curvature (slope) of the valleys, the stacking fault ribbon width and the dislocation content are different for the two valleys. The relationship defining the geometry of the restructuring process, which was given previously in section 1.3, $\tan\psi = \tan(\varphi/2) \,/\, \sin(\theta/2)$, is illustrated in Fig. 4.12 (b)[163].

Next, the degree of out-of-plane rotation and dislocation content information for each grain boundary is extracted from the STM topography. Using this information combined with the Frank's equation (Eq. 3.15) and restructuring geometry, a selection of grain boundaries typically observed in our NC Cu film are further analysed.

4.3.3. Low-angle/high-angle grain boundaries

The arrangement of dislocations forming the grain boundary results in a short-range elastic stress field and the excess energy associated with it. For grain boundaries with higher degrees of misorientation, more dislocations are required to accommodate for the high mismatch. The formal classification of the grain boundaries in terms of the degree of misorientation is generally governed by the distinction in the behaviour of grain boundary energy given by Eq. 3.18, which increases as θ increases, up to $\theta \leq 15°$. As mentioned in section 3.2.2, we refer to grain boundaries with $\theta \leq 15°$ as low-angle and those with $\theta > 15°$ as high-angle grain boundaries.

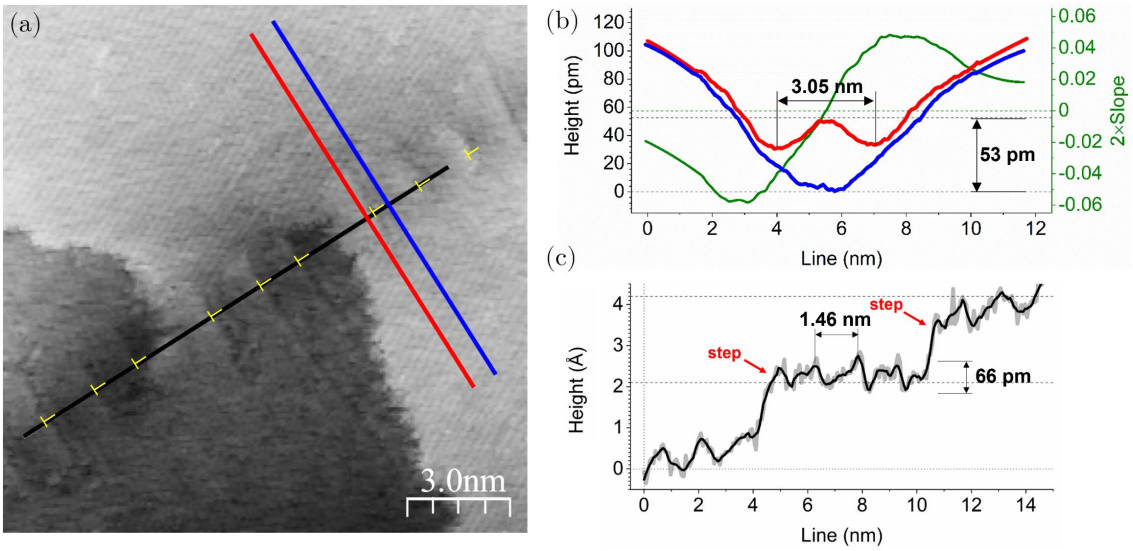

Figure 4.13: STM measurement of a low-angle emergent grain boundary (a) STM topography image of a low-angle grain boundary showing the array of edge dislocations, each one marked by the dislocation sign ⊥ in yellow to guide the eye. Imaging conditions: 50 pA, 0.3 mV (b) line profiles obtained across the grain boundary over the stacking fault ribbon, and between two dislocations, indicated by red and blue lines, respectively. The out-of-plane angle is obtained from the calculated slope of the blue curve, indicated by green. (c) line profile along the grain boundary, indicated by black line.

The close-up STM topography shown in Fig. 4.13 (a) reveals a valley type emergent grain boundary lying across the atomic steps with height of ~2.1 Å. These steps nucleating from the boundary, referred to as screw dislocations, might be an indication of a twist component to the boundary itself. At the nucleation zone of these screw dislocations, the macroscopic uniformity of the average dislocation spacing of ~1.46 nm, is observed to be disrupted. Applying Frank's equation (Eq. 3.15) for $\boldsymbol{b} = a/\sqrt{2}\langle 110\rangle$=2.55 Å, the in-plane (misorientation) angle θ is calculated as approximately 10.02°. This suggests that the grain boundary in Fig. 4.13 (a) is a low-angle tilt grain boundary. The line profiles across the boundary show the valley character of the grain boundary groove clearly. At the core of the 3.05 nm-wide stacking fault ribbon, the corrugation amplitude of the stacking fault partials stepping up the surface is measured about 53 pm, which is slightly below the theoretical value of the height of a Shockley partial on (111) surface corresponding to 70 pm.

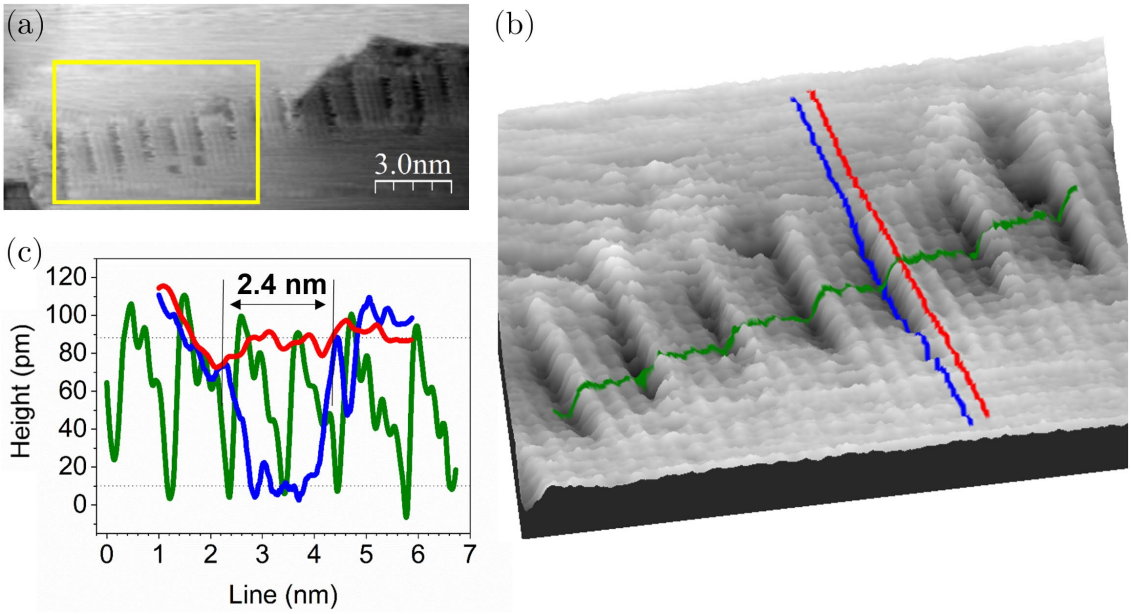

Figure 4.14: STM measurement of a low-angle emergent grain boundary (a) Large scale STM topography image of a low-angle grain boundary showing the array of edge dislocations. (b) 3D perspective view of the area marked by the yellow box on (a). Imaging conditions: 200 pA, 0.05 V (c) line profiles obtained across the grain boundary over the stacking fault ribbon, and between two dislocations indicated by red and blue lines, respectively. The line profile along the grain boundary, indicated by green.

The groove profile shown in Fig. 4.13 (b) corresponds to a φ=0.06 rad (3.44°) out-of-plane tilting, which confirms the misorientation angle $\theta \cong 10.02°$ by the geometrical relationship (assuming the minimum energy configuration of restructured GB with $\psi = 19.47°$). Note that, the groove angle of 3.44° extends to about 3.5 nm on either side of the grain boundary core.

Another example of a low-angle emergent grain boundary, as suggested by the widely spaced dislocations, is presented in Fig. 4.14 (a). A zoom-in 3D view of the area framed by the yellow box in Fig. 4.14 (a), shown in Fig. 4.14 (b), reveals the boundary topography in detail. The line profile obtained across the boundary shows the ~50 pm high protrusion introduced by the Shockley partial pairs on the (111) surface. The average dislocation spacing a the boundary (green line) is measured as ~1.16 nm, which roughly corresponds to a misorientation angle $\theta \cong 12.6°$.

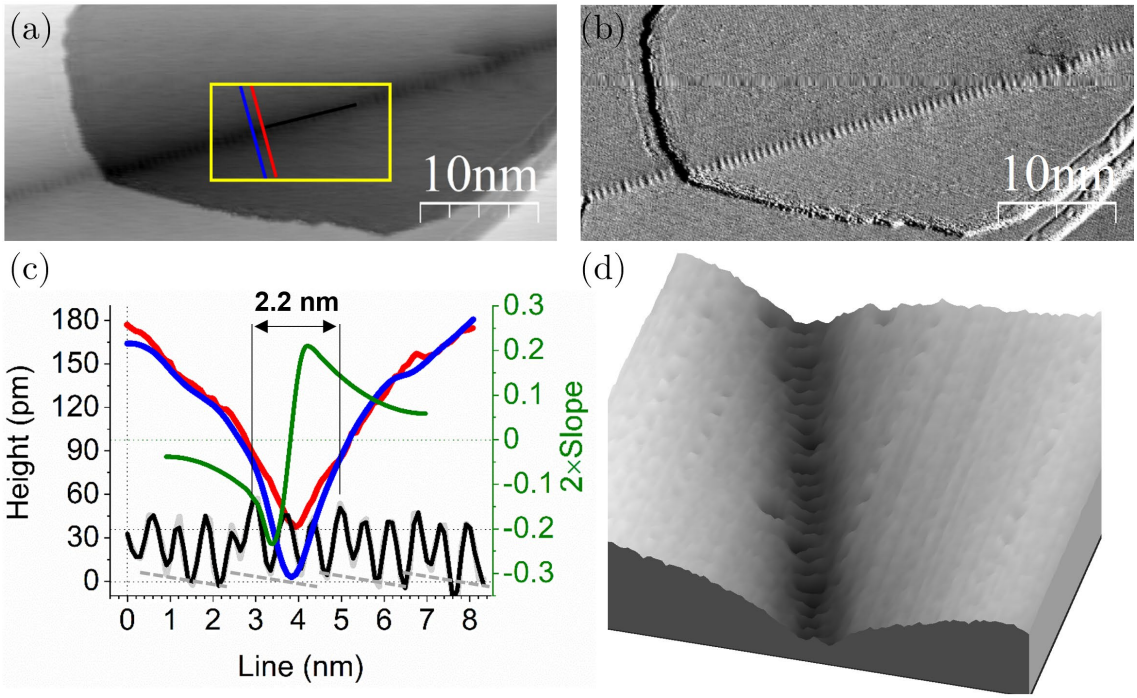

Figure 4.15: STM measurement of a high-angle emergent grain boundary (a) topography image of high-angle grain boundary showing the array of edge dislocations (b) tunnel current error image showing the array of dislocations. Imaging conditions: 50 pA, 300 mV (c) line profiles obtained across the grain boundary over the stacking fault ribbon, and between two dislocations, indicated by red and blue lines on (a) in the yellow box, respectively. Line profile along the grain boundary, indicated by black line and out-of-plane angle is obtained from the calculated slope of the blue curve, indicated by green. (d) 3D perspective view of the area marked by the yellow box on (a).

Note the deviations in the dislocation periodicity observed in the 3D perspective view, as the number of atomic rows in between partials is varied. At room temperature, the fluctuations in the grain boundary structure cannot be easily attributed to a single mechanism. The presence of nearby point defects and steps, or tip-induced effects[307–309] (*i.e.,* atomic diffusion due to tip-induced local electric field and electrostatic interaction) taking into account the high diffusivity of copper, may result in disturbances in the ideal GB structure. The precise measurement of the misorientation angle using STM requires consideration of a period vector determined by atomic resolution, which will be shown in a grain boundary with a similar degree of misorientation, in chapter 5.

Fig. 4.15 (a) shows a grain boundary with a significantly different dislocation

content from the previous boundaries presented in Fig. 4.13 and Fig. 4.14. The array of dislocations along the grain boundary can be seen in the current error image in Fig. 4.15 (b) more clearly. The average spacing between dislocations obtained from the line profile along the grain boundary as marked by the black line in Fig. 4.15 (a) is approximately 6.2 Å, which is significantly smaller than the dislocation spacing of previously shown low-angle grain boundaries. Following the previous methodology, using Eq. (3.15), this corresponds to a misorientation angle of about $\theta \cong 23.7°$, indicating a high-angle grain boundary. A detailed inspection of the dislocation array line profile in Fig. 4.15 (c) indicates a periodicity in every 3 dislocations (marked by grey dashed line) corresponding to a distance of 1.86 nm, but the atomic structure needs to be confirmed by high-resolution STM imaging or by MD simulations.

At the core of the 2.2 nm-wide stacking fault ribbon, the corrugation amplitude is measured about 35 pm, a relatively smaller value suggesting the possibility of a bias-dependent effect, which will be discussed in more detail, in chapter 5. The analysis of groove profile obtained from the line profile across the boundary indicates an out-of-plane rotation of approximately φ=0.2 rad (11.46°), slightly above the value predicted by the geometrical relation φ=0.15 (8.59°). This difference in the out-of-plane angle calculated from the measured dislocation spacing by applying Frank's equation (Eq. 3.15) could indeed be an indication of the reduced validity of Eq. 3.15 to describe high-angle symmetrical tilt grain boundaries. As displayed in Fig. 4.15 (c), the periodicity of dislocation spacing in every ~3 dislocations might indicate the necessity to consider a decomposed periodicity at the grain boundary, which challenges the direct application of Eq. 3.15. Notably, the groove is localized in just about a 1 nm distance around the grain boundary, and the groove angle approaches to zero globally. This is better

visualized in the 3D perspective view presented in Fig. 4.15 (d), revealing the localization of the groove and near-zero global angle.

Comparison of the low-angle grain boundary shown in Fig. 4.13 with the high-angle grain boundary in Fig 4.15 marks the difference in the grooving behaviour of these valley type boundaries. Clearly, the local groove angle observed in the high-angle grain boundary approaches to a near-zero angle globally whereas the curvature of low-angle grain boundary has a wider extent. By geometry, this indicates that the extent (depth) of the inclination of the dislocation line within the film, or the depth of core-shifted boundary, is varied for grain boundaries of different misorientation angles. This requires further confirmation by computational modelling and/or TEM measurement of the core-shifted boundary.

4.4. Conclusion

In this chapter, the grain boundaries on the surface of well-annealed 50 nm thick NC Cu films are explored and their structuring on the surface is analysed using STM in UHV at room temperature. The NC Cu film is prepared by first removing the copper oxide using glacial acetic acid, followed by the thermal processing in UHV. TM-AFM, SEM and STM measurements were performed on the samples annealed up to 450℃. The AFM measurements on samples annealed at 400℃ revealed the formation of voids (holes) at the grain boundaries and triple junctions. Further annealing at 450℃ resulted in breakages due to the initiation of dewetting in the film surface. Detailed AFM measurement on these breakages showed circles of exposed substrate with central protrusions attributable to the formation of Cu_3Si due to interlayer diffusion, accompanied by the dewetting of Cu film.

The optimized annealing temperature range for enabling recovery and subsequent grain growth was determined as 350-380℃. The STM measurements on the NC Cu

film annealed at 380℃ revealed a clean Cu (111) surface with an optimized texture comprised of a rich variety of grain boundaries. Remarkably, the 3D perspective STM images showed a symmetrical out-of-plane tilting of grains about the boundary plane, parallel to the surface normal, which contributed to the surface roughness through the introduction of valleys and ridges over the film. A set of valley type grain boundaries as revealed by their STM topography images were selected for further analysis of out-of-plane rotation in the context of grain boundary restructuring phenomenon.

The grain boundaries were analysed in terms of their dislocation content and their geometry relationship which relates the degree of out-of-plane rotation φ, dislocation line inclination ψ, and the misorientation angle θ (for the minimum energy configuration inclination angle $\psi = 19.47°$). An approximate misorientation angle is calculated using Frank's formula, and experimentally measured dislocation spacing, which indicated low-angle ($\theta \cong 10.02°$ and $\theta \cong 12.6°$) and high-angle ($\theta \cong 23.7°$) grain boundaries. The measured groove angle was verified by the geometrical relationship for $\psi = 19.47°$, for each calculated misorientation angle.

In both low-angle and high-angle grain boundaries, the groove profiles across the stacking fault maxima indicated an average of 50-70 pm step on the Cu (111) surface, corresponding to the Shockley partials (70 pm). The distinction in the structure of the low-angle and high-angle grain boundaries is successfully defined in terms of the dislocation spacing, and also behaviour of the groove. In low-angle grain boundaries, the groove angle is found to extend wider, referred to as global angle, whereas high-angle grain boundaries revealed a localized groove, which tends to zero further from the boundary.

In this chapter, the unique perspective STM provides in examining the grain boundaries on surfaces of NC Cu films was successfully shown. The restructuring

phenomenon of grain boundaries by the out-of-plane grain rotation, previously only shown for a single boundary, was observed and analysed for various grain boundaries on our film, consistent with the existence of a ubiquitous grain boundary restructuring phenomenon. However, for the precise detection of the Burgers vector and for boundaries with complex periodicity, atomic resolution is needed, as well as computational modelling of the boundary for further confirmation.

On the other hand, it is to be noted that high-resolution STM measurement, particularly on the low index surfaces of noble metals with very small corrugations and interatomic distance such as Cu (111), is challenging mainly due to the high mobility of copper at room temperature. Hence, the investigation of the grain boundary fine structure in atomic resolution requires low-temperature STM measurements. In fact, the surface revealed dynamics around the steps and screw dislocations at room temperature, due to the high diffusion coefficient of copper, presumably also aided to some extent by the stimulation from the STM tip.

In the next chapter, we present the findings on a bicrystal comprised of a single engineered grain boundary with misorientation angle θ=13.17°, similar to that presented in Fig. 4.13. The grain boundary is investigated using STM, both at room temperature and low-temperature (77 K) and the atomic structure of the grain boundary is revealed, following a similar methodology to that described in this chapter, with further exploration of other grain boundary related phenomena.

5. Emergent Grain Boundary on Cu (111) Bicrystal

It is now established that NC thin films comprise a grain boundary-rich microstructure which can be further optimized upon thermal processing by the relaxation of defects and dislocations, and the excess energy associated with elastic distortion due to grain rotation. The high-temperature treatments that enable these processes may however result in Mullins grooving via diffusion - a highly effective mechanism in shaping the macroscopic structure of the grain boundary triple junctions. In nanocrystalline Cu thin films supported on substrates, high-temperature annealing can lead to detrimental processes such as void growth at triple junctions, which may eventually cause dewetting and breakages in the thin film.

Beyond these fundamental observations, as demonstrated in chapter 4, grain boundaries emerging at the surface of nanocrystalline Cu thin films on a Ta/Si substrate layer exhibit a restructuring of the grain boundaries to achieve low energy configurations manifested by an out-of-plane tilting of adjoining grains. This grain tilt results in the creation of valleys and ridges at the triple junctions where two grains meet at the surface, which is driven by the minimization of the dislocation core energy by the inclination of the dislocation core line. The out-of-plane grain rotation does not only result in an atomic scale surface roughness in nanocrystalline films, it also introduces an elastic stress field at the triple junction which is balanced by the depth of the restructuring of the dislocation cores within the film. For grain boundaries with different characteristics and dislocation contents, the level of restructuring was observed to vary. The manifestation of this effect on the surface was demonstrated by the relatively smaller degree of out-of-plane rotation in low-angle grain boundaries (LAGB), while high-angle grain boundaries (HAGB) rather

exhibit a larger out-of-plane rotation that is confined to a localized groove extending along the triple junction. Beneath the surface, the restructuring of the dislocation cores can extend from a few nanometres to much deeper within the film, so that this difference in the depth of subsurface restructuring demands a detailed consideration of the extent of the stress field[167]. In particular, in very thin films ($t \leq 20$ nm) in which the core-shifted (CS) boundary can extend throughout the film thickness, the interaction effects from substrate/film interfacial energy and strain field may be expected to be more pronounced.

In order to investigate the generality of the restructuring observed in nanocrystalline Cu thin films, a Cu bicrystal (BC) with an engineered grain boundary is studied using STM and the results are presented in this chapter. The bicrystal system with a single, macroscopically uniform grain boundary of misorientation angle 13.17° provides an ideal environment for the comparative study of the emergent grain boundary restructuring behaviour at the Cu (111) surface. Furthermore, the employment of a single grain boundary also allows for the accurate inspection of other grain boundary related phenomena, while eliminating the substrate/film interfacial stress and the complexity of the residual film stresses, and their influence on grain boundary development during thin film growth[140].

This chapter begins by providing a geometrical description of the bicrystal engineered grain boundary with 13.17° misorientation angle. The method for the specification of five macroscopic degrees of freedom is followed by defining the Rodrigues vector for the desired symmetric pure tilt rotation, as described in chapter 3, and the crystallography is described using median lattice[161]. Cu BC sample structure is briefly outlined and SEM and EBSD characterizations are presented, in section 5.1. In section 5.2, the initial large-scale UHV-STM analysis

of the general structure of the Cu bicrystal surface and the grain boundary are presented. *In situ* preparation of the sample in UHV is briefly explained, along with the presentation of the surface structure in the early stages of the preparation process, including the emergence of a distinctive structure with low levels of oxidation localized at the step edges and grain boundary. In section 5.2.1, the atomically clean Cu BC surface features and STS spectrum are shown. In this section, dynamic rearrangement of screw dislocations around the grain boundary is displayed, observed during room-temperature STM measurement. This is followed by the detailed STM analysis of the grain boundary structure and periodicity at low-temperature (77 K). Then, the out-of-plane grain tilt is measured in a similar fashion to that performed in section 4.5.2. The grain boundary structure is presented with atomic resolution, and the periodicity is confirmed with the crystallography on the Cu BC surface. Finally, the results of the MS simulation of the Cu BC 13.17° are presented.

5.1. Bicrystal geometry

The symmetrical tilt grain boundary design with a misorientation angle of 13.17°, tilt axis [111], mean boundary plane $(1\bar{1}0)$ and mean period vector $[\bar{1}\bar{1}2]$ is shown in Fig. 5.1. Here, the grains denoted as Grain 1 (black) and Grain 2 (white) are tilted by equal and opposite rotations of $\theta/2 \cong 6.85°$ about the [111] tilt axis. Upon proper rotation, as discussed in section 3.2.1, the construction of a grain boundary is defined by five macroscopic degrees of freedom, which reduces to two (for boundary plane) for symmetric tilt boundaries[161,254].

The periodicity of the grain boundary can be defined by the boundary period vectors along the boundary plane, $\boldsymbol{p}'$ and $\boldsymbol{p}$, and the boundary normal vectors in each grain, $\boldsymbol{n}'$ and $\boldsymbol{n}$ for Grain 1 and Grain 2, respectively. Following the median

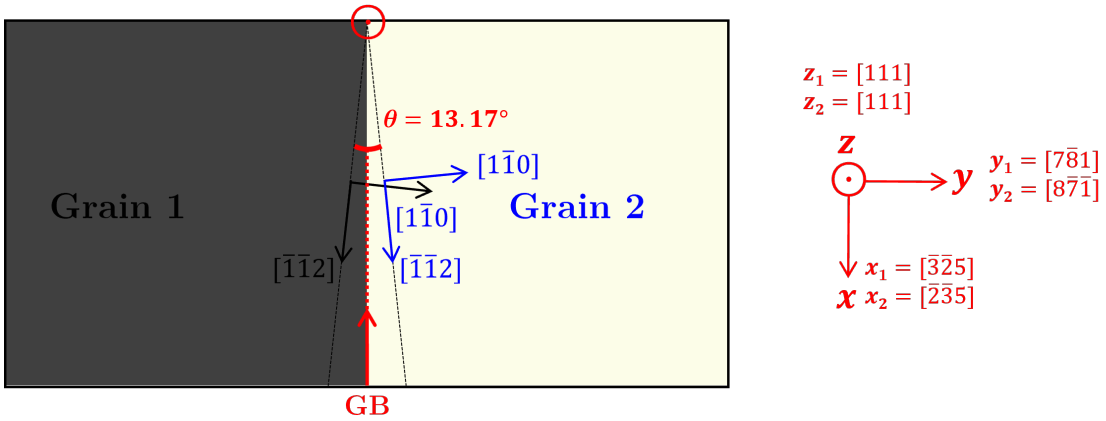

Figure 5.1: Schematic of Cu BC geometry. Symmetric tilt grain boundary with mean boundary plane (1$\bar{1}$0), mean period vector [$\bar{1}\bar{1}$2], and misorientation angle θ=13.17° is constructed upon equal and opposite rotation of Grain 1 and Grain 2 by $\pm\theta/2$, about [111]. On the right panel, the crystallography of each grain is expressed in the coordinate system of grain boundary (median lattice), boundary normals $\boldsymbol{n}'$ and $\boldsymbol{n}$ and period vectors $\boldsymbol{p}'$ and $\boldsymbol{p}$.

lattice methodology explained in chapter 3, to identify the boundary normal vectors, we first define the boundary plane normal $\boldsymbol{N} = [1\bar{1}0]$, and the Rodrigues vector (Eq. 3.12) as $\boldsymbol{\rho}^R = \hat{\boldsymbol{\rho}} \tan\theta/2 = 1/\sqrt{3}\ [111]\ 0.115$ where $\theta = 13.17°$. Using Eq. 3.11, the boundary normal vectors are obtained as $\boldsymbol{n}' = [7\bar{8}1]$ and $\boldsymbol{n} = [8\bar{7}\bar{1}]$. Consequently, the boundary period vectors are obtained as $\boldsymbol{p}' = \boldsymbol{n}' \times [111] = [7\bar{8}1] \times [111] = [\bar{3}\bar{2}5]$ for Grain 1 and similarly $\boldsymbol{p} = \boldsymbol{n} \times [111] = [8\bar{7}\bar{1}] \times [111] = [\bar{2}\bar{3}5]$ for Grain 2, as shown in the right panel of Fig. 5.1.

The Cu BC is prepared by MaTeck GmbH based on our design. The 0.6 mm thick BC sample of dimensions 7×3 mm^2 comprises a single boundary, approximately at the centre of the sample. The sample is polished on one side with a roughness <0.01 μm and the orientation accuracy is <0.1°. The Cu BC, the geometry of which is explained above, is studied by STM and the results are shown.

The SEM image of a region in the centre of the Cu BC shows the macroscopically continuous GB located in the middle of the sample revealing the facets of two grains

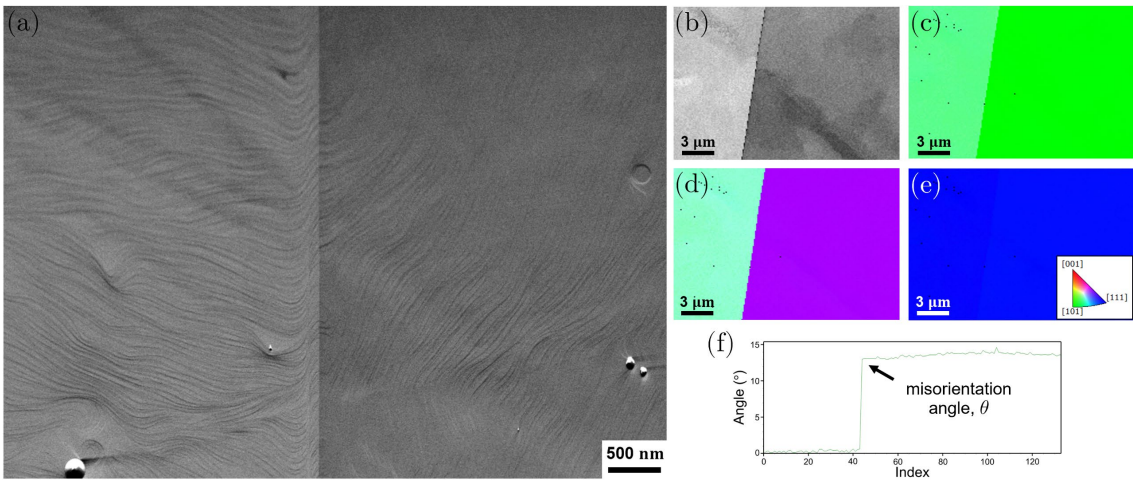

Figure 5.2: SEM and EBSD analysis of Cu BC surface. (a) SEM image of the bicrystal with two grains on either side of the grain boundary (b) EBSD pattern quality map shows the continuous and clean structure of two grains and the grain boundary as dark line in between them. (c) inverse pole figure x-map, (d) inverse pole figure y-map and (e) inverse pole figure z-map of the same area in (b). (e) shows the [111] texture of both grains as indicated by the colour map (d) the misorientation tilt angle $\theta \approx 13°$ as measured by the disorientation angle frequency distribution.

on either side, as shown in Fig. 5.2 (a). To the immediate left of the boundary, it is possible to trace the high level of facets parallel to the grain boundary. This shows the macroscopic thermal groove in which the boundary is accommodated, as also observed in the large scale STM results. Fig. 5.2 (b)-(d) shows the EBSD analysis of the Cu BC sample. The pattern quality map illustrated in Fig. 5.2 (b) reveals the structure of two continuous grains on either side of the grain boundary (dark line across the middle of the image) with no significant damage to the surface structure. The inverse pole figure z-map displays the uniform [111] texture of both grains, as indicated by the colour code. The misorientation angle θ~13° between two grains is confirmed by the disorientation angle frequency distribution, as shown in Fig. 5.2 (d).

5.2. STM results on Cu bicrystal emergent grain boundary

The bicrystal is transferred into the UHV chamber for *in situ* preparation to obtain

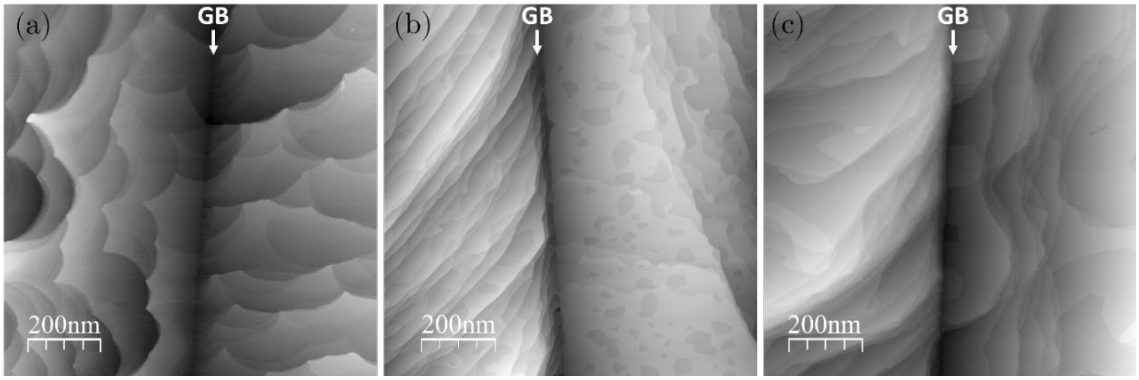

Figure 5.3: STM topography images of 1x1 um^2 areas of Cu BC showing evolution of macroscopic step morphology in the vicinity of the grain boundary. (a) after initial cycles of Ar^+ ion sputtering and annealing at ≈450℃ showing pinned steps with Rq=1.42 nm (b) after further *in situ* treatment cycles surface reveals increased bunching of steps and formation of vacancy islands resulting in Rq=1.58 nm (c) steps upon further sputtering/annealing display rounded edges and surface shows a significant reduction in the vacancy island density, resulting in Rq=1.14 nm. Imaging conditions: (a) 50 pA, -0.2 V (b) 23 pA, 0.2 V (c) 22 pA, 0.2 V.

an atomically clean surface. Cu BC is prepared in the UHV preparation chamber by subsequent cycles of Ar^+ ion sputtering and annealing to approximately 450℃, in a similar fashion to that performed for NC Cu thin films. Then, the sample is transferred to the STM chamber for analysis.

A series of the large-scale RT-STM topography images of Cu BC is shown in Fig. 5.3. The STM images of the Cu BC surface at different stages of *in situ* preparation cycles reveal a high density of steps across either side of the boundary indicating a twist mismatch between the two grains. The step morphologies in these three images in Fig. 5.3 show slight differences. The 1×1 μm^2 STM topography at initial stages in the sputtering/annealing cycles shown in Fig. 5.3 (a) reveals pinned steps at the edges with large terraces, displaying an RMS surface roughness of Rq=1.42 nm. The same scale image in Fig. 5.3 (b) obtained after further cycles of sputtering/annealing shows an increased bunching of steps as well as vacancy islands, resulting in Rq=1.58 nm. Fig. 5.3 (c) shows the STM topography image of the Cu BC surface after further *in situ* treatment resulting in a step structure with

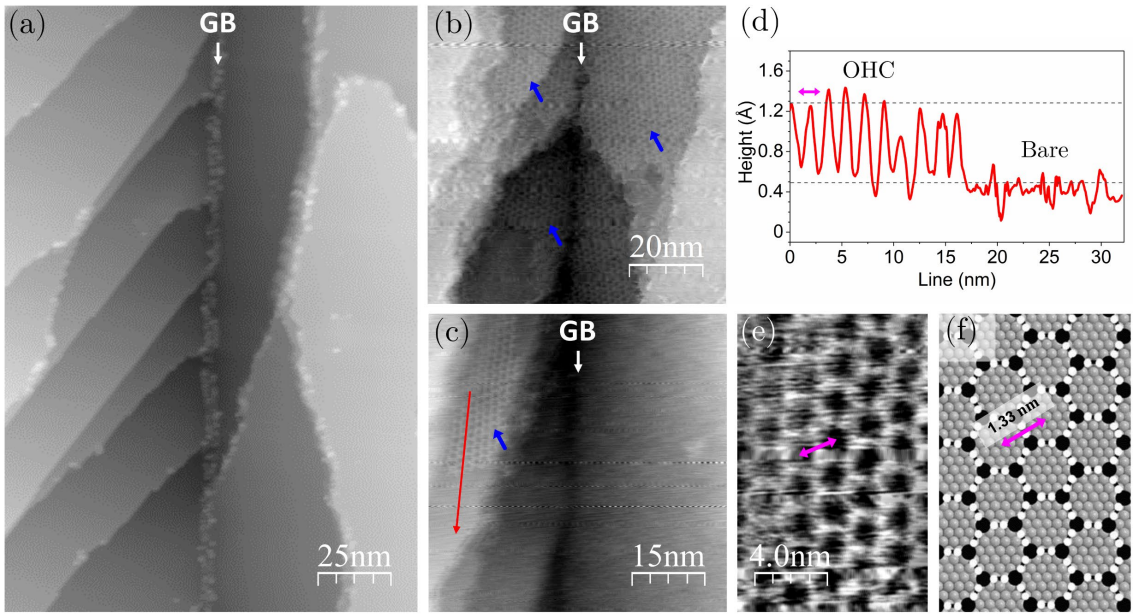

Figure 5.4: Localized contamination of Cu BC surface recorded at 298 K. (a) STM topography image showing the localization of contamination on the step edges and grain boundary. (b) close view STM topography image of Cu BC surface, showing the contamination in areas indicated by blue arrows, surrounding the grain boundary and nearby terraces. (c) close view STM topography image of the partially contaminated terrace indicated by the blue arrow, in the immediate vicinity of the grain boundary. A line profile obtained from the contamination down to the bare surface is shown in (d). Details of the contamination reveals a 2D open honeycomb pattern (OHC) as shown in (e), and the simulation model in (f), proposed by Matencio et al.[109]. Imaging conditions (a) 23 pA, 2 V (b) 22 pA, 0.4 V (c)-(e) 31 pA, 0.2 V.

rounded edges, and reduced vacancy islands, with Rq=1.14 nm. Notably, the density of the steps on either side of the boundary shows small variations along the boundary.

As explained above, the procedure for preparing the surface to an atomically clean state consisted of repeated cycles of Ar^+ ion sputtering and annealing. After every 5-7 cycles, the sample was transferred to the STM chamber and the surface morphology, step edges, interlayer distance (step height) and cleanliness of the grain boundary were analysed by STM topography as well as scanning tunneling spectroscopy (STS) measurements, and the cycles were repeated until eventually an atomically clean surface was achieved.

At early stages, traces of contaminations were found on the Cu BC surface. Remarkably, these were observed to be localized at the defect sites such as step edges and, in particular, at the grain boundary. In Fig. 5.4 (a), for instance, the grain boundary in the middle of the image denoted by the white arrow is almost fully covered by the contaminants, observed as bright protrusions, and the steps are only partially covered at the edges. Fig. 5.4 (b) shows a close view STM topography of the grain boundary, and the steps in its immediate vicinity that are covered by a layer that is distinguishable from the bare surface, measured at room temperature. Moving along the grain boundary, the layer was observed to be localized around the boundary and nearby steps, and comprised of an ordered 2D hexagonal structure, as shown in Fig. 5.4 (c). The line profile, shown in 5.4 (d), which crosses the over layer and the bare surface on the copper terrace in Fig. 5.4 (c), corresponds to a height corrugation difference of ≈0.7 Å, and a lattice periodicity of ≈1.6 nm as indicated in the zoomed in view in Fig. 5.4 (e).

A similar 2D layer structure was recently reported by Matencio et al., representing a novel open honeycomb (OHC) model for Cu_3O copper oxide phase[109]. The OHC framework was reported to coexist with several other distinct types of copper oxides including the well-ordered long-range Cu_2O (111)-like '44' and '29' structures with distorted hexagonal symmetry[112,113], and the short-range 5-7 defective phase of honeycomb layer[310]. The OHC layer structure is distinguishable from these other structures by its lower-oxygen content visualized as hollow sites, and its large lattice periodicity ≈1.33 nm (Fig. 5.4 (f)).

The 2D hexagonal honeycomb pattern observed in Fig. 5.4 (e) is clearly distinguished from the other well-ordered phases of Cu_xO possessing a much smaller lattice constant of ≈ 0.6 nm, and O atoms located on six-fold symmetry sites. Based on the measured close lattice constant (≈1.6 nm) of hollow sites of hexagons in Fig.

5.4 (e), representing missing O sites, we attribute this pattern to the novel OHC copper oxide model, despite the difficulty in resolving individual atomic sites at room temperature.

It is well established in the literature that the ordered structures of copper oxides observed on Cu (111) are formed by a transition from a disordered surface oxide to ordered structures upon annealing in O_2 or air at high temperatures, or directly by O_2 exposure of Cu (111) at high temperatures[106–108,311,312]. That being said, there could be two possible explanations for the formation of these low-oxygen-content 2D OHC structures in our observations. Firstly, due to the presence of a very small leak of ambient air into the gas line that is used for argon sputtering, which might have led to the formation of this low oxygen content copper oxide phase. However, the gas line was flushed through and refilled with Ar, prior to each *in situ* preparation session, and no significant levels of the constituent gases (H_2O, O_2, O, N_2, N) from ambient air were detected in the residual gas analysis spectrum acquired during the preparation process. Secondly, due to high temperature annealing in UHV, a disordered copper oxide layer that was formed (in air) prior to the sample transfer might have transitioned into an ordered low-oxygen-content structure, forming the OHC pattern. Alternatively, considering the high diffusion constant at the grain boundaries, potential pathways of diffusion, the oxide within the bulk could have diffused through the GB, upon sputtering and annealing[116].

Crucially, the selective partial coverage of the Cu (111) surface at localized defect sites *i.e.*, step edges and the grain boundary, clearly demonstrates the high reactivity of these sites. This is expected since grain boundaries, which possess a significantly higher degree of disorder and an associated excess energy compared to copper surface atoms at (111) terraces, are the preferred nucleation sites for surface reactions.

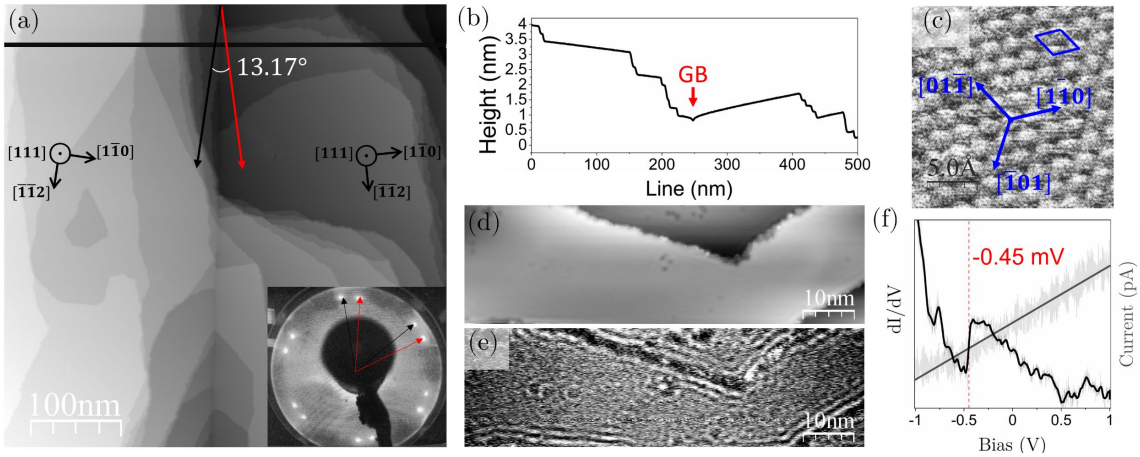

Figure 5.5: STM measurements on the clean Cu BC surface recorded at 77 K (a) STM topography of clean Cu BC surface shows the straight grain boundary. Inset shows the LEED pattern obtained from grain boundary region at an energy of E=56 eV, illustrating two hexagonal patterns rotated by $\theta \approx 13°$ (b) steps and the macroscopic groove of grain boundary is shown in the line profile obtained on (a). (c) atomic resolution surface structure and close-packed directions (d) STM topography and (e) differential conductance dI/dV map of the area in (d). (f) dI/dV - STS showing the characteristic sharp decrease of the Cu (111) LDOS, at -0.45 eV. Imaging conditions: (a) 22 pA, -1 V (c) 3 nA, -10 mV (d) 100 pA, -0.1 V (e) 100 pA, -0.1 V, 10 mV, 961 Hz (f) 50 pA, 1 V, $V_{p\text{-}p}$: 50 mV, 961 Hz.

5.2.1. Clean Cu (111) bicrystal surface

Figure 5.5 (a) shows the LT-STM topography image of atomically clean Cu (111) surface with monatomic steps with heights of 0.21 nm, along with the grain boundary located in the centre of the macroscopic thermal groove. The cross section in Fig. 5.5 (b) shows the presence of step bunching close to the boundary. The surface cleanliness of Cu (111) was confirmed by the LEED pattern presented in the inset of Fig 5.5 (a), obtained by targeting the grain boundary region, at an energy of E=56 eV. The LEED pattern shows two hexagons with diffraction spots of 6-fold symmetry shifted by approximately 13°, corresponding to the two misoriented grains.

The Shockley-type surface states of the free-electron-like Cu (111) results in electron scattering from defects such as step edges, point defects or vacancy or adsorbed atom sites as clearly observed in the differential conductance map in Fig.

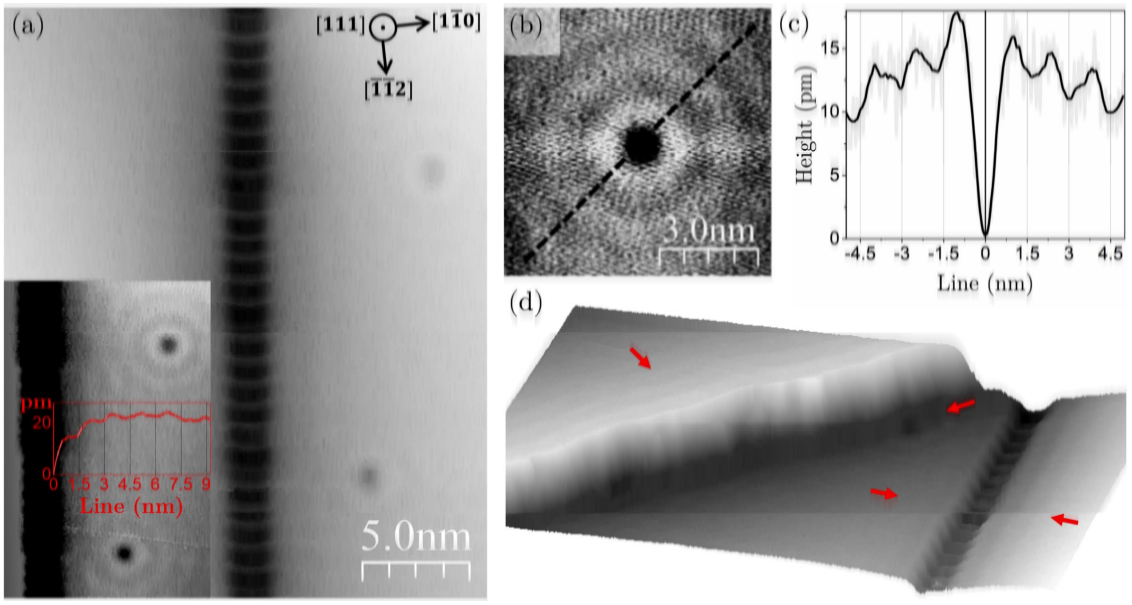

Figure 5.6: Standing waves on Cu BC surface in the vicinity of the grain boundary (a) STM topography image of the grain boundary array of edge dislocations showing the nearby point defects. Inset shows (a) with increased contrast. Line profile shows the standing wave oscillations in the corrugation amplitude in every 1.5 nm. (b) close view STM topography of one point defect cropped from (a), showing the concentric rings. (c) line profile obtained across the point defect in (b) shows the oscillations with 1.5 nm period, emanating from the centre of the point defect. (d) 3D view of the surface showing the standing waves emanating from the step edge, the point defect and the grain boundary, indicated by the red arrows. Imaging conditions: (a)-(b)-(d) 21 pA, -0.01 V.

5.5 (e), which corresponds to STM imaged area shown in Fig. 5.5 (d). In Fig. 5.5 (f), dI/dV STS measurement on defect-free regions of clean Cu (111) terrace shows the onset of the surface state as a sharp decrease in the local density of states (LDOS) at -0.45 eV (below Fermi level) referred to as the band edge of copper[304,305]. The atomic scale STM topography in Fig. 5.5 (c) shows the atomic structure of clean Cu (111) surface and a nearest neighbour distance of $a/\sqrt{2} = 2.55$ Å measured along the identified $\langle 110 \rangle$ close-packing directions.

The aforementioned surface states due to standing waves of scattered electrons are also observed in STM topography channel as oscillations localized around step edges or point defects, acquired with low sample bias of V_b=-10 mV as shown in Fig. 5.6 (a). Here, the closeup STM image reveals the grain boundary comprising an array

of edge dislocations, the atomic structure of which will be discussed in detail in the next section. The two nearby defects, despite the lack of clarity as to the source of these, may be due to adsorbates, *i.e.* water or CO, or to groups of missing Cu atoms[305,313,314]. Their presence represents a measure of the contamination level of the copper surface.

The standing waves of concentric rings from individual defects as shown in the cross section in Fig. 5.6 (b) exhibit a period of 1.5 nm, and decrease in amplitude with increasing distance from the point defect. This period is determined by the Fermi wave vector (described in section 2.1.1) as $2k_{\mathrm{F}}$, that is characteristic of the energy band structure of Cu (111), and observed as $\lambda_{\mathrm{F}} = \pi/k_{\mathrm{F}}$ in STM[315,316]. According to Crommie et al., these changes in the height corrugation amplitude, in case of such low biases and the small tip z-position variations, can be regarded to be in direct correlation with the perturbations in the LDOS at Fermi level[190].

As visualized in the 3D view in Fig. 5.6 (d), similarly, the electronic surface states are observed around the point defect, near the step edge, and also parallel to the grain boundary. These spatial oscillations near the boundary are observed as local depressions in the height corrugation at every 1.5 nm, reducing with increasing distance from the boundary core, as seen in the cross section (Fig. 5.6 (a)-inset) obtained just near the grain boundary, in a manner identical to that for the point defect in Fig 5.6 (b-c).

5.2.2. STM measurement on emergent grain boundary in nanoscale

So far, the grain boundary geometry is described within the median lattice concept and the crystallography of the two grains are defined. The fundamental topographic and electronic characteristics of clean Cu (111) surface are explained along with a detailed description of the grain boundary on the Cu BC surface.

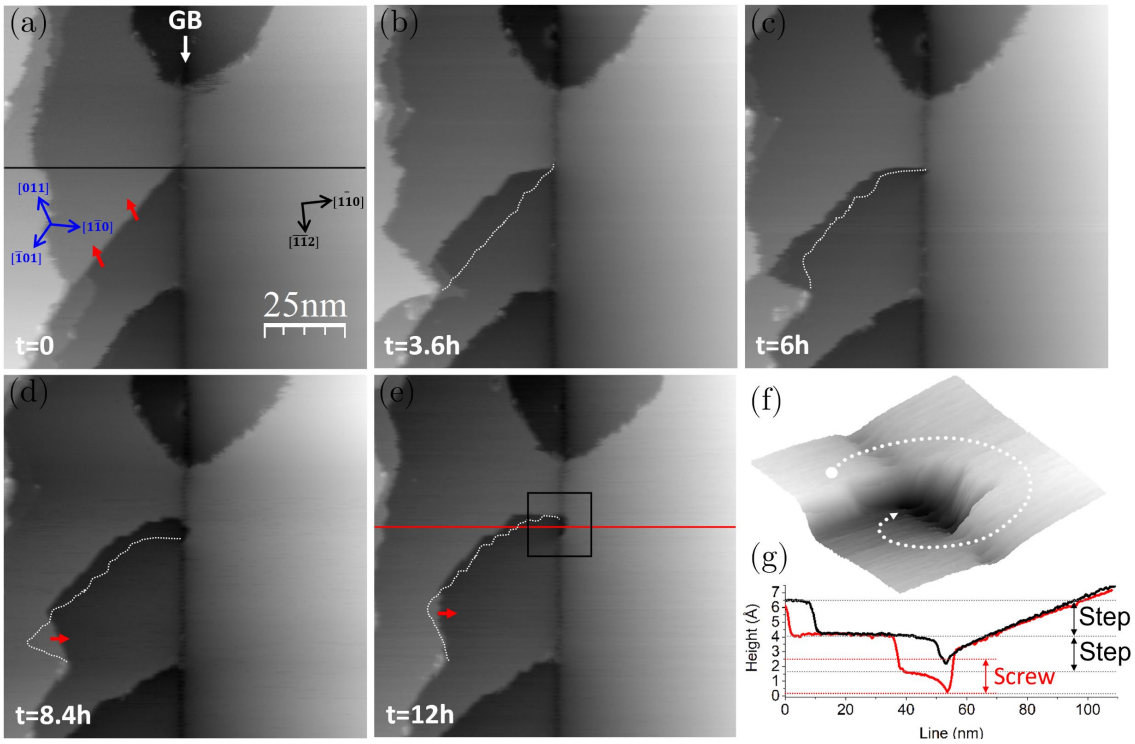

Figure 5.7: STM topography images showing the screw dislocation dynamics across the grain boundary, obtained at room-temperature (293 K) (a) Initial configuration of the surface. The motion of the step is indicated by red arrows (b)-(c) stages in surface readjustment towards nucleation of screw dislocation shown in (d). (e) final configuration of surface showing the screw dislocation formed on Grain 2. (f) 3D view of the region marked by the box in (e), showing the helical path created by the screw dislocation (g) line profile obtained across the grain boundary, marked by the red line in (e) shows the evolution of a ~2.1 Å depression due to screw dislocation. Previous position of the step is marked by dashed white line, in each STM image. Imaging conditions: (a)-(e) 23 pA, 0.5 V.

The accommodation of the emergent grain boundary on the surface, specifically the twist component (rotation axis $[1\bar{1}0]$) in this Cu BC sample, requires the relaxation of the associated strain, which manifests as screw dislocations. As will be shown throughout this chapter, screw dislocations are frequently observed along the boundary. At room temperature, the rearrangement of unstable steps and screw dislocations searching for more stable configurations can be observed dynamically using STM. This mechanism, which occurs via thermally activated rearrangement of non-equilibrium steps emanating from the grain boundary – screw dislocations – can be observed dynamically in the STM topography images.

An example of one such rearrangement is presented in Fig. 5.7 in the sequential room temperature STM topography images obtained over a total of ~12 hour time scale, where each image required about 1.2 hours to record. Time stamps are displayed on each image, and the intermediate stages are detailed in the Appendix A. 1. The previous position of the step relative to each image is marked by the dashed white lines. To the left of the grain boundary (Grain 1), initially there are two monatomic height steps forming as screw dislocations emanating from the boundary (Fig. 5.7 (a)). In the following images, the step denoted by the red arrows in Fig. 5.7 (a) rearranges in a series of new configurations and eventually crosses the grain boundary, forming a helix (Fig. 5.7 (e)).

At the initial stages (Fig. 5.7 (a)-(c)), the reconfiguration process begins with the movement of the initially straight step edge towards [011] (Fig. 5.7 (a)) and the total step edge length is increased by zig-zags positioning along ⟨110⟩ direction. Here, the step edges are arranged to lie along stable configurations, and a distinction between smooth (and stable) segments along ⟨110⟩ direction and frizzy edges is observed. This process of step adjustment takes about 6 hours, until the screw dislocation passes beyond the grain boundary. From Fig. 5.7 (c) to Fig 5.7 (d), the step movement reverses locally (red arrows) towards where it is pinned, and once the screw dislocation (partial) passes the grain boundary, it creates a depression on the right of boundary (Grain 2), connecting the upper terrace with the lower terrace. Later, the range of motion reduces significantly, and only small-scale adjustments are observed at the step edges. As shown in Fig. 5.7 (f), the overall path of displacement follows a helicoid, a characteristic of screw dislocation, and creates a monatomic step.

The formation mechanism of dislocations in fcc metals was previously explained in chapter 3, in terms of the dissociation of a perfect dislocation into Shockley partials,

by Frank's energy criterion (Eq. 3.6). Each of the edge dislocations forming the array that builds the grain boundary are in the form of Shockley partials by dissociation of $a/2[1\bar{1}0] \rightarrow a/6[2\bar{1}1] + a/6[1\bar{2}\bar{1}]$, on (111) surface. Similarly, the formation of a screw dislocation occurs by the dissociation of $a/2[110] \rightarrow a/6[211] + a/6[12\bar{1}]$[277,317].

The combined effect of the high diffusion coefficient of copper with the presence of high energy sites (e.g. steps) leads to the appearance of frizzy edges at monatomic steps, due to the increased mobility of kinks at room temperature[308] . As the screw dislocations emerge from the grain boundary, a reduced monatomic step height is observed at the segment nearest the boundary. The edges of these segments, as they adjust to lie along $\langle 110 \rangle$ directions, possess a smoother texture even at room temperature, as they represent stable bulk defects[318]. As shown in Fig. 5.7, these smooth edges at the segments with reduced step height are observed where the screw dislocation merges with the boundary.

The observation of large scale dynamics on Cu (111) surface in the vicinity of unstable sites, a significant example being the grain boundary, occurs very often during STM imaging of the surface at room temperature and more examples are provided in the Appendix (A. 2-A. 3-A. 4). In general, these dynamics were observed to continue until some kind of metastable equilibrium was established.

The mechanisms resulting from the dislocation-grain boundary interaction, such as dislocation adsorption or dissociation at the boundary, are reported to be dependent on the energetic stability of the grain boundary[319]. The structural and energetic stability of the grain boundaries is achieved through several types of relaxation mechanisms. These may include local atomic rearrangements, rigid-body transformations, or boundary dissociation by formation of stacking faults through nucleation and emission of partial dislocations[320]. All of these mechanisms depend

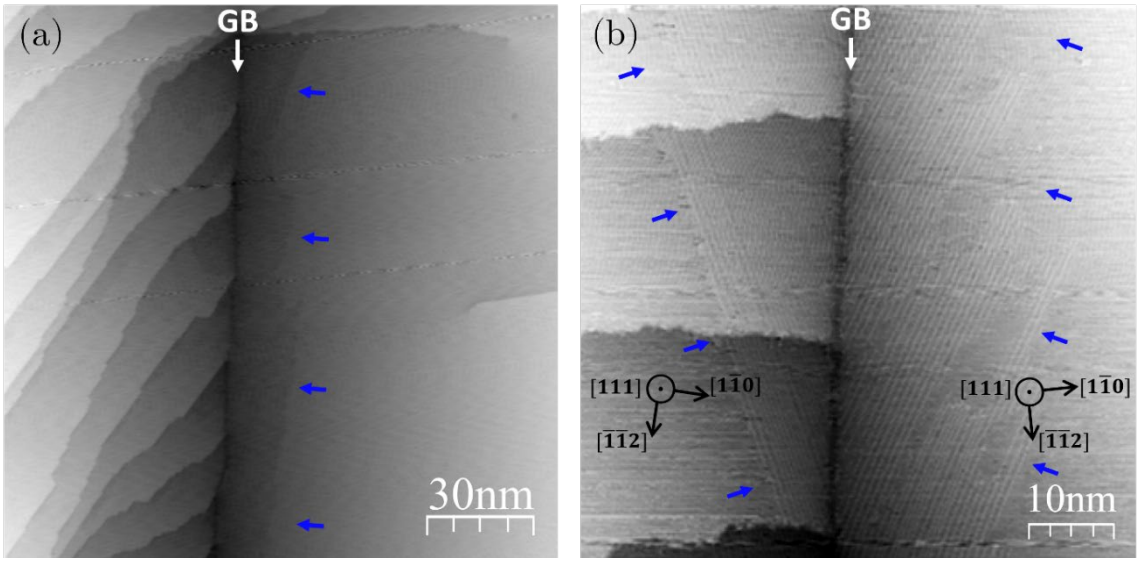

Figure 5.8: STM topography images showing the dislocation pattern emanating from the grain boundary. (a) 200×200 nm^2 STM topography shows the distinct contrast difference along the boundary, indicated by the blue arrows near the boundary. (b) close view 60×60 nm^2 STM topography shows the detail of regions marked in (a), comprised of bright stripes emanating from the boundary, symmetrically, marked by blue arrows. Imaging conditions: (a) 50 pA, 0.2 V, (b) 50 pA, -50 mV.

on grain boundary characteristics; geometry and energy; as well as the properties of the material, such as stacking fault energy, interatomic interactions or resolved shear stress (in nanocrystalline materials)[321].

The relaxation, shown above in Fig. 5.7, manifested as reconfiguration of screw dislocations near the grain boundary is an indication of the level of excess stress present in the sputtered and annealed bicrystal. Interestingly, in the absence of such large-scale dynamics near the boundary, STM images recorded at room temperature reveal a different phase along the grain boundary, as shown in Fig 5.8 (a). The close-up view STM image of these regions, presented in Fig 5.8 (b), displays a pattern of stripes emanating from the grain boundary. The in-plane angle of the stripes with respect to the boundary is arranged so that the stripes lie along the ⟨110⟩ close-packed directions on both sides of the boundary, corresponding to the preferential slip directions for edge dislocations on (111) slip plane on both grains. These stripes form a fishbone-like pattern, generated by the emission of dislocations,

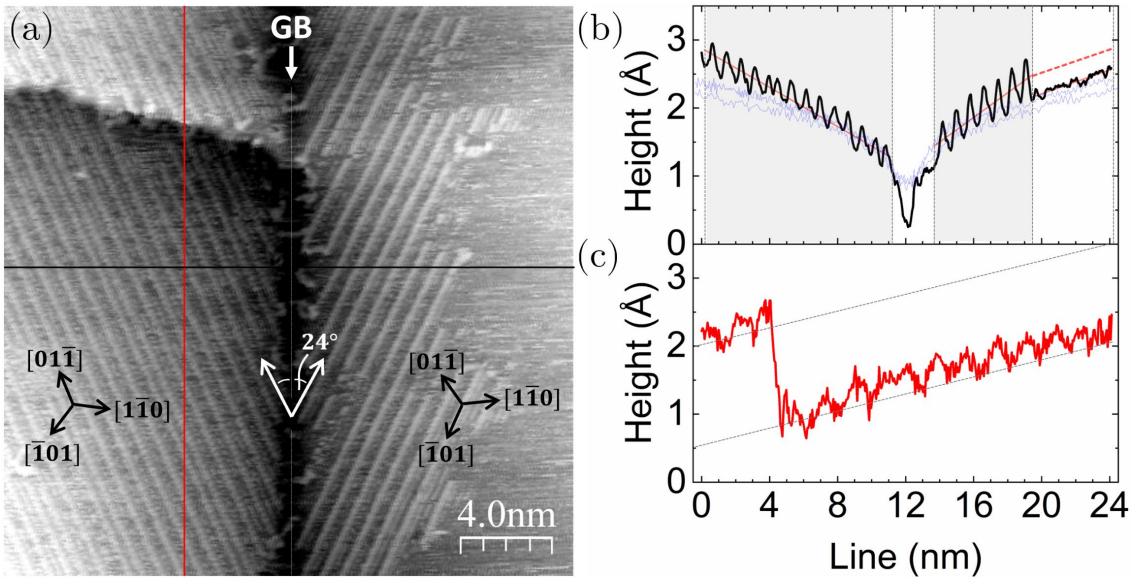

Figure 5.9: Dislocation pattern near grain boundary and the corresponding cross sections (a) STM topography image showing the dislocation stripes emanating from the grain boundary with ~24° in-plane angle, positioned along close-packed $[01\bar{1}]$ and $[10\bar{1}]$, in Grain 1 and Grain 2. These close-packed slip directions on (111) slip plane are shown on both grains. Cross-sections (b) across and (c) along the boundary shows the periodic increases in corrugation amplitude due to protrusions of dislocations. The linear fit of each region is indicated by dashed red lines on each region. (c) shows dislocation stripes extending over a step. (a) Imaging conditions: (a) 50 pA, -50 mV.

presumably to lower the energy within or near the grain boundary.

Notably, the horizontal extent of the dislocation stripes is not uniform on either side of the boundary and it is observed to extend further in the absence of steps, or other defects, which act as barriers. The maximum horizontal distance that the dislocation stripes extend on either grain measured on this particular bicrystal θ=13.17° is ~28 nm, whereas on another Cu bicrystal with a high-angle [111] (θ=26.01°) tilt grain boundary (provided in Appendix A. 6), it was found to be confined to ~10 nm. Fig. 5.9 (a) shows in more detail the arrangement of these dislocation stripes emanating from the boundary. The in-plane angle measured between the stripes and the grain boundary on both side of the boundary is ~ ± 24°. On Grain 1, the dislocation stripes extend over a screw dislocation step, which reveals a slightly reduced monatomic step height of ~1.6 Å as it emerges from the

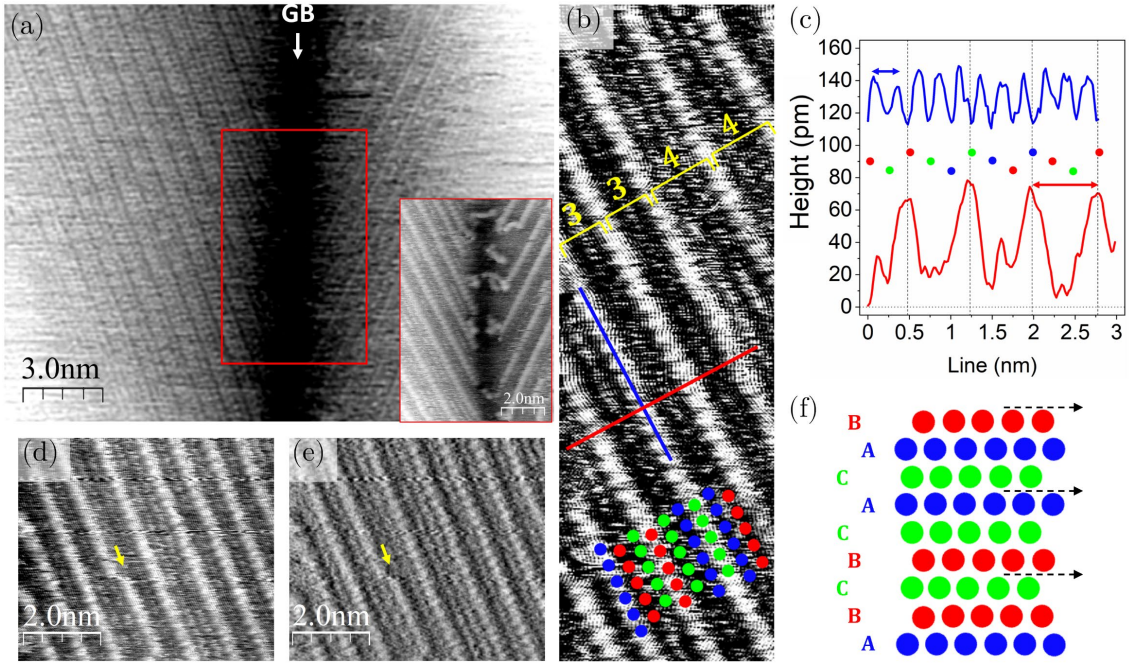

Figure 5.10: STM topography images showing the 9R-like metastable phase formation near the grain boundary (a) with increased contrast for enhanced visualization of the structure near the boundary, inset shows the area marked by the red box in (a). (b) atomic resolution shows the Cu (111) nearest neighbour distance periodicity along the dislocation stripes and periodic protrusions (bright) of dislocation stripes in every 3 atomic planes, illustrated by the blue line andthe red line in (c), respectively. (d) STM topography and corresponding (e) current error channel showing regions of distorted 9R, marked by yellow arrows. (f) schematic of 9R phase shows the partial dislocations (dashed arrows) in every 3 {111} planes. Imaging conditions: (a)-(a) inset-(b)-(d)-(e): 50 pA, -50 mV.

boundary as shown in Fig. 5.9 (c), whereas on Grain 2, they terminate at about 8 nm from the boundary.

The line profile measured across the grain boundary reveals the periodic increases in the corrugation amplitude, corresponding to the dislocation stripes in the shaded regions in Fig. 5.9 (b). Line profiles of the well-annealed and fully relaxed Cu bicrystal grain boundary groove, as measured on low-temperature STM topography images that do not display the dislocation stripes, are provided as reference (blue curves) in the plot. Note the surface planes of dislocation networks are tilted away from the bare (111) plane, as illustrated by the dashed red lines of individual linear fits on each segment in Fig. 5.9 (b), which presumably occurs in order to

accommodate the compressive stress associated with these regions as they emerge on the (111) surface, continuing the close-packed layers. Both the frizzy appearance of the bare surface, and the local shifts in the periodicity of dislocation protrusions - which will be discussed in detail shortly - indicate the level of mobility on the surface at room temperature, as copper atoms migrate to low-energy thermal equilibrium configurations.

Further inspection of these regions reveals the periodicity of this phase in greater detail, as shown in Fig. 5.10. The line profile measured along the dislocation stripes as shown in Fig. 5.10 (b) reveals a spacing of 2.55 Å, corresponding to the periodicity of Cu (111) surface. Remarkably, the ~70 pm corrugation amplitude increase in every ~0.76 nm, as shown in the line profile measured perpendicular to dislocation stripes, reveals a periodicity of 3 interatomic distances corresponding to 3 {111} planes emerging on the surface, forming a pattern similar to the commonly demonstrated microstructure of the 9R phase.

The 9R phase was observed both by experimental and computational studies of the relaxation mechanisms and structural stability of grain boundaries. It is formed by the introduction of an intrinsic stacking fault in every third close-packed {111} plane in a total of 9 repeating atomic planes, resulting in the transition from the perfect $ABC/ABC/ABC$ fcc stacking to $ABC/BCA/CAB$. This stacking arrangement is illustrated in Fig. 5.10 (f).

The 9R phase is a metastable phase formed by the emission of Shockley partial dislocations in low stacking fault energy fcc metals. So far, thin 9R slabs of a few nanometres have been observed to accompany the grain boundary relaxation by dissociation, mostly at the Σ3 incoherent twin boundaries in Au[322,323], Cu [324–326] and Ag[327,328]. Experimental studies have also provided proof of shear deformation-induced formation of wider 9R phases accompanying heterophase interphases[329], or

twinning in single crystal fcc metals, extending to tens of nanometres[330–332].

As will be shown later by the STM measurements at low-temperature, the well-annealed (fully-relaxed) θ=13.17° emergent grain boundary shows no evidence of 9R formation. Therefore, the generation of a metastable polytype phase observed near the emergent grain boundaries in copper bicrystals at room temperature is predicted to be due to the relaxation of the grain boundary by emission of Shockley partial dislocation loops, mediated by the high density of mobile defects, and driven by the intrinsic elastic stresses in the grain boundary. Notably, in the bicrystal, the residual stresses from the film growth process, thickness and grain size effects, film-substrate thermal expansion incompatibility and interfacial energy are eliminated and so the likely origin of this stress is from local boundary restructuring phenomenon that characterizes these emergent boundaries. The 9R phase was also routinely observed in room temperature STM images of nanocrystalline Cu (111) films.

The sensitivity of the observed phase to the local variations of elastic stress field manifests as the distortions in the 9R periodicity through shifts to 12R, and possibly to other unidentified polytype phases, as shown in Fig. 5.10 (d) and Fig. 5.10 (e). These observations agree with the literature, where the demonstrated effect of the shear strain results in expansion or distortions in the 9R phase[325,333–335]. Furthermore, small thermal fluctuations are also considered to trigger these distortions by facilitating the slip of dislocations during scanning. Occasionally, dislocation stripes were observed to change to another slip direction on (111) slip system, by 120° rotations with respect to their initial orientation, yet this was not captured dynamically.

As shown in the section that follows, the well-annealed fully-relaxed grain boundary does not reveal the formation of such metastable phases near the boundary. This

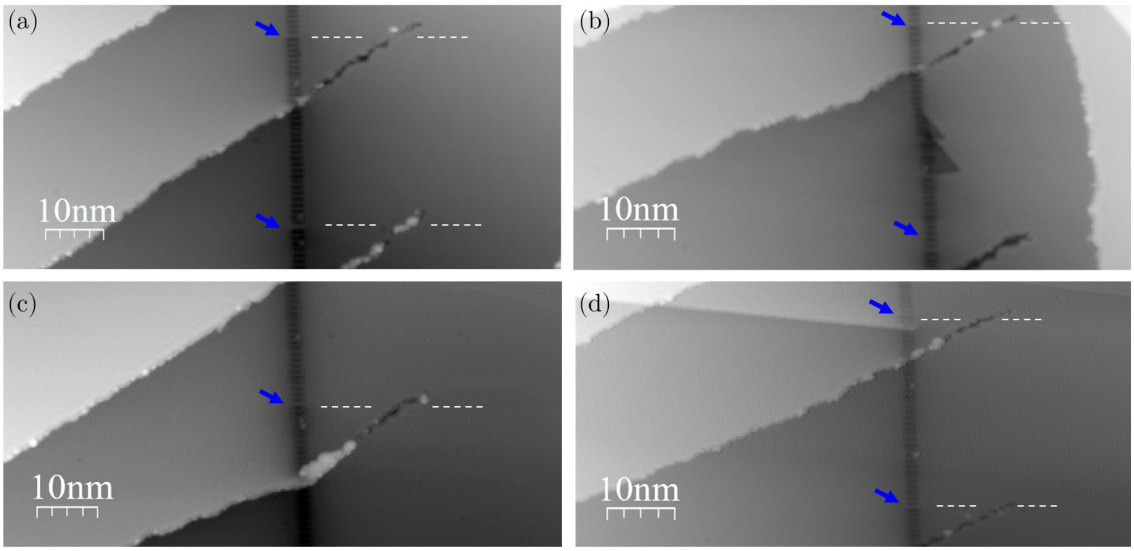

Figure 5.11: STM topography images obtained at low-temperature (77 K) showing the regions of screw dislocations crossing the grain boundary. Blue arrows indicate the local distortions at the edge dislocation as indicated by high corrugation amplitude, induced by the pinned screw dislocation on Grain 2. Imaging conditions: (a)-(d) 20 pA, -0.01 V.

demonstrates the effect of annealing to further relax defects within or near the boundary, to reduce the intrinsic stacking faults and the elastic stress associated with these. Although these observations fit well with the structural and stress-induced description of 9R/12R polytypes, to clarify the subsurface partial dislocation emission mechanism that leads to these metastable phases in [111] tilt emergent grain boundaries and its interaction with the core-shifted boundary, molecular dynamics simulations are necessary.

The effects of the boundary twist are also manifested at low-temperature. In Fig. 5.11, a series of STM topography images obtained from different regions along the boundary demonstrate the influence of screw dislocations on the grain boundary structure at the nanoscale. Here, the screw dislocations are pinned at the grain boundary, but their trace extends across the boundary for about 20 nm, towards Grain 2. As explained previously, screw dislocations are observed along the boundary to relax the high elastic strain due to the twist component of the bicrystal and to accommodate the mismatch between two grains.

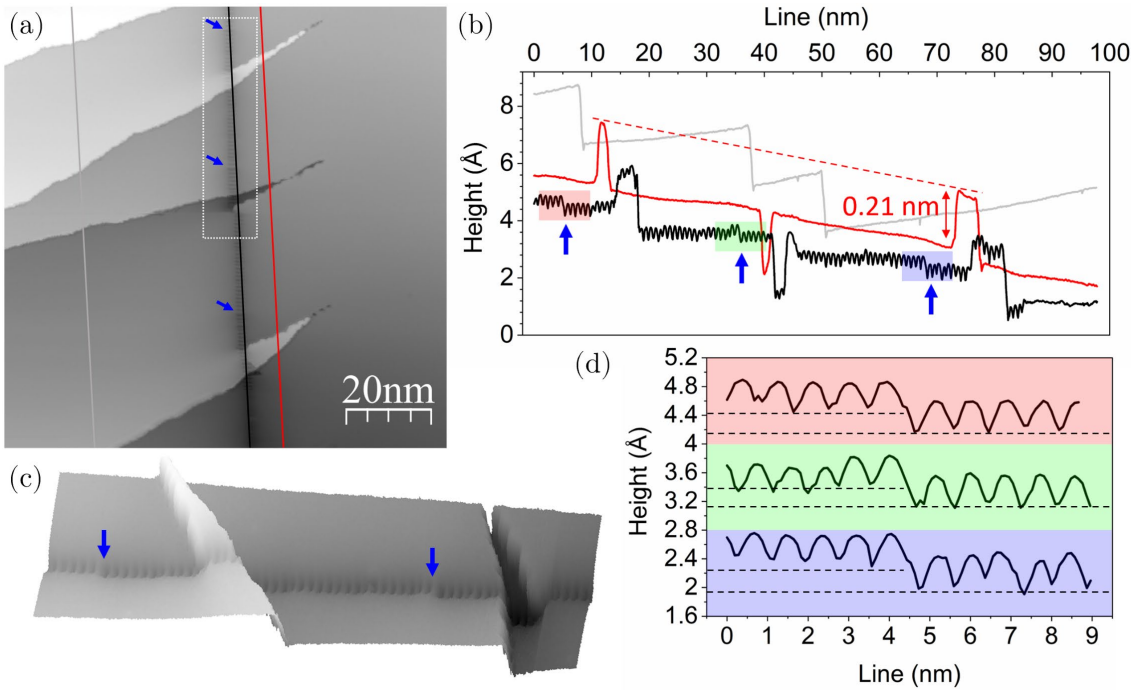

Figure 5.12: STM topography image obtained at low-temperature (77 K) showing the regions of screw dislocations crossing the grain boundary. Blue arrows indicate the local distortions at the edge dislocation as indicated by high corrugation amplitude, induced by the pinned screw dislocation on Grain 2. The line profiles are plotted in (b), showing the monatomic step height of screw dislocations on Grain 2 (red) and on Grain 1 (grey). The black line corresponds to the line profile along the grain boundary. (d) Zoom-in plots of line profiles in regions of distorted sites indicated by blue arrows and matching colours in (b), showing the down-shift of the boundary surface level, after the distortion. (c) 3D perspective view of the region marked by the box in (a), visualizes the distorted dislocations. Imaging conditions: (a) 20 pA, -0.01 V.

Of note, especially in surfaces such as those presented in Fig. 5.11, where the screw dislocations are pinned and incapable of arranging themselves freely, the equilibrium configuration might not have been achieved. Consequently, as the observations in Fig. 5.11 suggest, the effect of these pinned screw dislocations is manifested by the local vertical rearrangements of the stacking faults along the boundary. In each image, the blue arrows indicate distortions in the otherwise perfect structure of the edge dislocation array. At these points, there is an out-of-plane (normal to the surface) jump, localized at a single edge dislocation aligning with where the screw dislocations end (marked by dashed white lines) in Grain 2.

This out-of-plane dislocation jump is more clearly seen in Fig. 5.12 (a), which shows the STM topography from a different region in the surface, with a similar screw dislocation arrangement to that showed in Fig. 5.11. The full-scale STM topography image without the line profiles, which displays the grain boundary clearly is provided in the Appendix A. 7. The line profiles obtained along the boundary, across the steps and across the screw dislocation extensions in Grain 2, are presented in Fig. 5.12 (b). In order to better visualise the distortions induced by the screw dislocations, a 3D view of the area marked on Fig. 5.12 (a) is displayed in Fig. 5.12 (c). Here, the distortions on the single edge dislocations are indicated by the blue arrows, revealing the localized height increase.

As shown in Fig. 5.12 (b), the line profile obtained across the steps (grey curve) indicate a 2.1 Å corrugation amplitude, representing monatomic steps. The cross section (red curve) across the screw dislocations extending to Grain 2 also appears to have formed monatomic steps of 2.1 Å, and the difference in slope along Grain 1 and Grain 2 arising from the twist component, is clearly observed. Along the grain boundary, the deviations from the regular pattern of the dislocation sequence induced by the distorted dislocation are emphasized in Fig. 5.12 (d). In zoomed-in line profiles obtained at the three features indicated by the blue arrows along the grain boundary, with horizontal positions corresponding to each one of the three screw dislocations, it is observed that the localized distortion is followed by a 30-40 pm down-shift. Interestingly, the middle line profile (green) corresponding to the middle feature, the only one with the screw dislocation extending into a vacancy island, first proceeds by an up-shift of about 20 pm, followed by the down-shift.

In chapter 4, the influence of emergent grain boundaries on the surface manifesting as out-of-plane rotation of grains due to the inclination of the dislocation cores into low-energy configurations was explained and illustrated both for low- and high-

angle grain boundaries. While the general behaviour is dictated by the geometrical relation between the misorientation angle θ, the out-of-plane angle φ and the inclination angle ψ, the accommodation of the out-of-plane angle in low- and high-angle grain boundaries was shown to be different in terms of their spatial extents. Such that, in high-angle grain boundaries, the out-of-plane tilt is more localized, whereas in low-angle grain boundaries a global angle is observed. This difference was explained as being due to variations in the extent of the subsurface inclination of the core-shifted boundary, being deeper in LAGBs and more shallow in HAGBs[167].

To explain the effect seen in Fig. 5.11 and Fig. 5.12, we speculate that, as observed in the behaviour of out-of-plane tilting, the stress field around the LAGBs extends wider, whereas in HAGBs, it is rather more localized and more dense in a shorter range. Hence, the elastic stress field of grain boundary, with the added increase in the dislocation energy at the free surface, is likely to be disturbed by the local variations in the nearby stress field due to the presence of the screw dislocation ending nearby, resulting in an out-of-plane faceting along the grain boundary plane. From the results presented thus far, it is understood that the twist across the grain boundary is macroscopically compensated by the formation of a high density of screw dislocations. In nanoscale, as observed in Fig. 5.11 and 5.12, the presence of nearby non-equilibrium configurations of screw dislocations is reflected on the otherwise perfect arrangement of the edge dislocations along the boundary, resulting in a downshift, at locations where the boundary plane intersects the free surface. In the absence of nearby screw dislocations, a different compensation mechanism is observed along the non-interrupted boundary.

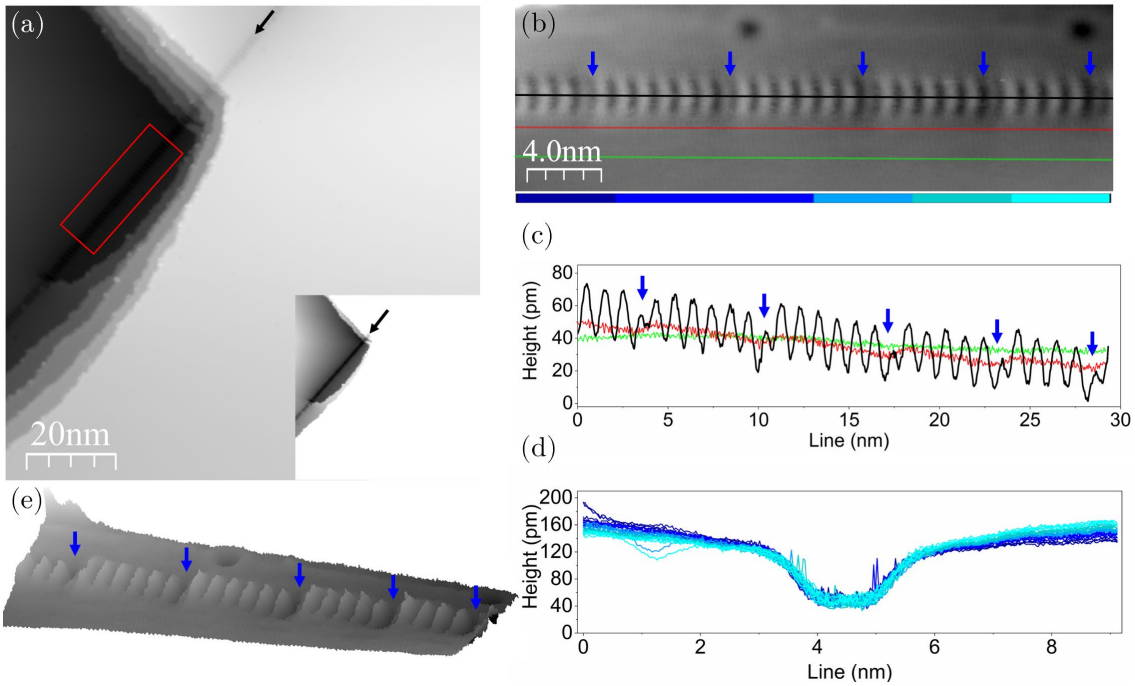

Figure 5.13: (a) STM topography image obtained at low-temperature (77 K), grain boundary is marked by the black arrow (b) close view STM topography of the area marked by the red box in (a). The suppressed dislocations are marked by the blue arrows. (c) Line profiles obtained on the surface in (b), at 1 nm (red) and 3 nm (green) distance from the boundary. Line profile along the boundary (black) shows the suppressed dislocations, marked by blue arrows. (d) Cross section measured across the boundary, over each depression between stacking faults, from left to right, as indicated by the colour scale in (b), parallel to arrows. (e) 3D perspective view of the region in (each row was aligned by median line subtraction for better visualization of suppression effect in 3D) (b). Imaging conditions: (a)-(b) 20 pA, -0.01 V.

A clear example of this is presented in Fig. 5.13. In addition, this effect can also be observed in Fig. 5.6 (also provided in Appendix A. 5), as well as in the screw dislocation-free parts of the grain boundary in Fig. 5.11 and Fig. 5.12. Due to the wide z-range in Fig. 5.13 (a), it is difficult to visualize the grain boundary and a high contrast image showing the grain boundary is provided in the Fig. 5.13 (a) inset and also in the Appendix A. 9 for better visualization. The close view STM topography image of the region marked in Fig. 5.13 (a) is displayed in Fig. 5.13 (b) for better visualization.

The line profiles recorded along the boundary, and 1 nm and 3 nm away (red and

green curves, respectively) from the boundary presented in Fig. 5.13 (c) reveal the reduced corrugation amplitude of individual dislocations in every 4-6 dislocations. These suppressed dislocations are indicated by blue arrows both in the STM topography (Fig. 5.13 (b)) and in the line profile (Fig. 5.13 (c)). These segments of dislocations generate vertical facets along the boundary with a slope corresponding to ∼0.15°, which is not observed at 3 nm distance from the boundary.

The cross sections obtained across each depression along the boundary indicate a twist of ∼0.23° between two grains, in this region. The suppression, and the inclination that follows, are less prominent on the surface at 1 nm from the boundary, and not observed at all 3 nm from the boundary, indicating that it is localized just at the boundary. Notably, there is no clear indication of a correlation between the presence of point defects and the occurrence of dislocation suppressions, although the stress field interactions cannot be ignored. We therefore attribute these suppressions creating a sawtooth-like profile along the grain boundary to the readjustment of the grain boundary plane as it meets the twist-induced sloping of surface plane, in the absence of screw dislocations. The 3D view of the same region (Fig. 5.13 (b)), illustrated in Fig. 5.13 (d), provides a better visualization of the suppressed dislocation steps along the grain boundary subjected to twist. This boundary plane vertical faceting, to our knowledge, has not been reported before. We thus emphasize that confirmation by MD simulations will be necessary to achieve a deeper understanding and to quantitatively explain these observations.

Another notable observation on the relaxed Cu bicrystal was disconnections, which occur due to the shift of the grain boundary plane to another plane, normal to the grain boundary. These line defects are frequently observed along the grain boundary, and reportedly play an important role in the dynamic processes

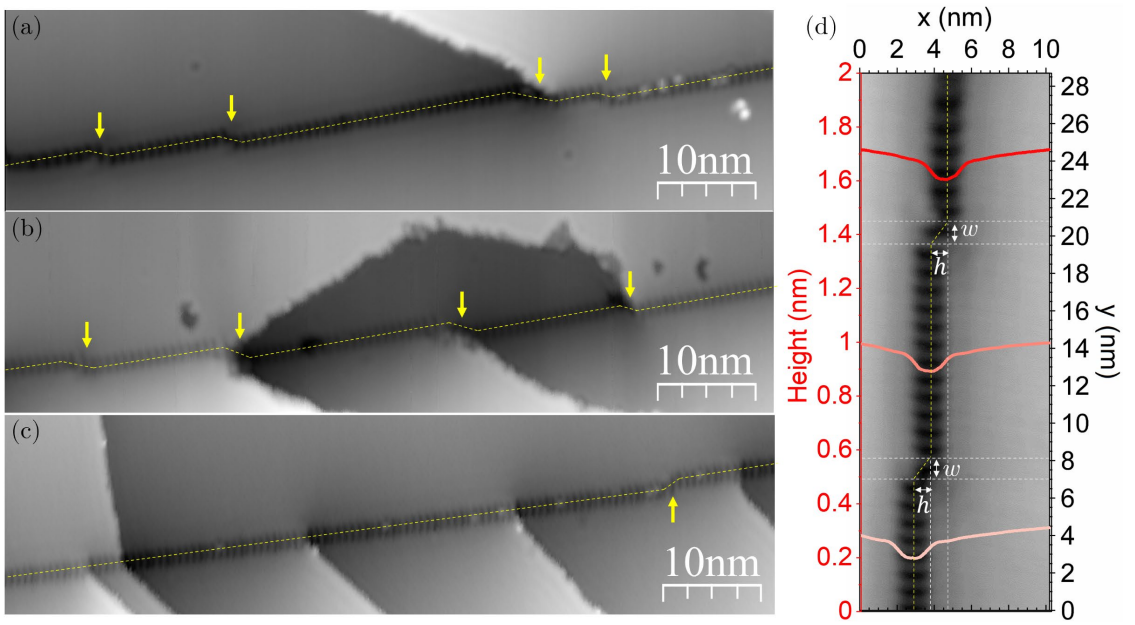

Figure 5.14: STM topography images obtained at low-temperature (77 K) showing disconnections on grain boundary. Yellow arrows indicate the disconnections along the boundary in (a), (b) and (c). (d) shows the width and height of the disconnection dislocations on a close view area in (a). Imaging conditions: (a) 22 pA, 0.2 V (b) 23 pA, 0.2 V (c) 24 pA, -0.01 V.

governing the mechanical response and plastic deformation of materials through grain boundary migration[336–339].

Presented in Fig 5.14, in-plane (lateral) shifts normal to $(1\bar{1}0)$ grain boundary plane are observed along the Cu BC boundary. At low temperature, these configurations are observed to be stable, with no evidence of further stepping or evolution. The disconnections at each STM topography image are indicated by yellow arrows, reflecting the direction of the motion. Following each disconnection, the grain boundary plane adjusts itself back to $(1\bar{1}0)$. The step height (h) and width (w) of each of the observed disconnections, except at the screw dislocation-boundary intersections, are observed to be equal in nanoscale as measured in Fig. 5.14 (d), with values of ~0.78 nm and ~1.16 nm, corresponding to a step of approximately 3 atomic planes and Burgers vector content of approximately $\sim 5a/\sqrt{2}$ along $[\bar{1}01]$, respectively.

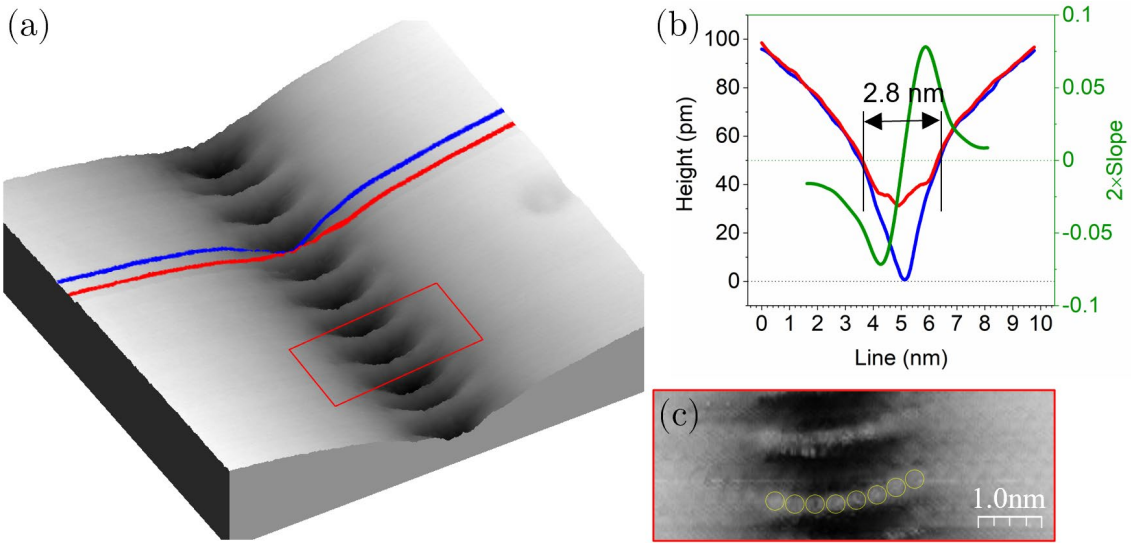

Figure 5.15: STM measurement of the emergent grain boundary groove profile, low-temperature (a) 3D view of the grain boundary, from 2D image size: 9.8×9.8 nm^2 (b) line profiles obtained across the grain boundary over the stacking fault ribbon, and between two dislocations indicated by red and blue lines, respectively. The out-of-plane angle is obtained from the calculated slope of the blue curve, indicated by green. (c) a close view STM image of the area corresponding to the area marked by the box in (a), showing the details of the 8 atoms making up the width of the stacking fault. Imaging conditions: (a) 20 pA, -0.01 V (c) 2.2 nA, -0.01 V.

5.2.3. STM measurement on emergent grain boundary in atomic scale

Fig. 5.15 (a) shows the 3D view of the periodic dislocation array along the Cu BC grain boundary. Similar to the demonstrated out-of-plane tilt as part of the restructuring of the emergent grain boundaries creating valleys and ridges on the surfaces of NC Cu (111) films, the emergent grain boundary in the Cu BC is also observed to adjust itself into a valley by the out-of-plane rotation, as indicated by the line profiles recorded across the boundary.

At the core of the 2.8 nm-wide stacking fault ribbon, the groove depth is measured approximately ~50 pm, as shown in Fig. 5.15 (b). In order to investigate the validity of this value and check the groove profile dependence on the bias, the boundary was scanned with different biases. These multiple bias scans (provided in the Appendix A. 10) show a decreasing groove profile depth with the increasing

energy, 0.5 V above the Fermi level (E_F), whereas no significant variations were observed in the corrugation amplitude measured with different biases below E_F.

Further analysis of groove profile obtained from the line profile across the boundary indicates an out-of-plane rotation of approximately φ=0.073 rad (4.18°), just below that predicted by the geometrical relation (φ=0.08, 4.58°). Here, the out-of-plane tilt of grains in Cu BC ($\theta = 13.17°$) is predominantly determined by its global angle.

The stacking fault ribbon created by the out-of-plane stepping of Shockley partials exhibits a curved structure, as shown in Fig. 5.15 (a). The grain boundary is formed by the arrangement of these stacking faults, with a characteristic periodicity determined by the degree of misorientation. The curvature of the stacking faults as viewed along x-axis, is a result of the deformed {111} planes as they extend from Grain 1 to Grain 2, to compensate the mismatch between the two grains. The close view atomic resolution STM topography image of each one of these stacking faults presented in Fig. 5.15 (c) reveals the 8 atoms with higher corrugation amplitude, making up the width of the stacking fault ribbon. These are also clearly observed in the top view of the MS simulated structure, shown in Fig. 5.18 (a).

Fig. 5.16 shows the atomic resolution STM topography image of the grain boundary. The boundary period vectors, along with the crystallographic orientations of both grains marked on the image, experimentally confirms the previously calculated bicrystal boundary configuration. In defect-free regions, the grain boundary reveals the distinct periodicity of partial dislocations with Burgers vector content $\boldsymbol{b} = a/\sqrt{2}$ in every five atomic rows, denoted as $[5, 1]$.

Consequently, the period vector of length $|\boldsymbol{p}| = a\sqrt{4 + 9 + 25}/2 = 11.16$ Å, is also confirmed by the dislocation spacing $d \approx 11.06$ Å, measured on the line profile (Fig. 5.16 (c)) obtained across the boundary in Fig. 5.16 (a) and $d \approx 11.23$ Å, measured

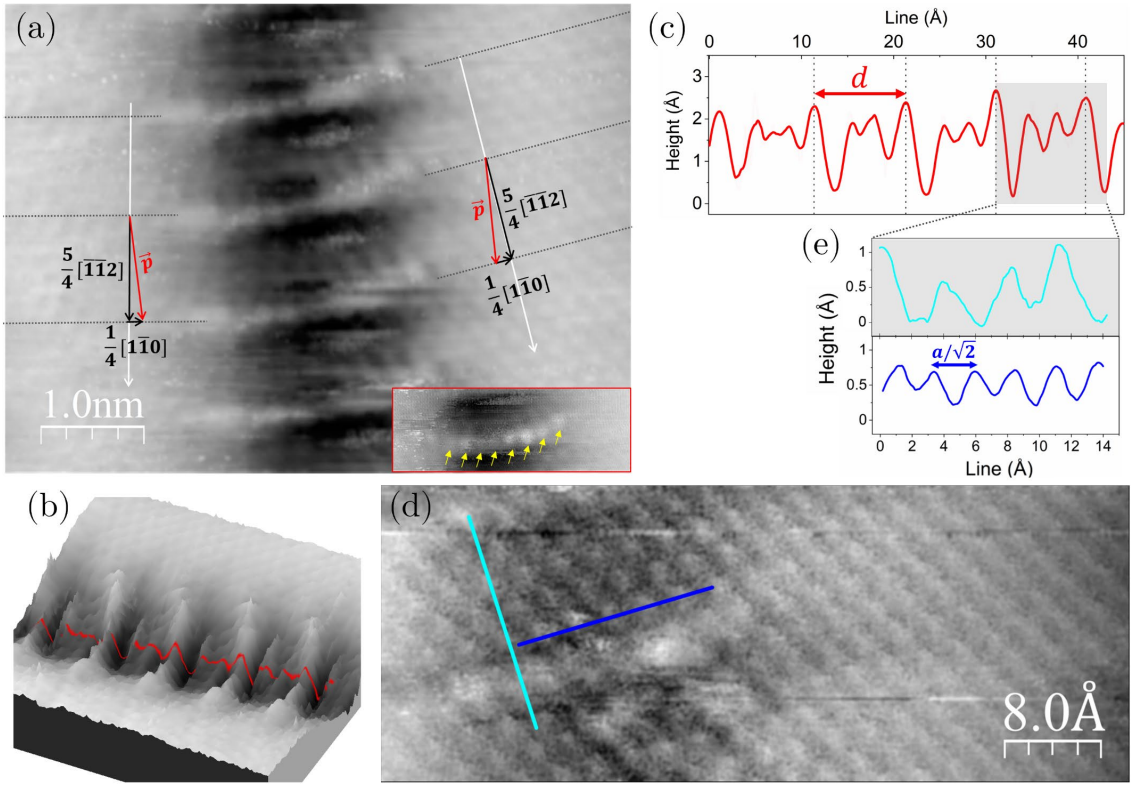

Figure 5.16: Atomic structure of the emergent grain boundary on Cu BC surface (a) Atomic resolution STM image showing the periodicity of the eGB of misorientation angle $\theta = 13.17°$, along with the boundary period vectors, boundary normal vectors and mean period vectors in both grains. The grey dotted lines are along $[1\bar{1}0]$ and white solid lines are along $[\bar{1}\bar{1}2]$, in units of the lattice constant a. The inset shows the 8 atoms above the surface level, making up the stacking fault width. (b) 3D view of (a). (c) Line profile obtained along the boundary on as marked by the red line in (b). (d) atomic resolution STM image showing the 5 atomic rows between the stacking faults. The line profiles obtained on (d), are shown in (e). Imaging conditions: (a)-(a)-inset-(b) 3 nA, -0.01 V (d) 3.1 nA, -0.01.

on the line profile (Fig. 5.16 (e)) obtained across the atomic resolution image of the region between partials. Following the methodology from chapter 4, by Frank's equation $\sin(\theta/2) = |\boldsymbol{b}|/2|\boldsymbol{p}| = |\boldsymbol{b}|/2\bar{d}$ (Eq. 3.15), the experimentally measured misorientation angle is confirmed as $\theta = 13.04°$. As shown in the Fig. 5.16 (a) inset, 8 atoms comprising the separation width of Shockley partials are observed to be higher above the 5 rows comprising the periodicity dislocations, indicated by the yellow arrows. This region of 5 atomic rows between the dislocations is better resolved in Fig. 5.16 (d), but the resolution of the high corrugation atoms is reduced. A high-contrast STM topography image is provided in the Appendix A. 11.

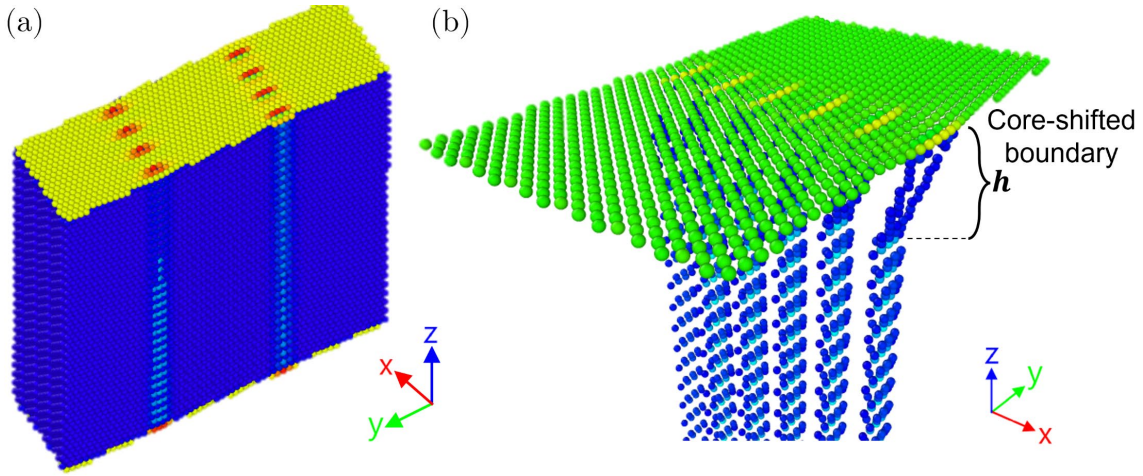

Figure 5.17: Molecular statics simulations of Cu BC grain boundary with $\theta = 13.17°$ (a) perspective view of the simulation cell (b) perspective view of the core-shifted grain boundary.

These experimental observations are also confirmed in the MS simulations. The grain boundary was compared with the simulations developed using LAMMPS to confirm the experimental results and to further understand, quantify and visualize the extent of subsurface grain boundary relaxation, as described in chapter 2.

The emergent symmetric tilt grain boundaries with subsurface inclinations leading to symmetric out-of-plane rotation of the grains, namely core-shifted emergent boundaries, can be modelled as straight wedge disclinations. The simulation cell, as displayed in Fig. 5.17 (a), containing two grain boundaries with equal and opposite misorientation ($\theta = \pm 13.17°$) was built and periodic boundary conditions in x ($\perp$ to the boundary plane normal $\widehat{\boldsymbol{N}}$), y ($\parallel$ to the boundary plane normal $\widehat{\boldsymbol{N}}$) and z (along surface normal [111]) were applied. Grain boundaries were then calculated by using embedded atom method (EAM) interatomic potential for Cu[214,215]. The geometry of the CS eGB, shown in the perspective view in Fig. 5.17 (b), of misorientation angle $\theta = 13.17°$ is described by a wedge disclination of misorientation angle $\theta = 13.17°$, rotation depth h, and width $2 \cdot h \cdot \tan \varphi/2$, where φ is the out-of-plane rotation angle. The structure is then relaxed to achieve the

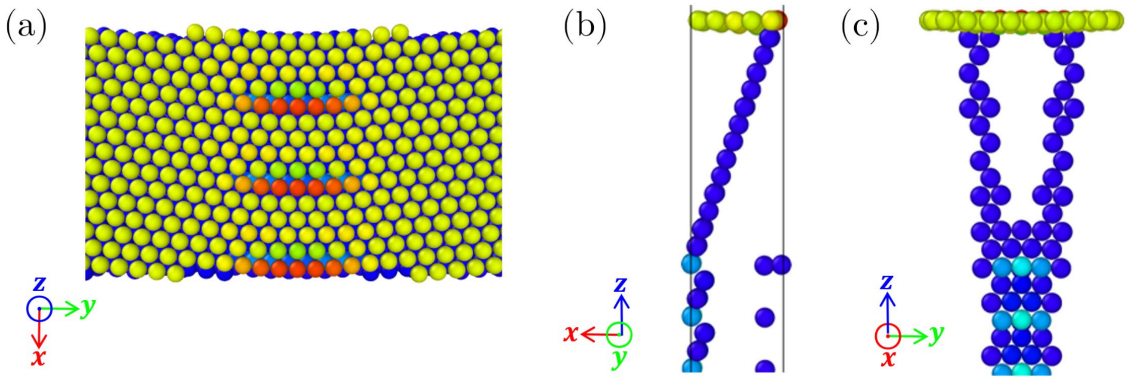

Figure 5.18: Molecular statics simulations of Cu BC grain boundary with $\theta = 13.17°$, colour coded by energy (a) top-view of a segment comprising 3 dislocations showing [5, 1] periodicity. (b) side view along y-axis shows the shifted dislocation core. The high energy atoms are deleted to show the low-energy dislocation core atoms. (c) side view along x-axis, showing the width of the stacking fault ribbon, becoming wider as approaches the surface.

lowest-energy configurations by energy minimization.

The CS eGB is built using a methodology based on an analogy to the climb mechanism of a single edge dislocation emerging on the free surface, which proceeds through the shift of the dislocation line (boundary core) along the boundary plane by the incorporation of point defects such as vacancies or interstitials to form, move, or annihilate jogs, as described in chapter 3[340]. A similar mechanism can be applied to the emergent grain boundary to shift the dislocation core, by systematically deleting or inserting core atoms, and valley or ridge emergent grain boundary structures are obtained[213].

Following this, the dislocation core of the relaxed ideal (zero atom deletions/insertions) grain boundaries in suspended films is shifted systematically to calculate the discrete energetics at each stage of the core shift, by means of the total of interfacial energy and relaxed ideal emergent grain boundary energies as a function of the number of deleted/inserted atoms. Through this method, the rotation depth (due to core-shift), as well as the volume to which it corresponds, can be calculated in terms of the geometry of the wedge-shape disclination.

The optimized core-shifted emergent grain boundary structure obtained in MS simulations, visualized in OVITO and colour coded by energy, are shown in Fig. 5.18. This restructured configuration corresponding to the optimized depth of $h =$ 2.49 nm is obtained upon deletion of a total of 30 atoms, as shown in the side-view in Fig. 5.18 (b). The grain boundary dislocation period of 5 atomic rows, as calculated by the period vector $\boldsymbol{p}$ using bicrystallography and measured experimentally, is also observed in the top-view of simulations as seen in Fig. 5.18 (a). The stacking fault that makes a step up on the surface, resulting in relatively higher corrugation amplitude as seen in experimental results, can also be seen in the top-view image in Fig. 5.18 (a) as higher energy atoms that are arranged periodically in every 5 atomic rows. Notably, as observed in the front-view presented in Fig. 5.18 (c), the stacking fault ribbon becomes wider as it intersects the free surface, as the Shockley partials reorienting themselves to align with the Burgers vector[317].

The optimization of h to achieve the triple junction configuration of minimum energy ($\psi = 19.5°$) for $\theta = 13.17°$ and $\varphi = 0.08°$ can be visualized more clearly in the plot presented in Fig. 5.19 (a). Here, the behaviour of the (intensive) core-shifted emergent grain boundary energy, as a function of depth h, is fitted by the parabolic equation[216],

$$\epsilon_{CSE} = u \cdot h^2 + v \cdot h + w \tag{5.1}$$

where the quadratic term $u \cdot h^2$ corresponds to the excess bulk energy due to rotation, and the linear term $v \cdot h$ is related to the interfacial energy due to grain boundary energy variation caused by the $[111] \rightarrow [112]$ shift and excess surface stress, associated with the creation of the wedge disclination. Through comparison of the quadratic term for minimum energy configurations of CS eGBs with different

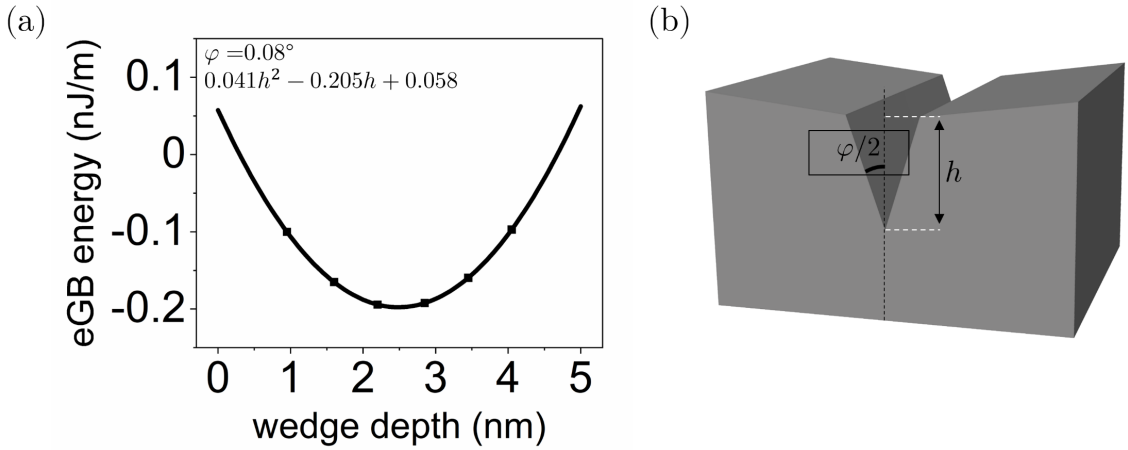

Figure 5.19: Molecular statics simulation optimization of rotation depth (a) core-shifted emergent grain boundary energy plotted as a function of the depth h, shows the fitted parabolic equation defining the interplay between elastic stress and the interfacial energy, through the quadratic term and linear term, respectively. (b) Schematic of the straight wedge disclination geometry in terms of the rotation depth and out-of-plane angle φ.

misorientation angles, the quadratic coefficient u is found to be a function of $\sim\varphi^2$, through a constant (~6.70) described by the elastic constants (shear modulus G and Poisson's ratio ν). Noticeably, in Fig. 5.19 (a), as h increases beyond the optimized depth, the CS eGBs energy increases due to the increased contribution of the excess elastic energy from the quadratic term. This demonstrates the effective interplay between the interfacial energy (determined by the linear term) and the elastic stress field introduced by out-of-plane rotation (determined by the quadratic term), hence the unavoidable nature of the restructuring behaviour of core-shifted emergent grain boundaries.

5.3. Conclusion

In this chapter, the out-of-plane tilting previously demonstrated to occur in nanocrystalline thin films was also shown to be present on the surface of a copper bicrystal comprising a single engineered grain boundary of misorientation angle $\theta =$ 13.17°. This shows that the energy minimization-driven out-of-plane tilting that comes with core-shifted emergent grain boundaries, due to the increased ability to

relax at the surface, is observed as a pronounced surface phenomenon.

The grain boundary geometry was described in terms of the five macroscopic degrees of freedom and the boundary was constructed by in-plane rotation of the two grains by $\theta/2 = \pm 6.85°$. Following the median lattice concept, grain boundary normal vectors and boundary period vectors were found as $\boldsymbol{n}' = [7\bar{8}1]$ and $\boldsymbol{p}' = [\bar{3}\bar{2}5]$ for Grain 1, and similarly $\boldsymbol{n} = [8\bar{7}\bar{1}]$ and $\boldsymbol{p} = [\bar{2}\bar{3}5]$ for Grain 2. The SEM and EBSD characterizations of the Cu BC sample revealed the macroscopically uniform grain boundary located approximately in the centre of the sample with uniformly [111] textured surface. The disorientation angle frequency distribution displayed a misorientation angle of θ~13°. A 2D layer of OHC copper oxide was found to form on the Cu BC at early stages of *in situ* cleaning. This low-oxygen-content form of 2D ordered copper oxide was localized around the grain boundary and nearby steps, indicating the high reactivity at these sites due to the high energy associated with the high degree of disorder.

On clean Cu BC surface at room temperature, the surface was frequently observed to be undergoing dynamic changes, especially on the regions of high step and screw dislocation density. This was attributed to the thermodynamically unstable sites evolving into thermal equilibrium configurations, at room temperature. The edges of monatomic steps of screw dislocations emanating from the grain boundary towards the grain on one side (Grain 1) were observed to readjust and move past the boundary, transmitting the screw dislocation to the other grain (Grain 2). Once this occurred and a metastable configuration was achieved, the extent of dynamics near the boundary was observed to reduce significantly and was limited to minor adjustments of the step edges at kink sites. In configurations where dynamics were minimized, a distinct phase was observed to accompany the relaxation near the grain boundary, with a periodicity similar to that of 9R phase.

At low temperature, the STM measurements revealed the significance of the twist in the Cu BC. It was found that, in the presence of incomplete screw dislocations terminating nearby, the grain boundary down-shifts by 30-40 *pm*. This down-shift was observed to begin at a single dislocation horizontally aligned with the screw dislocation step end, and no other down-shift was observed until another screw dislocation is seen. This is thought to be the grain boundary plane compensating as part of relaxation in response to the variations in the nearby stress field.

Any misorientation arising from the twist of the grains is compensated by the screw dislocations at the grain boundary, where two grains meet. An alternative mechanism was observed to occur at the boundary, in regions free of screw dislocations and where the grain boundary is not interrupted by the presence of screw dislocations. Here, the twist is not compensated by the screw dislocations. Rather, it is compensated by the out-of-plane readjustments at the grain boundary. This process was observed to occur by the suppression of a dislocation once in every 4-6 dislocations along the boundary, realigning the boundary plane into a sawtooth-like configuration as it emerges on the surface. Currently, however, the periodicity and its variational dependence, as well as the atomic scale readjustment of this relaxation are not yet clarified.

The analysis of grain boundary and groove profile at atomic scale confirmed the out-of-plane tilt due to subsurface dislocation core line relaxation by inclination, creating a valley. The stacking fault of 2.8 nm width was observed to be located in a groove of ~50 pm depth and out-of-plane rotation of approximately φ=0.073 rad (4.18°) was measured. The characteristic periodicity of Cu BC $\theta = 13.17°$ is verified by the atomic resolution STM topography imaging as [5,1], corresponding to one dislocation in every 5 rows. The measured dislocation spacing of $d \approx 11.06$ Å was observed to be in good agreement with the boundary period vector of length $|\boldsymbol{p}| =$

11.16 Å, as calculated by the median lattice in section 5.1. The close view atomic resolution STM topography of a single stacking fault in Fig. 5.12 (c) and Fig. 5.13 (a)-inset revealed the 8 atoms comprising the stacking fault to be higher than the surface level, with a higher corrugation amplitude. Considering the relatively small corrugation amplitude and lattice constant of Cu (111), the capability of resolving such small differences in corrugation amplitude was limited by the configuration and shape of the STM tip apex.

Nevertheless, these results reflect the remarkable power of STM as a tool for the investigation of emergent grain boundaries and how they interact with the free surface as they intersect.

Finally, the experimental observations were compared with the MS simulation of the core-shifted emergent grain boundary. The out-of-plane tilted, core-shifted emergent grain boundary geometry was described as a straight wedge disclination. Relaxed ideal CS eGBs on suspended films were used to create a valley from the out-of-plane tilt of grains, by deleting a single core atom from the top layers leading to the shift of the dislocation core. The low-energy CS eGB configuration with optimized rotation depth confirmed the periodicity observed in the experimental results. In addition, the subsurface structure of the core-shifted emergent grain boundary was revealed.

6. Conclusion & Future Work

The presence of grain boundaries has been regarded as a major challenge in the downscaling industrial microelectronic applications of Cu thin films due to the increased contributions to resistivity and the consequent increase in RC delay. In the past few decades, it has also been shown that grain boundaries comprising high atomic disorder, especially those that emerge at the surfaces, are of significant potential in enhancing the performance in some other applications of thin films, including the metal electrodes commonly used as electrocatalysts. These applications rely not only on the unique characteristics of grain boundaries, but also how they restructure at the triple junctions as they emerge on the surfaces of thin films.

In this thesis, the emergent [111] tilt grain boundaries on Cu (111) surfaces have been studied using scanning tunneling microscopy. Firstly, in chapter 4, the grain boundaries on the surface of 50 nm thick NC Cu films have been explored. With the aim of optimizing the surface morphology, the effect of temperature on the microstructural evolution of the thin film surface has been investigated using AFM and STM. It has been demonstrated that the surface morphology of 50 nm NC Cu films are optimized at ~380℃ and reveal an atomically clean surface with a texture comprising a rich variety of grain boundaries, whereas increasing the temperature further has been observed to initiate the breakup and dewetting of the film.

It has been shown that the grain boundaries, as they emerge at the triple junctions, introduce an out-of-plane rotation on the surface. This out-of-plane grain tilt has been demonstrated to manifest as valleys and ridges on the thin film surface, as part of the grain boundary restructuring phenomenon of core-shifted emergent grain

boundaries, driven by the minimization of the dislocation core energy.

The STM analysis of the microstructurally optimized surface of NC Cu (111) films at room temperature revealed that emergent tilt grain boundaries consist of arrays of edge dislocations, forming the stacking fault ribbon along the boundary. The width of the edge dislocations, each comprising two Shockley partials, and the spacing between them have been shown to vary depending on the degree of misorientation. The spacing between dislocations and the width of stacking fault ribbon was shown to decrease with the increasing misorientation angle, which was calculated using Frank's formula.

Through analysis of various low- and high-angle grain boundaries of valley type, it has been found that the degree of out-of-plane rotation due to restructuring varies among grain boundaries of different in-plane angle. The out-of-plane rotation of low-angle grain boundaries extend wider, whereas high-angle grain boundaries show a local groove.

Although these comparative evaluations revealed the typical trend in the restructuring behaviour of emergent grain boundaries on the surface of NC Cu thin films, accurate detection of the misorientation angle, Burgers vector and fine structure of the grain boundaries require low-temperature STM measurements to achieve atomic resolution, which was challenging at room temperature. In addition, molecular statistic simulations of each grain boundary is a powerful technique to reveal the quantitative description of the out-of-plane restructuring, as a function of the subsurface dislocation core restructuring and misorientation angle.

Secondly, in chapter 5, a copper bicrystal with an engineered grain boundary ($\theta = 13.17°$) was utilized to explore the emergent grain boundary structure, in a system where any residual stress from thin film growth process and substrate/film interface were eliminated. During the early stages of sample preparation and measurements,

any contamination was initially found to be present at the grain boundary and its vicinity, attributed to the increased reactivity of these high energy sites and low level of oxidation.

At room temperature, less stable regions of the bicrystal surface frequently revealed step dynamics. During these measurements, the readjustment of a screw dislocation via diffusion was captured dynamically, in real time. At metastable sites, while no significant dynamics were observed, a polytype phase with a periodicity similar to that of the 9R phase was found. This was attributed to the emission of Shockley partial dislocation loops as part of the relaxation near the surface at the triple junction, facilitated by the high mobility of intrinsic defects and copper atoms, at room temperature. In the future, it is aimed to simulate this mechanism using molecular dynamics, to understand the dislocation emission mechanism and the conditions that lead to this experimental observation.

At low temperature, a significant observation was vertical faceting of the boundary plane that is localized along the grain boundary itself, accommodated by the periodic vertical displacement of edge dislocations that comprise the boundary. Although this was attributed to the relaxation of the elastic strain due to the low twist component in the absence of screw dislocations, the precise degree of twist and the corresponding dislocation arrangement remains unclear, which we aim to uncover in future work.

The restructuring observed on the NC Cu thin films has also been observed on the surface of fully-relaxed well-annealed Cu (111) bicrystal, confirmed by the measured out-of-plane angle which is in good agreement with the geometrical relationship. The periodicity and misorientation angle of this emergent tilt grain boundary ([111], $\theta = 13.17°$) has been confirmed in atomic detail, and it was shown that the [111]

rows of atomic planes bend as they extend from one grain towards the other, accommodating the mismatch in a continuous and organised fashion.

Finally, the experimental results were compared with the molecular statics simulations of [111], $\theta = 13.17°$ core-shifted emergent tilt boundary, the geometry of which is described as a wedge disclination at the free surface. The optimized depth of rotation (extent of restructuring), demonstrated to correspond to the energy minimum, is determined by the interplay between the interfacial energy and the elastic stress. In the future, it would be a crucial step on the way to complete the picture of grain boundary restructuring, to confirm the subsurface restructuring using transmission electron microscopy. However, it is acknowledged that an extensive effort is required to minimize the external stress induced by lamella preparation, to allow the precise detection of the relatively shallow subsurface restructuring in the relaxed boundary.

These findings also lead the future of this research towards the exploration of the restructuring mechanism in other materials, specifically fcc metals, to further enlighten the effect of material properties and intrinsic surface stress (*i.e.*, Au (111)) on the mechanism that drives the grain boundary restructuring.

The interaction of the grain boundaries with the free surface in copper, as this work aimed to explore, facilitates the manifestation of the boundary core restructuring, at/near the surface. The grain boundary restructuring, the extent of which mainly depends on grain boundary characteristics, is expected to play a determining role in the applications of nanocrystalline thin films that rely on mechanisms governed by the surface quality, grain boundary density and character. Specifically, for the microelectronics industry relying on the electron transport mechanisms within thin film interconnects, electrocatalysis applications determined by the site-specific

selective catalytic activity, or in developing high-strength nanomaterials, it is believed that the restructuring at the grain boundaries will have a significant effect in the overall performance. Beyond completing the picture of the restructuring mechanism experimentally and theoretically, high performance nanomaterial systems can be engineered by discovering and developing methods for selective grain growth so as to enhance the density of favoured core-shifted emergent grain boundaries.

Bibliography

[1] H. Gleiter, Prog. Mater. Sci. **33**, 223 (1989).

[2] Grand View Research Inc., *Nanomaterials Market Size, Share & Trends Report* (2020).

[3] C. Suryanarayana and C.C. Koch, Hyperfine Interact. **130**, 5 (2000).

[4] W. Hoenlein, F. Kreupl, G.S. Duesberg, A.P. Graham, M. Liebau, R.V. Seidel, and E. Unger, IEEE Trans. Components Packag. Technol. **27**, 629 (2004).

[5] S.J. Chang, T.H. Meen, S.D. Prior, L.W. Ji, and S.J. Young, J. Nanomater. **2015**, (2015).

[6]*International Technology Roadmap for Semiconductors: Interconnect Summary* (2013).

[7] J.M. Martínez-Duart, R.J. Martín-Palma, and F. Agulló-Rueda, *Nanotechnology for Microelectronics and Optoelectronics* (Elsevier B.V., 2006).

[8] M. Mabrouk, D.B. Das, Z.A. Salem, and H.H. Beherei, Molecules **26**, 1 (2021).

[9] O. Rubilar, M. Rai, G. Tortella, M.C. Diez, A.B. Seabra, and N. Durán, Biotechnol. Lett. **35**, 1365 (2013).

[10] K. McNamara and S.A.M. Tofail, Adv. Phys. X **2**, 54 (2017).

[11] J. Ahlawat, R. Hooda, M. Sharma, V. Kalra, J.S. Rana, and B. Batra, Nanotechnol. Life Sci. 227 (2020).

[12] N. Asim, M. Mohammad, and M. Badiei, *Novel Nanomaterials for Solar Cell Devices* (Elsevier Inc., 2018).

[13] R. Tala-Ighil, in *Handb. Nanoelectrochemistry* (Springer International Publishing, Cham, 2015), pp. 1–18.

[14] R.G. Mariano, M. Kang, O.J. Wahab, I.J. McPherson, J.A. Rabinowitz, P.R. Unwin, and M.W. Kanan, Nat. Mater. **20**, 1000 (2021).

[15] R.G. Mariano, K. McKelvey, H.S. White, and M.W. Kanan, Science (80-.). **358**, (2017).

[16] C.W. Li, J. Ciston, and M.W. Kanan, Nature **508**, 504 (2014).

[17] M. V. Landau, R. Vidruk, D. Vingurt, D. Fuks, and M. Herskowitz, Rev. Chem. Eng. **30**, 379 (2014).

[18] X. Feng, K. Jiang, S. Fan, and M.W. Kanan, ACS Cent. Sci. **2**, 169 (2016).

[19]*Semiconductor Industry Association, Interconnects Section, in International Technology Roadmap for Semiconductors (ITRS) - Interconnects* (2005).

[20] T. Watanabe, Res Mech. **11**, 47 (1984).

[21] T. Watanabe, J. Mater. Sci. **46**, 4095 (2011).

[22] T. Watanabe, Le J. Phys. Colloq. **49**, 507 (1988).

[23] S. Kobayashi, S. Tsurekawa, and T. Watanabe, Beilstein J. Nanotechnol. **7**, 1829 (2016).

[24] V. Randle, Mater. Sci. Technol. **26**, 253 (2010).

[25] V. Randle, Acta Mater. **52**, 4067 (2004).

[26] T. Watanabe and S. Tsurekawa, Acta Mater. **47**, 4171 (1999).

[27] T. Watanabe and S. Tsurekawa, J. Mater. Sci. **40**, 817 (2005).

[28] A.J. Schwartz, W.E. King, and M. Kumar, Scr. Mater. **54**, 963 (2006).

[29] A. Pineau, A. Amine Benzerga, and T. Pardoen, Acta Mater. **107**, 508 (2016).

[30] G. Palumbo, International Patent Classification C21D 8/00 8/10 C22F 1/10 1/08, no. WO 94/14986 (1994).

[31] X. Geng, S. Li, J. Heo, Y. Peng, W. Hu, Y. Liu, J. Huang, Y. Ren, D. Li, L. Zhang, and L. Luo, Adv. Funct. Mater. **32**, (2022).

[32] X. Feng, K. Jiang, S. Fan, and M.W. Kanan, J. Am. Chem. Soc. **137**, 4606 (2015).

[33] R. Jiang, J. Fu, Z. Wang, and C. Dong, Appl. Sci. **12**, (2022).

[34] W.J. Dong, J.W. Lim, D.M. Hong, J. Kim, J.Y. Park, W.S. Cho, S. Baek, and J.L. Lee, ACS Appl. Mater. Interfaces **13**, 18905 (2021).

[35] R. Bernasconi and L. Magagnin, J. Electrochem. Soc. **166**, D3219 (2019).

[36] J. Bardeen and W.H. Brattain, Phys. Rev. **74**, 230 (1948).

[37] W. Shockley, IEEE Trans. Electron Devices **23**, 597 (1976).

[38] J.S. Kilby, US3138743A (1959).

[39] J.S. Kilby, IEEE Trans. Electron Devices **23**, 648 (1976).

[40] R.N. Noyce, US2981877A (1961).

[41] G.E. Moore, Electronics **38**, 114 (1965).

[42]*The International Roadmap for Devices and Systems: More Moore* (2022).

[43] P.L. Pai and C.H. Ting, 258 (1989).

[44] C.S. Chang, K.A. Monnig, and M. Melliar-Smith, Proc. IEEE 1998 Int. Interconnect Technol. Conf. IITC 1998 **1998-June**, 3 (1998).

[45] J.R. Black, IEEE Int. Reliab. Phys. Symp. Proc. 1 (2005).

[46] I.A. Blech and C. Herring, Appl. Phys. Lett. **29**, 131 (1976).

[47] F.M. D'heurle, Proc. IEEE **59**, 1409 (1971).

[48] P.S. Ho, J. Appl. Phys. **49**, 2735 (1978).

[49] P.S. Ho and T. Kwok, Reports Prog. Phys. **52**, 301 (1989).

[50] J.J. Bart and C.M. Walter, in *20th Int. Reliab. Phys. Symp.* (IEEE, 1982), pp. 285–287.

[51] F.M. D'heurle and R. Rosenberg, in (1973), pp. 257–310.

[52] M.J. Attardo and R. Rosenberg, J. Appl. Phys. **41**, 2381 (1970).

[53] M.J. Attardo, R. Rutledge, and R.C. Jack, J. Appl. Phys. **42**, 4343 (1971).

[54] P.B. Ghate, Annu. Proc. - Reliab. Phys. 292 (1982).

[55] D. Edelstein, J. Heidenreich, R. Goldblatt, W. Cote, C. Uzoh, N. Lustig, P. Roper, T. McDevitt, W. Motsiff, A. Simon, J. Dukovic, R. Wachnik, H. Rathore, R. Schulz, and L. Su, Tech. Dig. - Int. Electron Devices Meet. IEDM **4**, 773 (1997).

[56] T. Takewaki, T. Ohmi, and T. Nitta, Dig. Tech. Pap. - Symp. VLSI Technol. **922**, 31 (1995).

[57] S. Venkatesan, A. V. Gelatos, V. Misra, B. Smith, R. Islam, J. Cope, B. Wilson, D. Tuttle, R. Cardwell, S. Anderson, M. Angyal, R. Bajaj, C. Capasso, P. Crabtree, and S. Das, Tech. Dig. - Int. Electron Devices Meet. IEDM 769 (1997).

[58] J.D. McBrayer, R.M. Swanson, and T.W. Sigmon, J. Electrochem. Soc. **133**, 1242 (1986).

[59] K. Holloway, P.M. Fryer, C. Cabral, J.M.E. Harper, P.J. Bailey, and K.H. Kelleher, J. Appl. Phys. **71**, 5433 (1992).

[60] H. Kitada, T. Suzuki, T. Kimura, H. Kudo, H. Ochimizu, S. Okano, A. Tsukune, S. Suda, S. Sakai, N. Ohtsuka, T. Tabira, T. Shirasu, M. Sakamoto, A. Matsuura, Y. Asada, and T. Nakamura, Proc. IEEE 2007 Int. Interconnect Technol. Conf. - Dig. Tech. Pap. 10 (2007).

[61] J. Gambino, F. Chen, and J. He, Proc. Cust. Integr. Circuits Conf. 141 (2009).

[62] R.S. Smith, E.T. Ryan, C.K. Hu, K. Motoyama, N. Lanzillo, D. Metzler, L. Jiang, J. Demarest, R. Quon, L. Gignac, C. Breslin, A. Giannetta, and S. Wright, AIP Adv. **9**, (2019).

[63] D. Josell, S.H. Brongersma, and Z. Tokei, Annu. Rev. Mater. Res. **39**, 231 (2009).

[64]*Semiconductor Industry Association, Interconnects Section, in International Technology Roadmap for Semiconductors (ITRS)* (IEEE, 2007).

[65] W. Wu, S.H. Brongersma, M. Van Hove, and K. Maex, Appl. Phys. Lett. **84**, 2838 (2004).

[66]*International Technology Roadmap for Semiconductors: Interconnect* (2003).

[67] J.R. Sambles, Thin Solid Films **106**, 321 (1983).

[68] J.J. Plombon, E. Andideh, V.M. Dubin, and J. Maiz, Appl. Phys. Lett. **89**, (2006).

[69] K. Fuchs, Math. Proc. Cambridge Philos. Soc. **34**, 100 (1938).

[70] E.H. Sondheimer, *The Mean Free Path of Electrons in Metals* (1952).

[71] S.B. Soffer, J. Appl. Phys. **38**, 1710 (1967).

[72] A.F. Mayadas and M. Shatzkes, Phys. Rev. B **1**, 1382 (1970).

[73] J.R. Sambles and T.W. Preist, J. Phys. F Met. Phys. **12**, 1971 (1982).

[74] P.M.T.M. Van Attekum, P.H. Woerlee, G.C. Verkade, and A.A.M. Hoeben, Phys. Rev. B **29**, 645 (1984).

[75] K.R. Coffey, K. Barmak, T. Sun, A.P. Warren, and B. Yao, Proc. 2013 IEEE Int. Interconnect Technol. Conf. IITC 2013 13 (2013).

[76] T. Sun, B. Yao, A.P. Warren, K. Barmak, M.F. Toney, R.E. Peale, and K.R. Coffey, Phys. Rev. B - Condens. Matter Mater. Phys. **79**, 1 (2009).

[77] Y. Kitaoka, T. Tono, S. Yoshimoto, T. Hirahara, S. Hasegawa, and T. Ohba, Appl. Phys. Lett. **95**, 1 (2009).

[78] T.H. Kim, X.G. Zhang, D.M. Nicholson, B.M. Evans, N.S. Kulkarni, B. Radhakrishnan, E.A. Kenik, and A.P. Li, Nano Lett. **10**, 3096 (2010).

[79] H. Bishara, S. Lee, T. Brink, M. Ghidelli, and G. Dehm, ACS Nano **15**, 16607 (2021).

[80] G. Yang and S.J. Park, Materials (Basel). **12**, (2019).

[81] C.E. Carlton and P.J. Ferreira, Acta Mater. **55**, 3749 (2007).

[82] S.N. Naik and S.M. Walley, J. Mater. Sci. **55**, 2661 (2020).

[83] R.W. Armstrong, Metals (Basel). **9**, 1 (2019).

[84] C. Hahn, T. Hatsukade, Y.G. Kim, A. Vailionis, J.H. Baricuatro, D.C. Higgins, S.A. Nitopi, M.P. Soriaga, and T.F. Jaramillo, Proc. Natl. Acad. Sci. U. S. A. **114**,

5918 (2017).

[85] Y. Hori, R. Takahashi, Y. Yoshinami, and A. Murata, J. Phys. Chem. B **101**, 7075 (1997).

[86] A. Verdaguer-Casadevall, C.W. Li, T.P. Johansson, S.B. Scott, J.T. McKeown, M. Kumar, I.E.L. Stephens, M.W. Kanan, and I. Chorkendorff, J. Am. Chem. Soc. **137**, 9808 (2015).

[87] S. Choudhary, J.V.N. Sarma, S. Pande, S. Ababou-Girard, P. Turban, B. Lepine, and S. Gangopadhyay, AIP Adv. **8**, (2018).

[88] L. De Los Santos Valladares, D.H. Salinas, A.B. Dominguez, D.A. Najarro, S.I. Khondaker, T. Mitrelias, C.H.W. Barnes, J.A. Aguiar, and Y. Majima, Thin Solid Films **520**, 6368 (2012).

[89] H. Derin and K. Kantarli, Appl. Phys. A Mater. Sci. Process. **75**, 391 (2002).

[90] V. Figueiredo, E. Elangovan, G. Gonçalves, P. Barquinha, L. Pereira, N. Franco, E. Alves, R. Martins, and E. Fortunato, Appl. Surf. Sci. **254**, 3949 (2008).

[91] A.O. Musa, T. Akomolafe, and M.J. Carter, Sol. Energy Mater. Sol. Cells **51**, 305 (1998).

[92] G. Papadimitropoulos, N. Vourdas, V.E. Vamvakas, and D. Davazoglou, J. Phys. Conf. Ser. **10**, 182 (2005).

[93] F. Marabelli, G.B. Parravicini, and F. Salghetti-Drioli, Phys. Rev. B **52**, 1433 (1995).

[94] J. Ghijsen, L.H. Tjeng, J. van Elp, H. Eskes, J. Westerink, G.A. Sawatzky, and M.T. Czyzyk, Phys. Rev. B **38**, 11322 (1988).

[95] F.A. Akgul, G. Akgul, N. Yildirim, H.E. Unalan, and R. Turan, Mater. Chem. Phys. **147**, 987 (2014).

[96] S.M. Merchant, S.H. Kang, M. Sanganeria, B. Van Schravendijk, and T. Mountsier, Jom **53**, 43 (2001).

[97] H. Ohmi, J. Sato, Y. Shirasu, T. Hirano, H. Kakiuchi, and K. Yasutake, ACS Omega **4**, 4360 (2019).

[98] J. Ruzyłło, T. Hattori, R.L. Opila, and R.E. Novak, *Cleaning Technology in Semiconductor Device Manufacturing VIII* (The Electrochemical Society, Inc., 2004).

[99] A.N. Saxena, *Invention of Integrated Circuits* (World Scientific Publishing Co. Pte. Ltd., 2009).

[100] T. Gupta, *Copper Interconnect Technology* (Springer New York, New York, NY,

2009).

[101] R. Tadepalli and C. V. Thompson, Proc. IEEE 2003 Int. Interconnect Technol. Conf. IITC 2003 36 (2003).

[102] K.L. Chavez and D.W. Hess, J. Electrochem. Soc. **148**, G640 (2001).

[103] J.R. Davis, *Metals Handbook*, 2nd ed. (ASM International, 1998).

[104] N.D. Altieri, J.K.-C. Chen, L. Minardi, and J.P. Chang, J. Vac. Sci. Technol. A Vacuum, Surfaces, Film. **35**, 05C203 (2017).

[105] G.H. Chan, J. Zhao, E.M. Hicks, G.C. Schatz, and R.P. Van Duyne, Nano Lett. **7**, 1947 (2007).

[106] Y.J. Lee, T.T. Ly, T. Lee, K. Palotás, S.Y. Jeong, J. Kim, and A. Soon, Appl. Surf. Sci. **562**, (2021).

[107] C. Gattinoni and A. Michaelides, Surf. Sci. Rep. **70**, 424 (2015).

[108] T. Matsumoto, R.A. Bennett, P. Stone, T. Yamada, K. Domen, and M. Bowker, Surf. Sci. **471**, 225 (2001).

[109] S. Matencio, E. Barrena, and C. Ocal, Phys. Chem. Chem. Phys. **18**, 33303 (2016).

[110] Y.J. Kim, D. Kim, Y. Kim, Y. Jeong, B. Jeong, and J.Y. Park, (2023).

[111] J. Bloch, D.J. Bottomley, S. Janz, H.M. Van Driel, and R.S. Timsit, J. Chem. Phys. **98**, 9167 (1993).

[112] F. Jensen, F. Besenbacher, E. Lægsgaard, and I. Stensgaard, Surf. Sci. **259**, L774 (1991).

[113] F. Jensen, F. Besenbacher, and I. Stensgaard, Surf. Sci. **269**–**270**, 400 (1992).

[114] G. Zhou, L. Wang, and J.C. Yang, J. Appl. Phys. **97**, (2005).

[115] Z. Han, L. Lu, H.W. Zhang, Z.Q. Yang, F.H. Wang, and K. Lu, Oxid. Met. **63**, 261 (2005).

[116] B. Maack and N. Nilius, Phys. Status Solidi Basic Res. **257**, 1 (2020).

[117] R. Abbaschian, L. Abbaschian, and R.E. Reed-Hill, *Physical Metallurgy Principles*, 4th ed. (Cengage Learning, 2009).

[118] J.E. Burke and D. Turnbull, Prog. Met. Phys. **3**, (1952).

[119] M. Ohring, *Materials Science of Thin Films: Deposition and Structure*, 2nd ed. (Academic Press, New Jersey, 2002).

[120] D.J. Srolovitz and S.A. Safran, J. Appl. Phys. **60**, 247 (1986).

[121] M.J. Rost, Phys. Rev. B - Condens. Matter Mater. Phys. **87**, 1 (2013).

[122] D. Amram, L. Klinger, N. Gazit, H. Gluska, and E. Rabkin, Acta Mater. **69**, 386 (2014).

[123] R. Saxena, M.J. Frederick, G. Ramanath, W.N. Gill, and J.L. Plawsky, Phys. Rev. B - Condens. Matter Mater. Phys. **72**, 1 (2005).

[124] T. Nolan, R. Beyers, and R. Sinclair, MRS Proc. **202**, 95 (1990).

[125] W.W. Mullins, J. Appl. Phys. **28**, 333 (1957).

[126] A. Tsoga and P. Nikolopoulos, J. Am. Ceram. Soc. **77**, 954 (1994).

[127] B. Chalmers, R. King, R. Shuttleworth, and P.R.S.L. A, Proc. R. Soc. London. Ser. A. Math. Phys. Sci. **193**, 465 (1948).

[128] W.W. Mullins and P.G. Shewmon, Acta Metall. **7**, 163 (1959).

[129] R.R. Hough, Scr. Metall. **4**, 559 (1970).

[130] P. Tritscher and P. Broadbridge, Proc. R. Soc. London. Ser. A Math. Phys. Sci. **450**, 569 (1995).

[131] D.B. Butrymowicz, J.R. Manning, and M.E. Read, J. Phys. Chem. Ref. Data **2**, 643 (1973).

[132] C. V. Thompson, Annu. Rev. Mater. Res. **42**, 399 (2012).

[133] C.M. Müller and R. Spolenak, Acta Mater. **58**, 6035 (2010).

[134] J.Y. Choi and P.G. Shewmon, Trans. Met. Soc. **224**, (1962).

[135] P.G. Shewmon and J.Y. Choi, Trans. Met. Soc. **524**, (1963).

[136] T.P. Nolan, R. Sinclair, and R. Beyers, J. Appl. Phys. **71**, 720 (1992).

[137] M.J. Rost, D.A. Quist, and J.W.M. Frenken, Phys. Rev. Lett. **91**, 1 (2003).

[138] C. V. Thompson, Annu. Rev. Mater. Sci. **20**, 245 (1990).

[139] H. Krishna, R. Sachan, J. Strader, C. Favazza, M. Khenner, and R. Kalyanaraman, Nanotechnology **21**, (2010).

[140] W.D. Nix and B.M. Clemens, J. Mater. Res. **14**, 3467 (1999).

[141] Thomas Young, Philos. Trans. R. Soc. London. B, Biol. Sci. **95**, 65 (1805).

[142] P.R. Gadkari, A.P. Warren, R.M. Todi, R. V. Petrova, and K.R. Coffey, J. Vac. Sci. Technol. A Vacuum, Surfaces, Film. **23**, 1152 (2005).

[143] S.H. Kwon, H.J. Choe, H.C. Lee, C.W. Chung, and J.J. Lee, J. Nanosci. Nanotechnol. **13**, 6109 (2013).

[144] J.Y. Kwon, T.S. Yoon, K.B. Kim, and S.H. Min, J. Appl. Phys. **93**, 3270 (2003).

[145] D. Sonawane, A. Choudhury, and P. Kumar, Langmuir **36**, 5534 (2020).

[146] D.J. Srolovitz and M.G. Goldiner, JOM **47**, 31 (1995).

[147] H.C. Sorby, J. Iron Steel (1887).

[148] L. Bragg and J.. Nye, Proc. R. Soc. London. Ser. A. Math. Phys. Sci. **190**, 474 (1947).

[149] J.M. Hedges and J.W. Mitchell, London, Edinburgh, Dublin Philos. Mag. J. Sci. **44**, 223 (1953).

[150] S. Amelinckx, Philos. Mag. **1**, 269 (1956).

[151] T.R. Society, Proc. R. Soc. London. A. Math. Phys. Sci. **371**, 160 (1980).

[152] P.B. Hirsch, R.W. Horne, and M.J. Whelan, Philos. Mag. **1**, 677 (1956).

[153] P.B. Hirsch, Her. Russ. Acad. Sci. **76**, 430 (2006).

[154] A.J. Schwartz, M. Kumar, B.L. Adams, and D.P. Field, *Electron Backscatter Diffraction in Materials Science* (Springer US, Boston, MA, 2000).

[155] G. Duscher, M.F. Chisholm, U. Alber, and M. Rühle, Nat. Mater. **3**, 621 (2004).

[156] T. Meiners, T. Frolov, R.E. Rudd, G. Dehm, and C.H. Liebscher, Nature **579**, 375 (2020).

[157] P.R. Cantwell, T. Frolov, T.J. Rupert, A.R. Krause, C.J. Marvel, G.S. Rohrer, J.M. Rickman, and M.P. Harmer, Annu. Rev. Mater. Res. **50**, 465 (2020).

[158] P.R. Cantwell, M. Tang, S.J. Dillon, J. Luo, G.S. Rohrer, and M.P. Harmer, Acta Mater. **62**, 1 (2014).

[159] S.J. Dillon, M. Tang, W.C. Carter, and M.P. Harmer, Acta Mater. **55**, 6208 (2007).

[160] M.P. Harmer, Science (80-.). **332**, 182 (2011).

[161] A.P. Sutton and R.W. Baluffi, *Interfaces in Crystalline Materials* (Clarendon Press, 1995).

[162] P.M. Derlet and H. Vxn Swygenhoven, Philos. Mag. A Phys. Condens. Matter, Struct. Defects Mech. Prop. **82**, 1 (2002).

[163] X. Zhang, J. Han, J.J. Plombon, A.P. Sutton, D.J. Srolovitz, and J.J. Boland, Science (80-.). **357**, 397 (2017).

[164] A. Samsavar, E.S. Hirschorn, T. Miller, F.M. Leibsle, J.A. Eades, and T.C. Chiang, Phys. Rev. Lett. **65**, 1607 (1990).

[165] J. Christiansen, J. Christiansen, K. Morgenstern, K. Morgenstern, J. Schiøtz, K.W. Jacobsen, K.F. Braun, K.H. Rieder, E. Lægsgaard, and F. Besenbacher, Phys. Rev. Lett. **88**, 2061061 (2002).

[166] Á.K. Kiss, E.F. Rauch, B. Pécz, J. Szívós, and J.L. Lábár, Microsc. Microanal. **21**, 422 (2014).

[167] X. Zhang, M. Wang, H. Wang, M. Upmanyu, and J.J. Boland, Acta Mater. **242**, 118432 (2023).

[168] X. Zhao, T. Gunji, F. Lv, B. Huang, R. Ding, J. Liu, M. Luo, Z. Zou, and S. Guo, ACS Mater. Lett. **3**, 622 (2021).

[169] G. Binnig, H. Rohrer, C. Gerber, and E. Weibel, Appl. Phys. Lett. **40**, 178 (1982).

[170] G. Binnig, H. Rohrer, C. Gerber, and E. Weibel, Phys. Rev. Lett. **49**, 57 (1982).

[171] D.J. Griffiths, *Introduction to Quantum Mechanics*, 2nd ed. (Pearson, 2005).

[172] L.D. Landau and E.M. Lifshitz, *Quantum Mechanics*, 3rd ed. (Pergamon Press, Oxford, 1977).

[173] J. Bardeen, Phys. Rev. Lett. **6**, 57 (1961).

[174] H.J. Reittu, Am. J. Phys. **63**, 940 (1995).

[175] R. Wiesendanger, Scanning Probe Microsc. Spectrosc. (1994).

[176] C.J. Chen, *Introduction to Scanning Tunneling Microscopy*, 2nd ed. (Oxford University Press, 1994).

[177] J. Tersoff and D.R. Hamann, Phys. Rev. Lett. **50**, 1998 (1983).

[178] J. Tersoff and D.R. Hamann, Phys. Rev. B **31**, 805 (1985).

[179] V.M. Hallmark, S. Chiang, J.F. Rabolt, J.D. Swalen, and R.J. Wilson, Phys. Rev. Lett. **59**, 2879 (1987).

[180] C. Wöll, S. Chiang, R.J. Wilson, and P.H. Lippel, **39**, 114 (1989).

[181] J. Wintterlin, J. Wiechers, H. Brune, T. Gritsch, H. Höfer, and R.J. Behm, Phys. Rev. Lett. **62**, 59 (1989).

[182] P.H. Lippel, R.J. Wilson, M.D. Miller, C. Wöll, and S. Chiang, Phys. Rev. Lett. **62**, 171 (1989).

[183] C.J. Chen, Phys. Rev. Lett. **65**, 448 (1990).

[184] P.M. Morse and H. Feshbach, *Methods of Theoretical Physics* (McGraw-Hill, New York, 1953).

[185] C.J. Chen, J. Vac. Sci. Technol. A Vacuum, Surfaces, Film. **6**, 319 (1988).

[186] B. Voigtländer, *Scanning Probe Microscopy* (Springer Berlin Heidelberg, Berlin, Heidelberg, 2015).

[187] C. Bai, *Scanning Tunneling Microscopy and Its Application* (2000).

[188] A. Selloni, P. Carnevali, E. Tosatti, and C.D. Chen, Phys. Rev. B **31**, 2602 (1985).

[189] R.S. Becker, J.A. Golovchenko, and B.S. Swartzentruber, Phys. Rev. Lett. **55**, 987 (1985).

[190] M.F. Crommie, C.P. Lutz, and D.M. Eigler, Nature **363**, 524 (1993).

[191] J.P. Ibe, P.P. Bey, S.L. Brandow, R.A. Brizzolara, N.A. Burnham, D.P. DiLella, K.P. Lee, C.R.K. Marrian, and R.J. Colton, J. Vac. Sci. Technol. A Vacuum, Surfaces, Film. **8**, 3570 (1990).

[192] G. Binnig, C.F. Quate, and C. Gerber, Phys. Rev. Lett. **56**, 930 (1986).

[193] Y. Martin, C.C. Williams, and H.K. Wickramasinghe, J. Appl. Phys. **61**, 4723 (1987).

[194] B. Bhushan, J.N. Israelachvili, and U. Landman, Nature **374**, 607 (1995).

[195] M.P. Murrell, M.E. Welland, S.J. O'Shea, T.M.H. Wong, J.R. Barnes, A.W. McKinnon, M. Heyns, and S. Verhaverbeke, Appl. Phys. Lett. **62**, 786 (1993).

[196] V. Yanev, T. Erlbacher, M. Rommel, A.J. Bauer, and L. Frey, Microelectron. Eng. **86**, 1911 (2009).

[197] Y. Martin and H.K. Wickramasinghe, Appl. Phys. Lett. **50**, 1455 (1987).

[198] F.J. Giessibl, Science (80-.). **267**, 68 (1995).

[199] C.A.J. Putman, K.O. Van Der Werf, B.G. De Grooth, N.F. Van Hulst, and J. Greve, Appl. Phys. Lett. **64**, 2454 (1994).

[200] P.K. Hansma, J.P. Cleveland, M. Radmacher, D.A. Walters, P.E. Hillner, M. Bezanilla, M. Fritz, D. Vie, H.G. Hansma, C.B. Prater, J. Massie, L. Fukunaga, J. Gurley, and V. Elings, Appl. Phys. Lett. **64**, 1738 (1994).

[201] C. Bustamante and D. Keller, Phys. Today **48**, 32 (1995).

[202] R. García and R. Pérez, *Dynamic Atomic Force Microscopy Methods* (2002).

[203] T.R. Albrecht, P. Grütter, D. Horne, and D. Rugar, J. Appl. Phys. **69**, 668 (1991).

[204] R. García, *Amplitude Modulation Atomic Force Microscopy* (Wiley-VCH Verlag GmbH & Co. KGaA, Weinheim, Germany, 2010).

[205] G. Meyer and N.M. Amer, Appl. Phys. Lett. **57**, 2089 (1990).

[206] R.W. Carpick and M. Salmeron, Chem. Rev. **97**, 1163 (1997).

[207] S. Tegen, B. Kracke, and B. Damaschke, Rev. Sci. Instrum. **68**, 1458 (1997).

[208] R. Garcia, A.W. Knoll, and E. Riedo, Nat. Nanotechnol. **9**, 577 (2014).

[209] T. Michels and I.W. Rangelow, Microelectron. Eng. **126**, 191 (2014).

[210] B.Y.A.P. Suttont and V. Vitek, Philos. Trans. R. Soc. London A **309**, 1 (1983).

[211] Y. Mishin, M. Asta, and J. Li, Acta Mater. **58**, 1117 (2010).

[212] J. Chen, IOP Conf. Ser. Earth Environ. Sci. **128**, (2018).

[213] X. Zhang, I. Demirel, and J.J. Boland, Scr. Mater. **234**, 115562 (2023).

[214] X. Zhang and J.J. Boland, Phys. Rev. Res. **5**, 013223 (2023).

[215] Y. Mishin, M.J. Mehl, D.A. Papaconstantopoulos, A.F. Voter, and J.D. Kress, Phys. Rev. B - Condens. Matter Mater. Phys. **63**, 2241061 (2001).

[216] T. Radetic, F. Lançon, and U. Dahmen, Phys. Rev. Lett. **89**, 085502/1 (2002).

[217] A. Stukowski, Model. Simul. Mater. Sci. Eng. **18**, (2010).

[218] C.W. Oatley, J. Appl. Phys. **53**, (1982).

[219] D.C. Joy, Curr. Opin. Solid State Mater. Sci. **2**, 465 (1997).

[220] K.D. Vernon-Parry, III-Vs Rev. **13**, 40 (2000).

[221] H. Seiler, J. Appl. Phys. **54**, (1983).

[222] A.J. Wilkinson and T. Ben Britton, Mater. Today **15**, 366 (2012).

[223] F.J. Humphreys, Scr. Mater. **51**, 771 (2004).

[224] N. Yao and Z.L. Wang, *Handbook of Microscopy for Nanotechnology* (2005).

[225] T.B. Britton, J. Jiang, Y. Guo, A. Vilalta-Clemente, D. Wallis, L.N. Hansen, A. Winkelmann, and A.J. Wilkinson, Mater. Charact. **117**, 113 (2016).

[226] W. Friedrich, P. Knipping, and M. Laue, Ann. Phys. **346**, 971 (1913).

[227] M. Laue, Ann. Phys. **346**, 989 (1913).

[228] D. Hull and D.J. Bacon, *Introduction to Dislocations*, 5th ed. (Elsevier, 2011).

[229] R.A. Johnson, J. Phys. F Met. Phys. **3**, 295 (1973).

[230] F.G. Fumi, London, Edinburgh, Dublin Philos. Mag. J. Sci. **46**, 1007 (1955).

[231] H.B. Huntington and F. Seitz, Phys. Rev. **61**, 315 (1942).

[232] W.M. Lomer, Prog. Met. Phys. **8**, 255 (1959).

[233] R.A. Johnson and E. Brown, Phys. Rev. **127**, 446 (1962).

[234] V. Volterra, **24**, 401 (1907).

[235]Proc. R. Soc. London. Ser. A. Math. Phys. Sci. **199**, 376 (1949).

[236] J.A. Ewing and W. Rosenhain, Proc. R. Soc. London **65**, 85 (1899).

[237] J.A. Ewing and W. Rosenhain, Philos. Trans. R. Soc. London. Ser. A, Contain. Pap. a Math. or Phys. Character **195**, 279 (1900).

[238] E. Schmid and W. Boas, in *Kristallplastizität* (Springer Berlin Heidelberg, Berlin, Heidelberg, 1935), pp. 15–24.

[239] E. Orowan, Zeitschrift Für Phys. **89**, 634 (1934).

[240] M. Polanyi, Zeitschrift Für Phys. **89**, 660 (1934).

[241] G.I. Taylor, Proc. R. Soc. London. Ser. A, Contain. Pap. a Math. Phys. Character **145**, 362 (1934).

[242] J.M. Burgers, Proc. K. Ned. Akad. van Wet. **42**, 293 (1939).

[243] J.M. Burgers, Proc. Phys. Soc. **52**, 23 (1940).

[244] A.P. Sutton, *Physics of Elasticity and Crystal Defects* (Oxford University Press, 2020).

[245] J.P. Hirth and J. Lothe, (1982).

[246] A.. Cottrell, *Dislocations and Plastic Flow in Crystals*, 2nd ed. (Clarendon Press, Oxford, 1953).

[247] F.C. Frank, London, Edinburgh, Dublin Philos. Mag. J. Sci. **42**, 809 (1951).

[248] R.D. Heidenreich and W. Shockley, Rep. Conf. Strength Solids 27 (1948).

[249] F.C. Frank and J.F. Nicholas, London, Edinburgh, Dublin Philos. Mag. J. Sci. **44**, 1213 (1953).

[250] N. Thompson, Proc. Phys. Soc. Sect. B **66**, 481 (1953).

[251] W.T. Read, *Dislocations in Crystals* (McGraw-Hill, New York, 1953).

[252] S. Amelinckx, Le J. Phys. Colloq. **35**, (1974).

[253] R.W. Cahn, Proc. Phys. Soc. Sect. A **63**, 323 (1950).

[254] A.P. Sutton, E.P. Banks, and A.R. Warwick, Proc. R. Soc. A Math. Phys. Eng. Sci. **471**, (2015).

[255] W.T. Read and W. Shockley, Phys. Rev. **78**, 275 (1950).

[256] F.C. Frank, in *A Symp. Plast. Deform. Cryst. Solids* (Mellon Institute/US Office

of Naval Research, Pittsburgh, PA, 1950), p. 150.

[257] J.F. Nye, Acta Metall. **1**, 153 (1953).

[258] N.A. Gjostein and F.N. Rhines, Acta Metall. **7**, 319 (1959).

[259] M.L. Kronberg and F.H. Wilson, Jom **1**, 501 (1949).

[260] P. Lejcek, *Grain Boundary Segregation in Metals* (Springer Berlin Heidelberg, Berlin, Heidelberg, 2010).

[261] V. Randle, Mater. Charact. **47**, 411 (2001).

[262] D. Cheng, Z.J. Zhao, G. Zhang, P. Yang, L. Li, H. Gao, S. Liu, X. Chang, S. Chen, T. Wang, G.A. Ozin, Z. Liu, and J. Gong, Nat. Commun. **12**, 1 (2021).

[263] W. Wu and K. Maex, 2001 6th Int. Conf. Solid-State Integr. Circuit Technol. ICSICT 2001 - Proc. **1**, 416 (2001).

[264] K.J. Ganesh, A.D. Darbal, S. Rajasekhara, G.S. Rohrer, K. Barmak, and P.J. Ferreira, Nanotechnology **23**, (2012).

[265] P. Taylor, P. V Andrews, M.B. West, and C.R. Robeson, 37 (2006).

[266] S.H. Brongersma, E. Kerr, I. Vervoort, A. Saerens, and K. Maex, J. Mater. Res. **17**, 582 (2002).

[267] P. Gadkari, Growth (Lakeland) 1 (2005).

[268] J. Schiøtz, F.D. Di Tolla, and K.W. Jacobsen, Nature **391**, 561 (1998).

[269] W.M. Tong and R.S. Williams, *Kinetics of Surface Growth: Mechanisms of Smoothening and Roughening* (1994).

[270] T. Sun, B. Yao, A.P. Warren, K. Barmak, M.F. Toney, R.E. Peale, and K.R. Coffey, Phys. Rev. B - Condens. Matter Mater. Phys. **81**, 1 (2010).

[271] J. Schiøtz and K.W. Jacobsen, Nat. Mater. **16**, 1059 (2017).

[272] M.J. Rost, Phys. Rev. Lett. **99**, 1 (2007).

[273] H. Bishara, S. Lee, T. Brink, M. Ghidelli, and G. Dehm, (2021).

[274] D.G. Cahill, P. V. Braun, G. Chen, D.R. Clarke, S. Fan, K.E. Goodson, P. Keblinski, W.P. King, G.D. Mahan, A. Majumdar, H.J. Maris, S.R. Phillpot, E. Pop, and L. Shi, Appl. Phys. Rev. **1**, (2014).

[275] K.L. Merkle, J. Phys. Chem. Solids **55**, 991 (1994).

[276] M.J. Mills, M.S. Daw, G.J. Thomas, and F. Cosandey, Ultramicroscopy **40**, 247 (1992).

[277] K. Morgenstern, E. Lægsgaard, and F. Besenbacher, Phys. Rev. B - Condens.

Matter Mater. Phys. **71**, 1 (2005).

[278] Z. Qu, X. Wang, X. Shen, and H. Zhou, Nanomaterials **12**, (2022).

[279] M. Canavan, A Microscopy Study of PVD Grown Cu: Sample Preparation, Optimisation and in-Situ Analysis, Trinity College Dublin, 2018.

[280] Y. Zhu, K. Mimura, and M. Isshiki, Corros. Sci. **47**, 537 (2005).

[281] W. Gao, H. Gong, J. He, A. Thomas, L. Chan, and S. Li, Mater. Lett. **51**, 78 (2001).

[282] M. O'Reilly, X. Jiang, J.T. Beechinor, S. Lynch, C. NíDheasuna, J.C. Patterson, and G.M. Crean, Appl. Surf. Sci. **91**, 152 (1995).

[283] G. Garnaud, Oxid. Met. **11**, 127 (1977).

[284] J.E. Boggio, J. Chem. Phys. **70**, 5054 (1979).

[285] I. Platzman, R. Brener, H. Haick, and R. Tannenbaum, J. Phys. Chem. C **112**, 1101 (2008).

[286] J. Iijima, J.W. Lim, S.H. Hong, S. Suzuki, K. Mimura, and M. Isshiki, Appl. Surf. Sci. **253**, 2825 (2006).

[287] T.L. Barr, J. Phys. Chem. **82**, 1801 (1978).

[288] S.K. Chawla, B.I. Rickett, N. Sankarraman, and J.H. Payer, Corros. Sci. **33**, 1617 (1992).

[289] K.C. Russell, Acta Metall. **26**, 1615 (1978).

[290] V. Derkach, A. Novick-Cohen, and E. Rabkin, Scr. Mater. **134**, 115 (2017).

[291] P. Jacquet, R. Podor, J. Ravaux, J. Lautru, J. Teisseire, I. Gozhyk, J. Jupille, and R. Lazzari, Acta Mater. **143**, 281 (2018).

[292] L. Stolt, A. Charai, F.M. D'Heurle, P.M. Fryer, and J.M.E. Harper, J. Vac. Sci. Technol. A Vacuum, Surfaces, Film. **9**, 1501 (1991).

[293] K. Holloway and P.M. Fryer, Appl. Phys. Lett. **57**, 1736 (1990).

[294] Y. Lu, Y.X. Xiao, T. Dai, C.P. Wang, S.Y. Yang, and X.J. Liu, J. Electron. Mater. **49**, 4231 (2020).

[295] T. Laurila, K. Zeng, J.K. Kivilahti, J. Molarius, and I. Suni, Thin Solid Films **373**, 64 (2000).

[296] K.P. Yap, H. Gong, J.Y. Dai, T. Osipowicz, L.H. Chan, and S.K. Lahiri, J. Electrochem. Soc. **147**, 2312 (2000).

[297] D. Nečas and P. Klapetek, Cent. Eur. J. Phys. **10**, 181 (2012).

[298] I. Horcas, R. Fernández, J.M. Gómez-Rodríguez, J. Colchero, J. Gómez-Herrero, and A.M. Baro, Rev. Sci. Instrum. **78**, (2007).

[299] C.Y. Yang, J.S. Jeng, and J.S. Chen, Thin Solid Films **420–421**, 398 (2002).

[300] B.M.C. Oliveira, R.F. Santos, and M.F. Vieira, Appl. Sci. **12**, (2022).

[301] Y. Hasegawa, J.F. Jia, K. Inoue, A. Sakai, and T. Sakurai, Surf. Sci. **386**, 328 (1997).

[302] W.M. Haynes, J. Struct. Geol. **33**, 169 (2013).

[303] C. Kittel, *Introduction to Solid State Physics*, 5th ed. (John Wiley & Sons, Inc, 1976).

[304] M.F. Crommie, C.P. Lutz, D.M. Eigler, and E.J. Heller, Surf. Rev. Lett. **02**, 127 (1995).

[305] E.Z. Rokžitko, H.J.P. Van Midden, I. Muševič, and A. Prodan, Croat. Chem. Acta **82**, 485 (2009).

[306] P.O. Gartland, S. Berge, and B.J. Slagsvold, Phys. Rev. Lett. **28**, 738 (1972).

[307] F. Dulot, J. Eugène, B. Kierren, and D. Malterre, Appl. Surf. Sci. **162–163**, 86 (2000).

[308] M. Giesen, *Step and Island Dynamics at Solid/Vacuum and Solid/Liquid Interfaces* (2001).

[309] F. Besenbacher, Reports Prog. Phys. **59**, 1737 (1996).

[310] F. Yang, Y. Choi, P. Liu, D. Stacchiola, J. Hrbek, and J.A. Rodriguez, J. Am. Chem. Soc. **133**, 11474 (2011).

[311] C. Pérez León, C. Sürgers, and H. V. Löhneysen, Phys. Rev. B - Condens. Matter Mater. Phys. **85**, 1 (2012).

[312] F. Wiame, V. Maurice, and P. Marcus, Surf. Sci. **601**, 1193 (2007).

[313] L. Bartels, G. Meyer, and K.H. Rieder, Surf. Sci. **432**, (1999).

[314] L. Bartels, G. Meyer, and K.H. Rieder, Appl. Phys. Lett. **71**, 213 (1997).

[315] J. Friedel, Nuovo Cim. **7**, 287 (1958).

[316] Y. Hasegawa and P. Avouris, Phys. Rev. Lett. **71**, 1071 (1993).

[317] J. Engbæk, J. Schiøtz, B. Dahl-Madsen, and S. Horch, Phys. Rev. B - Condens. Matter Mater. Phys. **74**, 1 (2006).

[318] J.F. Wolf, B. Vicenzi, and H. Ibach, Surf. Sci. **249**, 233 (1991).

[319] C. Kura, M. Wakeda, K. Hayashi, and T. Ohmura, Sci. Rep. **12**, 1 (2022).

[320] K.L. Merkle, Microsc. Microanal. **3**, 339 (1997).

[321] M.A. Tschopp, G.J. Tucker, and D.L. Mcdowell, Comput. Mater. Sci. **44**, 351 (2008).

[322] D.L. Medlin, S.M. Foiles, and D. Cohen, Acta Mater. **49**, 3689 (2001).

[323] Y.F. Woguem, P. Godard, J. Durinck, and S. Brochard, Materialia **27**, (2023).

[324] U. Wolf, F. Ernst, T. Muschik, M.W. Finnis, and H.F. Fischmeister, Philos. Mag. A Phys. Condens. Matter, Struct. Defects Mech. Prop. **66**, 991 (1992).

[325] G.H. Campbell, D.K. Chan, D.L. Medlin, J.E. Angelo, and C.B. Carter, Scr. Mater. **35**, 837 (1996).

[326] F. Ernst, M.W. Finnis, A. Koch, C. Schmidt, B. Straumal, and W. Gust, Zeitschrift Fuer Met. Res. Adv. Tech. **87**, 911 (1996).

[327] J. Rittner, D. Seidman, and K. Merkle, Phys. Rev. B - Condens. Matter Mater. Phys. **53**, R4241 (1996).

[328] F. Ernst, M.W. Finnis, D. Hofmann, T. Muschik, U. Schönberger, U. Wolf, and M. Methfessel, Phys. Rev. Lett. **69**, 620 (1992).

[329] J.D. Zuo, C. He, M. Cheng, K. Wu, Y.Q. Wang, J.Y. Zhang, G. Liu, and J. Sun, Acta Mater. **174**, 279 (2019).

[330] S. Dymek and M.X. Wróbel, Mater. Chem. Phys. **81**, 552 (2003).

[331] J. Chen, W. Yan, and X.H. Fan, Trans. Nonferrous Met. Soc. China (English Ed. **19**, 108 (2009).

[332] S. Xue, Z. Fan, O.B. Lawal, R. Thevamaran, Q. Li, Y. Liu, K.Y. Yu, J. Wang, E.L. Thomas, H. Wang, and X. Zhang, Nat. Commun. **8**, 1 (2017).

[333] D.L. Medlin, G.H. Campbell, and C.B. Carter, Acta Mater. **46**, 5135 (1998).

[334] Y. Li, H. Xue, X. Zhou, F. Tang, X. Li, J. Ren, and X. Lu, Curr. Appl. Phys. **28**, 19 (2021).

[335] J. Wang, O. Anderoglu, J.P. Hirth, A. Misra, and X. Zhang, Appl. Phys. Lett. **95**, 1 (2009).

[336] J.P. Hirth, J. Phys. Chem. Solids **55**, 985 (1994).

[337] J. Han, S.L. Thomas, and D.J. Srolovitz, Prog. Mater. Sci. **98**, 386 (2018).

[338] I.S. Winter, T. Oppelstrup, T. Frolov, and R.E. Rudd, Acta Mater. **237**, 1 (2022).

[339] L. Zhang, J. Han, D.J. Srolovitz, and Y. Xiang, Npj Comput. Mater. **7**, 1 (2021).

[340] R.W. Balluffi, Phys. Status Solidi **31**, 443 (1969).

Appendix

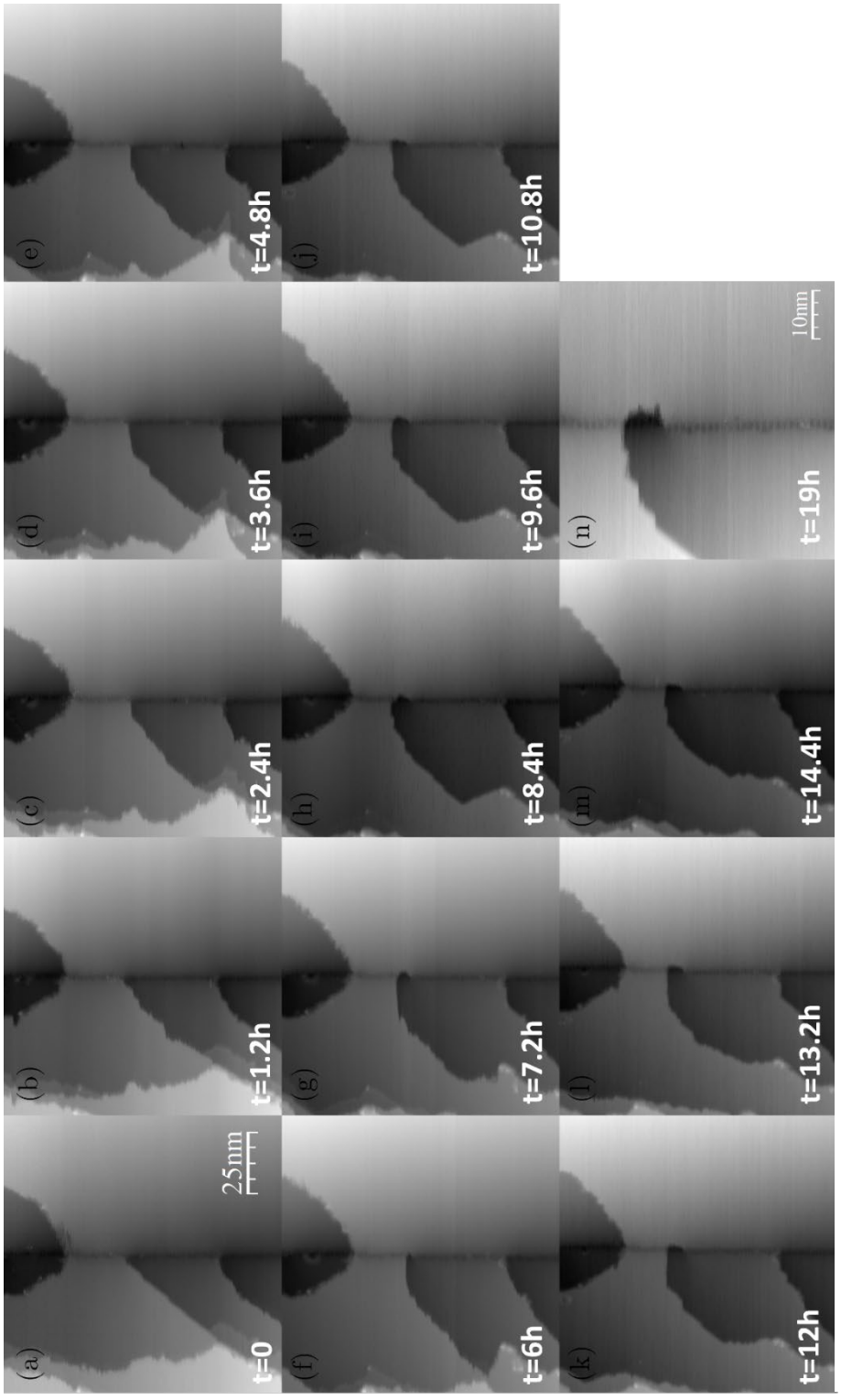

A. 1: STM topography images showing the screw dislocation dynamics across the grain boundary until a metastable configuration is reached in a total of 19 hours, at room-temperature (293 K) Imaging conditions: (a)-(n) 23 pA, 0.5 V.

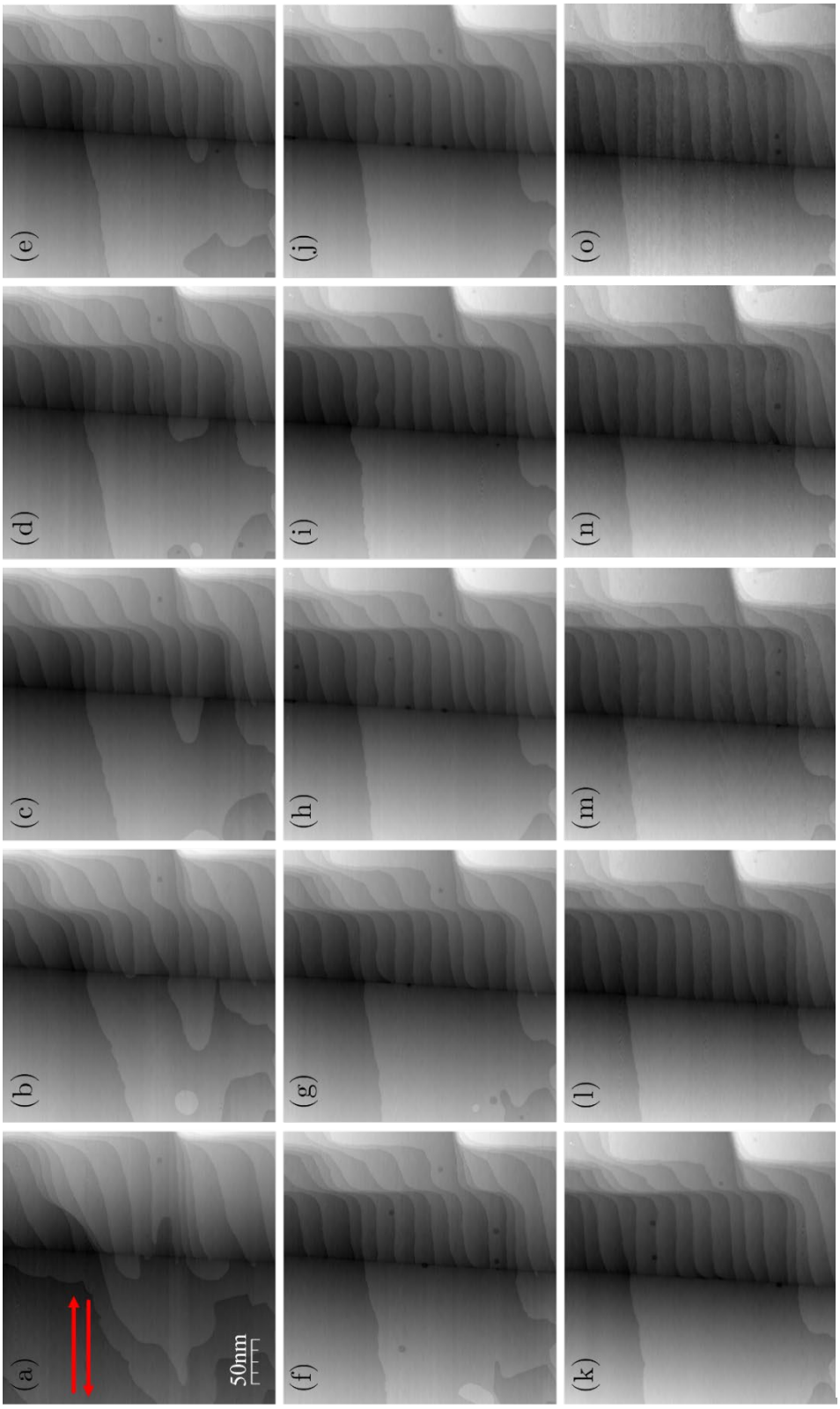

A. 2: STM topography images showing the step dynamics along the grain boundary, in a total of 8 hours, at room-temperature (293 K) Imaging conditions: (a)-(o) 50 pA, -0.2 V.

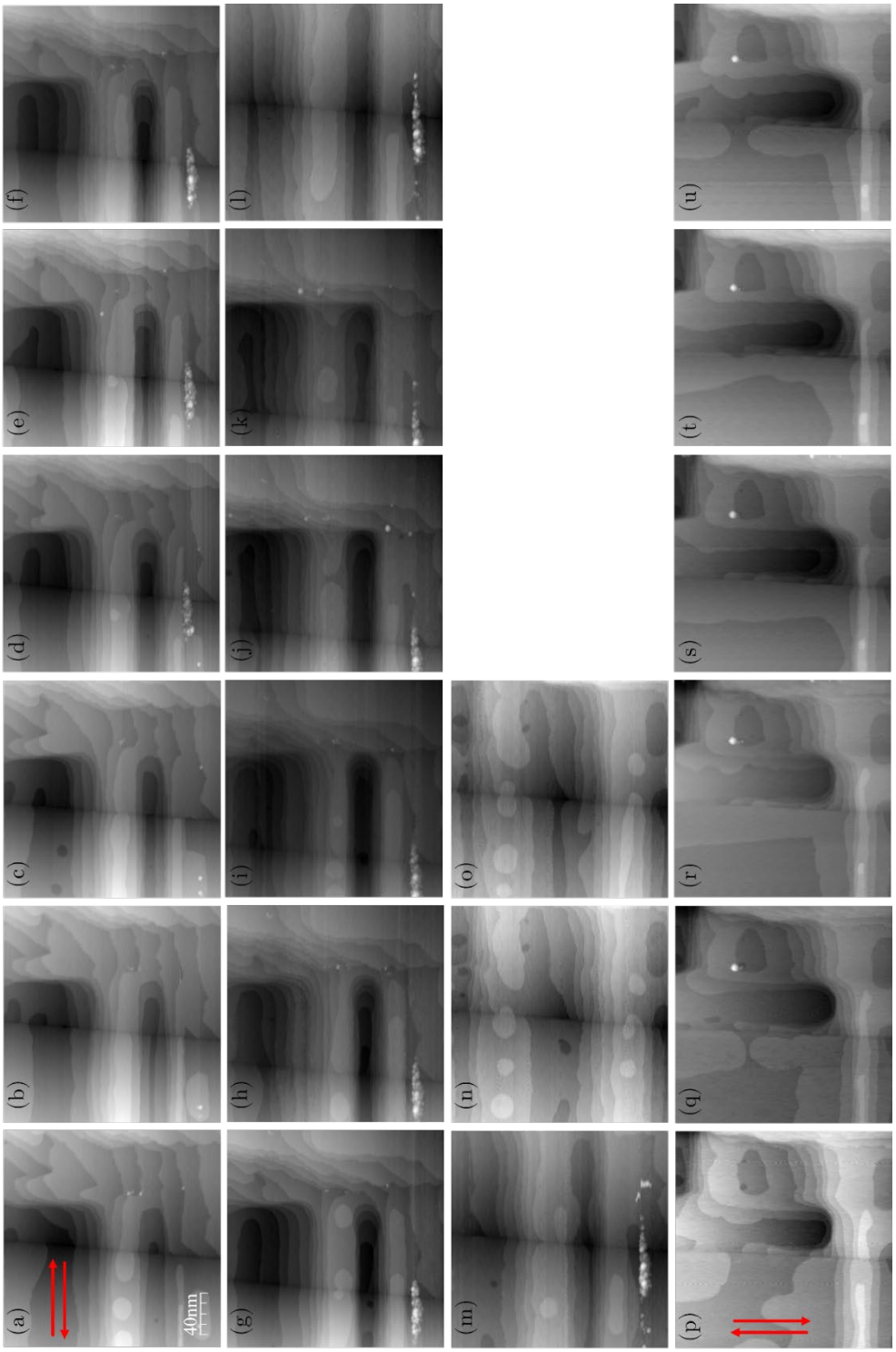

A. 3: STM topography images showing the step dynamics along the grain boundary, in a total of 11.5 hours, at room-temperature (293 K) Imaging conditions: (a)-(u) 50 pA, -0.3 V. Scan direction is perpendicular to the GB from (a) to (o), and parallel to GB from (p) to (u).

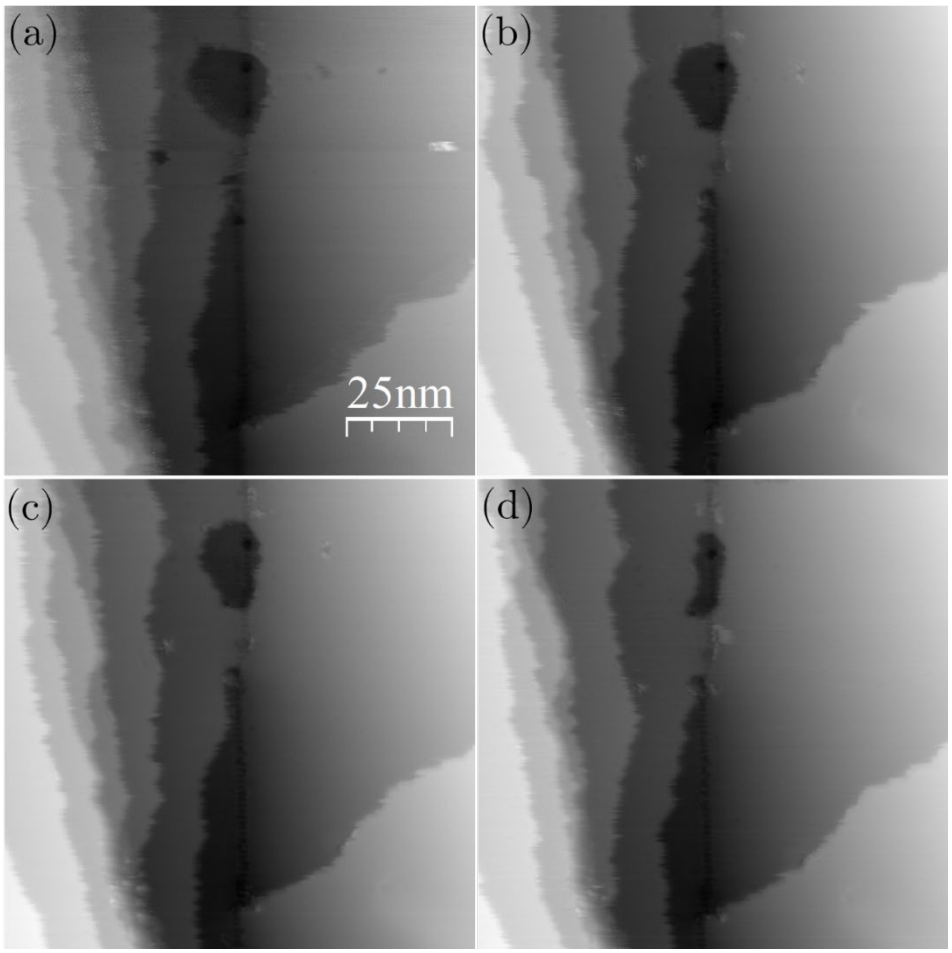

A. 4: STM topography images showing the dynamics along the grain boundary, in a total of 13 hours, at room-temperature (293 K) Imaging conditions: (a)-(d) 22 pA, -0.2 V.

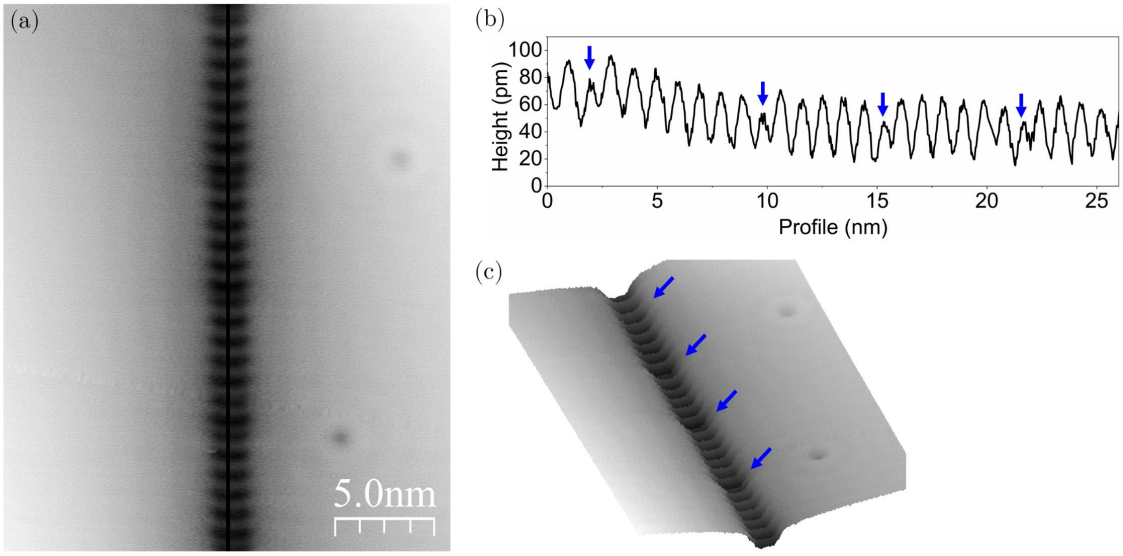

A. 5: STM topography corresponding to Fig. 5.6, with line profile along the grain boundary, suppressed dislocations are marked by blue arrows and (c) 3D view. Imaging conditions: 21 pA, -0.01 V.

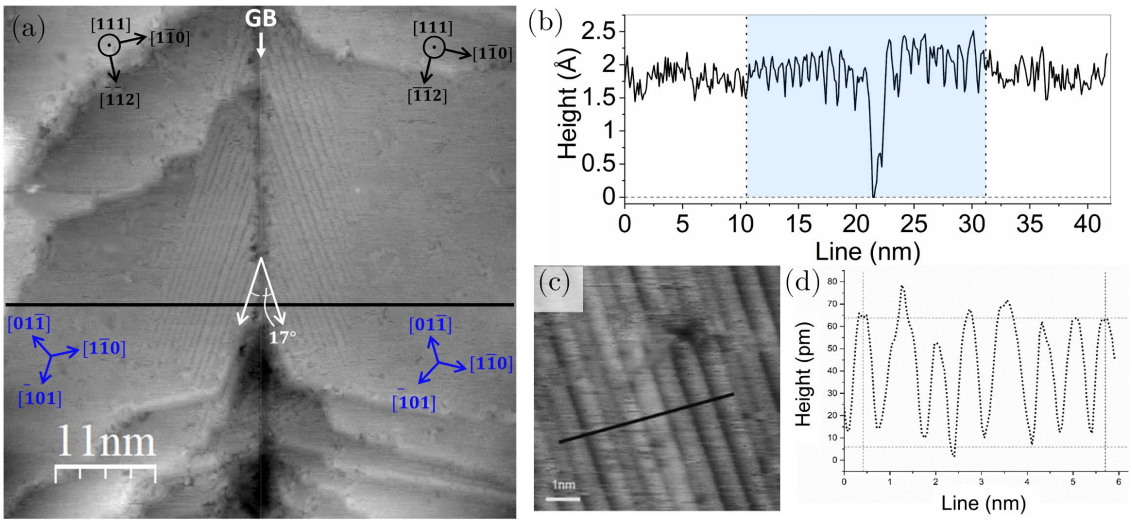

A. 6: STM topography of dislocation pattern near Cu BC ($\theta = 26.01°$) grain boundary (a) STM topography image showing the dislocation stripes emanating from the grain boundary with ~17° and the corresponding cross section in (b). (c) shows a zoom-in view and (d) line profile corresponding to the height corrugation amplitude of stripes. Imaging conditions: 20 pA, 0.1 V.

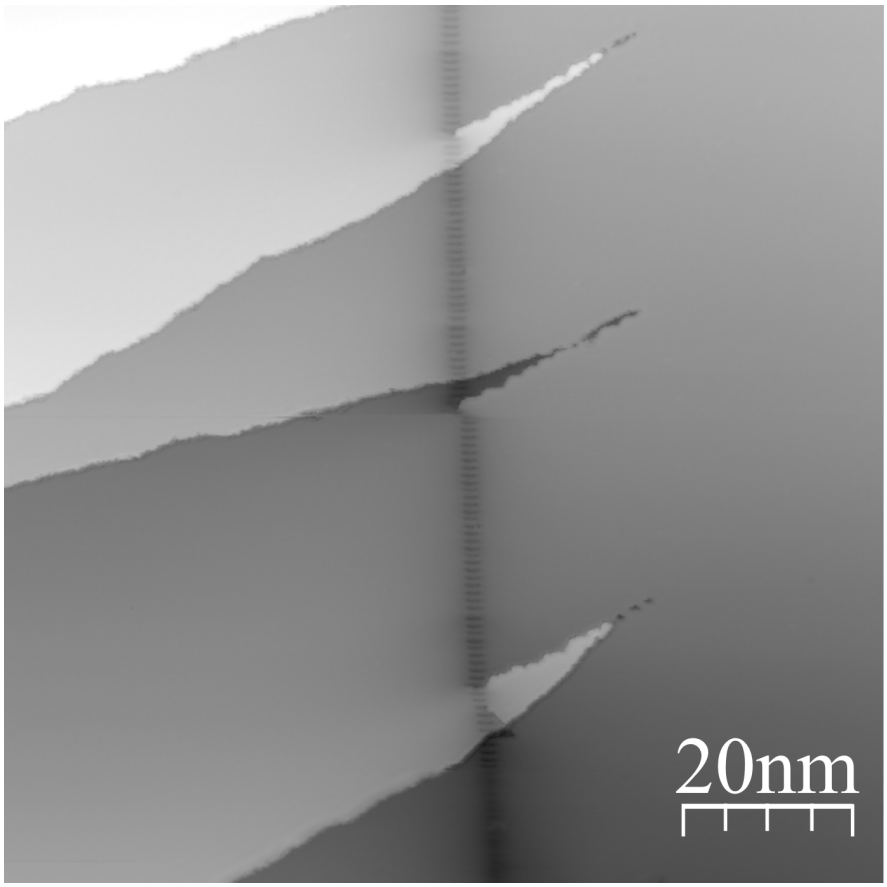

A. 7: LT-STM topography image shown in Fig. 5.12 (a), displayed without line profiles. Imaging conditions: (a) 20 pA, -0.01 V.

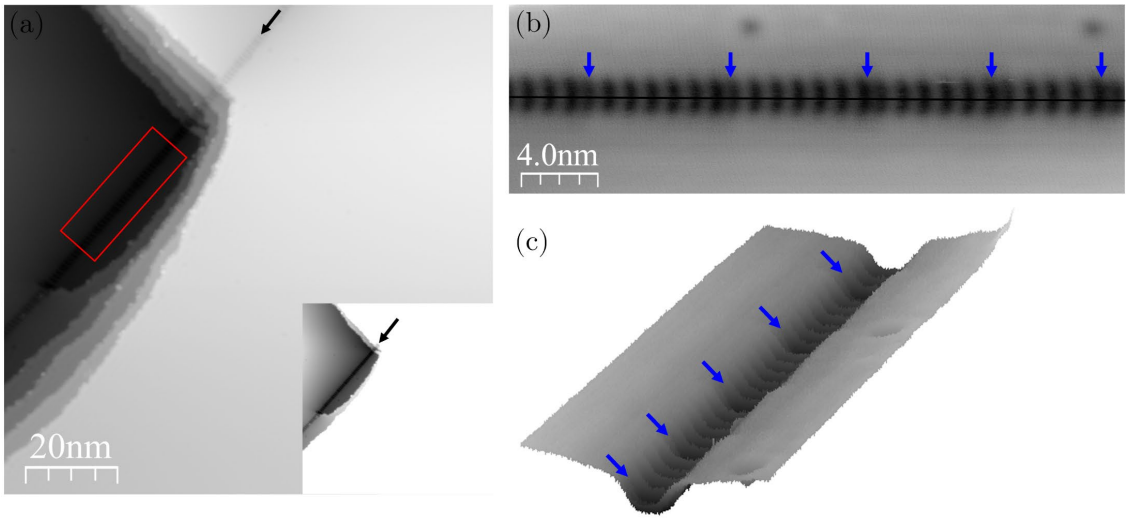

A. 8: STM topography images corresponding to Fig. 5.13, without line-correction. Suppressed dislocations are marked by blue arrows. Imaging conditions: (a)-(b) 20 pA, -0.01 V.

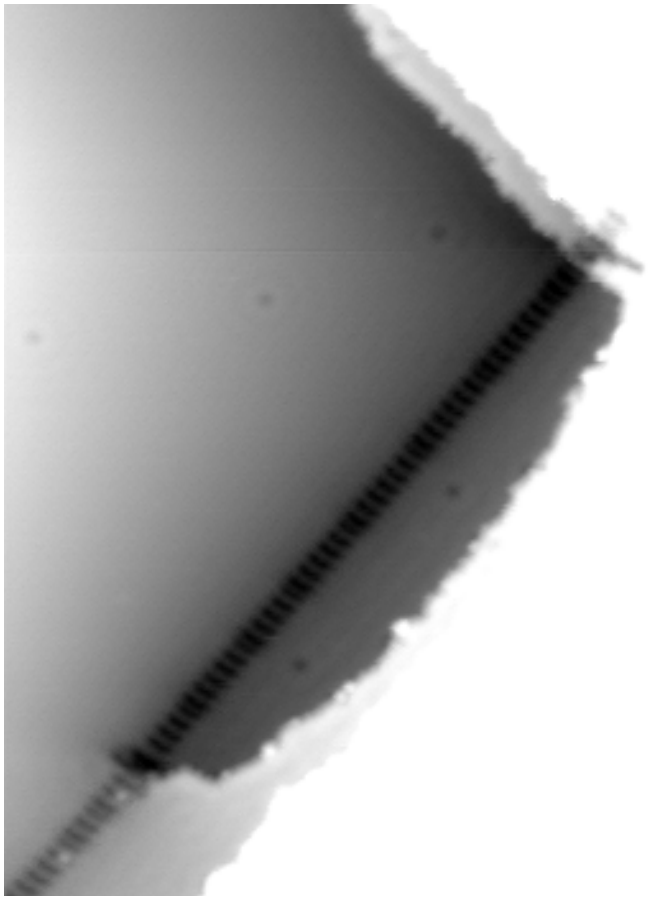

A. 9: STM topography image corresponding to Fig. 5.13 (a), displayed with high-contrast for better visualisation of the grain boundary across the steps. Imaging conditions: (a)-(b) 20 pA, -0.01 V.

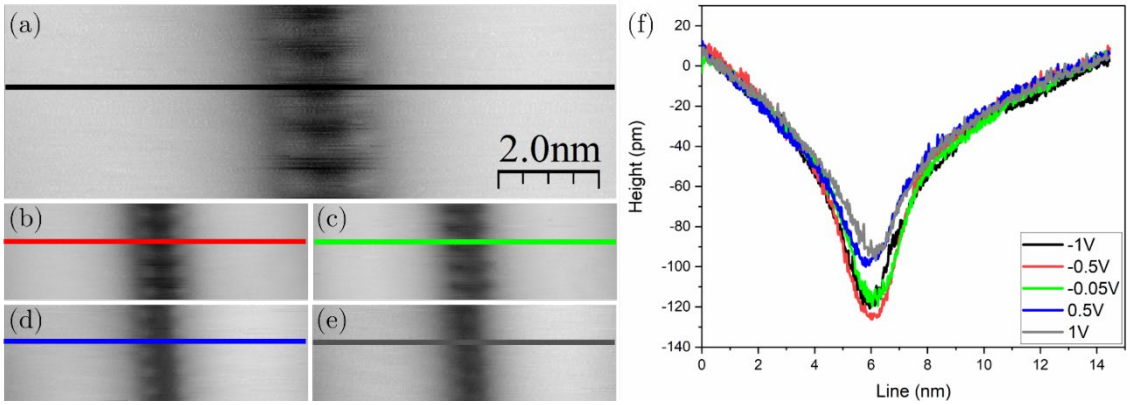

A. 10: Multiple-bias LT-STM topography images and the corresponding groove profile for each. Imaging conditions: (a) 0.3 nA, -1 V (b) 0.3 nA, -0.5 V (c) 0.3 nA, -0.05 V (d) 0.3 nA, 0.5 V (e) 0.3 nA, 1 V.

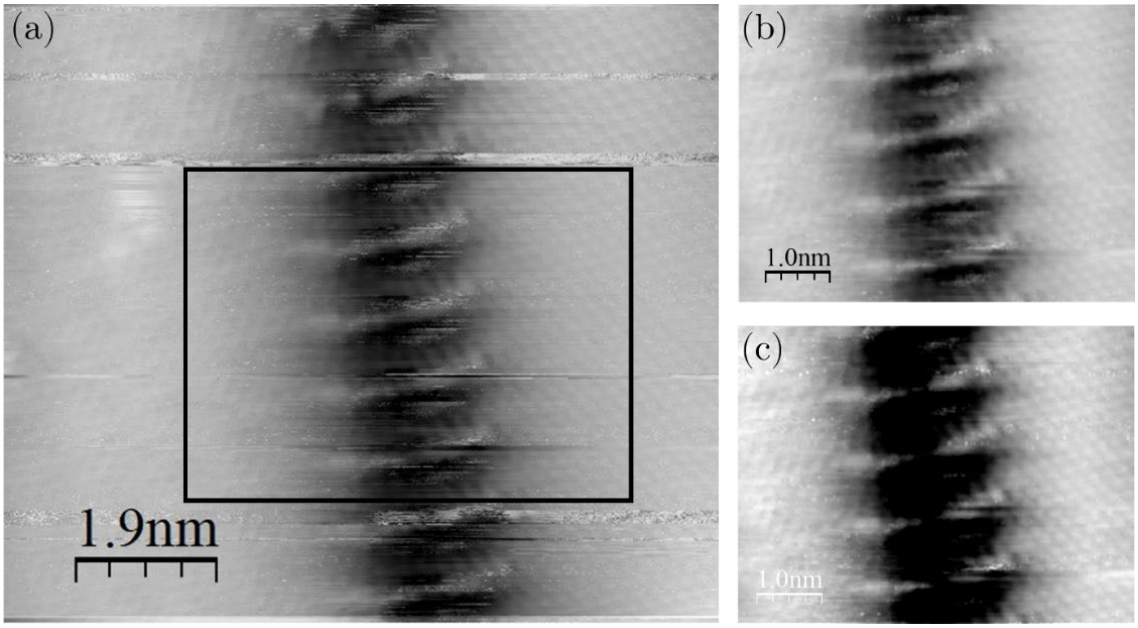

A. 11: LT-STM topography atomic-resolution images corresponding to Fig. 5.13 (a). Cropped area (b) is displayed with high-contrast in (c) Imaging conditions: 3 nA, -0.01 V.